



Royal Military Academy



Université de Liège

Numerical Assessment of Non-Lethal Projectile Thoracic Impacts

Ndompetelo Nsiampa, ir.

Dissertation submitted for the Degree of
Doctor of Engineering Science

Brussels, May 2016

Thesis Directors: Professeur Marc Pirlot (RMA)
Professeur Jean-Philippe Ponthot (ULg)

*In memory of my mother
who passed away
almost one year ago.*

*There are things that are known,
There are things that are unknown,
Between them, there are doors,
All in life is about finding keys
to unlock doors between the two worlds.
Unknown author".*

Acknowledgements

I express my gratitude to my promotor (I have learned from them that the value of great men is their simplicity):

- Professor Jean-Philippe Ponthot from Université de Liège, for his guidance, his continuous advice, his patience when things were getting tough for me. I have learned a lot in numerical methods thanks to his expertise in Computational Mechanics. Thank you, JP.

- Professor Marc Pirlot, the head of the Department ABAL who gave me, the opportunity to work with such passionate and dynamic people; a man for whom the well-being of his collaborators is one of his priorities. I can not help refer to Amar's words about him, "one can be a great chief and a good colleague. His knowledge and his enthusiasm at work are certainly the keys of the department's success". I couldn't dream better. Thank you, Marc.

Thanks to Major Alexandre Papy who worked with me on daily basis supervising this thesis. His expertise on the "Non-Lethal" field is well known, a true "maestro" who helped us as a team to play a Non-Lethal symphony of very high value. A pleasure to work with him. Thank you, Alex.

"If you want to go fast, go alone. If you want to go far, go together" says an african proverb. With this proverb, I would like to thank Dr Cyril Robbe and Dr Amar Oukara, my research teammates for their help all these years. Your collaboration was really valuable for this thesis at different levels, but especially for your experimental inputs. The experimental work you have done has provided experimental data used for the validation of the finite element models developed in this thesis. Working with you was really a pleasure. Thank you, Cyril and Amar.

Thanks to Colonel Gunther Dyckmans for his support all these years, a man who guided my first steps in the ballistic research field. Thank you, Gunther.

Thanks to Adjudant Alain Vanhove for his contribution to this thesis by providing me with the projectile pictures. He was always available to help even when he had to take the same picture many times.

Special thanks to Mr André Chabotier, my officemate for all these years in the department. Thanks to Dr. Lt-Colonel Johan Gallant for his help during the redaction of this thesis, Dr. Major Frederik Coghe for his expertise in Terminal Ballistics and Material Science, Ir. Captain-commandant Marc Maldague, Ir. Captain Elie Truyen, Alain Doucet, Alain Vanhove, Ana, the rest of my colleagues at the Department of Weapon Systems and Ballistics for your help at different levels.

Many other people helped me all these years through their continuous support both spiritually and materially, and their friendship. Time would not permit to name them all, but to name a few, Bro Albert Zumbua and his wife Fifi, Srs Denise Monteiro, Bro François Kasusula and his wife Karol, Bro Willy Kabengele and his wife Anne-Marie, Mulongo's family (Mama, Srs Constance and Srs Brigitte) and Srs Malou.

May the Most High bless you all.

Abstract

Anti-personnel Non-Lethal Weapons (NLW) are weapons that are designed to impart sufficient effect onto a person in order to deter uncivil, suspect or hazardous behaviour with a low probability of severe or fatal injury. They are used both by military and law enforcement in situations of low-intensity conflicts like riot control, access denial, peacekeeping missions i.e. situations where the use of lethal force is not appropriate nor desired. The most used of these weapons are the Kinetic Energy Non-Lethal Weapons (KENLW).

The underlying principle of KENLW is to launch a projectile with a mass varying between 5 g and 140 g at initial velocity up to 160 m/s, which by a mechanical action on the target, will cause enough physical pain to incapacitate or repel the target while minimising the risk of severe injuries. But their use is not without risk as in practice, the impacts of Kinetic Energy Non-Lethal (KENL) projectiles on the human thorax resulted in injuries, some of the them were severe even fatal. Therefore there is a need to develop methods of assessment.

These assessment methods are essential in order to help deciders in charge of non-lethal weapon procurement with technical information so they can choose the best product (weapon or projectile) available on the market; to give relevant information to the manufacturers in either developing new weapons or projectiles that are more effective, or improving the existing ones, and finally to the end-users (military or police forces) of these weapons, information on operational distance of engagement.

In practice, it has been observed that the thorax is the body region of where the impacts of KNL projectiles led to more significant injuries than other parts of the body apart from the head which is never targeted at. Therefore in the present thesis, only assessment of thoracic impacts will be investigated.

Besides tests on PMHS (Post Mortem Human Subjects), animals or human surrogates, one powerful tool that is used nowadays to assess the thoracic impacts is the finite element method (FEM). It has many advantages like the capability of accounting for complex geometries or complex material modelling and its cost-effectiveness. It also gives insight on physical variables (stresses, strains,...) inside the material

which are inaccessible by other means. It helps for a better understanding of the injury mechanism. Moreover, it helps to reduce cadavers or animal testings. In the present thesis, only FEM will be considered as tool for injury risk assessment.

On the one hand, a thorax finite element (FE) model, the SHTIM (Surrogate Human Thorax Impact Model) has been developed for the injury risk assessment. Number of assumptions has been made relative to the thorax geometry and the material characteristics are based on literature. The model has been validated thanks to the results of experiments carried out by professor C. Bir. A viscous injury criterion were defined as the parameter relevant for the occurrence of the thorax skeletal injury. This criterion is used for the prediction of the thoracic injury outcome.

On the other hand, FE models of six projectiles have been developed where most of material characteristics were taken from the literature. For the 40 mm sponge grenades, a new method of characterising the deformable nose has been developed. The projectile FE models were validated by comparing numerical results to experimental results obtained from real firing testings of the projectile against a rigid wall structure. These testings have been performed within the Department ABAL. Good correspondence was found.

Once the thorax FE model and the projectile FE models validated, numerical simulations of the impact between the thorax and the projectile were performed. Using the viscous injury criterion, risk assessment of the thorax impacts was carried out. For each projectile, a critical velocity was determined which thanks to the retardation can be linked to a minimum firing distance, the safe distance. This is the distance below which an impact will result in a higher risk of skeletal thoracic injury. This information is very important for the end-users (military, police). Moreover comparison of the performance of different KENL projectiles was carried out.

Few years ago, the Department ABAL acquired a thorax mechanical surrogate, the 3RBID (3 Rib Ballistic Impact Dummy) for the prediction of thoracic injury. It was an opportunity to compare both surrogates and to see if the SHTIM results are consistent with the 3RBID results. Good correspondence has been found especially for projectiles with larger diameter for example the 40 mm sponge grenades.

Table of Contents

Acknowledgements	v
1 Introduction	1
2 Formulation of the problem and objectives	5
2.1 Background	5
2.2 Definition	9
2.3 Technologies	10
2.4 KENLW	12
2.4.1 History of KENLW Projectiles	13
2.4.2 Projectile description and characteristics	14
2.4.2.1 Geometrical characteristics	17
2.4.2.2 Material characteristics	17
2.4.2.3 Brügger&Thomet SIR-X projectile	18
2.4.2.4 CONDOR NT901 projectile	18
2.4.2.5 Nobel Sport (NS) Spartan LE 40 Schock projectile	19
2.4.2.6 L5 projectile	19
2.4.2.7 RB1FS projectile	20
2.4.2.8 FN303 projectile	20
2.5 Literature review of effects of KENLWs	22
2.5.1 Field case reports	22

2.5.2	Conclusions	26
2.6	Goal of the thesis	27
2.7	Original contribution of this thesis	28
3	State of the Art	31
3.1	Thorax anatomy	31
3.2	Thorax injury biomechanics	33
3.2.1	Injury mechanisms	34
3.2.2	Thorax biomechanical response	35
3.2.2.1	Lesional (or medical) perspective	36
3.2.2.2	Engineering perspective	39
3.2.3	Thoracic injury criterion	43
3.2.3.1	Definition	43
3.2.3.2	Blunt criterion	45
3.2.3.3	Viscous criterion	46
3.2.4	Blunt thoracic impacts - WSU experiments	47
3.2.4.1	WSU experiments	47
3.2.4.2	Determination of biomechanical corridors	48
3.2.4.3	Determination of viscous criterion $(VC)_{max}$	49
3.2.4.4	Development of a surrogate for non-lethal thoracic impacts	51
3.2.5	Literature review of KENLW surrogates	51
3.2.5.1	KENLW mechanical or numerical surrogates	52
3.2.5.2	The mechanical Anthropomorphic Test Device (ATD)	54
3.2.5.3	The ABAL 3RBID	54
3.2.5.4	The Human Body Finite Element Models (HBFEM)	55
3.2.6	NATO Group	59
3.2.7	Conclusions	60

4	Methodology for non-lethal thoracic impacts	61
4.1	The Finite Element Method applied to impact problems	61
4.1.1	Conservation laws	62
4.1.2	Discretization methods	63
4.1.3	Types of elements	64
4.1.4	Formulation description	65
4.1.5	Contacts	66
4.1.5.1	Definitions	67
4.1.5.2	Conditions of contact and sliding	70
4.1.5.3	Contact problem	73
4.1.5.4	Penalty method	75
4.1.6	Material models	77
4.1.6.1	Linear elastic material model	78
4.1.6.2	Hyperelastic material model	80
4.1.6.3	Viscoelastic material model	84
4.1.6.4	Visco-hyperelastic material model	86
4.1.7	Material model parameter identification	86
4.2	Methodology for non-lethal thoracic impacts	89
4.2.1	Conclusions	91
5	Thorax Finite Element model	93
5.1	Development of the thorax FE model	93
5.1.1	The SHTIM model	93
5.1.2	The SHTIM model description	94
5.1.2.1	Geometry and mesh characteristics	95
5.1.2.2	Material characteristics	97
5.1.3	L5 projectile FE model	100

5.1.3.1	Geometry and mesh	100
5.1.3.2	Material characteristics	100
5.1.4	Validation	101
5.1.4.1	Setup	101
5.1.4.2	Filtering problematic	101
5.1.4.3	Results of SHTIM validation	102
5.1.4.4	Discussions	105
5.1.5	Conclusions	106
6	KENL projectile models	107
6.1	KENL projectile FE modelisation	107
6.1.1	Rigid Wall setup	109
6.1.2	Dynamic characterisation method for sponge grenades	111
6.1.2.1	Assumptions	112
6.1.2.2	Methodology	112
6.1.2.3	Practical aspects of the non-lethal projectile characterisation method	116
6.1.3	SIR-X projectile FE model	117
6.1.3.1	Experimental results	117
6.1.3.2	Geometry and mesh	123
6.1.3.3	Data preparation for material characterisation	124
6.1.3.4	Material characteristics	126
6.1.3.5	Validation	127
6.1.3.6	Discussions	128
6.1.3.7	Validation in NATO standardisation framework	133
6.1.3.8	Conclusions	135
6.1.4	CONDOR NT901projectile FE model	136
6.1.4.1	Experimental results	136

6.1.4.2	Geometry and mesh	137
6.1.4.3	Material characteristics	138
6.1.4.4	Validation	139
6.1.4.5	Discussions	140
6.1.4.6	Conclusions	144
6.1.5	Nobel Sport (NS) Spartan LE 40 Schock projectile FE model .	144
6.1.5.1	Experimental results	144
6.1.5.2	Geometry and mesh	146
6.1.5.3	Material characteristics	146
6.1.5.4	Validation	146
6.1.5.5	Discussions	147
6.1.5.6	Conclusions	152
6.1.6	FN303 projectile FE model	153
6.1.6.1	Experimental results	153
6.1.6.2	Geometry and mesh	153
6.1.6.3	Material characteristics	154
6.1.6.4	Validation	154
6.1.6.5	Discussions	156
6.1.6.6	Conclusions	157
6.1.7	RB1FS projectile FE model	158
6.1.7.1	Experimental results	158
6.1.7.2	Geometry and mesh	158
6.1.7.3	Material characteristics	159
6.1.7.4	Validation	159
6.1.7.5	Discussions	161
6.1.7.6	Conclusions	161
6.1.8	Main conclusions	162

7	Thorax Injury Risk Assessment	165
7.1	Some considerations of the evaluation process	165
7.2	Thorax impact assessment	168
7.2.1	SIR-X projectile evaluation	168
7.2.1.1	Thorax dynamics	168
7.2.1.2	Comparison of SIR-X dynamics on rigid wall and on thorax	170
7.2.1.3	SIR-X risk assessment	172
7.2.1.4	SIR-X versus assumed SIR-X rigid projectile	175
7.2.1.5	Conclusions	177
7.2.2	CONDOR projectile evaluation	179
7.2.3	NS projectile evaluation	180
7.2.3.1	NS risk assessment	180
7.2.3.2	Comparison of NS dynamics on rigid wall and on thorax	181
7.2.3.3	NS projectile versus assumed NS rigid projectile	182
7.2.3.4	Conclusions	183
7.2.4	FN303 projectile evaluation	184
7.2.4.1	FN303 risk assessment	184
7.2.4.2	Conclusions	185
7.2.5	RB1FS projectile evaluation	186
7.2.5.1	RB1FS risk assessment	186
7.2.5.2	Conclusions	187
7.2.6	L5 projectile evaluation	188
7.2.7	Summary of all projectiles	189
7.3	Comparison of SHTIM model and the 3RBID surrogate	190
7.3.1	3RBID setup	190
7.3.2	Comparison of SHTIM and 3RBID for SIR-X projectile	191

7.3.3	Comparison of SHTIM and 3RBID for all projectiles	193
7.3.3.1	Results	193
7.3.3.2	Discussions	193
7.4	Conclusions	195
8	Conclusions and avenues for future investigation	197
8.1	Aim	197
8.2	Achievements and results	197
8.3	Avenues for future investigation	199
	Bibliography	201
	Annexes	218
A	A few key results of the WSU study by C. Bir	221
B	Influence of HU and SHAPE parameters	223
C	Publications in the framework of the present thesis	227
1	As first author	227
1.1	Articles in a peer-reviewed journal	227
1.2	Conference proceedings and presentations	227
2	As co-author	228
2.1	Articles in a peer-reviewed journal	228
2.2	Conference proceedings and presentations	228
3	Works conducted as supervisor by the present thesis author	230

List of Figures

2.1	Gradual approach in the use of the force	8
2.2	Example of a force continuum scheme	9
2.3	KENLW effectiveness.	12
2.4	12 gauges projectiles+ FN303 projectile.	15
2.5	40 mm diameter projectiles	15
2.6	Launcher types.	16
2.7	Proportions of projectiles available on the market	18
2.8	40mm Sponge Grenades.	19
2.9	L5 projectiles.	20
2.10	RB1FS projectile.	21
2.11	FN303 projectile.	21
2.12	Injury repartition	24
2.13	Method for KENLW assessment.	28
3.1	Thoracic cage and internal organs	32
3.2	Thorax structure	33
3.3	Comparison of a non-lethal impact and car crash impact	34
3.4	Crush/shear and viscous injury mechanisms	35
3.5	Injury response scheme.	36
3.6	Examples of injuries from rubber bullet impacts	37
3.7	soft tissue thoracic injuries	37

3.8	Injury risk curve.	44
3.9	viscous mechanism and calculation of the injury criterion	47
3.10	Impact force on a PMHS thorax	49
3.11	PMHS thorax displacement as a function of time	50
3.12	3RBID thoracic surrogate	52
3.13	Different model types for injury assessment.	52
3.14	Examples of anthropomorphic test devices	53
3.15	ABAL-3RBID with the LED system	55
3.16	ABAL-3RBID scheme with accelerometer.	55
3.17	FEM of the human thorax and their applications	56
3.18	Comparison between the FE model and a real human torso	57
3.19	MTHOTA FE model	58
3.20	ATBM model	58
3.21	HUBYX model	59
4.1	Discretization of the body Γ	64
4.2	Eulerian, Lagrangian and ALE formulations	65
4.3	SPH formulation	66
4.4	Configurations of the two bodies in contact problem - $\Omega_0^{(i)}$: bodies in the reference (material) configuration - $\Omega^{(i)}$: bodies in the current (spatial) configuration. Adapted from [1].	68
4.5	(a) Contact zone: contact pressure on body $\Omega^{(1)}$ - (b) Friction model of Coulomb.	69
4.6	Stress-strain curves for elastic materials	78
4.7	Body motion	79
4.8	Viscoelastic materials	85
4.9	Procedures of material card generation	88
4.10	Steps for solving (dynamic) problems	88
4.11	Model building scheme.	90

4.12	Methodology for KENLW assessment.	91
5.1	Different thorax models.	94
5.2	Thorax model	95
5.3	Modelled organs	96
5.4	Load curve (LC) for the "flesh", aorta and trachea material models .	99
5.5	PVC projectile characteristics.	100
5.6	Setup for normal impacts.	102
5.7	Thorax responses for an impact velocity of 40 m/s	103
5.8	Comparison of numerical results at different velocities	104
6.1	Validation of non-lethal projectile model.	107
6.2	RW setup [2, 3].	110
6.3	Resonance of excited RW structure; Adapted from [3].	111
6.4	Schematic compressive stress-strain response for elastomeric foams [4].	113
6.5	Projectile impact dynamics characteristics.	114
6.6	Main steps for non-lethal characterisation method.	115
6.7	Experimental results of the the impact of the SIR-X projectile on RW at different impact velocities.	118
6.8	Impact sequences - main features.	120
6.9	Impact sequences - Variation of strain rate during the impact event at 58 m/s.	122
6.10	SIR-X projectile characteristics.	123
6.11	Engineering strain-strain curves for impact velocities 30 m/s, 58 m/s and 81 m/s.	125
6.12	Compressive loading curve at 58 m/s.	126
6.13	SIR-X engineering stress-strain characteristics.	127
6.14	Comparison of numerical results for the baseline data and the modi- fied baseline data taking into account tensile curve as loading curves at 58 m/s.	128

6.15	Comparison between experimental and numerical results at 58 m/s.	129
6.16	Comparison between experimental and numerical results at 30 m/s and at 81 m/s.	130
6.17	Energies of the SIR-X projectile parts at 58 m/s.	131
6.18	Ratio of total kinetic energy to initial energy at 58 m/s.	132
6.19	Comparison of internal and hourglass global energies at 58 m/s.	133
6.20	Validation of SIR-X projectile using corridors defined in [5].	135
6.21	Experimental results of the the impact of the CONDOR projectile on RW at different impact velocities.	137
6.22	CONDOR projectile characteristics.	138
6.23	CONDOR projectile nose with four holes.	138
6.24	CONDOR engineering compressive smoothed stress-strain curve.	139
6.25	CONDOR compressive loading curve derived from characteristics at 38 m/s.	140
6.26	Comparison between CONDOR experimental and numerical results at 38 m/s.	141
6.27	Comparison between CONDOR experimental and numerical results at 63 m/s and at 88 m/s.	142
6.28	Comparison of CONDOR results using the baseline loading curve (LC) and the extended loading curve	143
6.29	CONDOR hole influence: Case A-same nose density, Case B-same sabot density, Case C-actual projectile.	144
6.30	NS experimental results on RW.	145
6.31	NS projectile characteristics.	146
6.32	Loading curve for the NS projectile nose [6].	147
6.33	Comparison between NS experimental and numerical results at 36 m/s and at 60 m/s.	148
6.34	Cross-section NS impact sequences at 60 m/s.	149
6.35	Energy histories for the NS projectile at 60 m/s.	150

6.36	Velocity along the projectile longitudinal axis of node A corresponding to the projectile nose tip for an impact velocity of 60 m/s	151
6.37	Velocity of nose nodes located along the radial direction for an impact velocity of 60 m/s.	151
6.38	Experimental results of FN303 impacts on RW at different velocities.	153
6.39	FN303 projectile geometrical and mesh characteristics.	154
6.40	Comparison between FN303 experimental and numerical results for different impact velocities.	155
6.41	FN303 projectile breaking: Dynamic Increase of impact surface	157
6.42	Experimental results of RB1FS impacts on RW at different velocities.	158
6.43	RB1FS projectile characteristics.	159
6.44	Comparison between RB1FS experimental and numerical results for different impact velocities.	160
7.1	Normal impact.	167
7.2	Thorax dynamics for an impact velocity of 80 m/s.	169
7.3	Comparison of SIR-X impact dynamics on RW at 58 m/s and on thorax at 80 m/s.	170
7.4	Thorax $(VC)_{max}$ calculation for SIR-X impact velocities of 40 m/s and 80 m/s.	174
7.5	$(VC)_{max}$ for different velocities for SIR-X projectile.	175
7.6	Comparison of SIR-X impact and the corresponding rigid one impact on the thorax at 80 m/s.	176
7.7	Comparison of $(VC)_{max}$: SIR-X projectile vs SIR-X assumed rigid projectile.	177
7.8	$(VC)_{max}$ for different impact velocities of the CONDOR projectile on thorax.	179
7.9	Comparison of NS impact on thorax for 40 m/s and 80 m/s.	180
7.10	$(VC)_{max}$ for different impact velocities of the NS projectile on thorax.	181
7.11	Comparison of NS impact dynamics on RW at 36 m/s and on thorax at 40 m/s.	182

7.12	Comparison of thorax displacement and velocity at 80 m/s: NS vs assumed NS Rigid projectiles.	183
7.13	Comparison of $(VC)_{max}$: NS vs assumed NS Rigid projectiles.	183
7.14	Thorax dynamics due to the impact of FN303 projectile at 90 m/s.	184
7.15	$(VC)_{max}$ for different impact velocities of the FN303 projectile on thorax.	185
7.16	Thorax dynamics due to the impact of RB1FS projectile at 90 m/s.	186
7.17	$(VC)_{max}$ for different impact velocities of the RB1FS projectile on thorax.	187
7.18	$(VC)_{max}$ for different impact velocities of the L5 projectiles on thorax.	188
7.19	$(VC)_{max}$ summary for impact of different projectiles on thorax.	190
7.20	3RBID setup.	191
7.21	Comparison between 3RBID and SHTIM surrogates at 56 m/s and 86.5 m/s.	192
7.22	Comparison between 3RBID and numerical results for SIR-X projectile.	192
7.23	Comparison of SHTIM and 3RBID results.	194
A.1	PMHS thorax displacement at the point of impact as a function of time for impact condition B [7].	221
A.2	PMHS thorax displacement at the point of impact as a function of time for impact condition C [7].	222
B.1	SIR-X impact force on rigid wall as a function of time at $v=61$ m/s.	224
B.2	Displacement of the rear face of the SIR-X projectile as a function of time at $v=61$ m/s.	224
B.3	SIR-X impact force on rigid wall as a function of time at $v=61$ m/s.	225
B.4	Displacement of the rear face of the SIR-X projectile as a function of time at $v=61$ m/s.	225
B.5	Internal energy of the SIR-X projectile as a function of time at $v=61$ m/s.	226

B.6 Internal energy of the SIR-X projectile as a function of time at $v=61$ m/s.	226
---	-----

List of Tables

2.1	Classification of Non-Lethal Weapons	11
2.2	Projectile characteristics	14
2.3	Injuries sustained by patients during Northern Ireland disturbances.	22
2.4	AIS of the injuries sustained by patients.	23
2.5	Injuries caused by rubber bullets	24
2.6	Blunt injuries to the chest	24
2.7	Cross-Classification in function of the struck area	25
2.8	Cross-classification in function of distance	25
3.1	Abbreviated Injury Scale (AIS) applied to the thorax	39
3.2	Numerical values of the WSU corridors	50
3.3	$(VC)_{max}$ boundaries for the thorax validation	51
5.1	Material characteristics of the SHTIM parts.	98
5.2	Different properties of the PVC projectile.	101
5.3	Injury criterion $(VC)_{max}$ comparison	105
6.1	Rebound velocity and strain rate calculation.	122
6.2	Different properties of the SIR-X projectile.	127
6.3	Comparison between experimental and numerical rebound velocities.	128
6.4	Material characteristics of the CONDOR projectile.	139
6.5	Material characteristics of the NS projectile.	147

6.6	Comparison between experimental and numerical rebound velocities.	150
6.7	Material characteristics of the FN303 projectile.	156
6.8	Material characteristics of the RB1FS projectile.	159
7.1	Final result of the lethality analysis of the SIR-X projectile.	173
7.2	Final result of the lethality analysis of the CONDOR projectile	179
7.3	Final result of the lethality analysis of the NS projectile	181
7.4	Final result of the lethality analysis of the FN303 projectile fired from the FN303 launcher.	185
7.5	Final result of the lethality analysis of the RB1FS projectile.	187
7.6	Comparison of numerical results with the 3RID $(VC)_{max}$ results.	192
A.1	Measured $(VC)_{max}$ values obtained while firing non-lethal projectiles on PMHS thorax, condition A, B and C [7].	222

List of Acronyms

Accronym	Meaning
3RBID	3 Rib Ballistic Impact Dummy
3RCS	3 Rib Chest Structure
AAP 6	Allied Administrative Publication No 6
ABAL	Weapon Systems and Ballistics department
AEP	Attenuated Energy Projectile
AIS	Abbreviated Injury Scale
ALE	Arbitrary Lagrangian Eulerian
ATD	Anthropomorphic Test Device
ATBM	Advanced Total Body Model
BABT	Behind Armour Blunt Trauma
BC	Blunt Criterion
CAD	Computer Aided Design
CFC	Channel- Frequency-Class
DGA	Direction Générale des Armements - France
EOS	Equation of State
FDM	Finite Difference Method
FE	Finite Element
FEM	Finite Element Method
FVM	Finite Volume Method
FN (Herstal)	Fabrique Nationale
FRF	Frequency Response Function
HBFEM	Human Body Finite Element Model
HUBYX	Hermaphrodite Universal yx Model
KENL	Kinetic Energy Non-Lethal
KENLW	Kinetic Energy Non-Lethal Weapons

Acronym	Meaning
MTHOTA	Mechanical Thorax fro Trauma assessment
NATO	North Atlantic Treaty Organization
NLKE ToE	Non-Lethal Kinetic Energy Team of Experts
NLW	Non-Lethal Weapons
PMHS	Post Mortem Human Subjects
PVC	Polychlorure of Vinyl
RCA	Riot Control Agents
RMA	Royal Military Academy
RW	Rigid Wall
SHTIM	Surrogate Human Thorax Impact Model
SPH	Smooth Particle Hydrodynamics
$(VC)_{max}$	Viscous criterion
WSU	Wayne State University

Chapter 1

Introduction

The non-lethal concept as we know it today dates back in the fifties. It was initiated by the political change which occurred in the world especially in western countries. The fulfilment of police tasks by military defence forces in peacekeeping and humanitarian missions is one of the major factors that has contributed to the rapid development of non-lethal weapons in the military forces. Such weapons are well suited in situations of low-intensity conflicts like riot control, access denial, peacekeeping missions i.e. situations where the use of lethal force is not appropriate nor desired. Non-lethal weapons come into play when the use of excessive force is not appropriate nor necessary and the (physical) presence or the use of verbal commands seems to be ineffective.

Non-lethal weapons offer a gradual approach in the use of force and provide police and military forces with additional capabilities in conflict situations. Several non-lethal technologies are currently available. They mainly use, in some way or another, electric, electromagnetic, acoustic or kinetic energy. The present thesis is limited to kinetic energy non-lethal weapons (KENLW), the most frequently used category. The underlying principle of KENLW is to impart kinetic energy to a projectile, the impact of which will cause enough physical pain to incapacitate or repel the target while minimising the risk of severe injuries. The review of the literature indicates that the thorax is the most often targeted zone of the body and can sometimes sustain severe injuries if hit by a kinetic energy non-lethal (KENL) projectile. The focus in this thesis will be on thoracic impacts.

Unlike the conventional weapons that may cause severe or fatal injuries, the non-lethal weapons are designed for temporary incapacitation with reversible consequences or minor damage to the human body. There are two main issues that raise concern when using KENLW: the safety issue (avoid permanent or severe injury in normal conditions of operation) and the effectiveness (achieve the desired effect for

the fulfilling of the mission). Different questions must be answered. What are the limits (tolerance levels) beyond which non-lethal weapons could cause irreversible (severe or fatal) damage? How to assess the associated risk of injury? What are the operational conditions of use i.e. the minimum and the maximum firing distances at which range they can be used (effective distance)?

The answers to these questions call for a better understanding of injury mechanisms resulting from the use of KENLW projectiles and for the necessity of developing assessment methods for the injury risk assessment. They will provide non-lethal weapon procurement divisions with enough technical information allowing them to select the best available product (weapon or projectile). They will provide manufacturers with relevant information allowing them to improve their current products or to develop more effective non-lethal weapons or projectiles. And finally, they will provide the end-users (military or police forces) of these weapons with information on operational distances of engagement. The emphasis in the present work is put on the safety issue i.e. what is the minimum requirement when using KENLW to avoid severe injuries. Additional to that, wherever the information about dispersion of the KENLW is available, maximum distance of engagement, can be determined.

When studying KENLW, it is desirable to develop tools that render experiments on human beings or animals unnecessary. In general, two main types of tools have been developed namely the mechanical surrogates and the virtual surrogates (numerical models). Compared to mechanical surrogates, virtual surrogates (numerical modelling) are very cost-effective, they are easily adaptable and have interesting predictive capabilities. The present study is about the development of numerical tools for thoracic injury risk assessment of the KENL projectiles.

This thesis is structured as follows.

Chapter 2 is an introduction to non-lethal weapons. The variety of NLW technologies is briefly described. Emphasis is put on KENLW and the characteristics of many KENL projectiles are described. The literature review presented in this chapter shows that apart from the head, most of the serious injuries has been attributed to thoracic impacts. The purpose of the thesis is also presented, the development of numerical tool for thoracic injury risk assessment of the KENL projectiles.

Chapter 3 provides an introduction to the biomechanics of the thorax. The concepts of injury mechanisms, injury criteria, the tolerance levels and the injury risk curve are covered in this chapter. The studies carried out on the subject by Wayne State University (WSU) in the United States of America is exposed as it is the only open-source literature available where tests have been carried out on Post-Mortem Human Subjects (PMHS) for the study of KENLW. Therefore these studies are important for the present thesis as they provide the baseline data that

are used for the validation of the thorax FE model. A literature review of FE models that has been developed for KENL projectile impacts is carried out and the differences with the mechanical surrogates are highlighted. The 3RBID (3 Rib Ballistic Impact Dummy), a thoracic mechanical surrogate acquired by ABAL (Department of weapon systems and ballistic) is also described. Data obtained from the KENL projectiles impacts were used in order to compare the two systems (the 3RBID and the SHTIM).

Chapter 4 gives a general introduction to FE method. The types of FE discretization, contacts as well as material models especially elastic materials are covered. To carry out the numerical simulations, a general methodology has been defined for the evaluation of the impact of the projectile on thorax. It consists of three main steps: the building of the thorax model as well as the projectile models, the validation of these models and finally the evaluation of the impact of the projectile on the thorax.

Chapter 5 concerns the development of the thorax FE model. This development is divided into many steps. Firstly the thorax geometry is obtained from a CAD software, then it is meshed. Secondly, material properties of different parts is obtained from the literature. The FE model of the projectile used for the validation of the thorax model is developed and finally the SHTIM is validated by using biomechanical corridors defined in Bir's experiments.

Chapter 6 concerns the development of projectile FE model. This development is divided into many steps. For each projectile, the geometry is generated from a CAD software, then it is meshed. Secondly, material properties of different organs is obtained from the literature except for the 40 mm sponge grenades. A new method of material characterization has been developed in order to obtain the material properties of the deformable nose of the 40 mm sponge grenade. It consist in using the direct firings of the projectile against a rigid wall (RW) structure. This method is described in the same chapter. Finally for each projectile, the FE model is validated by using the same firings data on RW.

Chapter 7 presents the injury risk assessment results of the thoracic impacts. Some considerations about this assessment are given. For each projectile, simulations are performed at different impact velocities and the viscous criteria are computed. Assessment is carried out by comparing the values of the computed viscous criterion for each velocity to the threshold value. This results in the determination of the critical velocity. Using the retardation, the minimum firing distance is determined for each projectile. Then the comparison between the 3RBID and the SHTIM model is made.

In the last chapter, conclusions are presented. Some recommendations and different axes where future investigations are possible are presented.

Chapter 2

Formulation of the problem and objectives

This chapter will cover the concept of KENLW and the underlying principles, their employment and usefulness. Several categories of current weapons will be discussed, although the focus will be on the study of kinetic energy non-lethal anti-personnel weapons. A review of the literature on these specific systems will then be presented, highlighting the critical body regions for study. The chapter will conclude with a comprehensive, clear and precise outline of the goal of this thesis.

2.1 Background

The concept of "non-lethal" is not new, at least in its principle. This principle can already be found in Sun-Tzu's statement (5th century BC) [8]:

"The practical art of war, the best thing of all is to take the enemy's country whole and intact; to shatter and destroy it is not so good. So, too, it is better to recapture an army entire than to destroy it, to capture a regiment, a detachment or a company entire than to destroy them. Hence to fight and conquer in all your battles is not supreme excellence; supreme excellence consists in breaking the enemy's resistance without fighting."

Even if the principle was already known, the "non-lethal" term and the non-lethal weapons were effectively introduced much later [9]. Most of early non-lethal development programs were undertaken by US and UK [10]. Nevertheless, impact

weapons such as the truncheons, the billy clubs or the straight wood batons can be considered as the first non-lethal impact weapons. They have been used by the police for more than one hundred years. They were the precursors of the actual batons (telescopic, side-handled or expandable batons...), more ergonomic and efficient [11]. Unlike the batons used in a one-to-one confrontation, another type of non-lethal weapons that have been used by the police for many years as riot control agents (RCA) is the chemical agents. The best known are CN (Chloroacetoneph- none), CS (2-chlorobenzyliden malonitrile) and OC (oleoresin capsicum) used as tear gas. The use of KENLWs started in the 1950s in Hong Kong, where wooden bullets ammunitions were used by the UK police for riot control [12].

The "non-lethal" concept as we know it today dates back to the fifties and sixties initiated by the political change which occurred in the world especially in US and UK. As stated by Weinberger and Hambling [13], *"Although many of the "non-lethal" weapons available to the police at this time were products of military research and development, the military were yet to take a significant interest in the concept. During the 1980s this situation did not change greatly since the technological arms race was driven by the Cold War stand-off between NATO (North Atlantic Treaty Organization) and the Warsaw Pact countries focusing primarily on nuclear weapons development"*.

But it was much later in the 1990s that we saw the ever growing interest of the armed forces in the development and the use of non-lethal weapons. The intervention of the military force, assuming the missions of police, in the context of peacekeeping and humanitarian missions, is one of the major factors that have contributed to the rapid development of these weapons. The first conflicts in the post-Cold War era have highlighted the existence of a gap between the military presence and the use of lethal force as the US forces were confronted to a new type of wars, the asymmetric wars (as opposed to conventional wars), which they were not prepared to. This gap unfortunately has been exploited by the local combatants in many crisis situations in which the US forces were involved [14].

For example, in Iraq and Afghanistan, we have seen people being used as human shields around neuralgic points, combatants and/or terrorists mingled with the population [14, 15]. This raised major problems to the US forces and their allies as the threat was no more clearly identified (difficulty of discriminating combatants and non-combatants) and the risk of civilian casualties was greater. In Somalia, engaged in urban operations, combatants of warlords were hiding among women and children and were using them as cover while attacking US troops [14]. The way the latter react is generally on scrutiny as there are rules or principles defined in international law of armed conflicts to which they are supposed to comply and one of the basic principles in operations is the principle of discrimination i.e. avoiding

2.1 Background

non-combatants casualties [16]. The highly extended coverage of the media of these conflicts and the concerns raised about civilian casualties since combatants were mingled with civilians were factors that generally could fuel anytime the reactions among local and (inter)national population. As a result, on the one hand, local population might be less cooperative and show more hostility towards the foreign troops who were engaged on peacekeeping missions for example. On the other hand, the public opinions in democratic countries might not continue to support their government and their troops because of the unnecessary losses among civilians. It is in the wake of those events that many non-lethal weapons were developed.

The situation of the UK which is also one of the forerunners in the development of non-lethal weapons was a little bit different. Already in the early 70s, non-lethal weapons were developed and used in order to deal with the uncivil rest in Northern Ireland. This conflictual situation between the Unionists and the Nationalists has made the island one of the first test fields of non-lethal weapons. During their policing operations, the British armed forces have repeatedly used non-lethal ammunition (rubber bullets and later plastic bullets) in the streets of Northern Ireland cities [17, 18].

These aforementioned situations are few examples of non-conventional situations encountered by armed forces with one major concern, minimizing civilian casualties or collateral damage. This changed the way armed forces have to intervene in these forms of conflicts where traditional warfare methods are no more appropriate. Non-lethal weapons then provide additional capabilities in order to fill this gap between the use of excessive force, in this case, not appropriate and the non-use of force, ineffective. The non-use of force can be characterised by the sole (physical) military presence or by the use of verbal commands.

Thanks to the technological advances in those years, different types of weapons have been developed that allow a gradual approach in the use of force (Figure 2.1) making the application of the principle of proportionality ¹ even more suitable [19]. This is another basic principle, part of human rights law, to which the military forces are supposed to comply in operations other than wars. Proportionality is based on the idea that it is unjust to inflict greater harm than that unavoidable to achieve legitimate military objectives [14]. Figure 2.2 gives an example of a force continuum scheme describing the gradual response of the military force to a given

¹The notion of proportionality is a very ancient concept in its principle (code of Hammurabi 1772 BC). It was first and formally stated by the Federal Constitutional Court of Germany. Three elements were taken into account for defining the principle of proportionality : (i) Suitability (the measure should be suitable for achieving the desired objective); (ii) Necessity (a less restrictive means should be used if it is equally effective); and (iii) Proportionality in the strict sense (the measure should not be disproportionate to the objective) [19].

situation. *"Without access to non-lethal means, commanders have no intermediate choices on the continuum between 'detect' and 'destroy'. Non-lethal weapons add 'delay', 'deny', and 'defeat' as intermediate steps in the range of options available to the commander. If full spectrum dominance can be described as a ladder, non-lethal weapons put the bottom rung on that ladder by allowing warfighters the potential to smoothly ratchet up the level of force as the situation warrants)" [16].*

It appears that non-lethal weapons are well suited in situations of low-intensity conflicts like access denial, peacekeeping operations ... and provide, to the military forces and to the police forces as well, means enabling them to cope with the variety of conflicting situations they may encounter in operation fields. The field of operations of these weapons is very wide, hostage taking, riot control, counter-drug, prison management, counter-terrorism operations ...[16, 20].

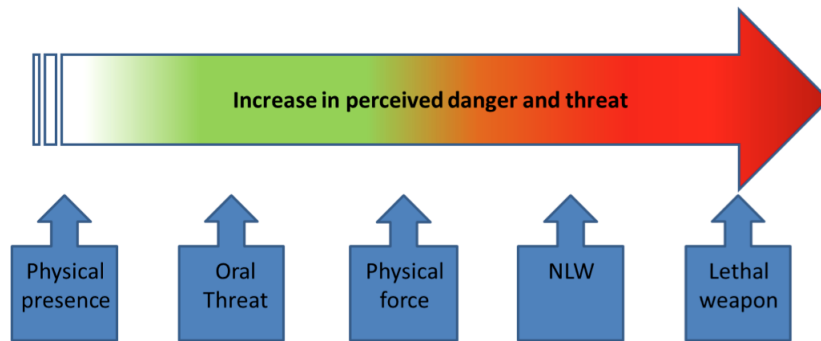


Figure 2.1. *Gradual approach in the use of the force (Force continuum)[21].*

Although this seems obvious, a non-lethal weapon is a weapon. As such a certain risk is related to its use. Thus it is not a gadget. Generally when people speak of a weapon, the first idea that comes to the mind is a device generally associated with wars, criminal activities, murder ... a device designed to kill or to inflict great harm. Therefore, we naturally think 'lethal weapon' or 'firearm' when we speak about a weapon. Conversely, referring to a non-lethal weapon could then be confusing in the mind of many people. Because of that, the term 'non-lethal' has been the cause of a lot of controversy and up to date there is no consensus about the better terminology to design such weapons among the community members. As John B. Alexander states: *"It is important that the fundamental issues and concepts are understood in the context of current geopolitical realities. In many future military missions, as well as with police protecting our citizenry, use of deadly force will necessarily be minimized . The name applied to that task is not really important. Providing appropriate weapons options for field commanders and law enforcement officers is [12] "*. Now, many other terminologies such as less-lethal, less-than-lethal, sub-lethal or AEP (Attenuating Energy Projectile)... weapons, have emerged. We will stick

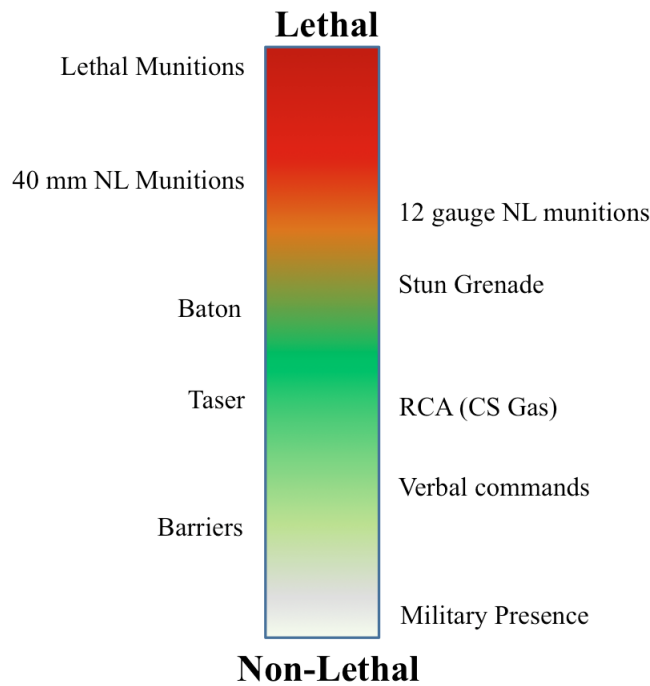


Figure 2.2. *Example of a force continuum scheme. Adapted from [14].*

in the present work to the terminology and the definition that are used by US DoD (United States Department of Defense) and within NATO ([22],[23]).

2.2 Definition

"A non-lethal weapon is a weapon that is explicitly designed and primarily employed to incapacitate or repel persons or to disable equipment, while minimising fatalities, permanent injury and damage to property and the environment" (AAP-6(2008) - glossary NATO).

In its policy ([23]), the DoD states that

a. Unlike conventional lethal weapons that destroy their targets principally through blast, penetration, and fragmentation, NLW employ means other than gross physical destruction to prevent the target from functioning. NLW are intended to have relatively reversible effects on personnel or material.

b. NLW are capable of delivering a level of force that achieves immediate target response and can provide predictable and intended reversible effects, allowing the affected target to return to pre-engagement functionality.

c. NLW are developed and used with the intent to minimize the probability of producing fatalities, significant or permanent injuries, or undesired damage to materiel, but do not, and are not intended to, eliminate risk of those actions entirely.

One thing that transpires from the definition as well as in the DoD's statement is that the focus in the definition is put on the intent, not on the description of the system nor its effect. Generally, the intent does not guaranty that in practice, it will be 100% safe as casualties can occur even though one of the goals is to minimize them. This raises another issue, what could be the acceptable number of casualties? (refer to Chapter III). Therefore a gap still exists however between the intent and the reality, both in terms of technical realization and in the use of such weapons (deployment, ethics).

Another thing to be considered is that the definition does not refer to any means to achieve this goal. On the one hand, everything can be lethal or non-lethal depending among other factors, the condition of its use. For example, a KENLW, described as non-lethal at 30 meters, may become lethal if it is used at a closer range. Conversely, a lethal weapon does not necessarily lead to a permanent or fatal outcome. Therefore clear rules of engagement have to be defined as without a concrete and operational definition, the concept of non-lethal weapons can be misinterpreted. On the other hand, as the means to be used and the intended effects are not specified, this has opened large possibilities for the development of a wide spectrum of weapons based on diverse technologies. In the following section, an overview of different technologies will be given with a particular emphasis on KENLW.

2.3 Technologies

Traditionally, the evolution of the (non-lethal) weapons is closely tied to the evolution of technology. Depending on the used technologies, the effects can be different and conversely, depending of the intended effects, a specific technology can be used [24]. The scientific and technology advances combined with an increasing need of non-lethal capabilities in the late 20th century result in a boosting effect on the development of non-lethal weapons. Based on diverse technologies, different types of non-lethal weapons were developed. They can be grouped into different categories depending on the nature of the technology upon which they are built [16, 25]. We can distinguish kinetic energy, electrical, chemical, biological, optical, acoustic or directed energy NLWs.

Another way of grouping non-lethal weapons is according to the type of the target. We distinguish [16]: the anti-personnel non-lethal weapons and the anti-material ones (Table 2.1). The interested reader can find a good summary of the different weapon types and the corresponding technologies in [2, 3]. In the present thesis, we will only consider the anti-personnel non-lethal weapons which can be divided as seen previously in function of acoustic, electric, electromagnetic, chemical,..., or kinetic technology. Exposed to such weapons, the human body will respond through different mechanisms in a way that will affect the human physiology or alter the human's behaviour. When considering non-lethal weapons, one can paraphrase Paracelsus² the quantity or the dose of the 'non-lethal weapon' stimulus (stimulus force or intensity) determines whether the effects are lethal or not. In addition to dose, other factors may also influence the lethality of a non-lethal weapon such as the route of entry, the duration and the frequency of exposure, variations between different species (interspecies) and variations among members of the same species (intraspecies)[26].

Because each non-lethal technology covers a broad subject, the scope of this study is limited to KENLWs as they are the most widely used weapons both by civil and military forces [27, 28].

Core Capability	Functional Area with Core Capability
Counter-Personnel	Crowd control Clear facilities of personnel Incapacitate personnel Deny an area to personnel Neutralisation of individuals and groups Crowd control Dispersion of crowd Protection of individuals and groups Rescuing of individual/groups
Counter-Materiel	Deny an area to vehicles, vessels, aircraft Neutralisation of infrastructure and equipment Protection of facilities and equipment Disable equipment and facilities Clearing a facility Neutralisation of communications

Table 2.1. *Classification of Non-Lethal Weapons according to the target and functional area. Adapted from [29]*

²Paracelsus suggests, the quantity or the dose of the substance determines whether the effects of the chemical are toxic, nontoxic or beneficial. In addition to dose, other factors may also influence the toxicity of the compound such as the route of entry, duration and frequency of exposure, variations between different species (interspecies) and variations among members of the same species (intraspecies).

2.4 KENLW

The underlying principle of KENLW is to impart kinetic energy to a projectile, which by a mechanical action on the target, will inflict instant physical pain sufficient to incapacitate or repel the target without penetrating but causing however a blunt trauma. KENLWs provide to the military or the police forces a way of incapacitating a suspect over a distance without putting themselves in danger. The main characteristics of a system <KENLW and ammunition> are the projectile mass, the projectile material characteristics, the nominal velocity, the range, the ballistic stability and the accuracy. They play a key role in the performance of the system and naturally in the terminal effects i.e. the global impact effectiveness in terms of pain level or injury severity on human target.

Compared to conventional weapons, KENLWs are devices that fire projectiles at relatively low velocity (70-160 m/s). As a consequence, they have a limited range and generally their accuracy drops rapidly as the distance increases. This means that at a relatively limited distance, either people are more likely to be struck at unintended places such as the head and neck, the most sensitive and vulnerable parts of the body or the likelihood of striking unintended people (collateral damage) is greater [3, 24].

As the head is never aimed at [3, 30] as Bozeman et al. also pointed out "Users of less lethal kinetic impact munitions are trained to target the torso and proximal extremities of a suspect while avoiding the head, neck, precordium and groin areas" [31]. This sets an upper limit, the maximum effective distance in order to avoid such negative effects. Conversely, a relatively closer distance to the target increases the likelihood of severe injuries. This sets a lower limit, the minimal safe distance (Figure 2.3). The effective range is generally a result of a balance between safety and effectiveness i.e. non-lethal weapons "must achieve an appropriate balance between the competing goals of having a low probability of fatality or permanent injury, with minimal undesired damage, and a high probability of having the desired effects" [31]. The ideal for the manufacturer as well as the user would be a weapon that would have a larger effective range and at the best would have a minimum safe distance being equal to zero.

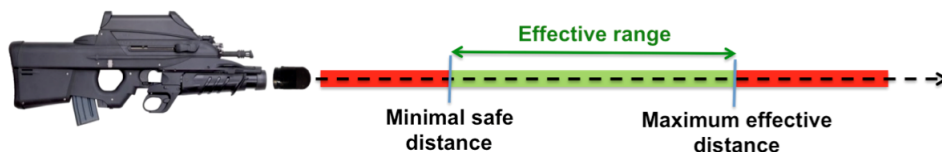


Figure 2.3. *KENLW effectiveness.*

2.4.1 History of KENLW Projectiles

The first use of KENLW can be traced back in the late of 1950s in Hong Kong, where cylindrical inch-long bullets made of teak were used by the British colonial police for riot control. They were skip-fired³ off the ground with the aim of striking people in the legs [10]. But they were too dangerous. No one could predict the bullet's path after the impact or rebounding on the ground with the risk of hitting unintended body area; on the ground, they could also shatter. As they could cause serious injury, even death, they were ruled out during the Northern Ireland civil disturbances and new bullets made of hard rubber were used by British Army, namely the L2A2 that was first introduced in 1970 [32]. The bullets had a mass of 140 g and were 150 mm long, 35 mm in diameter. They were also skip-fired like the teak bullets from a smooth barrel. But because of rubber elasticity, they would rebound much higher than the latter increasing the risk of hitting the head and therefore the risk of serious injuries.

In an attempt to reduce fatalities, the rubber bullets were replaced by plastic bullets, a shorter, much lighter and more accurate bullets as they were gyroscopically stabilized. They were designed to be directly fired at a person and have a relatively low muzzle velocity. The first plastic bullet was made of PVC and was 89 mm long, 38 mm in diameter and weighed approximately 131 g [33]. Different plastic bullets such as L5A7 and L21A1 bullets were developed. They proved also to be dangerous at short range([10], [32]). For example the L21A1 more recent than the L5A7 has a mass of 98 g and its dimensions are 100 x 37 mm. It has a muzzle velocity of about 72 m/s and has been used since 2001 by the British police. But in 2005, it was replaced by the AEP (Attenuated Energy Projectile) that has almost the same characteristics but with a reduced injury risk especially to the head [34].

In the late 1960s and the early 1970s, contrary to the UK where 37mm-plastic bullets were widely used and fired from dedicated launchers, in the US, the 12-gauge beanbag rounds have been the most widely among the different types of projectiles. Its success was due to the fact that it could be direct fired from any standard shotgun rather than requiring a specific launcher. The beanbag consists of a cotton or nylon casing containing 9 lead pellets . It has a mass of 40 g and is drag-stabilized. The muzzle velocity of the projectile is about 90 m/s. At the impact, the energy is distributed over a larger surface area, thus limiting the physical damage. The minimum distance at which this type of weapon is to be used is 6 m and at a distance greater than 21 m, the weapon is inaccurate [35]. Many other KENLW

³skip-fire rounds are intended to be fired into the ground in front of the target, where they dissipate some energy and then rebound into the target

munitions of different diameters were developed later on among which the XM1006 sponge grenade, deployed to Bosnia and Kosovo for peacekeeping missions [29, 36].

During the Israeli-Arab conflict in 2000, Israeli Defense Forces and Israeli police used KENL ammunition of two types, the RCC-95 and the MA/RA-88 [12]. They could be fired from a standard M16 rifle or any other rifle with a NATO 22 mm flash suppressor. The RCC-95 is a blunt cylindrical projectile composed of three metal cores coated by a layer of rubber shell 2 mm thickness. The projectile has a mass of 48 grams and a diameter of 18 mm with a muzzle velocity of 130 m/s. These projectiles may be used at a distance of 40 to 70 meters. Serious injuries may result if it is shot at closer distance (<40m). The MA/RA-88 projectile consists of fifteen rubber bullets that have a metal core specifically designed for crowd control. The diameter of the balls is 17 mm and the mass 17 g. With a muzzle velocity of 78m/s, the recommended target engagement range is between 30m and 80m [32].

2.4.2 Projectile description and characteristics

There exists a great variety of projectiles currently available on the market (Table 2.2). Some of them are represented on Figures 2.4-2.5. These projectiles are launched using either conventional existing weapons or dedicated weapons (Figure 2.6) and have mass that varies from 5 g to 140 g. They can be drag-stabilized, fin-stabilized or gyroscopically stabilized. They can be divided in function of their physical, geometrical and material characteristics (Table 2.2).

Projectile	Material	Diameter (mm)	Mass (g)	Muzzle velocity (m/s)
Rubber bullets	Rubber	7.5 to 18.5	6.5 to 15	100 to 152
FN303	Hollow plastic ball full of bismuth and glycol	17.2	8.2	90
Beanbag	textile bag full of lead balls	18.5	40	70 to 90
Baton rounds	rubber, wood, PVC, polyurethan	35 to 38	90 to 140	58 to 73
40mm sponge grenades	Plastic projectile with rubber or foam nose	40	27 to 60	85 to 105
Flash-Ball	Rubber	44	28	85 to 125

Table 2.2. *Projectile characteristics [37].*

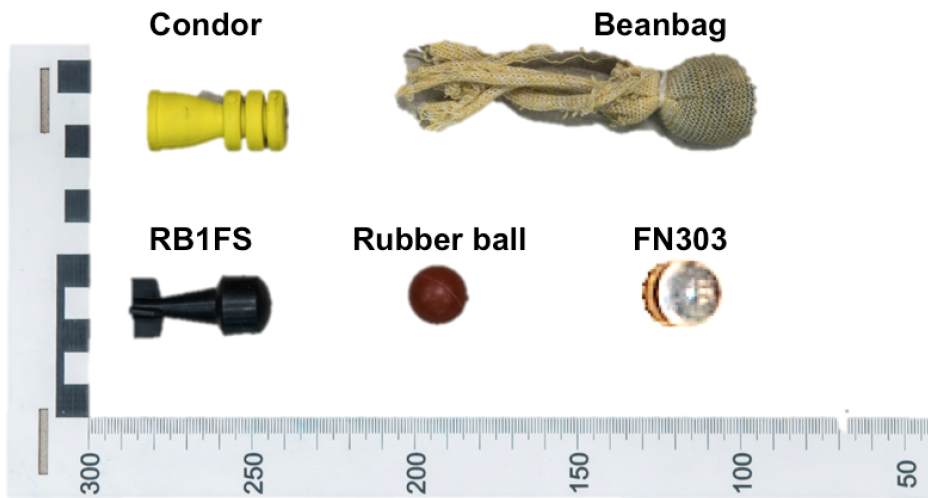


Figure 2.4. 12 gauges projectiles+ FN303 projectile.

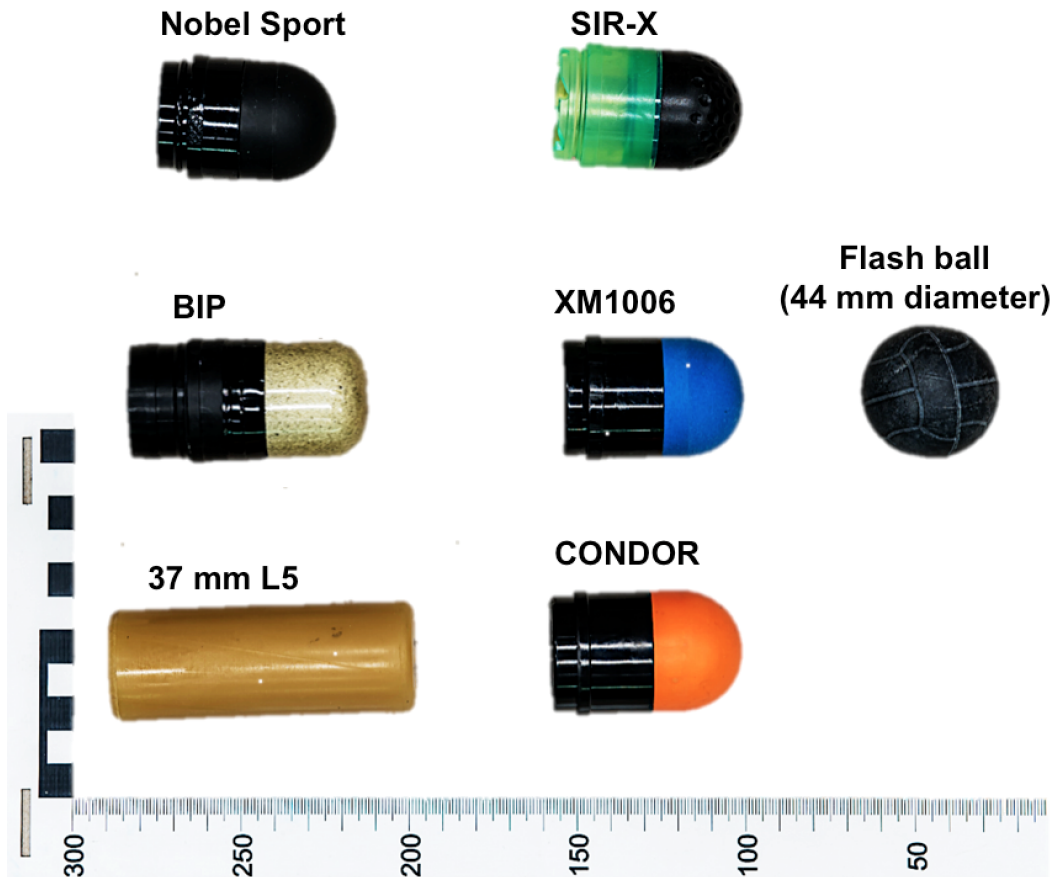
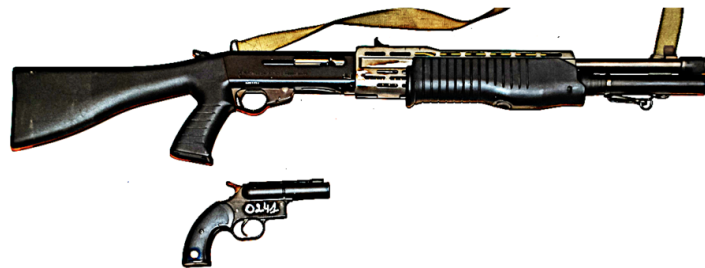


Figure 2.5. 40 mm diameter projectiles



Dual purpose launchers for 12 gauge projectiles.



Dedicated launcher used for FN303 projectiles



Examples of launchers for 40 mm diameter projectiles

Figure 2.6. *Launcher types.*

2.4.2.1 Geometrical characteristics

One of the main geometrical characteristics is the projectile diameter⁴. The database ("EWG-NLW Commercial Technology Table - Kinetic Energy Devices v9.0") contains most of the KENL (Kinetic Energy Non-Lethal) projectiles and gives a good idea of the general trends in KENL ammunition currently available on the market [38]. The relative proportion of each projectile when we consider the projectile diameter is given in Figure 2.7. The most used projectile caliber types are 17-18,5 mm caliber projectiles (Figure 2.4) which can be launched with 12 gauge launchers or dedicated launcher for FN303 projectiles and 37-40 mm caliber projectiles (Figure 2.4) which can be fired with 40 mm launchers.

Generally, projectiles with small caliber ($\leq 18.5mm$) are more likely to cause penetrating injury than projectiles of greater caliber. This means that the skin penetration will be generally a critical injury factor in the evaluation of such projectiles. Conversely, for the projectiles with larger caliber ($\geq 37mm$), the skin penetration is not generally an issue but other injuries are likely to occur like fracture of ribs in case of thoracic impacts.

The shape is another geometrical factor that has also an influence on the projectile ballistics. The new non-lethal projectile generation has generally a round nose which gives better penetration in the air improving the retardation factor. It also has no sharp edge compared to cylindrical-like projectiles (old generation). Projectile with sharp edges increases the likelihood of (skin) penetrating injury. In effort to reduce permanent injury, another parameter which plays a role in the terminal effects is the projectile material.

2.4.2.2 Material characteristics

The projectiles may be considered as rigid like the L5 projectile, deformable (like SIR-X sponge grenade) or can break at the impact (like the FN303 bullet) (Figures 2.5-2.4). They can be made monolithic or composite (made of two or more different parts). In order to reduce the likelihood of severe injuries, most of the new projectiles are either made of deformable material or have generally a deformable nose. This means that a part of the energy is absorbed by the projectile during the impact. As a consequence, the energy transmitted to the human target is reduced, so is the likelihood of severe injury.

⁴the projectile diameter or 'caliber' is different from the actual caliber of the weapon from which it is launched although this difference may be slight.

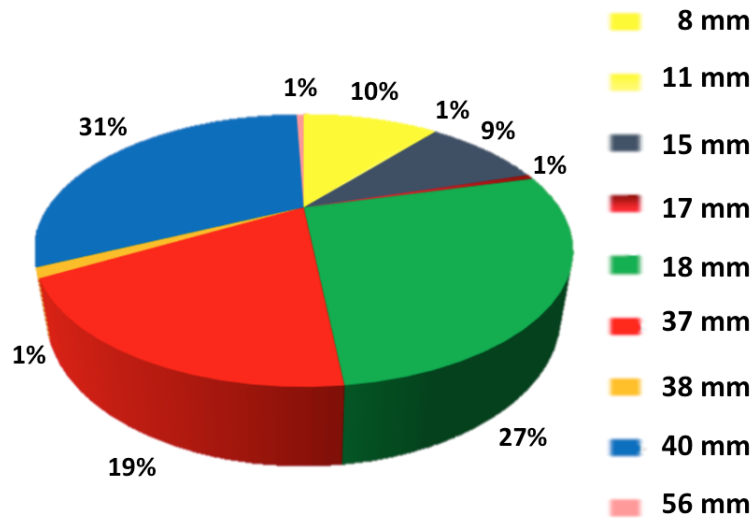


Figure 2.7. Proportions of projectiles found in the EWG-NLW document in function of caliber [38, 39]

In the perspective of modelling, at least one projectile of each KENLW projectile types is chosen as reference. A more detailed description is given for each.

2.4.2.3 Brügger&Thomet SIR-X projectile

The Brügger&Thomet SIR-X projectile ⁵ is a 40 mm sponge grenade made of two parts which are glued together: a plastic body and a full solid deformable hemispherical nose in foam material (Figure 2.8(a)). It has a nominal diameter of 40 mm, a mass of 32 g and a nominal velocity of 105 m/s. The mass of the nose and the sabot are 7.2 g and 24.8 g, respectively. This projectile has also been chosen in the NATO framework as one of the reference projectiles for validation process of thorax surrogates.

2.4.2.4 CONDOR NT901 projectile

The CONDOR NT901 projectile ⁶ is a 40 mm sponge grenade similar to the the SIR-X projectile (Figure 2.8(b)). It is made of two parts which are glued together: a plastic body and a full solid hemispherical deformable nose in foam material. It has a nominal diameter of 40 mm, a mass of 27.8 g and a nominal velocity of 105 m/s. The mass of the nose and the sabot are 9.5 g and 18.3 g, respectively. The nose structure is slightly different from the SIR-X projectile as it has four 5 mm

⁵For the sake of simplicity, it is called SIR-X projectile in the present thesis

⁶For the sake of simplicity, it is called CONDOR projectile in the present thesis

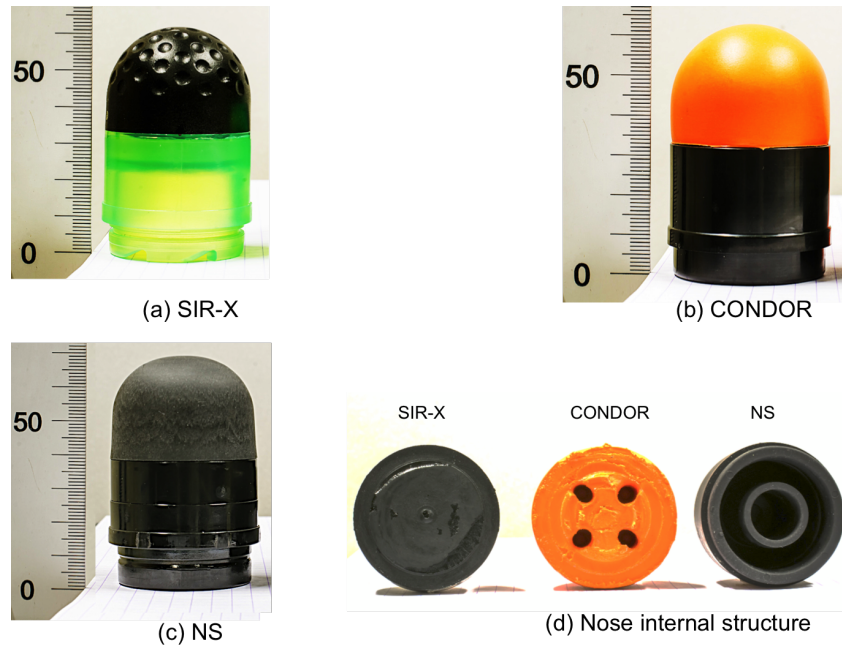


Figure 2.8. *40mm Sponge Grenades.*

diameter cylindrical holes in a symmetric pattern with respect to the longitudinal projectile axis.

2.4.2.5 Nobel Sport (NS) Spartan LE 40 Schock projectile

The NS (Nobel Sport spartan LE 40 schock) projectile For the sake of simplicity, it is called NS projectile in the present thesis is a 40 mm sponge grenade different from the SIR-X projectile and the CONDOR projectile although they look like (Figure 2.8(c)). It is made of two parts which are glued together: a plastic body and a deformable nose in rubber material. It has a nominal diameter of 40 mm, a mass of 41.2 g and a nominal velocity of 92 m/s. The mass of the nose and the sabot are 18.2 g and 23.0 g, respectively. The NS projectile nose has a hollow structure with a hollow cylindrical column as it is shown in (Figure 2.8(d)).

2.4.2.6 L5 projectile

The L5 cylindrical projectiles, the so-called 'baton projectiles' are made of non-compressible polyvinyl chloride (PVC) material. There are two types of projectiles, a long projectile and a short projectile (Figure2.9). They have a diameter of 37mm and their masses are 140 g and 30 g respectively. These projectiles are usually

considered as "rigid" projectiles ⁷. They belong to the first generation projectiles and are no longer used. They are important as they were used in Bir's experiments [40] to define the biomechanical corridors which serve as validation data for the thorax model developed in the framework of this thesis.



Figure 2.9. *L5 projectiles.*

2.4.2.7 RB1FS projectile

The RB1FS is a projectile made EPDM rubber ⁸ material. It is a mono-material projectile. Its diameter is 18.5 mm and its mass is 6.5 g (Figure 2.10). It has a thin long piece of wood in the tail. Its nominal velocity is 152 m/s. It is considered as a reference projectile for the injury penetration study [41, 42]. Although the projectile is no more available on the market, the interest in the present work is to see how a small KENLW projectile perform in term of thoracic injury assessment. Another KENLW small caliber projectile that will be studied is the FN303 projectile.

2.4.2.8 FN303 projectile

The FN303 is a 17.3 mm diameter projectile from FN Herstal designed to break at impact. It is composed of a semi-round front part filled with bismuth, a rear part

⁷"Rigid" is taken in a sense that the strains induced in the projectile during impacts are very small compared to the characteristic dimensions of the projectile that they can be neglected

⁸EPDM=Ethylene Propylene Diene Monomer rubber



Figure 2.10. *RB1FS* projectile.

filled with a liquid (glycol) and a polystyrene disk ensuring a seal between the two parts and a polystyrene body that contains the three parts (Figure 2.11) [43]. The projectile mass is 8.5 g, and the average muzzle velocity is 90 m/s.

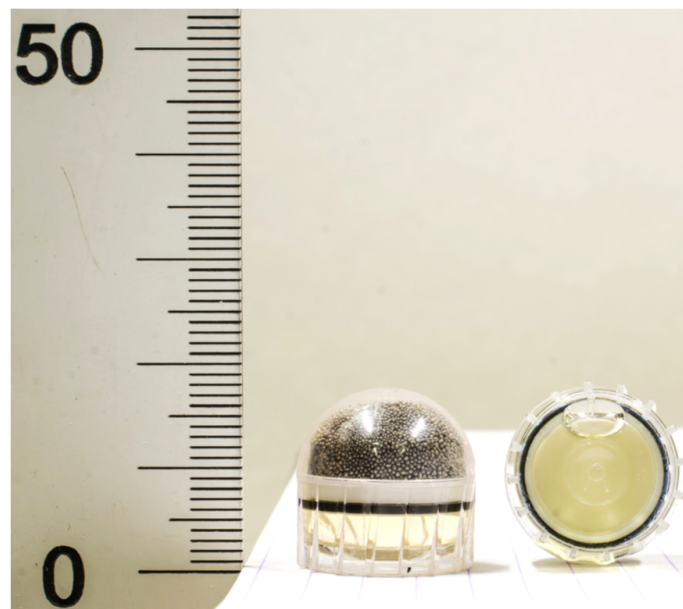


Figure 2.11. *FN303* projectile.

2.5 Literature review of effects of KENLWs

As previously mentioned, KENLWs , *if they are not properly used*, may cause serious injuries. Generally, it is difficult to get reliable information of incidents that occurred during the use of these weapons except in cases of serious injuries or deaths. One possible cause is that nobody would like to be arrested if he was for example one of the rioters or if he found himself in a place where he should not. Therefore, most information about the use of non-lethal projectiles and their effects on human body or part of the body are to be found in medical records in hospitals or in related publications. This information is often about the lesions sustained by the person and their severity, but most of the time the information is not complete. It is for instance not always possible to know the type of projectile used, the velocity of the projectile or the stand-off distance. This section describes few reports and studies that have been carried out when different KENLWs were used and their corresponding effects on different human body areas. Some statistics are also given.

2.5.1 Field case reports

In 1992, Ritchie released a report [44] on injuries that were caused by non-lethal projectiles during public disorder and riot control in Northern Ireland. He collected data from Belfast hospital on people who sustained injuries from plastic bullets impacts. He did this over a period of 14 years (1975-1989). In the hospital, 123 patients were treated in the emergency department of which 38 were admitted to the hospital for further treatment. The author divided injuries into serious and non-serious injuries. Some injuries were open injuries. Injuries to soft tissues were considered as non-serious. He found that 41% of people who were hit above to the diaphragm sustained death or serious injuries. There was one patient who died from chest serious injury. Table 2.3 gives a summary of the injuries in different body parts.

	Injuries	
	non-serious	serious
Head/jaw (n=29)	17	12
Chest (n=22)	13	9*
Abdomen(n=17)	16	1
Limbs (upper/lower) (n=57)	50	7
Groin (n=1)	1	0
n= number of patients - (*) 1 patient dead		

Table 2.3. *Injuries sustained by patients during Northern Ireland disturbances.*

Maguire et al. [34] presented a medical review of patients who sustained injuries caused by the AEP after three episodes of serious civil disturbance in Northern Ireland from July to September 2005. 14 patients with 18 injuries were identified. 33% of injuries were to the head and neck, 17% of the injuries were to the chest and the rest was limb injuries. There were no abdominal injuries. AIS (Abbreviated Injury Score) score [45, 46] was used for the severity of injuries (Table 2.4).

	AIS Score		
	1	2	3 or +
Face/head/neck (n=6)	1	1	4
Thorax (n=3)	2	1	
Limbs (upper/lower) (n=9)	8	1	
n= number of casualties			

Table 2.4. *AIS of the injuries sustained by patients.*

During the Israeli-Arab conflict that took place in October 2000, non-lethal projectiles were used namely the RCC-95 bullets and the MA/RA-88 bullets as previously mentioned. Mahajana et al. [30] processed data of 595 casualties admitted to the hospitals during the riots. Out of 595 casualties, 201 were proven to be a result of plastic bullets impacts. He made an analysis of the 201 records based on different criteria such as the injury type, the injury mechanism (blunt or penetrating injury), the severity of injury (using AIS score) and the anatomical part of the body that has been hit and the final outcome.

They found that 61% of injuries were blunt, whereas 39% were penetrating injuries (Figure 2.12). They categorized the injuries in three levels: mild, moderately severe and severe ⁹, 46% injuries were mild, 35% were moderately severe, and 19% were severe. The impacts were distributed all over the body with 73 to limbs, 61 to the head, neck and face, 39 to the chest, 16 to the back and 12 to the abdomen, but the injuries to the limb were the less severe (Table 2.5). Three people died of their injuries, two being a result of severe ocular injury and a third died of complications after knee surgery for a severe rubber bullet injury. The authors could not always identify for superficial injuries what type of bullet has hit the person. For most people with moderate injuries and people with serious injuries, it could be established that they were hit by the RCC-95 bullets.

Out of 39 injuries to the chest, about half were blunt (Table 2.6). Generally, lacerations and contusions were inflicted. There were also cases of rib fractures and lung contusions without penetration. Some cases of pneumothorax and haemothorax due the penetrating injuries were monitored but without rib fracture. Table 2.5 shows the records of injuries due to rubber bullets.

⁹According to the author of this thesis and following the definition of KENLW, only mild injuries are therefore acceptable.

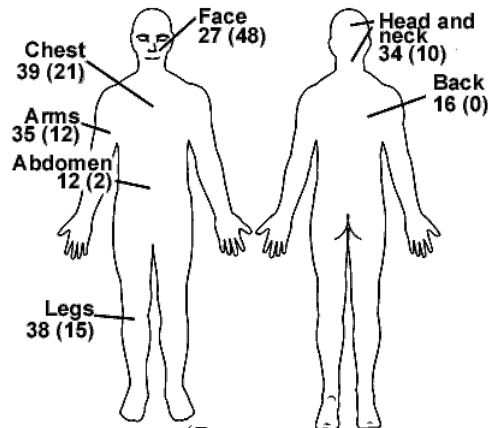


Figure 2.12. Injury repartition (Penetrating injuries are shown in brackets) [30].

	Type of injury		AIS (Severity of injury)		
	Blunt	Penetrating	1 (Mild)	2 (Moderate)	3 or + (Severe)
Face/head/neck (n=61)	33	28	21	21	19+2*
Thorax (n=39)	18	21	10	13	16
Abdomen (n=12)	10	2	4	5	3
Back (n=16)	16	0	9	7	0
Limbs (n=73)	47	24	49	24	1*

n= number of casualties - (*) Patient(s) died of the injury.

Table 2.5. Injuries caused by rubber bullets [30].

	Type of injury		Severity		
	Blunt	Penetrating	Mild	Moderate	Severe
Type of chest injury (n=39)					
Superficial laceration/ contusion of chest wall	18	0	10	8	0
Rib fractures and contusion of lung	0	8	0	2	6
Pneumothorax	0	6	0	2	4
Haemothorax	0	4	0	1	3
Contusion of heart	0	1	0	0	1
Pericardial tamponade	0	1	0	0	1
Tear of subclavian artery	0	1	0	0	1

Table 2.6. Blunt injuries to the chest [30].

From the above reports, the head (included the face and the neck) sustained more casualties than the other parts of the body and most of times the injuries were severe. Now let us look to the NIJ (National Institute of Justice) report [28]. This report is interesting in the sense that unlike the previous ones coming from military operations, it does come from law enforcement.

2.5 Literature review of effects of KENLWs

Ken Hubbs and David Klinger [28] of the NIJ delivered in 2004, a report on casualties that occurred between 1985 and 2000 in different situations where the police intervened. Different types of munitions were used: the beanbag round, the far most used projectile (65%), the 37 mm plastic bullet (28%) and other types (27%). The majority of the impacts concerned the abdomen (35%) and the thorax (19%). Only 2% concerned the head. There were 8 deaths whose six were fired at less than 10 m. Among the 8 deaths, 5 died as a result of the impact in the chest.

Area hit	Injury Sustained							Total
	Bruise	Abrasion	Laceration	Fracture	Penetration	Death	None	
Abdomen	158	62	8	9	2	—	14	254
Chest	69	49	3	6	6	5	7	146
Back	46	29	2	1	—	—	6	84
Groin	4	—	—	—	—	—	2	6
Leg	56	33	11	—	3	—	10	113
Arm	42	48	11	6	1	—	7	115
Buttocks	15	11	—	—	—	—	1	27
Head	3	2	7	5	2	—	—	19
Neck	1	3	1	—	—	1	—	5
Total	394	237	43	27	14	6	43	768

Table 2.7. *Cross-classification of area struck and injury sustained for 768 munitions Impacts [28].*

Distance	Injury Sustained							Total
	Bruise	Abrasion	Laceration	Fracture	Penetration	Death	None	
Below 3 m	23	13	1	5	—	1	8	51
3.0-5.8 m	124	61	13	8	6	1	10	224
6.1-8.8 m	81	61	14	4	2	4	7	171
9.1-11.9 m	56	48	4	6	4	—	13	131
12.2-14.9 m	25	11	1	1	—	—	5	43
15.2 m plus	24	3	3	2	2	—	—	34
Total	333	197	36	26	14	6	43	655

Table 2.8. *Cross-classification of distance and Injury for 655 munitions impacts [28].*

They found that:

- The most affected body areas were the abdomen and the thorax (Table 2.7). This seems normal from the point of view of the author as American police officers are trained to aim at the "center of mass" of an individual as we already mentioned.
- Impacts to the head tend to produce a greater proportion of serious injuries than impacts to any other area of the body.

- Most of the fatal outcomes (deaths) resulted from the thoracic impacts.
- One of the crucial issues in impact munitions concerns the relationship between the distance at which projectiles are fired and the degree of injury that subjects sustained (Table 2.8). The less is the distance to the target, the more is the likelihood of severe injuries.

2.5.2 Conclusions

From the literature review, some conclusions can be drawn.

- There are two types of injuries: the blunt and the penetrating injuries. Penetrating injuries are related to skin penetration, kind of injuries also found in the use of conventional firearms with the same risks. They can be serious, even fatal. This subject will not be covered in the present work [2].
- At the one hand, blunt injuries are characterised by superficial injuries to the skin and subcutaneous tissues like bruising, abrasion, lacerations. They are generally mild injuries. On the other hand, especially for thoracic impacts, deeper injuries like rib fractures and internal severe lesions (pneumothorax,...) can occur. They can even be fatal. This is therefore a crucial area of study.
- The head is the body part that is the most sensible and vulnerable to the KENLW impacts especially the face, the second part being the thorax (chest). The head injuries will not be covered here. The interested reader can refer to [3]. The thorax will be our focus as it is the body "centre of mass" and the main targeted area of the body.
- The information on the incidents is generally lacking or incomplete in most of the reports because of the difficulty to gather such data. Generally there is no record of the conditions of use, the bullet velocity or the stand-off distance. Nevertheless this information is relevant for the KENLW evaluation.
- All the reports currently focus on the injuries resulting from KENL projectiles impacts as safety is the primary concern. Little emphasis is placed on the effectiveness. In fact, the effectiveness is linked to the desired outcome of an event or situation - in the KENLW case, a human behaviour change such as compliance [47]. The desired effects of KENLW are inflicting to the human target a sharp pain for its neutralization. The question is then what is the minimal dose of pain that will provide the highest probability of compliance? This subject will not be investigated in the present work.

2.6 Goal of the thesis

The purpose of this thesis is to develop numerical tools for *thoracic* impacts assessment of KENLW in order to predict the injury risk associated to their use.

In the light of the review of the reported cases in the literature, the use of KENLW is not without risk. During blunt impacts, the body can sustain mild injuries but sometimes severe injuries that need urgent treatment. Even, fatal injury can occur. The type of injury and its severity depend on the impact zone of the body. Two zones are generally identified as the most critical: the head and the thorax.

A work has been carried out three years ago in order to propose a method of experimental assessment for studying the injury potential of thoracic impacts and the phenomenon of skin penetration by kinetic energy non-lethal projectiles [2]. But the skin penetration is out of the scope of this thesis. Alongside this work, a research was initiated for the development of numerical tools for the evaluation of thoracic impacts of KENLW. This PhD thesis is the result of the research.

Although both the experimental and the numerical tools offer the possibility to circumvent the use of PMHS and animal testings for different reasons ethical, technical or legal... numerical tools have many advantages compared to the experimental ones:

- The capability of accounting for complex geometries or complex material modelling;
- Its cost-effectiveness;
- It gives insight into local values of physical variables (stresses, strains,...) inside the material which are not accessible by other means;
- It allows parameter sensitivity study;
- it allows scaling techniques;
- It allows more detailed analysis at global and local levels...

In practice, the ultimate goal is to provide a help to deciders in charge of non-lethal weapon procurement with technical information so they can choose the best product (weapon system or projectile) available on the market; to give relevant information to the manufacturers in either developing new projectiles or improving the existing ones, and finally to the end-users (military or police forces) of these

weapons, information on operational distance of engagement (minimal and maximal).

The question is then *"how to assess the injury potential of a KENL projectile impact to the thorax and determine the corresponding effective range ?"*. In order to assess the effects of the impacts of kinetic energy non-lethal projectiles on the thorax, the idea is to come out for a given configuration with a *decision* about the lethality of the a given KENLW (dangerous or not). Once the thorax model as well as the projectile model has been validated, numerical impact is carried out and results are processed (Figure 4.12). Based on the output of the model and injury criterion corresponding to a specific type of injury, decision can be made about the projectile lethality and minimal distance of engagement can be determined thanks to the projectile retardation relation. When the information about the KENLW dispersion is available, maximum distance of engagement can also be determined. Both the minimal and the maximal distance will define the effective distance.

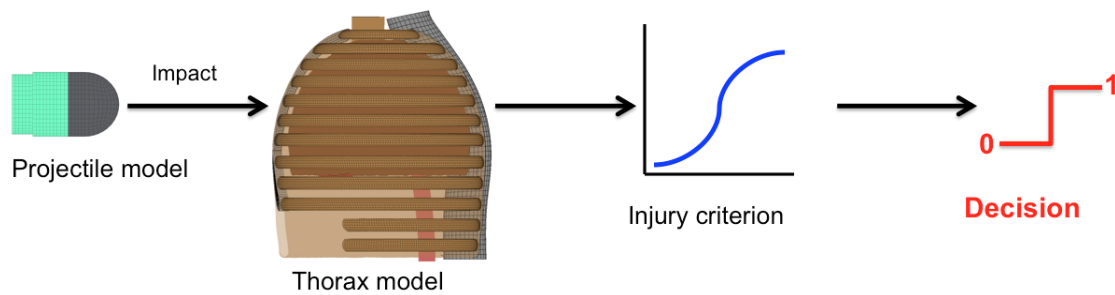


Figure 2.13. Method for KENLW assessment.

2.7 Original contribution of this thesis

The first contribution is the development of numerical tool for injury risk assessment of the impact of KENL projectiles on thorax. Its validation is based on the WSU studies and the viscous criterion $(VC)_{max}$. The proposed method is applicable to all types of KENL projectiles. It offers the possibility of investigating other injury criteria. The viscous criterion defined for stiff projectiles is extended to deformable projectiles and other types of projectiles. A thorax finite element model has been developed for the purpose.

A second contribution is the development of KENL projectiles FE models. Six KENL projectiles with different geometrical and material characteristics have been modelled.

Another contribution is the development of a characterisation method for deformable projectiles like the 40 mm sponge grenades. Only the deformable nose is

2.7 Original contribution of this thesis

concerned by this characterisation. This method has an advantage of characterising the nose material and at the same time the validation of the projectile is achieved.

Finally, in the framework of the participation of the Belgium to the NATO group on non-lethal capabilities, the results provided herein are valuable source. This can be a major contribution to the process of using numerical method as a tool of assessment of kinetic energy non-lethal projectiles impact at NATO level.

Chapter 3

State of the Art

In Chapter II, the concept of KENLW non-lethal weapons was introduced, the employment and usefulness, and their effects on the thorax. The development of assessment tools requires a better understanding of the thorax, how it reacts to an external stimulus e.g. KENLW impact, the occurrence of injury and the underlying injury mechanisms, the types of injuries and their severity. Therefore, in this chapter, firstly, a description of the anatomical structure of the thorax is given, secondly an introduction to the thorax injury biomechanics is given. Notions of injury criteria, injury risk curve are presented. Thirdly, for the KENLW evaluation and the injury risk assessment, physical and computational models have been developed. A literature review of these models for KENLW impact evaluation is made and finally conclusions are exposed.

3.1 Thorax anatomy

To better understand the injury mechanisms that trigger the onset of injuries, the knowledge of the anatomy of the thorax is necessary. The thorax is the part of the body that lies between the neck and the abdomen [48–50]. It is separated from the abdomen by the diaphragm. It consists of different organs that can be separated into two main groups (Figures 3.1-3.2):

- The thorax (chest) wall, an outer protective group composed of a skeletal structure made of the sternum, 12 paired ribs, the spine and a soft tissue group made of the costal cartilages, intercostal muscles (tissues between ribs), the flesh and the skin... The cartilages are dense connective tissues linking each rib to the sternum. On each side, the first 7 ribs (called the true ribs) are attached on their anterior side to the sternum via the costal cartilages, the

8th to 10th ribs called the false ribs are attached to the costal cartilage of the 7th rib and two remaining ribs (11th to 12th) are called floating ribs. All the ribs are attached on their posterior side to the thoracic vertebrae column. The vertebrae column is made of individual bones called vertebrae separated by spinal discs acting as a shock absorber, of muscles and highly sensitive nerves. It supports the body and holds the cervical spine.

- The internal structure consisting of vital organs: the lungs essential for respiration allows gas exchange. It is filled partially with air and blood. - the heart, which is a large muscle which acts like a pump distributing blood throughout the body - and various intrathoracic vessels, of different sizes in the thoracic region through which flow fluids or substances (blood, air, ...) to/from the major organs. The main vessels are the aorta, the venae cavae , the pulmonary veins/arteries, the trachea, ... The space in the thoracic cavity between organs are filled with fluid.

Each tissue or organ has its own biomechanical properties and its own shape. Due to external forces, it will react through injury mechanisms in its own way resulting in injuries which are typical to the organ. Therefore the biomechanical response of the thorax to the impact of projectiles is complex and depends of many parameters: the characteristics of each organ, the characteristics of the projectile and the mutual interactions between organs or with the projectile. Depending of the affected organ and the severity of the impact, the thoracic injury can be life threatening.

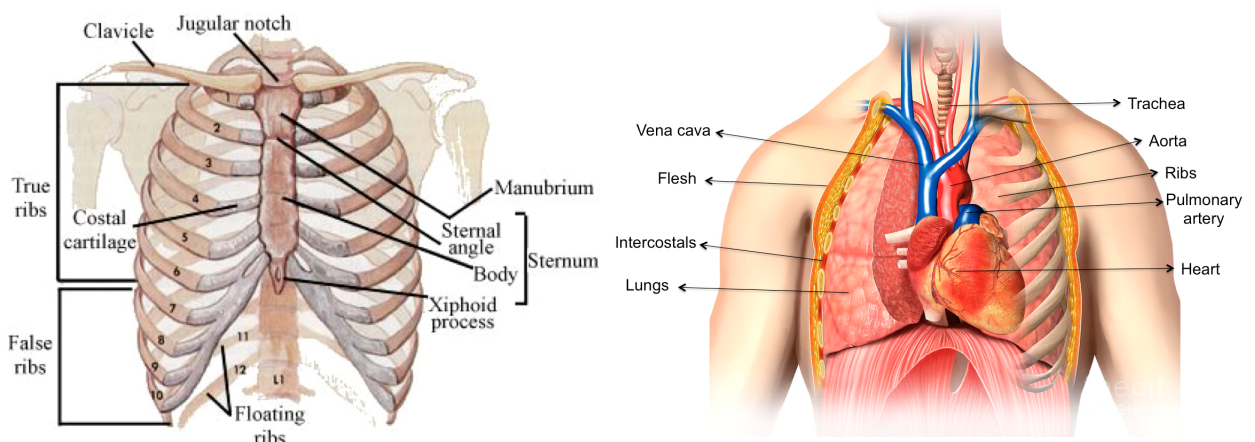


Figure 3.1. *Thoracic cage and internal organs [51–53].*

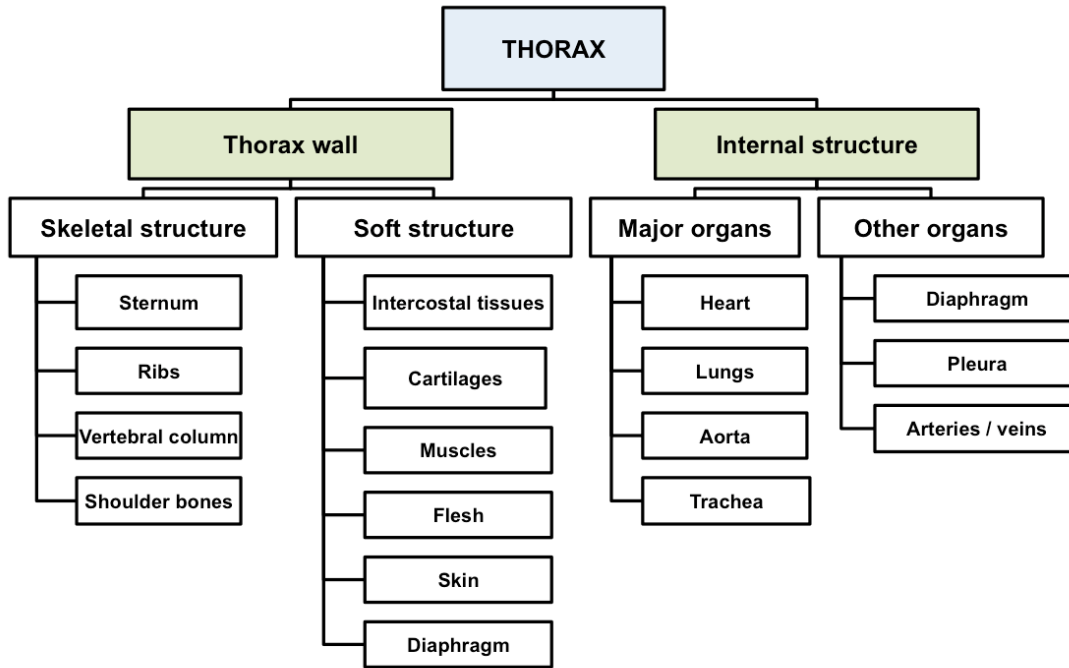


Figure 3.2. Thorax structure. Adapted from [54].

3.2 Thorax injury biomechanics

As the thorax is housing vital organs (heart, lungs,...) of the body, it should not be strained, if subjected to an impact, beyond the thorax tolerance limits otherwise injuries even severe may result. Therefore an injury is a result of the organ being strained beyond its tolerance limit. In the normal conditions of use of KENLW, non-lethal ballistic impacts are non-penetrating impacts that generally are the cause of blunt trauma. The same types of injuries are often found in the rear effects of personal ballistic protection (BABT (Behind Armour Blunt Trauma)) [55], in sport injuries and in motor vehicle accidents. As already stated, some types of injury are not acceptable in the KENLW framework.

Much research has been carried out for decades in the automotive field (crash tests) to improve the safety of passengers during accidents. A high expertise in understanding the injury mechanisms, proposing injury criteria and defining tolerance levels through years has been developed. Testing protocols were put in place and a lot of data were collected through testings and accident reconstructions for injury risk analysis.

To a certain extent, there is a similarity between the induced injuries and the underlying mechanisms in the automotive field and the non-lethal field that was developed much latter, many concepts and knowledge have been borrowed from

crash tests field specifically. Nevertheless, there are certain differences. Non-lethal impacts are characterised by low mass and high velocity impacts and the phenomena are more localized while the impacts (accidents) in automotive field are high mass and low velocity impacts and phenomena are more global (Figure 3.3).

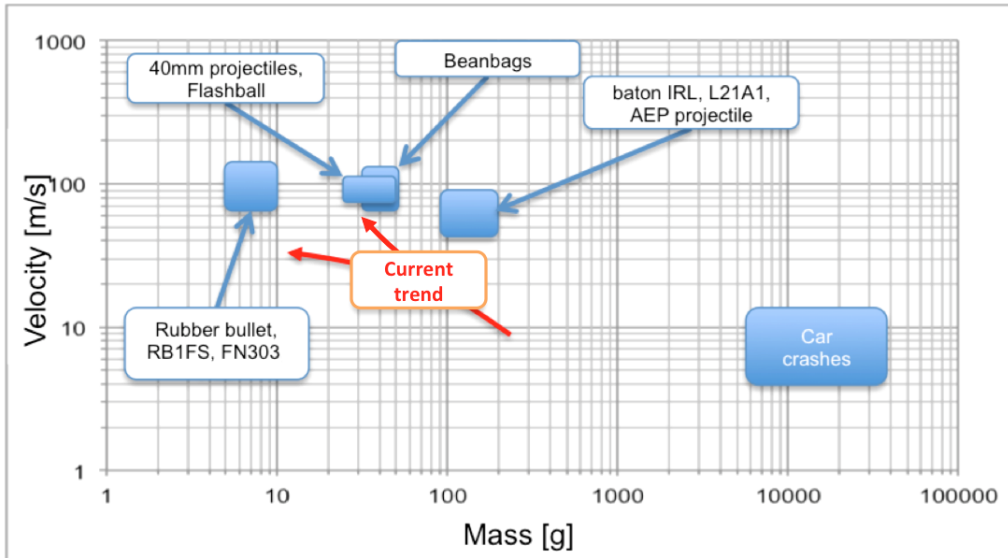


Figure 3.3. Comparison of a non-lethal impact and an impact resulting from a car crash [40].

The impact of non-lethal projectiles against the thorax induces a reaction or a response in terms of deformation which generally can lead to thoracic injury. There are two important considerations that must be taken into account for the evaluation and prediction of risk of injuries, injury mechanisms and thorax biomechanical response:

3.2.1 Injury mechanisms

Ballistic impacts on the human body may result in the alteration or the damage of tissues/organs and in physiological dysfunctions. The mechanisms or physical processes related to the occurrence of injury are called injury mechanisms. The main injury mechanisms involved during blunt impacts [56] as depicted in Figure 3.4 are:

- *The crush & shear mechanism:* it consists of the crushing and the shearing of the tissues and organs by a direct compression of the thorax wall during the impact [56, 57]. This mechanism is induced at low thorax deflection rates ($\leq 3m/s$). The biomechanical response in this case is generally an elastic resistive response of tissues and organs. When strained beyond the elastic limit of the tissues, injury will result.

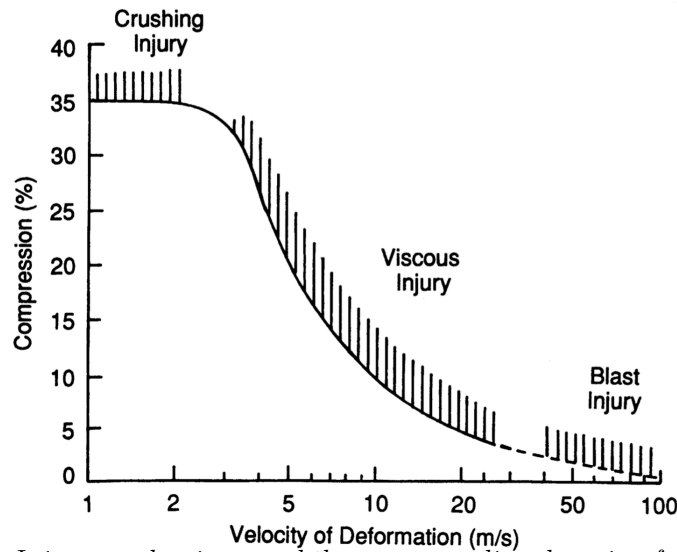


Figure 3.4. Injury mechanisms and the corresponding domain of validity: compression as a function of the velocity of deformation. ¹ [56].

- *The viscous mechanism* resulting from the viscous properties of tissues and organs. It is induced at high loading rates ($3\text{m/s} \leq v \leq 30\text{m/s}$). It is characterised by the propagation of pressure waves and the reflection of those waves at the interfaces of organs or of cell walls can lead to internal damage before any significant deflection of the outer structure [56, 57]. The internal damage can occur in both solid and air filled organs like the lungs.

For velocities higher than 30 m/s, it is the "blast injury" mechanism which becomes dominant and shock waves play an important role [56]. The blast injury begins to occur first in hollow organs like the lungs.

The biomechanical response of the human body to blunt trauma is generally a consequence of the activation of different injury mechanisms.

3.2.2 Thorax biomechanical response

The biomechanical response of the thorax to blunt trauma can be seen in two perspectives (Figure 3.5): the lesional (or medical) perspective and the engineering perspective. The lesional perspective is more a matter of medical doctors for the trauma diagnosis and the administration of trauma care while the engineering perspective is about the application of the laws of physics in the trauma problematic.

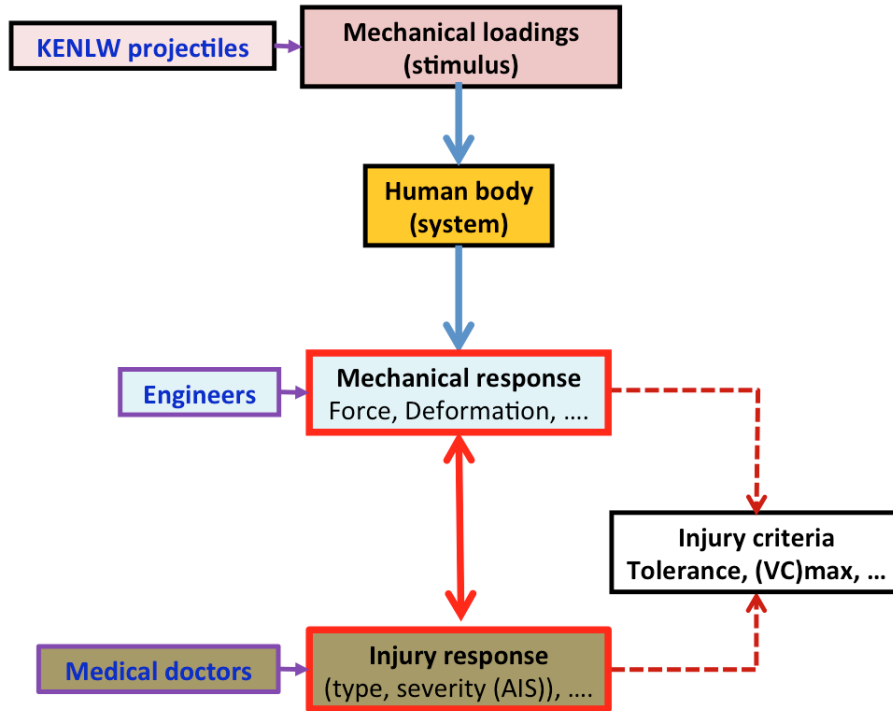


Figure 3.5. *Injury response scheme.*

3.2.2.1 Lesional (or medical) perspective of thoracic biomechanical response

In this section, different types of injuries sustained by the thorax will be described and the notions of severity score will be introduced.

a) *Types of injuries*

One distinguishes the type of injuries according to whether they occur in the chest wall or in the internal organs [58]:

- The parietal injuries: These are bone injuries or soft tissue injuries of the chest wall resulting from direct contact with the impacting object or when they occur at the impact location or at its immediate vicinity. The mechanism associated is the crush & shear injury. They manifest themselves in several ways.
 - *The superficial injuries (or bruises) on the skin and subcutaneous tissues.* They include different types of injuries [57–59]: abrasion (friction with epidermal stripping), bruise (hemorrhagic infiltration), hematoma (circumscribed collection of blood caused by a break in a blood vessel) and laceration (open injury). In Figure 3.6 is shown an example of injuries from rubber bullet impacts.
 - *Rib fractures* concern the fracture of one or more ribs. Depending on the number and their location, rib fractures are considered minor or life-threatening.



Figure 3.6. *Examples of injuries from rubber bullet impacts[60, 61].*

If the trauma is very important, flail chest (fracture of several ribs) can occur which is generally life threatening. Rib fractures are the most common injury following chest trauma [59].

- The internal organs injuries:

These are injuries of the internal organs of the thorax [57–59]. They are indirect injuries as they do generally occur far from the impact location (Figure 3.7). The cause of these injuries is due either to the pressure waves or to a significant compression of the rib cage during impact or to the fracture of the ribs.

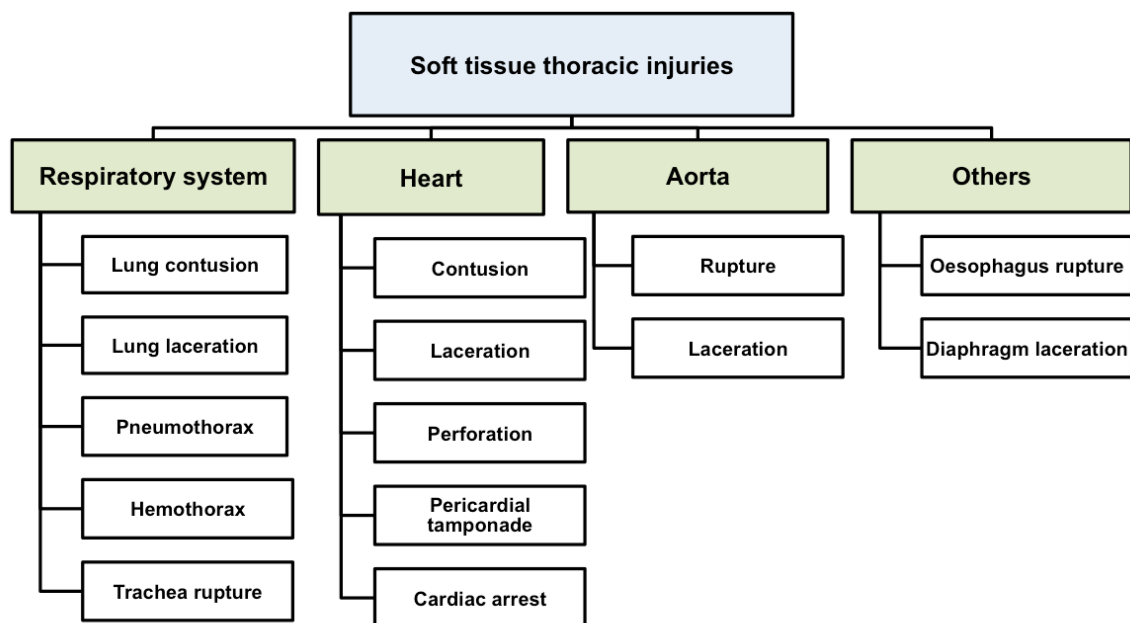


Figure 3.7. *Possible soft tissue thoracic injuries [46].*

They include:

- *Lung injuries*

There are different types of lung injuries: the pulmonary contusions, the pneumothorax which is the presence of air in the pleural cavity (cavity between the lung and chest wall) and the hemothorax which is the effusion of blood in the pleural cavity.

- *Heart injuries*

The principal heart injury is the cardiac contusion which can range from mild to severe. On the functional level, cardiovascular disorders may occur which can even be fatal. An example of such disorder is the commotio cordis. It is a cardiac arrest by ventricular fibrillation after a thoracic blow and without any underlying cardiac abnormality [57, 62].

- *Injuries of the intrathoracic vessels* concern mostly the rupture or the lacerations of the thoracic vessels.

It should be noted that the risk of internal injuries is greater when there are rib fractures. It is the reason that the main injury that is investigated for thoracic injury risk assessment is the rib fracture as we will see it in the section 3.2.4. However, in certain cases, even without rib fracture or other apparent injuries on the chest wall, internal injuries can occur.

b) Severity of injuries

The type and severity of an injury from blunt impacts depend upon the impacted region of the body and can be mild, severe or life-threatening. To use a universal common language when it comes to trauma injuries, injury coding systems were developed and the most well-known coding system is the Abbreviated Injury Scale (AIS) that was originally developed for use in automobile accident studies.

The Abbreviated Injury Scale (AIS)

The Abbreviated Injury Scale is an anatomical scoring system which describes the injury in terms of the type of injury and its relative severity according to the body region and the type of anatomical structure. This scale assesses tissue damage and threat to life on a six division ordinal scale running from minor, moderate, serious, severe, critical, to currently untreatable (usually fatal). It is now used universally in clinical and research studies as an agreed ranking of the severity of trauma [45]. The same scale is also adopted in the non-lethal field and Table 3.1 shows an example of this scale for the thorax injuries, adapted in accordance with [46, 57].

3.2 Thorax injury biomechanics

AIS score	Severity	Corresponding fracture	Injury of tissues
1	Minor	1 Rib fracture	Bronchial tube contusion
2	Moderate	2-3 rib fractures Breastbone fracture	Partial bronchial tube rupture
3	Severe non-life threat	More than 4 shoulder blade fracture 2-3 costal fracture et hemo- /pneumothorax	Lung bruise Minor heart bruise
4	Severe life threat	Flail chest >4 rib fractures (bilateral fracture) >4 rib fractures + hemo/pneumothorax	Bilateral lung lacerations Minor aorta laceration Major heart contusion
5	Critical	Bilateral thoracic flail	Major aorta laceration Lung laceration with pneumothorax
6	Maximal		Aorta laceration with massive hemorrhage

Table 3.1. *Abbreviated Injury Scale (AIS) applied to the thorax [46, 57].*

3.2.2.2 Engineering perspective of thoracic biomechanical response

Knowing that KENLW projectile impacts can lead to serious injuries, it is necessary to guarantee that their use will result, if not in zero-risk, but at least in a defined or a mitigated risk. This requires a better understanding of the physical processes that occurs during impacts in order to develop criteria that will allow the manufacturers to design, the procurement authorities to purchase and the end-users to use less-lethal ammunitions with a reasonable level of confidence.

Each region of the body (the thorax in our case) can be considered as a mechanical system to which the laws of physics apply. Under (dynamic) loadings, the thorax as a system will react such that the energy from the impacting objet is absorbed through reversible processes (elastic deformation) and through irreversible processes (injuries for example). The initial kinetic energy of the projectile is given by

$$E_{proj} = \frac{mv^2}{2} \quad (3.1)$$

- m [kg] is the projectile mass;
- v [m/s] is the initial projectile velocity

Upon the impact, this energy is absorbed by elastic deformation or dissipated by the thorax through the activation of injury mechanisms. The energy absorbed/dissipated

by the thorax during the activation of the two main injury mechanisms can be calculated [63, 64]:

By assuming a uniaxial problem and a linear viscoelastic behaviour, the energy density can be approximated.

For $v \leq 3m/s$, the thorax behaviour can be assumed as linear elastic. It corresponds to the crushing of the thorax (Figure 3.4) at very low rate (quasi-static deformation).

The energy density absorbed E_{crush} [J] by the tissues/organ before the onset of the injury, corresponding to the elastic strain energy is given by:

$$E_{crush/shear} = \int_0^{\varepsilon_{max}} \sigma \, d\varepsilon = \int_0^{\varepsilon_{max}} E\varepsilon^2 \, d\varepsilon = \frac{E\varepsilon_{max}^2}{2} \quad (3.2)$$

with

$$\sigma = E\varepsilon \quad (3.3)$$

where

- σ [Pa] is the average stress on the impact surface, in the direction of the impact.
- $\varepsilon = c/c_0$ [-] is the average strain in the direction of the impact; c is the displacement of the point of impact and c_0 the initial thoracic thickness c_0 , assuming that there is no displacement of the rear of the chest. It corresponds to the strain before the onset of injury.
- E [Pa] is the average Young's modulus for the thorax at the point considered and in the direction of impact.

The energy density absorbed by the tissue/organ is directly proportional to the square of the maximum strain.

For $3m/s \leq v \leq 30m/s$, the injury mechanism is the viscous response (Figure 3.4) and the behaviour of the thorax is assumed as linear viscoelastic. The injury in the organs occurs at the time of peak viscous response well before the maximum deflection [65]. The energy density dissipated $E_{viscous}$ [Pa] by the tissues/organ during the "viscous mechanism", before the onset on the injury can be approximated by:

$$E_{viscous} = \int_0^{\varepsilon_{max}} \tau \varepsilon \, d\varepsilon = \int_0^{t_{\varepsilon_{max}}} \eta \dot{\varepsilon}^2 \, dt = \eta \left([\varepsilon \dot{\varepsilon}]_0^{t_{\varepsilon_{max}}} - \int_0^{t_{\varepsilon_{max}}} \varepsilon \ddot{\varepsilon} \, dt \right) \quad (3.4)$$

with

$$\tau = \eta \dot{\epsilon} \quad (3.5)$$

- τ [Pa] is the average shear stress;
- $\dot{\epsilon} = v/c_0$ is the average impact surface strain rate, in the direction of the impact; v is the average velocity at the point of impact and c_0 is the initial thoracic thickness c_0 , assuming that there is no displacement of the rear of the thorax. This is only an approximation.
- η is the average dynamic viscosity of the thorax at the point considered and in the direction of impact.

The first term of Equation 3.4 which characterizes the viscous resistance of tissues. The second term corresponds to the tissue inertia. If the second term is neglected compared to the first term, then one can write [2]:

$$E_{viscous} \approx \eta [\epsilon \dot{\epsilon}]_0^{t_{\epsilon max}} \quad (3.6)$$

Under this approximation, the energy dissipated by the tissues/organ and the "viscous response" are closely linked.

To stop the projectile, the thorax has to react by applying a resistive force over a period of time. Each tissue has its own tolerance threshold and to avoid the onset of injuries, the force must be kept under this threshold. From the Newton's second law in its integral form applied to the projectile, one can write (Equation 3.7). As stated by Lu et al. [66], *"the peak reaction force of an energy absorber should be kept below a threshold; and ideally the reaction force should remain constant during the large deformation process of the energy absorbing structure"*. This gives a clue for the development of KENLW projectiles as the only variables that can be controlled in advance of impact on a human by KENL projectile are the projectile properties [67].

$$\Delta \vec{p} = m \dot{\vec{x}}(t_f) - m \dot{\vec{x}}(t_i) = \int_{t_i}^{t_f} \vec{F}_p(t) dt \quad (3.7)$$

and, by action and reaction

$$\vec{F}_p(t) = -\vec{F}_h(t) \quad (3.8)$$

- $\Delta \vec{p}$ [Kgm/s] is the change in momentum.

- m is the mass of the projectile, assumed to be constant during the impact.
- $\dot{\vec{x}}(t_i)$ is the velocity vector of the projectile's centre of gravity as a function of time prior the impact.
- $\dot{\vec{x}}(t_f)$ is the velocity vector of the projectile's centre of gravity as a function of time after the impact.
- $\vec{F}_p(t)$ [N] is the force acting on the projectile as a function of time during the impact. It is the contact forces between the projectile and the thorax and
- $\vec{F}_h(t)$ [N] is the force acting on the thorax during the impact.

From the above considerations, the force developed during the impact on the thorax before the onset of injury (damage of tissues) is a result of viscous, elastic, and inertial factors [68] which can be written in a classic form (Equation 3.9) when considering the thorax as a mechanical system with damping in one dimension.

$$\vec{F}(t) = K\vec{x}(t) + C\dot{\vec{x}}(t) + m\ddot{\vec{x}}(t) \quad (3.9)$$

- $\vec{x}(t)$ is the displacement vector of the thorax impact point as a function of time, $\dot{\vec{x}}(t)$, the corresponding velocity and $\ddot{\vec{x}}(t)$ the corresponding acceleration.
- K is the elastic spring constant, C is the viscous damping coefficient and m is the average effective mass.
- $\vec{F}(t)$ is the force acting on the thorax during the impact.

When taking into account what has been stated previously, apart from the material and geometrical characteristics of the thorax and the projectile (see Chapters V&VI), four important physical parameters play a key role in the occurrence of the injuries and in their evaluations:

- The part of the projectile kinetic energy absorbed by the thorax
- The projectile momentum change (before and after impact)
- The effective cross-section impact area
- The impact duration

The determination of human tolerance threshold requires dynamic loading testings ideally on living humans. For evident reasons, tests are performed on PMHS and animals although they probably have not the same characteristics as the living humans. Their disadvantage is the lack of repeatability and reproducibility. Therefore, the data collected from PMHS and animals are used as baseline data for the development of injury criteria and for validation purpose of the mechanical and virtual surrogates. These surrogates are more convenient to use for testing purposes because of their repeatability and reproducibility.

On the one hand, it is necessary to determine the measurable physical parameters relevant to quantify the loading and the mechanical response. The measurable physical parameters can be impact force, displacement... On the other hand, it is necessary to measure and collect experimental data from testings or/and real life situations on these physical parameters. The statistical analysis of these data is not only used to quantify the injuries on the chest, to find the best parameter predictor and the related probabilities for the occurrence of injuries, but also to built biomechanical corridors (section 3.2.4).

In fact, due to the difference in material and geometrical characteristics of the tested subjects (population), there are also differences in biomechanical response for the same impact conditions. To take this into account, biomechanical corridors are determined in order to validate physical and virtual surrogates.

The engineering perspective deals with data (quantification) and functions while the lesional perspective deals with injuries, damage to tissues. Therefore, to bridge the two perspectives, injury criteria are defined (Figure 3.5).

3.2.3 Thoracic injury criterion

3.2.3.1 Definition

An *"injury criterion"* is defined as a *"physical parameter or a function of several physical parameters which correlates well with the injury severity of the body region under consideration"* [69]. Under the same conditions of impact, people do not have exactly the same biomechanical response i.e will not sustain the same injury or at the same severity level due to factors like age, gender, anthropometric data, ... Because of this variability among people, injury criterion is defined in terms of probability. An injury criterion indicates therefore the probability of sustaining injury at a given AIS level. Different probabilistic functions (or injury risk curves) are used. One of

the most used is the logistic regression function given by the Equation 3.10.

$$p(x) = \frac{1}{1 + e^{-\alpha-\beta \cdot x}} \quad (3.10)$$

Where x is the predictor variable (discrete or continuous), $p(x)$ the corresponding probability of sustaining an injury of a given AIS level, α and β are parameters derived from statistical analyses of biomechanical tests. One key value of the injury

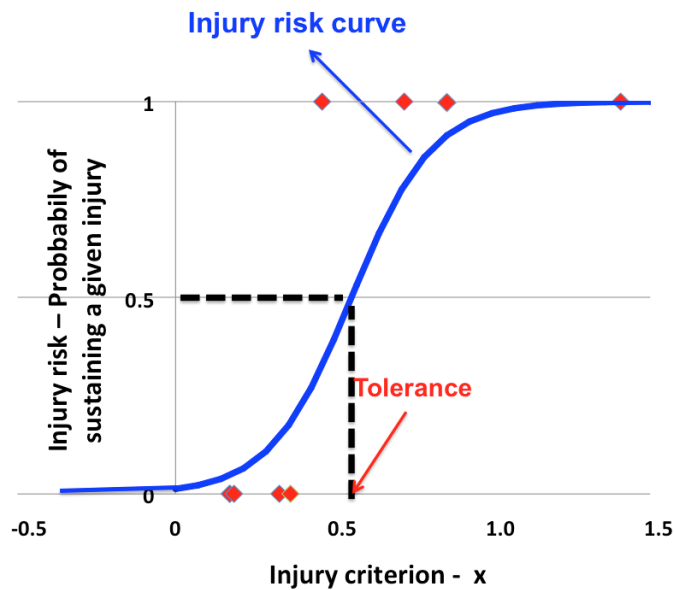


Figure 3.8. Injury risk curve.

criterion is the injury tolerance (called also tolerance limit or tolerance threshold).

The "injury tolerance" of a bodily region or organ is defined as the "magnitude of loading indicated by the threshold of the injury criterion, which produces a specific type of injury severity and risk". In other words, the injury tolerance level is the value of a known injury criterion which makes it possible to distinguish a non-traumatic from a traumatic event with a given statistical probability [2, 37, 57, 69].

By analogy to the ballistic limit V_{50} ² [70] or LD_{50} ³ the lethal dose fifty in epidemiology and toxicology [26], a reference value defined as the statistical estimate of the injury criterion corresponding to a probability of 50% which discriminates a traumatic from a non-traumatic event is determined. Generally it is a specific point of the injury risk curve where the uncertainty is minimal [2, 71, 72]. One has to

²The ballistic limit V_{50} is the velocity of the projectile corresponding to a probability of 0.5 (50%) that the defined projectile penetrates the test specimen.

³Lethal dose fifty (LD_{50}): A calculated dose of a substance which is expected to cause the death of 50 percent of an entire defined experimental animal population. It is determined from the exposure to the substance by any route other than inhalation.

note that other choices are possible like the injury tolerance corresponding to a probability of 10% but the uncertainty would be more important.

As previously mentioned, much of the knowledge in non-lethal blunt trauma comes from the automotive field where diverse injury criteria have been investigated and developed. Even though there are similarities between the two fields, only very few criteria have been adapted for non-lethal field.

3.2.3.2 Blunt criterion

It is a semi-empirical relation based on the projectile kinetic energy, the projectile diameter and the target size which correlates well with the observed injuries. It is given by

$$BC = \ln \left(\frac{mv^2}{2W^{1/3}TD} \right) \quad (3.11)$$

where

- m [kg] is the mass of the projectile.
- v [m/s] is the velocity of the projectile.
- W [kg] is the mass of the target.
- T [cm] is the thickness of the target's deformable wall.
- D [cm] is the diameter of the projectile.

The *Blunt Criterion (BC)* was developed by the US Army in 1970 for predicting the injury risk from thoracic blunt impacts using stiff flat-nose cylinders [73]. The (BC) has been historically used as a munition design criterion [74]. Later, Bir et al. [7] validated the criterion for thoracic impacts using stiff non-lethal projectiles. A value of $BC = 0.37$ m/s, is taken as the reference value corresponding to a 50 % probability of sustaining skeletal thoracic injury (rib fracture) of $AIS > 1$.

The problem with this criterion is that it does not take into account the material properties of the projectile as well as the target material properties. According to this criterion, a compliant or deformable projectile and a stiff projectile will have the same effect on the target as long as they have both the same initial energy and the same diameter. In reality, during the impact, the deformable projectile will behave differently from the stiff projectile in term of energy absorption, effective impact diameter,... thus the dynamics are different, so are they in term of injury.

Therefore this criterion is not suitable for deformable projectiles [22, 75–77] and will be disregarded from this point on.

3.2.3.3 Viscous criterion

The *viscous criterion* is one of the criteria developed for thoracic impact risk assessment especially in automobile field. It is based on the dynamic deflection of the thorax and is determined thanks to the viscous response (Equation 3.12) which is the product of the thorax deflection (compression) and the thorax deflection rate normalized by the thorax thickness. The viscous criterion $(VC)_{max}$ (Equation 3.13) is defined thus as the maximum of thorax viscous response (Figure 3.9). More details can be found in the literature [7, 78–80].

This criterion was proposed for non-lethal (rigid) projectiles evaluation in [7] after experimental tests carried out on PMHS. The type of injury that was investigated for the determination of this criterion was the rib fracture. A value of $(VC)_{max} = 0.8$ m/s, was determined as the reference value corresponding to a 50 % probability of sustaining skeletal thoracic injury (rib fracture) of AIS>1 [7].

$$\text{Viscous response} = (v(t).C(t)) \quad (3.12)$$

The "*Viscous Criterion*" $(VC)_{max}$ is given by:

$$(VC)_{max} = (v(t).C(t))_{max} \quad (3.13)$$

where the average compression $C(t)$ is expressed as the ratio between the average displacement of the impacted region $c(t)$ [m] and the length $c_0 = 0.236m$ [m] is the initial thickness of the thorax. It is assumed that the thorax rear point does not move during the impact. This can be explained by the localised characteristics of the KENLW impacts.

One has to point out that the viscous criterion was proposed and adapted by C. Bir on PMHS using stiff projectiles [7]. But there is no consensus on the relevance of the criterion for deformable KENL projectiles. Some progress has been made in the NATO framework where a group of experts namely NLKE ToE⁴ meet twice a year for information exchange and for defining non-lethal standardisation methods. A draft about this issue is under acceptance procedure [5] and use $(VC)_{max}$ as a injury criterion for thoracic impacts.

⁴Non-Lethal Kinetic Energy Team of Experts

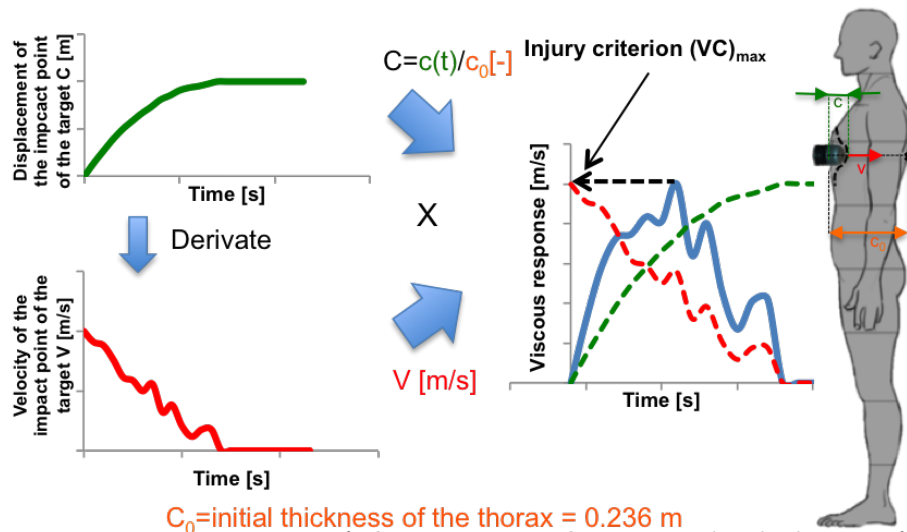


Figure 3.9. Representation of the viscous mechanism and calculation of the injury criterion[2].

3.2.4 Blunt thoracic impacts - WSU experiments

As the tests of KENLW projectile impacts on living humans are not feasible for risk of severe injury, the development of "biofidelic surrogates"⁵ mechanical or numerical is of major importance. They offer a great advantage of repeatability and the benefit to circumvent the use of PMHS and animals testings. PMHS and animals pose the same problem of repeatability and reproducibility as living humans. Nevertheless they are used as substitutes for injury analysis being the closest to the living humans, anatomically and anthropometrically for the former and physiologically for the latter. Therefore, tests on PMHS and animals are still necessary because they provide the baseline data for investigating injuries, developing injury criteria and tolerance levels, and for validating the surrogates.

Today there are few PMHS tests on KENLW projectiles available in the open literature. A reference work in the open literature is the one performed by Bir at the WSU [7]. The results from WSU constitute therefore the core of the present work. In the following section, a description of the WSU experiments is given.

3.2.4.1 WSU experiments

Bir performed tests of non-lethal projectiles on PMHS at WSU. The purpose was twofold:

⁵A biofidelic surrogate is a device or a model which mimics the biomechanical response of the human body or a body part under a given stimulus.

- Define biomechanical corridors and injury criteria which will serve as baseline data for validation of the surrogate and injury investigation;
- Build a biofidelic surrogate i.e. surrogate validated according to biomechanical corridors for KENLW assessment purpose.

The tests consisted in shooting rigid non-lethal cylindrical projectiles on 13 PMHS. Three impact conditions were considered by using two types of 37mm diameter projectiles:

- Condition **A** corresponding to the impact of the projectile with a length of 100 mm and a mass of 140 g at a velocity of 20 m/s.
- Condition **B** similar to condition **A** but with a velocity of 40 m/s.
- Condition **C** corresponding to a projectile with a length of 28.5 mm and a mass of 30 g at a velocity of 60 m/s.

These projectiles were equipped with an accelerometer from which the force as function of the time was derived and a high speed camera was used to track the thorax displacement at the point of impact.

The only injury that were investigated during these tests was the rib fracture.

It is worth noting that these types of projectiles are the first generation projectiles and they are no longer in use. Now they have been replaced by new generation projectiles which are mostly deformable ones.

3.2.4.2 Determination of biomechanical corridors

From the results of measurements, force-time and displacement-time curves were determined. But, due to the difference in the tested specimen characteristics, there was a variability in the biomechanical responses under the same conditions. Therefore to take into account this variability, biomechanical response corridors were defined (Figure 3.10-3.11). The other results are given in Annex A. These characteristics which take into account the dynamics of the impact (forces and motions) are important for the development of biofidelic surrogates as they are used for validation purposes. But some inconsistencies [81] were found in the force-time data presented by Bir as discussed by Robbe [2]:

- Energy issue: *If an energy or momentum assessment is carried out on these force-displacement curves, energy values are obtained which are not constant*

from one firing to the other. These values do not correspond to the kinetic energy supplied by the projectile. These considerations are spelled out in references [81, 82].

- Data processing issue: *Certain metrological data are incomplete, such as the description of filters that were used and the exact mass and velocity data for the instrumented projectiles.*

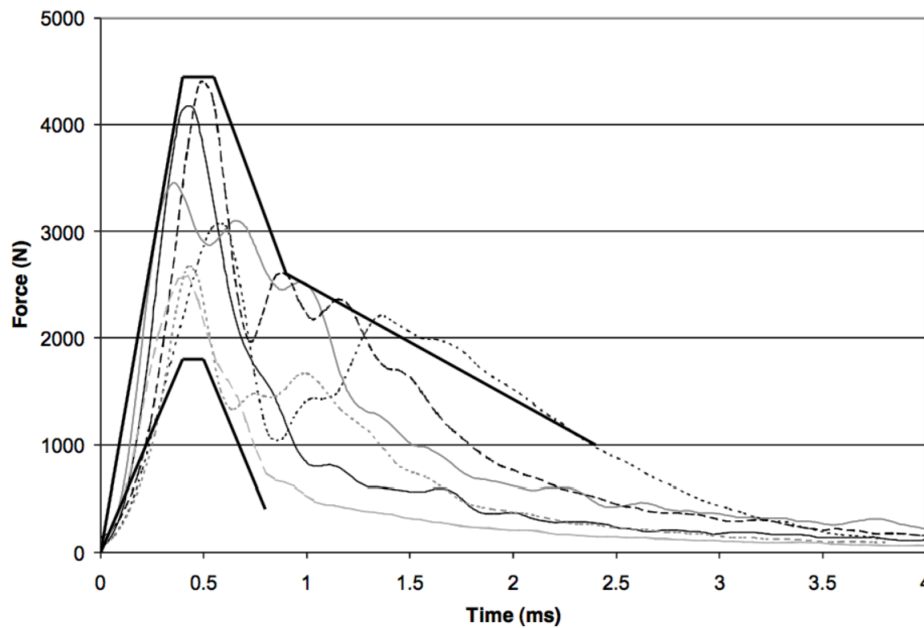


Figure 3.10. *Impact force on a PMHS thorax as a function of time for impact condition A [7].*

Because of these inconsistencies, there is more confidence in the displacement-time data than in the force-time data. Therefore only displacement-time data will be used for the validation of the numerical model. For a surrogate to be considered as validated, its displacement-time responses shall fall within the corridors defined for the considered impact velocities. Table 3.2 gives the corridor coordinates for the 3 impact conditions.

3.2.4.3 Determination of viscous criterion $(VC)_{max}$

The biomechanical corridors although important was not sufficient in order to discriminate the occurrence or non-occurrence of injuries. Other physical parameters or their combination were considered. It was found that the viscous criterion correlated well with the observed injury of a given AIS. Therefore for each test corresponds also a $(VC)_{max}$. Taking into account the variability of the biomechanical responses

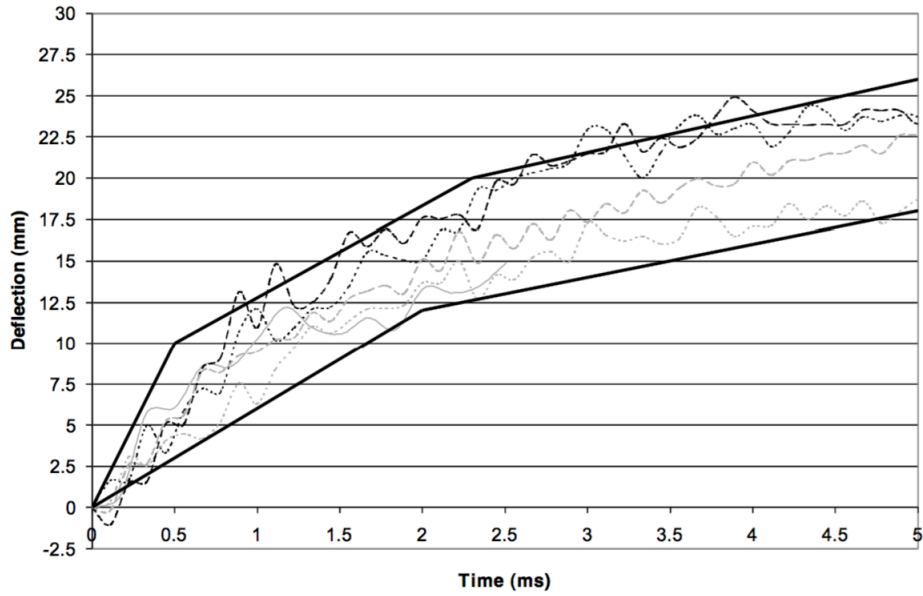


Figure 3.11. *PMHS thorax displacement as a function of time for impact condition A [7].*

of all the tested specimen [7], intervals of $(VC)_{max}$ (Table 3.3) were defined. In these intervals, the calculated values from the surrogate should fall in to be considered as validated for the same impact conditions (section 3.2.4.2). For injury occurrence, a value threshold of $(VC)_{max} = 0.8$ m/s, was determined as the tolerance level corresponding to a 50 % probability of sustaining skeletal thoracic injury (rib fracture) of AIS>1 [7].

Impact condition	Time Corridor min [ms]	Displacement corridor min [mm]	Time Corridor max [ms]	Displacement corridor max [mm]
case A	0	0	0	0
	2	12	0.5	10
	5	18	2.3	20
	-	-	5	26
case B	0	0	0	0
	2	20	1	40
	8	38	6	70
case C	0	0	0	0
	1	5	0.5	12.5
	8	12	8	38

Table 3.2. *Numerical values of the WSU corridors (adapted from [7]).*

Impact condition	$(VC)_{max}$ Boundaries [m/s]
condition A	[0.24-0.51]
condition B	[0.65-2.35]
condition C	[0.14-0.60]

Table 3.3. $(VC)_{max}$ boundaries for the thorax validation based on WSU data (adapted from [7]).

3.2.4.4 Development of a surrogate for non-lethal thoracic impacts

Bir [7] developed during her dissertation a human thorax substitute (Figure 3.12) based on a substitute used in the automotive industry: BIOSID (Biofidelic Side Impact Dummy) [7, 83, 84]. Three BIOSID ribs were attached to a spine box to which a damping material was also added. [7]. As the $(VC)_{max}$ is based on the dynamic deflection of the thorax, only the tracking of the deflection is needed. This is done thanks to an integrated LED-Based system. This surrogate is the first thoracic surrogate for non-lethal impacts (Figures 3.10 and 3.11), successively named *3RCS* (*3 Rib Chest Structure*), and *3RBID* (*3 Rib Ballistic Impact Dummy*) (Figure 3.12). It was validated using the biomechanical corridors defined previously.

Three years ago, ABAL⁶ acquired the updated version of this surrogate, namely the 3RBID (3 Rib Ballistic Impact Dummy). It increased the range of KENLW evaluation tools available in the department. Moreover, it opens an opportunity for comparing the impact results by using two different surrogates (see Chapter IV). A description of the ABAL 3RBID system will be given in section 3.2.5.3.

3.2.5 Literature review of KENLW surrogates

Assessing and predicting the KENLW ballistic effects on the human body is not easy because experimental testings on living humans are not possible for different reasons as mentioned previously. They raise ethical issues. There are different alternatives that can be used as shown in Figure 3.13 with their advantages and drawbacks. One alternative is to use PMHS and animals. PMHS best represent living humans in terms of anatomy and mass distribution but as all their physiological functions are definitely off, they can not provide living physiological responses. Nevertheless, they can give valuable insight concerning the structural injuries. Conversely, living animals, although not anthropometrically similar to humans, could be used to monitor the alteration of living tissues/organs and their physiological functions. The only problem is to know at which extent this can be extrapolated to humans. Both PMHS and animals present some drawbacks as tests are not repeatable and

⁶Department of Weapon Systems and Ballistics

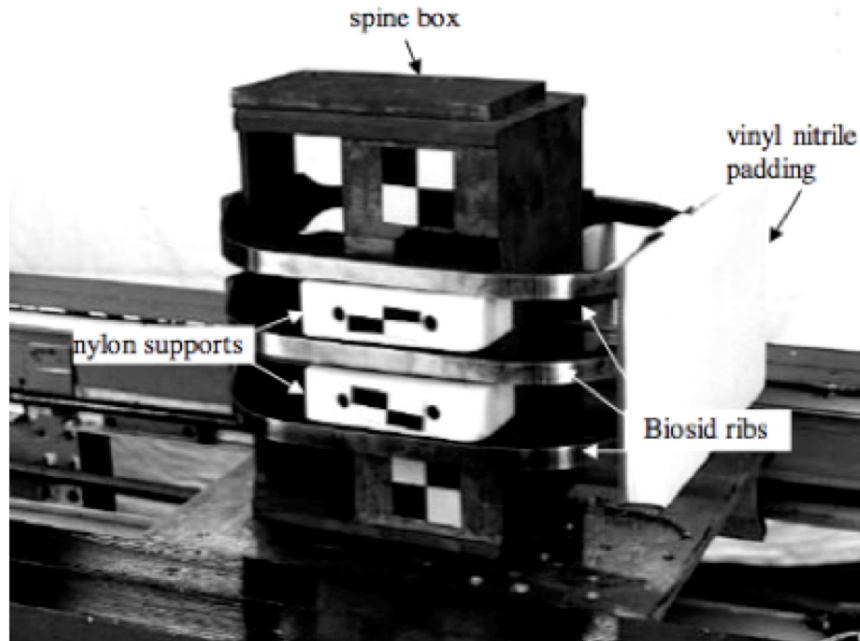


Figure 3.12. A thoracic surrogate [7].

reproducible. Nevertheless, they serve to gather baseline data for the injury criterion determination, the surrogate (mechanical or numerical) development. The other alternative is to use mechanical or numerical biofidelic surrogates.

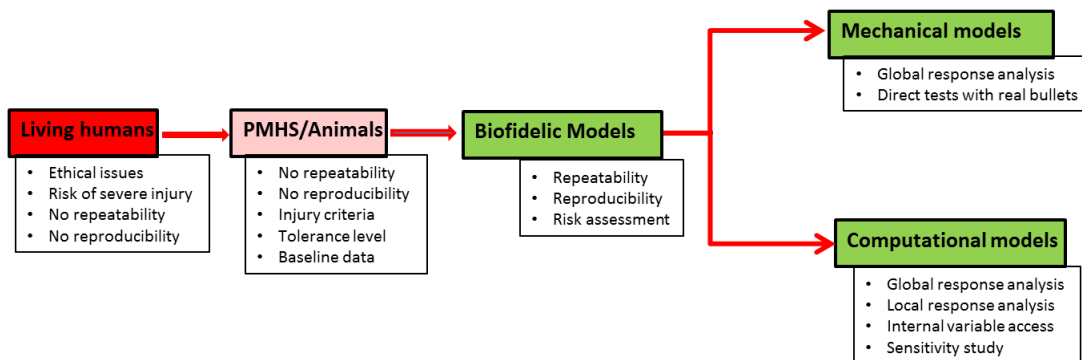


Figure 3.13. Different model types for injury assessment.

3.2.5.1 KENLW mechanical or numerical surrogates

Instead of using PMHS and animals which show limitations in their use, surrogates are developed for the evaluation of impact effects and the injury risk assessment. They have many advantages (Figure 4.1.6). Unlike the PMHS and animals which are prone to significant variability, they offer repeatable responses. There are two

main types of surrogates [85]: the physical surrogates namely the mechanical ATD (Anthropometric test Device) and the virtual (or numerical) surrogates especially those based on Finite Element Method called the HBFEM (Human Body Finite Element Models) or FEATD (Finite Element ATD) . Examples of the two types developed mostly for automotive field are given on Figure 3.14. These surrogates can represent all the human body, a substructure of it or an organ. Although the physical ATDs offer the great advantage by directly shooting the real non-lethal bullets against them and the results readily available, it has some drawbacks compared the numerical ones as generally only global response analysis can be carried out (Figure 4.1.6).

The HBFEM has many advantages:

- The capability of accounting for complex geometries or complex material modelling.
- Its cost-effectiveness.
- It gives insight into physical variables (stresses, strains,...) inside the material which are not accessible by other means.
- It allows parameter sensitivity study.
- It allows scaling techniques.
- It allows more detailed analysis at global and local levels...

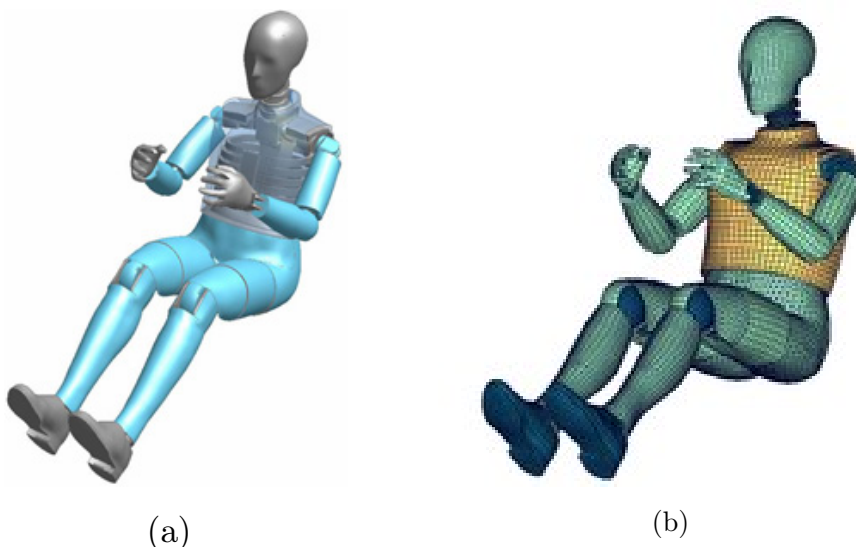


Figure 3.14. *Examples of anthropomorphic test device (50th Percentile) (a) Mechanical model - (b) The corresponding FE model.*

But the quality of the HBFEM depends on the quality of material models describing the response of organs under (dynamic) loadings, the reliable representation of the geometry of the organs and their interaction and the reliability of the experimental data used for the HBFEM validation.

3.2.5.2 The mechanical Anthropomorphic Test Device (ATD)

Different mechanical ATD have been developed through years especially in the automotive field where they are commonly referred to as crash test dummies. There is a wide variety of these ATDs with different sizes, different directions of impact (frontal, lateral). They are instrumented to measure parameters such as acceleration, force and deflection during impact. To the best knowledge of the author, none of these ATDs were validated for KENL impacts. But the only reference found in the literature, is the development of a surrogate from WSU derived from the BIOSID ribs for the risk assessment of KENLW (Section 3.2.4.4). In the following section, a description of the 3RBID (an updated version of the 3-RCS), recently acquired by ABAL is given.

3.2.5.3 The ABAL 3RBID

The ABAL 3RBID is an updated thorax mechanical surrogate of the 3-RCS surrogate for the evaluation of non-lethal impacts. It was developed by Humanetics⁷ and is composed of three adapted BIOSID high steel ribs attached to the spine at the back. On the impact side, protection plastic sheet fixed to the ribs through aluminium plate makes the link between the three ribs so the motions of the ribs are not independent. A foam material sheet placed on the plastic sheet provides damping characteristics as to ensure the biofidelity of the system.

To track the 3D displacements of the ribs, an integrated LED-Based system (RibEye) with a sampling rate of 20 kHz is used. To avoid external light interferences during the measurement, a covering system (neoprene coat) is put around the 3RBID. A built-in CFC filters are implemented in the acquisition software to eliminate undesired noise from the measured signal. In practice, the CFC-1000 filter is used [55]. Modification has been brought to the system by replacing the led-based measurement system by another system using accelerometer as shown in Figure 3.16. A detailed description of the 3RBID can be found in [55, 86]. The 3RBID was therefore validated using biomechanical corridors (sections 3.2.4.2 and 3.2.4.3).

⁷<http://www.humaneticsatd.com>

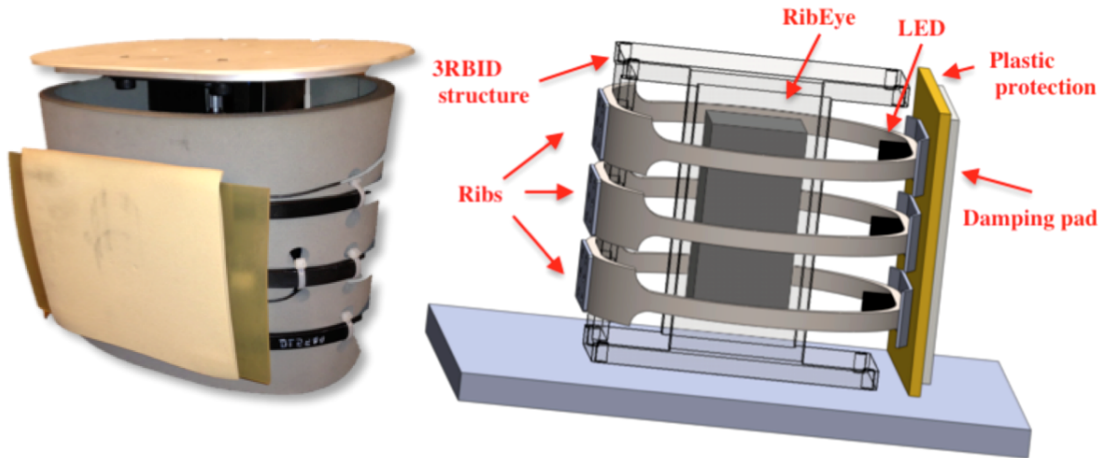


Figure 3.15. *ABAL-3RBID (left) and the corresponding scheme with LED system (Right).*

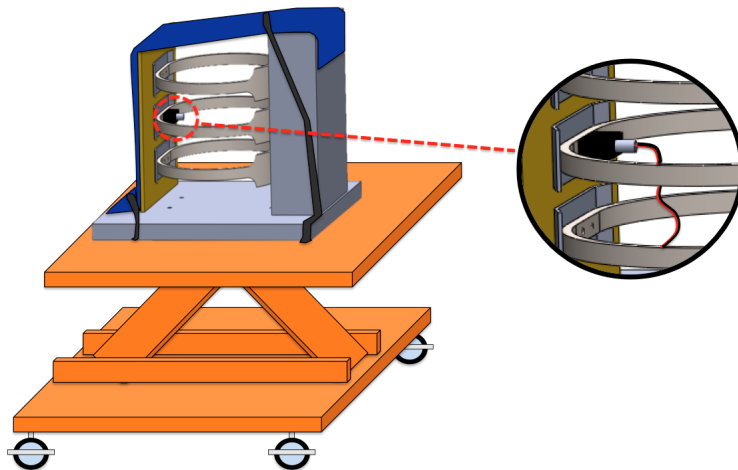






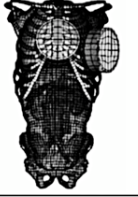

Figure 3.16. *ABAL-3RBID scheme with accelerometer.*

3.2.5.4 The Human Body Finite Element Models (HBFEM)

It is again in the field of the car crash studies that many efforts have been made to develop numerical models for crash injury risk assessment. Corresponding FE models of the physical ATD for virtual testings were also developed like the HYBRYD III FE models or SID FE models ([87–89]. They are just numerical counterparts of the physical ATD. In meantime, FE human body models that incorporated the modelling of organs/tissues (geometry and material model) were also developed. The first models were based on modelling bone structure of the thorax, the description of the internal organs were not taken into account or was very rudimentary. Linear material models were generally used. But over time, these models have evolved to include more and more features: internal organs of the chest, flesh surrounding the thoracic skeleton[85, 90–92] ...

Whether in the automotive field of crash tests or in the non-lethal domain, subjects on which the tests are carried out are the same. The only difference between these two domains resides in the impact dynamics. The automotive field of crash tests deals with large masses and low-speed impacts while the non-lethal impact domain deals with small masses and high-speed impacts. Therefore one could expect differences in the material properties of different organs because the types of loadings between the two domains are different. Therefore, to be used for KENLW impacts, models from automotive field might need further calibration and validation. Although there exists a lot of different numerical models developed for crash injury risk assessment and many have been validated for large masses and low velocities [91, 93, 94], to the best knowledge of the author, surprisingly none has been validated for non-lethal impacts. An interesting review of different models is given in [91].

Instead, since the growing interest in blunt trauma ballistic applications, few models have been exclusively developed for ballistic impacts. These FE models are ranging from simplified models (Figure 3.18-3.19) to complex models (Figure 3.20-3.21). Below the description of few of them.

First Author / Year	Huang 1994	Plank 1998	Lizee 1998 Petitjean 2003	Shah 2001	Ruan 2003	Kimpara 2005
Software	PAM-CRASH	LS-DYNA	Radioss	LS-DYNA	LS-DYNA	LS-DYNA
Size	50 th percentile male	50 th percentile male	50 th percentile male	50 th percentile male	50 th percentile male	5 th percentile female
Figure						
Rib	Elastic shells	Elastic solids	Elastic shells	Solids – trabecular bone Shells – cortical bone	Solids – trabecular bone Shells – cortical bone	Solids – trabecular bone Shells – cortical bone
Cartilage	Elastic shells	Elastic solids	Elastic shells	Elastic solids	Elastic solids	Elastic solids
Ligament and Muscle	Elastic membranes	Elastic shells	Elastic shells	Elastic shells	Elastic shells	Elastic shells
Vertebrae	Simplified Elastic solids	Simplified Elastic solids	Simplified Rigid	Simplified Elastic solids	Detailed description Elastic solids	Detailed description Elastic solids
Disc	Elastic solids	Viscoelastic solids	Viscoelastic solids	Elastic solids	Viscoelastic solids	Viscoelastic solids
Viscera	Homogeneous elastic solids and dampers	Homogeneous Viscoelastic	Upper and lower parts Viscoelastic	Detailed description Nonlinear foam material	Detailed description Viscoelastic	Detailed description Nonlinear foam material
Blood Vessels	–	–	–	Detailed description	Detailed description	Detailed description
Validation	<ul style="list-style-type: none"> • Side impact sled tests • Sled to sled tests • Pendulum tests 	<ul style="list-style-type: none"> • Cadaveric Force-Deflection corridors 	<ul style="list-style-type: none"> • Frontal, lateral, and oblique pendulum tests • Belt loading 	<ul style="list-style-type: none"> • Frontal and lateral pendulum tests 	<ul style="list-style-type: none"> • Frontal and side pendulum impacts in various speeds * • Belt loading * 	<ul style="list-style-type: none"> • Frontal, lateral, oblique pendulum impacts on small female * • Ballistic breast impact on small female *
Application	Side impact	Frontal and side impact	Frontal impact	Aortic injury prediction	Frontal and side impact	Rib fracture prediction for small female

Note: *: individual test data was used for validation instead of corridor
 --: not applicable

Figure 3.17. FEM of the human thorax and their applications [91].

Torso simplified model

This model is a FE torso simplified model and was developed at Valcartier [95] to investigate and predict the biomechanical response of an actual torso to blunt ballistic impacts. It was derived by extrusion from Human FE torso model developed for blast injury investigation [96–99] in order to accommodate blunt impacts. The

model was validated using the same projectiles and the biomechanical corridors developed in Bir's experiments.

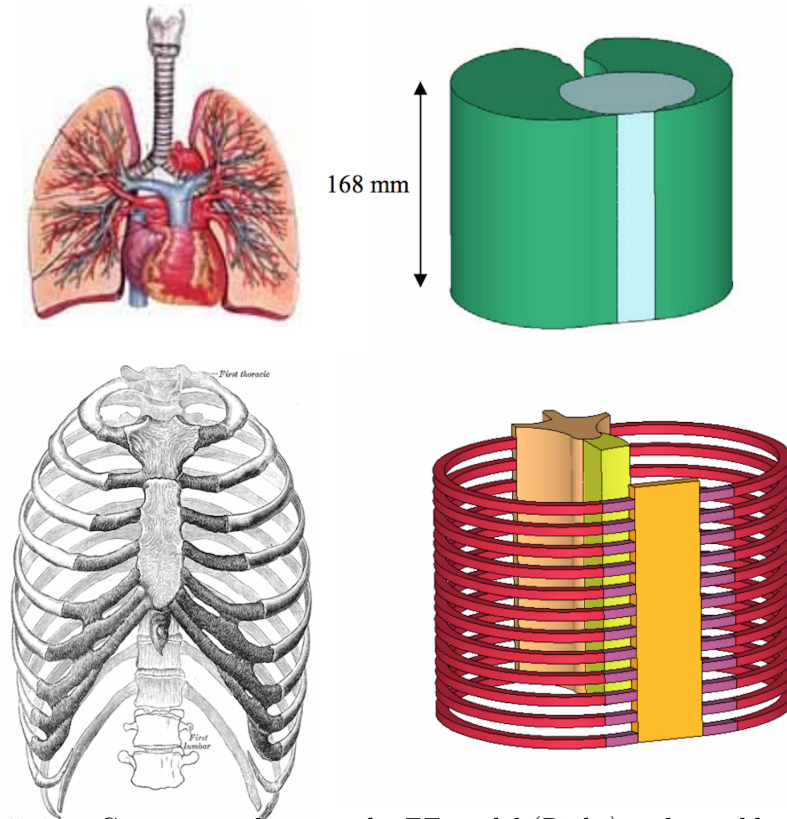


Figure 3.18. Comparison between the FE model (Right) and a real human torso (Left) [95].

MTHOTA FE (Mechanical THORax for Trauma Assessment FE)

The MTHOTA FE model is the counterpart model of the mechanical MTHOTA surrogate (Figure 3.19) and was developed for numerical evaluation of the KENL impacts by Thota et al. [100]. It consists of 7543 shell elements, 723 solid brick elements, 7 components (foam sheet, rigid impact plate, corrugated sheet, 4 plates) and 4 contact interfaces (including the interface between projectile and MHTOTA's impacted surface). Like the torso simplified model, validation was done using Bir's biomechanical corridors and projectiles [101].

Advanced Total Body Model(ATBM)

This model was developed and is applied by US Air Force [102]. It is a 50th percentile full scale human body model (head, thorax, neck, abdomen, skin and extremities), validated against animals and PMHS. Figure 3.20 shows the model corresponding to the thorax region. ATBM predicts a variety of injuries. The thoracic related injuries that can be predicted are rib fracture, lung contusions, pneumothorax, heart lesions, skin penetration... The injury criterion for the risk

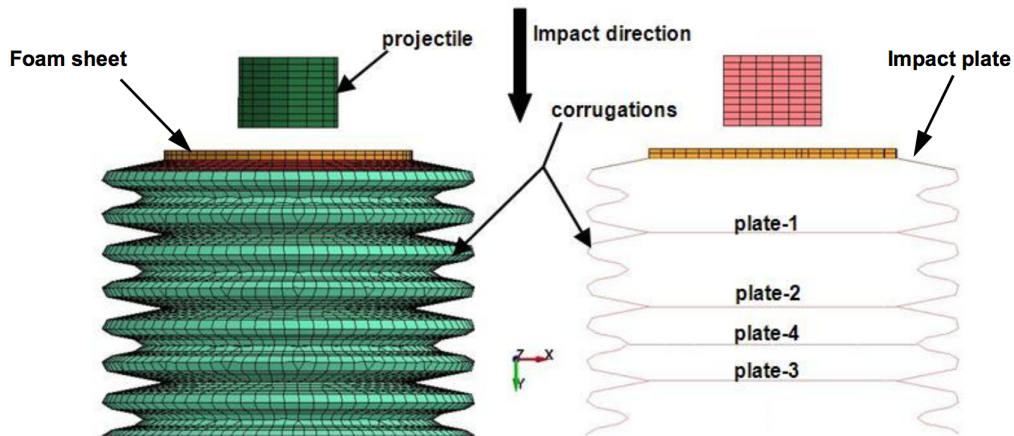


Figure 3.19. *FE model of the MTHOTA and its cross-section. Adapted from [101].*

injury assessment is the RSI (Risk of Significant Injury). The RSI is the probability that a NLW system will cause a significant injury when used as intended [102]. "Significant injury" refers to any injury requiring Health Care Capability indices 1 or 2, or to permanent injuries or to the death [103].

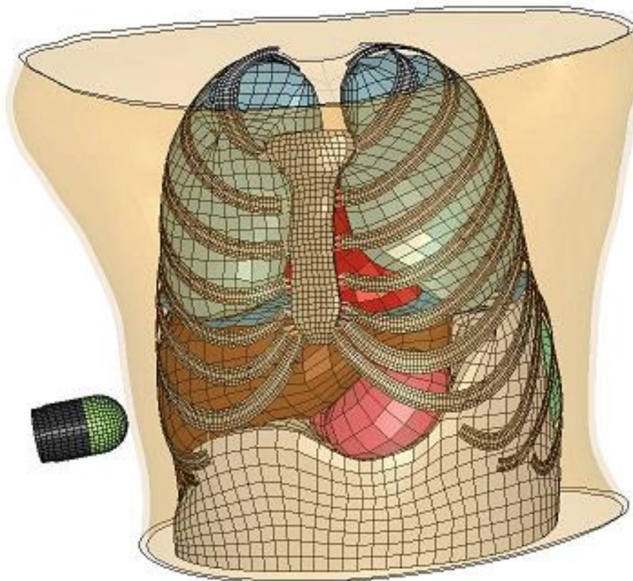


Figure 3.20. *ATBM:Thorax model[103].*

Hermaphrodite Universal Biomechanical YX model (HUBYX)

HUBYX (Figure 3.21) is a model developed at IRTES (UTBM)⁸ in France for injury risk assessment from ballistic impacts, blast, BAPT (Behind Armour Blunt

⁸IRTES: Institut de Recherche sur les Transports, l'Énergie et la Société - UTBM: Université Technologique de Belfort Montbéliard

Trauma)... [104, 105]. It includes the main internal organs and the skeleton [105]. The model includes 38600 brick elements, 77800 shell elements and 233 000 SPH particles. The model was validated for blunt impacts using Bir's data.

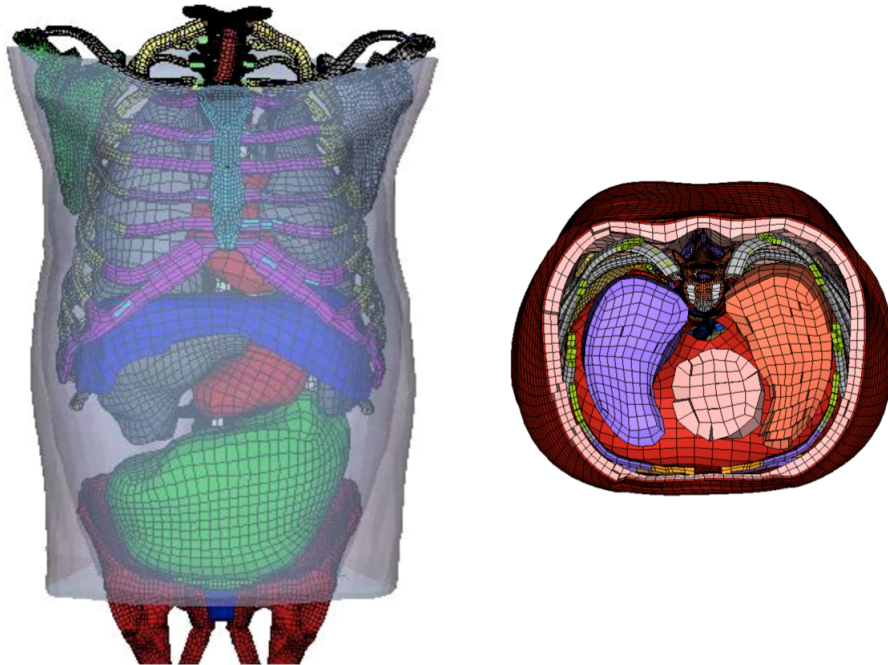


Figure 3.21. *HUBYX model (left) - internal organ cross-section (Right)[105].*

3.2.6 NATO Group

NLW are increasingly being used in the context of military operations. But each country has its own system and its own method of evaluation which makes the information exchange and the concept of interoperability impractical for countries that are expected to work together. Therefore much effort is done within NATO in order to work on methods of KENLW system characterization and evaluation. A group of experts at NATO level (NLKE ToE) chaired by Belgium is working on the elaboration of standardized test procedures on KENLW to which every KENLW system (surrogate) or projectile should comply to be valid within NATO. This group meets twice a year to discuss and exchange information on the progress made on thoracic and cranial impacts, penetration of the skin, the use of different types of surrogates, accuracy. A standard on the evaluation of thoracic impacts will be released soon [5]. Before using a surrogate (mechanical or numerical), it should be validated. The responses of the surrogate in terms of displacement as function of time and of the $(VC)_{max}$ should fall within the defined corridors and boundaries [7, 55]. The procedure consists in shooting the projectile on the 3RBID (section 3.2.5.3) a validated surrogate for assessing KENL impacts on the thorax. A reference projectile that has been chosen within the group is the SIR-X projectile.

Moreover one needs a validated numerical model of the projectile for the numerical surrogates. For the SIR-X projectile, corridors in terms of force and displacement as function of time have been determined by impacting the SIR-X projectile on a rigid wall structure [5]. In the present thesis, a finite element model (FEM) of the SIR-X projectile is developed.

3.2.7 Conclusions

In this chapter, the different notions on thorax biomechanics have been introduced. Injury criteria have been defined and in the present thesis, the viscous injury is used for assessing the impacts of KENL projectiles on the thorax. Data on KENL blunt impacts are rare and the only source found in the literature is the work performed by C. Bir. This study provides the baseline data that will be used for the validation of the thorax numerical model. There are two main types of surrogates, the mechanical surrogates and the numerical (virtual) surrogates. It has been shown that numerical models present more advantages compared to the mechanical surrogates. In the present work, a numerical surrogate is developed. A review of a few models used for assessing non-lethal impacts has been made. In the next chapter, a methodology that is used for the development of the numerical tools for the assessment of KENL projectile thoracic impacts is described.

Chapter 4

Methodology for non-lethal thoracic impacts

This chapter deals with the description of the methodology used to assess the KENLW thoracic impacts. Models especially FE-based models, have extended the spectrum of physical parameters that can be investigated for a better understanding of the (dynamic) phenomenon. The development of these models have been made possible thanks to the development of numerical techniques and powerful computing systems. On the one hand, thanks to CAD programs and imaging techniques, one can obtain detailed thorax organs/tissues geometries and projectile geometry. On the other hand, the increasing knowledge on material science has led to the development of material models that describe the dynamic material behaviour paving a way for a better assessment of non-lethal impacts. Precisely, this work focuses on the development of numerical models for the evaluation of thoracic impacts of non-lethal projectiles. In this chapter, an overview of FE method applied to impact problems is presented. Discretization techniques as well as material models are presented. Finally, the methodology for non-lethal thoracic impacts is explained.

4.1 The Finite Element Method applied to impact problems

Impact events are dynamic phenomena which are characterized by high strain rates, inertial effects and wave propagation effects. They are localised and highly non-linear and can manifest by large displacements and large strains, failure or damage to structures. For a better understanding of these phenomena and the different mechanisms involved, numerical tools (codes) are increasingly used. Codes in Solid

Mechanics are mostly based on FE methods. In the present thesis, LS-DYNA code will be used in order to simulate the non-lethal impacts.

LS-DYNA is a general-purpose finite element program developed at the Livermore Software Technology Corporation (LSTC) [106] and is capable of simulating complex real world problems. It is used in many fields: automobile, aerospace, civil engineering, military, manufacturing, and bioengineering industries. The code's origins lie in highly nonlinear, transient dynamic finite element analysis using explicit time integration. For pre-processing and post-processing, Ls-Prepost (also a product from LSTC) [106] is used. Another tool that interfaces with LS-DYNA solver is Ls-Opt that allows for complex optimization and sensitivity analysis [106].

These codes have seen significant growth over the last few years thanks to the development of numerical methods and the growing of the computing capabilities. The general principle of numerical methods is the following:

- The physical phenomenon is translated into mathematical models, often described in terms of differential equations.
- These equations are solved thanks to FE software which themselves use numerical techniques. The latter presupposes a discretisation of the space-time domain thus transforming a continuous problem with an infinite number of unknowns to a discrete problem with a finite number of unknowns.
- After the discretisation, it is necessary to determine how the unknown field (e.g. the displacement field) will be evaluated within each subdomain of the continuum (e.g. finite element method for spatial discretisation) and how to advance the solution in time (integration schemes for time discretisation).

Given the complexity of real problems, assumptions are usually made on the geometry, the material behaviour, the boundary conditions or the loadings. For impact problems, explicit codes are often used [107, 108].

Numerical methods for solving dynamic problems are based on the conservation laws which are fundamental physical laws independent of the material characteristics and the constitutive equations which take into the material characteristics.

4.1.1 Conservation laws

When submitted to loadings, a given body Γ will deform and its configuration will evolve. The dynamics of the problem can be expressed thanks to the conservation

4.1 The Finite Element Method applied to impact problems

laws described by the following differential equations given in spatial form [109?–111]:

- Mass conservation

$$\dot{\rho} + \rho \dot{x}_{i,i} = 0 \quad (4.1)$$

- Momentum conservation

$$\rho \ddot{x}_i = (\sigma_{ji})_{,j} + \rho f_i \quad (4.2)$$

- Moment of Momentum

$$\sigma_{ij} = \sigma_{ji} \quad (4.3)$$

- Energy conservation

$$\rho \dot{e} = (\sigma_{ji} \dot{x}_i)_{,j} + \rho \dot{x}_i f_i \quad (4.4)$$

where

- $\vec{x}_i = (\vec{x})_i$ is the component i of the displacement vector \vec{x} ;
- $\dot{\vec{x}}$ is the velocity vector;
- $\ddot{\vec{x}}$ is the acceleration vector;
- $\boldsymbol{\sigma}$ is the Cauchy stress tensor;
- \vec{f} is the body forces;
- e is the specific internal energy.

4.1.2 Discretization methods

To solve these equations, the principle can be summarised as follows:

- Divide the problem into 'small' problems (*Spatial discretizations*) (Figure 4.1).
- Transform each 'small' problem into a tractable problem (*algebraic equations*).
- Ensure the continuity of displacement across element boundaries.
- Assemble and obtain a solution in the entire domain (*solve the algebraic equations + boundary conditions*).

Different methods for solving these governing equations exist: the Finite Difference Method (FDM), the Finite Volume Method (FVM), the Finite Element Method (FEM), the Meshless Methods like the Smooth Particle Hydrodynamics (SPH),... Each method has its advantages and drawbacks [112–114].

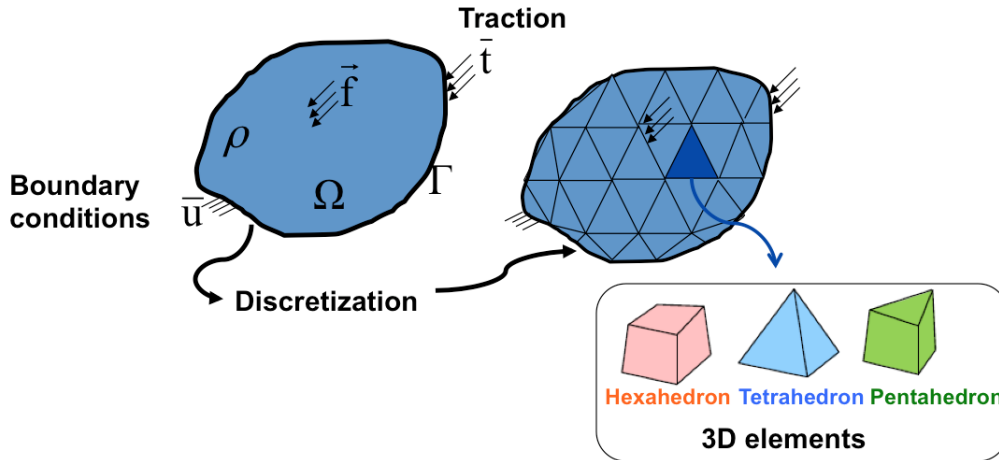


Figure 4.1. Discretization of the body Γ .

In Solids Mechanics, the FEM is mostly used and is implemented in many software. It is based upon a piecewise representation of the solution in terms of specified basis functions. The computational domain is divided into non-overlapping smaller domains (elements) and the solution in each element is constructed from the basis functions by using the integral form of the equations (Equations 4.1-4.4). The entire solution is obtained through the resolution of a set of algebraic equations derived by combining all the element equations and the boundary conditions. To advance the solution in time, the time is also discretized. Two great families of integration scheme are used: the explicit time integration schemes and the implicit time schemes [115]. Generally for dynamic problems like impact problems, explicit codes are used.

4.1.3 Types of elements

Different types of elements can be used 1D, 2D, 3D elements ([116]). In the present study, only 3D elements are used. Examples of 3D elements (hexahedron, tetrahedron or pentahedron) are given in Figure 4.1. Although there is a family of 3D elements, the most frequently used solid elements are the 4-node tetrahedron and the 8-node hexahedron [107]. Each type has its advantages and its drawbacks. Tetrahedron elements are easy to generate automatically. Conversely for hexahedron elements, the mesh generation process can be time consuming. Indeed for complex geometries, most of the work is to be manually done (splitting and cutting) [117, 118]. For most nonlinear problems, especially incompressible materials, linear tetrahedron elements generally poorly perform and suffer from locking problems while hexahedrons with a single integration point are computationally efficient but suffer from hourglass problems [119, 120].

4.1.4 Formulation description

There are two main types of motion description, the Lagrangian formulation and the Eulerian one. In the Lagrangian formulation, the computational domain (mesh) deforms with the material during the motion (Figure 4.2) while in the Eulerian formulation, the computational domain is fix and the material flows through it (Figure 4.2). The Lagrangian formulation is best suited for solid materials and allows an accurate material interface tracking but suffer from severe distortions under large deformations. This results in a loss of accuracy and of stability. Unlike the Lagrangian formulation, the Eulerian formulation accommodates with large deformations (no distortion problem) and is best suited for fluids. The major problem with this formulation is the material interface tracking [107].

Besides these two formulations, there exists other types of formulation. The ALE (Arbitrarily Lagrangian Eulerian) formulation is a generalization of the Lagrangian and Eulerian approaches. It tries to combine the advantages of both approaches while trying to minimize their respective drawbacks. The computational domain is no more attached to the material (Lagrangian), or fix (Eulerian) but attached to a reference configuration which has an arbitrary motion. The Lagrangian and Eulerian descriptions are therefore special cases of the ALE. It is best suited for fluid structure interaction (FSI) [121, 122].

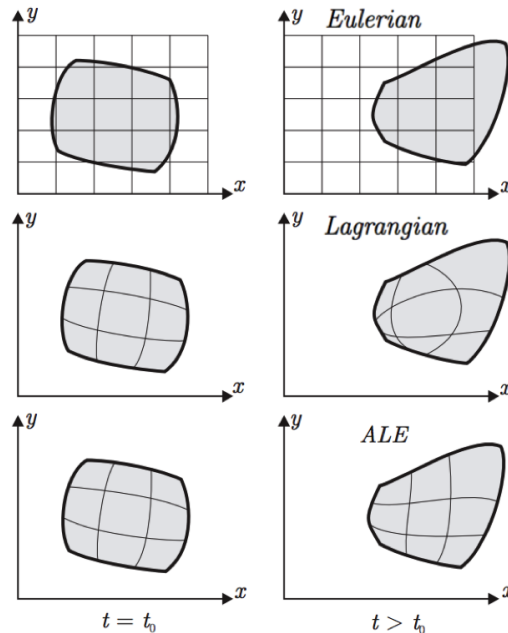


Figure 4.2. *Lagrangian, Eulerian and ALE formulations - Initial (or reference) configuration (left) and the deformed (or current) configuration(right)[121].*

Another discretization technique is the SPH (Smooth Particle Hydrodynamics). It was historically developed for astrophysical problems, but has now found

applications in other domains [123]. Unlike all the aforementioned discretization techniques, the computational domain of the SPH method is made of a set of *discrete particles* and there is no need to define in advance the connectivity between them (Figure 4.3). Like in FEM, the SPH uses the integral form of the governing equations from which the field variables at any particle are calculated thanks to interpolation functions called kernel functions. Therefore the kernel function is used to build continuous field quantities from discrete particles. It is defined on a support (region that defines the contribution to the field variable at a given point). One of the most significant advantage of this method is its adaptability, therefore it can naturally handle problems with extremely large deformations [123]. But this formulation is generally more expensive than the other ones and tensile instability which may lead to unphysical results may develop in this formulation [124].

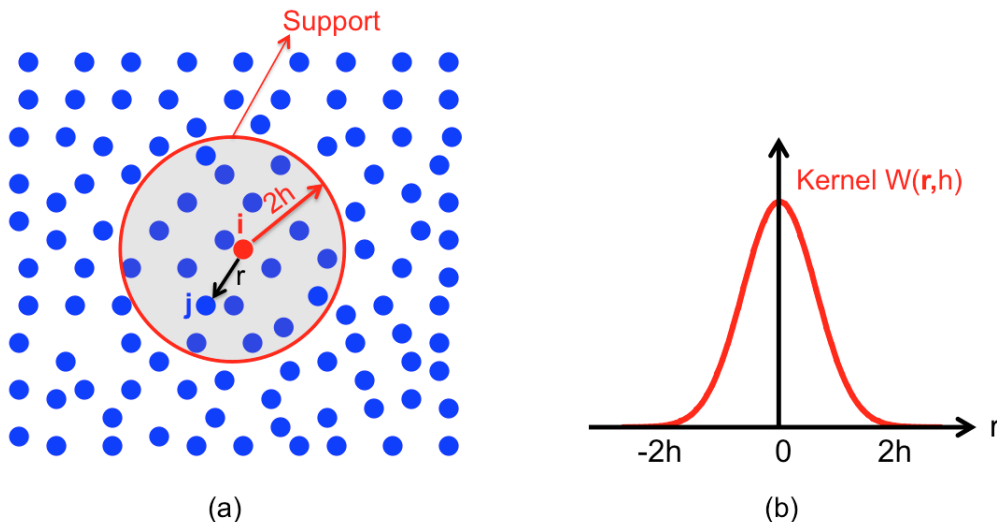


Figure 4.3. SPH formulation - (a) Support: all particles j within the support will contribute to the particle i 's field variable - (b) kernel function [123].

It is worth mentioning that depending of the problem, one formulation might be more appropriate than another one.

4.1.5 Contacts

During impact, contacts occur between the different thorax organs and it influences the whole dynamics of the thorax. Failing to correctly model the contacts will lead to invalid injury assessment. Therefore, they should be correctly defined in order to determine the forces developed at the body interfaces and to adequately capture the deformations of the bodies.

When two bodies come into contact, forces are generated at the body interfaces. The Figure depicts the evolution of the contact forces as a function of the distance

between the two bodies or penetration, when the two body come into contact. For the study of the contact behaviour, it is usual to consider the normal component and the tangential component. The normal forces are compressive forces which should satisfy the physical requirement "there should be no penetration between the two contacting bodies (*impenetrability condition*)" [125]. The tangential forces are linked to the frictional behaviour of the body surfaces in contact. They are two conditions related to this behaviour.

- The bodies in contact can stick together i.e. there is no relative displacement between them (sticking condition). The frictional force does not attain a threshold value.
- The bodies in contact can slide one another i.e. there is a relative displacement between them (sliding condition). This introduces the notion of friction between the body surfaces. The frictional force does attain the threshold value.

In order to judge whether the bodies are in contact and if they are, are they sticking or sliding, one needs criteria. To derive these criteria, definitions are introduced.

4.1.5.1 Definitions

Given two bodies $\Omega_0^{(i)} \subset \mathbb{R}^3$ ($i=1,2$) in the reference configuration which undergo large deformation (Figure 4.4), the motion of each body is described by a mapping $\varphi^{(i)} : \Omega_0^{(i)} \times [0, t_f] \rightarrow \mathbb{R}^3$

$$\vec{x}^{(i)} = \varphi^{(i)}(\vec{X}^{(i)}, t) \quad (4.5)$$

where $\vec{x}^{(i)}$ is the spatial position of the material point referenced by its position $\vec{X}^{(i)}$ in the reference configuration, $[0, t_f]$ is the time interval and t_f is the final time.

By dropping the superscript relative to the considered body, for each body, the deformation gradient \mathbf{F} is defined by

$$\mathbf{F} = \frac{\partial \vec{x}}{\partial \vec{X}} \quad (4.6)$$

The admissible configuration space \mathbb{X} of the deformed body is defined by a one-to-one relation i.e. the deformation gradient \mathbf{F} should satisfy Equation 4.7.

$$\det \mathbf{F} > 0 \quad (4.7)$$

It follows that

$$\mathbb{X} \equiv \vec{x} : \{ \Omega_0 \rightarrow \mathbb{R}^3 \mid [\det \mathbf{F} > 0 \quad \text{and} \quad \vec{x}|_{\gamma_{\bar{u}}} = \bar{\vec{x}}] \quad \forall \vec{X} \in \Omega_0 \} \quad (4.8)$$

The boundary $\partial\Omega_0^{(i)}$ of the body $\Omega_0^{(i)}$ is subdivided into the Dirichlet boundary $\Gamma_{\bar{u}}^{(i)}$ where displacements are prescribed, the Neumann boundary $\Gamma_{\bar{t}}^{(i)}$ where tractions are prescribed and the contact boundary $\Gamma_c^{(i)}$. $\Gamma_c^{(i)}$ is the set of material points that are in contact in the considered current configuration. These boundaries should not overlap i.e.

$$\begin{aligned}\partial\Omega_0^{(i)} &= \Gamma_{\bar{u}}^{(i)} \cup \Gamma_{\bar{t}}^{(i)} \cup \Gamma_c^{(i)} \\ \Gamma_{\bar{u}}^{(i)} \cup \Gamma_{\bar{t}}^{(i)} &= \Gamma_{\bar{u}}^{(i)} \cup \Gamma_c^{(i)} = \Gamma_{\bar{t}}^{(i)} \cup \Gamma_c^{(i)} = \emptyset\end{aligned}\quad (4.9)$$

The governing equations for each body for all $t \in [0, t_f]$ is given by

$$(4.10)$$

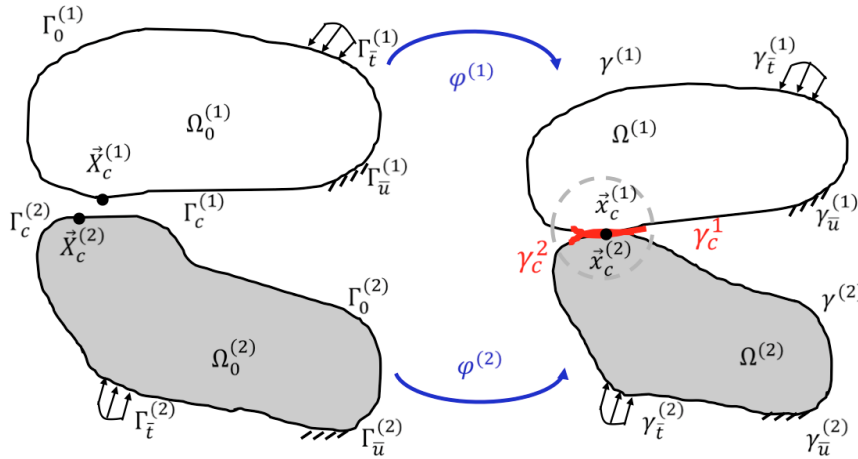


Figure 4.4. Configurations of the two bodies in contact problem - $\Omega_0^{(i)}$: bodies in the reference (material) configuration - $\Omega^{(i)}$: bodies in the current (spatial) configuration. Adapted from [1].

It is common in Continuum Mechanics to use the notion of traction \vec{t} which is defined by Equation 4.11.

$$\begin{aligned}\vec{F} &= \int_S \vec{t} dS \\ \vec{t} &= \boldsymbol{\sigma} \vec{n}\end{aligned}\quad (4.11)$$

where \vec{t} is the traction vector at a point on the surface representing the force acting on the surface per unit area of the deformed solid, and dS a elementary surface element.

Decomposed in its normal and tangential components, one obtain Equation 4.12.

$$\begin{aligned}\vec{t} &= \vec{t}_N + \vec{t}_T \\ \vec{t}_N &= (\vec{t} \cdot \vec{n}) \vec{n}\end{aligned}\quad (4.12)$$

4.1 The Finite Element Method applied to impact problems

where \vec{t}_N the normal component of \vec{t} (in the case of contact, it is the contact pressure) and \vec{t}_T its tangential component. During contact between the two bodies, they come into contact through their respective surfaces $\gamma_c^{(1)}$ and surface $\gamma_c^{(2)}$ (Figure 4.4). By considering for example the material points in contact given by their spatial positions $\vec{x}_c^{(1)}$ and $\vec{x}_c^{(2)}$ at their common interfaces, one can represent tractions in those points as depicted in Figure 4.5(a) corresponding to a zoom of the dashed circled region in Figure 4.4. To avoid overloading the figure, only tractions on body $\Omega^{(1)}$ are represented (the distance g has been willingly exaggerated as it will be used later, normally in contact $g = 0$). The body $\Omega^{(1)}$ will slide on body $\Omega^{(2)}$ with a sliding velocity $\vec{v}_{g_{1/2}}$ if certain conditions is met.

It is worth pointing out that the choice of the body $\Omega^{(1)}$ is arbitrary, one could likewise use $\Omega^{(2)}$. Taking into account the balance of forces across the contact interface, one obtains

$$\vec{t}_c^{(1)} = -\vec{t}_c^{(2)} \quad (4.13)$$

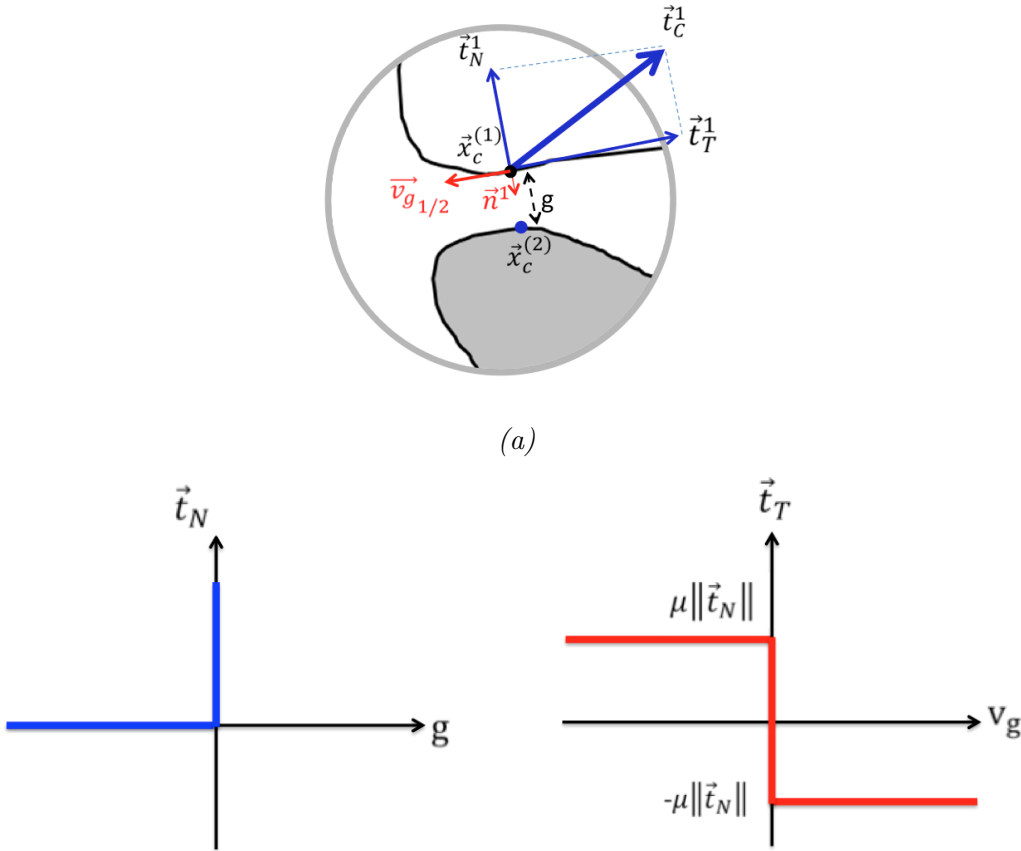


Figure 4.5. (a) Contact zone: contact pressure on body $\Omega^{(1)}$ - (b) Friction model of Coulomb.

Figure 4.5(b) shows how there is an abrupt change of contact forces (tractions) when two bodies come into contact showing that contact problems are highly non-linear problems. Moreover, it is not easy to find the solution as both displacement and contact force are generally unknown. Therefore one should proceed by iteration [125]. In this thesis, only Coulomb friction model will be considered. It stipules that the Coulomb friction force \vec{t}_t acts in the direction opposite to the motion (sliding motion \vec{v}_g) and that its magnitude is given by Equation 4.14.

$$\|\vec{t}_T\| = \mu_c \|\vec{t}_N\| \quad (4.14)$$

where μ_c is the friction coefficient. Its value depends of the state of the material properties of the bodies and the states of the surfaces in contact respectively.

4.1.5.2 Conditions of contact and sliding

They are two contact conditions that are considered: the conditions of contact defined by the normal contact constraints and the sliding conditions defined by the frictional sliding constraints.

- (i) The normal contact constraints

This condition is related to the impenetrability condition. It is assumed that the contacting body is the body $\Omega^{(1)}$ (the slave) and the target body $\Omega^{(2)}$ (the master). The choice of the master and the slave is arbitrary. This approach is called a "one-pass" approach. A "two-pass" approach has been proposed where the contact algorithm is applied a second time but by exchanging the master and the slaves surfaces. Here the "one-pass" approach is considered.

As the point $\vec{x}^{(1)}$ of the slave surface that is likely to come into contact is not a priori known, a search is made first based on the closest point belonging the master surface $\gamma^{(2)}$ in the current configuration to $\vec{x}^{(1)}$. The closest point is the point obtained by orthogonal projection of $\vec{x}^{(1)}$ on $\gamma^{(2)}$ and is found by minimizing the distance between the point and the boundary. The distance between the two points is given by the gap function g_N defined by

$$\begin{aligned} g_N(\vec{x}_0^{(1)}, t) &= \theta \|\vec{x}^{(1)} - \vec{x}^{(2)}\| \\ &= \theta \|\vec{x}^{(1)}(\vec{x}_0^{(1)}, t) - \vec{x}^{(2)}(\vec{x}_0^{(1)}, t)\| \\ &= \theta \min_{\vec{x}^{(2)} \in \gamma^{(2)}(t)} \|\vec{x}^{(1)}(\vec{x}_0^{(1)}, t) - \vec{x}^{(2)}(\vec{x}_0^{(1)}, t)\| \end{aligned} \quad (4.15)$$

where

$$\theta = \begin{cases} -1 & \text{if penetration,} \\ 1 & \text{if no penetration.} \end{cases}$$

If \vec{n} is the normal to $\gamma^{(2)}$ at the point of contact $\vec{x}^{(2)}$, the closest point can be determined by

$$0 = (\vec{x}^{(1)} - \vec{x}^{(2)}) \cdot \vec{n} \quad (4.16)$$

where $\vec{n} = \frac{\vec{t}_1 \wedge \vec{t}_2}{\|\vec{t}_1 \times \vec{t}_2\|}$, \vec{t}_1 and \vec{t}_2 are tangent vectors to $\gamma^{(2)}$ at the point of contact $\vec{x}^{(2)}$.

The normal gap g_N introduces a kinematic constraint but there is another constraint related to the forces exerted one against another as long as the bodies are in contact. This leads to the Kuhn-Tucker conditions for normal contact [115, 126, 127].

$$\begin{aligned} g_N(\vec{x}_0, t) &\geq 0 \\ t_N(\vec{x}_0, t) &\geq 0 \\ t_N(\vec{x}_0, t)g_N(\vec{x}_0, t) &= 0 \end{aligned} \quad (4.17)$$

where g_N is the scalar normal gap and the velocity $\vec{t}_N = t_N \frac{\vec{t}_N}{\|\vec{t}_N\|}$.

These conditions show that when there is contact between the bodies,

- $g_N \geq 0$: there should be no penetration between the bodies.
- if there is contact between the bodies, $g_N = 0$ and $t_N > 0$.
- otherwise $t_N = 0$ and $g > 0 \rightarrow$ no contact.

(ii) The frictional sliding constraints

Two bodies in contact can stick together or slide one on another. In the latter case, there is a sliding velocity \vec{v}_g which has an opposite direction to the vector \vec{t} . If there is friction, a friction model should be introduced. Likewise the relation 4.12, tangential relative displacement [128] can be introduced such as the path of point $\vec{x}^{(1)}$ on $\gamma^{(2)}$ is given by

$$\begin{aligned} d\vec{g}_T &= \vec{t}_\alpha d\xi^\alpha \\ g_T &= \int_{t_0}^t \|\dot{\xi}^\alpha \vec{t}_\alpha\| dt = \int_{t_0}^t \sqrt{\dot{\xi}^\alpha \dot{\xi}^\alpha t_{\alpha\beta}} dt \quad (4.18) \\ &(\alpha, \beta \in [1, 2]) \end{aligned}$$

where (ξ^1, ξ^2) are used to parameterise the surface $\gamma^{(2)}$ and $t_{\alpha\beta} = \vec{t}_\alpha \cdot \vec{t}_\beta$. The Einstein notation has been used.

To determine the sliding velocity implies first the determination of $\dot{\xi}$. The latter is given by Equation 4.19 [129]

$$\dot{\xi}^\alpha = \left[\dot{\vec{x}}^{(1)}(\vec{x}_0^1, t) - \dot{\vec{x}}^{(2)}(\vec{x}_0^{(2)}(\vec{x}_0^1, t), t) \right] \cdot \vec{t}_{d_\alpha} \quad (4.19)$$

where $\vec{t}_{d_\alpha} = m_{\alpha\beta} \vec{t}_\beta$ represents the dual basis to \vec{t}_β with

$$\begin{aligned} \vec{t}_{d_\alpha} \cdot \vec{t}_\alpha &= \delta_{\alpha\beta} \\ m^{\alpha\beta} &= \vec{t}_\alpha \cdot \vec{t}_\beta \end{aligned} \quad (4.20)$$

The sliding velocity \vec{v}_g is given by

$$\vec{v}_g = \dot{\vec{g}}_T = \dot{\xi}^\alpha \vec{t}_\alpha \quad (4.21)$$

The friction force is given by

$$\vec{t}_T = t_{T_\alpha} \vec{t}_{d_\alpha} \quad (4.22)$$

More details can be found in [115, 126, 127]. The sliding constraints are given by the following conditions (4.23)

$$\begin{aligned} \vec{v}_g &= -\gamma_c \frac{\vec{t}_T}{\|\vec{t}_T\|} \\ \Phi_c &\equiv \|\vec{t}_T\| - \mu_c t_N \leq 0 \\ \gamma_c &\geq 0 \\ \gamma_c \Phi_c &= 0 \end{aligned} \quad (4.23)$$

where $\frac{\vec{t}_T}{\|\vec{t}_T\|}$ is the unit tangential vector.

These conditions show that when there is contact between the bodies,

- if the contact is sticking i.e. no sliding, $\gamma_c = 0 \Leftrightarrow \vec{v}_g = \vec{0}$ and $\Phi_c < 0$.
- If there is sliding ($\vec{v}_g \neq \vec{0}$), $\gamma_c > 0$ and $\vec{v}_g = -\gamma_c \frac{\vec{t}_T}{\|\vec{t}_T\|}$ and $\Phi_c = 0$

4.1.5.3 Contact problem

The governing equations of the underlying problem is given by

$$\begin{aligned}
 \rho \ddot{\vec{x}} &= \nabla \cdot \Sigma + \rho \vec{b} \quad (\vec{x} \in \Omega) \\
 \vec{x} &= \vec{\bar{x}} \quad (\text{on } \Gamma_{\bar{u}}) \\
 \vec{t} &= \vec{\bar{t}} \quad (\text{on } \Gamma_{\bar{t}})
 \end{aligned} \tag{4.24}$$

under contact constraints (see also Equations 4.17-4.23)

$$\begin{aligned}
 g(\vec{x}_0, t) &\geq 0 \\
 t_N(\vec{x}_0, t) &\geq 0 \\
 t_N(\vec{x}_0, t)g(\vec{x}, t) &= 0
 \end{aligned} \tag{4.25}$$

and if in sliding state

$$\begin{aligned}
 \vec{v}_g &= -\gamma_c \frac{\vec{t}_T}{\|\vec{t}_T\|} \\
 \Phi_c &\equiv \|\vec{t}_T\| - \mu_c t_N \leq 0 \\
 \gamma_c &\geq 0 \\
 \gamma_c \Phi_c &= 0
 \end{aligned} \tag{4.26}$$

Because of these conditions, the problem becomes a problem under constraints. To solve the problem in the framework of finite element method, a variational equality formulation based on the virtual principle is used [130].

Let us first write the problem in the adequate continuum formulation and let us assume that the two bodies are in contact. By considering the equilibrium of only one body, the contact forces are then considered as external surface forces applied on the boundary γ_c of this body (the problem becomes then similar to the problem of prescribed traction). The variational equality formulation of the governing equation for the two bodies leads to Equation 4.27 [115, 126]. If there is no contact forces, the problem is solved in a classical way. If there is contact between the bodies, as these forces proceed from the contact are unknowns as well as the displacements. They have to be determined not using specific methods. There are different methods [125] that can be used by only the penalty method will briefly described. Only the penalty method is briefly described.

$$\begin{aligned}
 \int_0^{t_f} \sum_{i=1,2} \left\{ \int_{\Omega^i} \left[\rho \ddot{\vec{x}} \cdot \delta \vec{x} + \Sigma^T : \frac{\partial \delta \vec{x}}{\partial \vec{x}} - \rho \vec{b} \cdot \delta \vec{x} \right] d\mathbb{V}^i - \int_{\gamma_t^i} \left[\vec{t} \cdot \delta \vec{x} \right] d\mathbb{S}^i - \right. \\
 \left. + \int_{\gamma_c^i} \left[\vec{t}_c \cdot \delta \vec{x} \right] d\mathbb{S}^i \right\} dt = 0 \quad (4.27) \\
 \forall \delta \vec{x} \in \mathbb{D}
 \end{aligned}$$

where \mathbb{D} is defined as the set of kinematically admissible displacement such as

$$\mathbb{D} \equiv \{ \delta \vec{x} \in \mathbb{D} : \Omega_0 \rightarrow \mathbb{R}^3 \mid [\delta \vec{x} = 0 \text{ on } \gamma_u] \} \quad (4.28)$$

By defining δK , δW_{int} , δW_{ext} and δW_c as the virtual work done by inertial forces, the internal virtual work, the internal virtual work and the virtual work done by the contact forces respectively, Equation 4.27 is rewritten by

$$\delta K + \delta W_{int} - \delta W_{ext} + \delta W_c = 0 \quad (4.29)$$

where

$$\delta K = \sum_{i=1,2} \int_{\Omega^i} \left\{ \rho \ddot{\vec{x}} \cdot \delta \vec{x} \right\} d\mathbb{V}^i \quad (4.30)$$

$$\delta W_{int} = \sum_{i=1,2} \int_{\Omega^i} \left\{ \Sigma^T : \frac{\partial \delta \vec{x}}{\partial \vec{x}} \right\} d\mathbb{V}^i \quad (4.31)$$

$$\delta W_{ext} = \sum_{i=1,2} \int_{\Omega^i} \left\{ \rho \vec{b} \cdot \delta \vec{x} \right\} d\mathbb{V}^i + \sum_{i=1,2} \int_{\gamma_t^i} \left\{ \vec{t} \cdot \delta \vec{x} \right\} d\mathbb{S}^i \quad (4.32)$$

$$\delta W_c = \sum_{i=1,2} \int_{\gamma_c^i} \left\{ \vec{t}_c \cdot \delta \vec{x} \right\} d\mathbb{S}^i \quad (4.33)$$

Considering Equations 4.12-4.13 and

$$\vec{t}_c^1 d\mathbb{S}^1 = -\vec{t}_c^2 d\mathbb{S}^2 \quad (4.34)$$

the virtual work done by the contact forces (Equation 4.33) is given

$$\delta W_c = \int_{\gamma_c^1} \left\{ \vec{t}_c \cdot \delta(\vec{x}^1 - \vec{x}^2) \right\} d\mathbb{S}^1 = \int_{\gamma_c^1} \left\{ t_N \delta g_N + t_{T\alpha} \delta g_{T\alpha} \right\} d\mathbb{S}^1 \quad (4.35)$$

with $\vec{t}_T \cdot \vec{g}_T = T_\alpha \delta g_{T_\alpha}$.

More details can be found in [115, 126, 128]. It is worth pointing out that the friction is a dissipative mechanism. The friction dissipative power $\dot{\Delta}_{fric}$ is given by [115]

$$\dot{\Delta}_{fric} = \int_{\gamma^1} \left\{ \vec{t}_T \cdot \vec{v}_g \right\} dS^1 = \int_{\gamma^1} \left\{ \mu_c t_N \gamma_c \right\} dS^1 > 0 \quad (4.36)$$

4.1.5.4 Penalty method

The penalty is a method which consists, when there is penetration of one body into another to apply a force proportional to the magnitude of penetration (gap) in order to enforce the impenetrability condition. This is physically equivalent to add an additional fictitious linear spring between the contacted bodies. In LS-DYNA, this is the most used contact method. By considering only the contact contribution, when penetration occurs, Equation 4.35 can be written [125] as

$$\delta W_c = \int_{\gamma_e^1} \left\{ \lambda_N g_N \delta g_N + \lambda_T g_T \delta g_T \right\} dS^1 \quad (4.37)$$

where λ_N is the normal penalty factor and λ_T , the tangential penalty factor when there is sliding. The penalty factor parameter can be compared to the stiffness of a linear spring. The friction forces can then be written as

$$t_N = \lambda_N g_N \quad (4.38)$$

$$t_T = \lambda_T g_T \quad (4.39)$$

Using the FE discretisation, one obtains the global nonlinear finite element equation [131].

$$\mathbf{M} \ddot{\vec{x}} + [\mathbf{K} + \mathbf{K}_c] \vec{x} = \vec{\mathbf{F}}_{ext} - \vec{\mathbf{F}}_c \quad (4.40)$$

where \mathbf{M} is the global nodal matrix, \mathbf{K} and \mathbf{K}_c is the global stiffness matrix and the global penalty stiffness matrix respectively, $\vec{\mathbf{F}}_{ext}$ and $\vec{\mathbf{F}}_c$ are the global external force vector and the global contact force vector respectively. Details on the implementation can be found for example in [132].

They are generally two approaches that are used: the constraint-based approach where contact forces are computed through an optimisation formulation (Lagrange multiplier methods) and the penalty-based approach where a force (modelled as normal interface spring) proportional to the penetration depth is applied to resist the penetration [125]. There are many various types of contact that are defined in

LS-DYNA [116, 133], the penalty-based contacts are the most widely used ¹. They are many other types of contact in LS_DYNA ²

¹One distinguishes the "one-pass" contact like *CONTACT_AUTOMATIC_NODES_TO_SURFACE and *CONTACT_AUTOMATIC_ONE_WAY_SURFACE_TO_SURFACE: the slave side is defined by segments and only the slave segments are checked for penetration of the master segments.

*CONTACT_AUTOMATIC_SURFACE_TO_SURFACE is a "two-pass" contact algorithm and also the *CONTACT_AUTOMATIC_SINGLE_SURFACE suited for self-contact.

²CONTACT_TIED_NODES_TO_SURFACE and CONTACT_TIED_SURFACE_TO_SURFACE are kinematic constraint-based contacts where the slave nodes or the slave segments are tied to the master. Constraints are imposed on slave nodes. CONTACT_INTERIOR: defined for interior contact treatment within a part. It is especially for highly deformable materials like foams to resist highly deformed mesh under severe loading conditions and prevent volume negatives. The principle is the same as the classical contact types to keep the opposing surfaces of an element away from each other to avoid element inversion problem [134].

4.1.6 Material models

The mechanical behaviours of real materials are so complex that to fully described them with equations is not easy. Even for the same material, the behaviour can be different depending of the loading conditions. To take into account all theses considerations, from experimental observations, material models are developed based on certain assumptions [109, 111, 125, 135, 136]. Therefore each model has its validity domain.

A material model is a set of equations relating stress to strain (and possibly strain history, strain rate, and other field quantities) whose general expression can be expressed by Equation 4.41 [136]. It allows to distinguish one material from another. *Constitutive equations or material models* are used to model the material behaviour. Unlike the fundamental physical laws, they are fit to experimental measurements [?]. An example of such constitutive equations can be given by Equation 4.41. Temperature is not taken into account in this thesis.

$$\boldsymbol{\sigma} = \boldsymbol{\sigma}(\mathbf{F}, \dot{\mathbf{F}}) \quad (4.41)$$

where

- $\boldsymbol{\sigma}$ is the Cauchy stress tensor.
- \mathbf{F} the deformation gradient.
- $\dot{\mathbf{F}}$ the time derivative of \mathbf{F} .

There are a lot of material models that have been developed through these years to capture the mechanical behaviours of real materials. Concerning the human body, it is made of different types of tissues that are complex. They can be divided into two main categories, the hard tissues and the soft tissues. Concerning the projectiles, the description of the projectiles (refer to Chapter II) have shown that there have different material characteristics. Literature review has shown that most of the human tissue materials as well as projectile materials can be described as elastic ([111, 125, 137]). In the present thesis, all the materials are assumed to be elastic. Therefore only elastic models will be covered.

Elastic materials are a category of materials which deforms under loading, but returns to its original shape when the load is removed. The main characteristics of this kind of materials are:

- The stress tensor at a given point in the body can be expressed as a function of only the deformation gradient at that point [138]. Equation 4.41 becomes

$$\boldsymbol{\sigma} = \boldsymbol{\sigma}(\mathbf{F}) \quad (4.42)$$

- The material response loading path is the same as the corresponding unloading path (no hysteresis) which means that there is no energy dissipation (Figure 4.6).
- A strain energy density function W exists from which the stress can be obtained by differentiating this function with respect to strain.

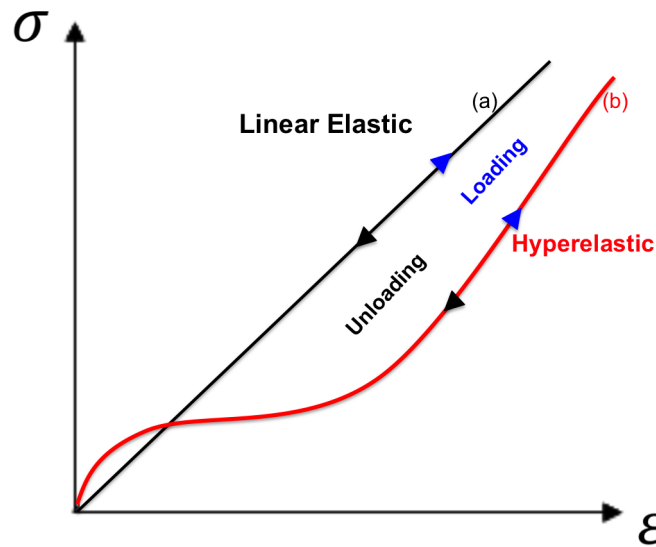


Figure 4.6. Elastic models (a) linear and (b) Hyperelastic.

4.1.6.1 Linear elastic material model

Linear elastic materials is a sub-category of elastic materials and constitute a good approximation for materials under small displacements,

For small displacements³, one can write (Equation 4.43)

$$\sigma = f(\epsilon) \tag{4.43}$$

where

- σ is the stress tensor;
- ϵ is the infinitesimal strain tensor;

³Infinitesimal strain theory is applied. It is when when the undeformed and deformed configurations are assumed to be identical. For large displacements, one uses the finite strain theory to describe the motion of the body. In this case, the undeformed and the deformed configurations of the body are significantly different.

Generally, the stress tensor is split into a spherical component (hydrostatic stress tensor) and a deviator component (deviatoric stress tensor) (Equation 4.44). As stresses induce strains in the body, likewise the strain tensor is divided into normal (or spherical) component (normal strain tensor) and deviatoric component (deviatoric strain tensor) both giving rise to the deformation of the body. The deformation of a body is therefore the result of a volume change through the normal stress tensor and a shape change through deviatoric strain tensor. Under loadings, the full deformation of an element of the body corresponds therefore to the straining of this element to which is superimposed the rigid body motion (Figure 4.7) [139].

Hydrostatic stresses and normal strains allow the definition of the equation of state (EOS) while deviatoric stresses and deviatoric strains allow the definition of the strength model (Figure 4.7). An important requirement on mechanical constitutive equations is that they should be *invariant under rigid translations and rotations* [109, 111, 125, 136].

$$\boldsymbol{\sigma} = p\mathbf{I} + \mathbf{S} \quad (4.44)$$

where p is the hydrostatic pressure; \mathbf{I} is the tensor-unit and \mathbf{S} , the deviator tensor.

$$\boldsymbol{\epsilon} = \frac{1}{3}\epsilon_v\mathbf{I} + \boldsymbol{\epsilon}_d \quad (4.45)$$

where $\boldsymbol{\epsilon}$ is the deviator strain tensor, ϵ_v is the volumetric strain; \mathbf{I} is the tensor-unit and $\boldsymbol{\epsilon}_d$, the deviator strain tensor.

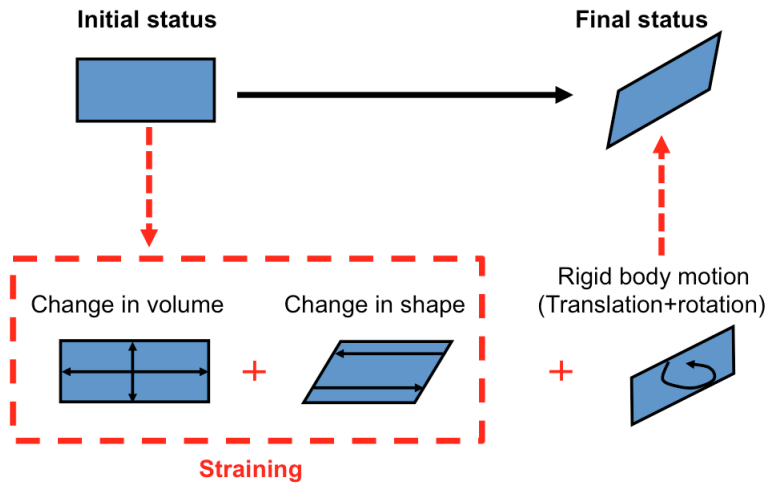


Figure 4.7. Material deformation: illustration of volume change (hydrostatic contribution) and shape change (deviatoric contribution) [139].

The relation between the loading (stress) and the material strain response is linear (Figure 4.6 - curve (a)). It is given by Hooke's law (Equation 4.46).

$$\boldsymbol{\sigma} = \mathbf{C}^{\text{el}}:\boldsymbol{\epsilon} \quad (4.46)$$

where \mathbf{C}^{el} is the stiffness tensor. For isotropic materials⁴, \mathbf{C}^{el} , the stiffness tensor can be written as function of the bulk modulus K (volumetric part) and of the shear modulus G (deviatoric part).

$$\mathbf{C}^{\text{el}} = \frac{1}{3}K\epsilon_v\mathbf{I} + 2G\boldsymbol{\epsilon}_d \quad (4.47)$$

where ϵ_v is the volumetric strain and $\boldsymbol{\epsilon}_d$ the deviatoric strain tensor.

The stress derives from the strain energy (Equation 4.48).

$$\boldsymbol{\sigma} = \frac{\partial W}{\partial \boldsymbol{\epsilon}} \quad (4.48)$$

where W is the strain energy density.

Equations 4.45-4.48 lead to the expression of the strain energy density given by Equation 4.49. It is clear that it has two contributions, the deviatoric deformation energy W_1 (due to the change of shape) and the volumetric (or dilatational) deformation energy contribution W_2 (due to the change volume change). It is worth pointing out that the two contributions are decoupled.

$$\begin{aligned} W &= G \boldsymbol{\epsilon}_d : \boldsymbol{\epsilon}_d + \frac{1}{2}K\epsilon_v^2 \\ &= W_1(\boldsymbol{\epsilon}_d) + W_2(\epsilon_v) \end{aligned} \quad (4.49)$$

where

$$\begin{aligned} W_1(\boldsymbol{\epsilon}_d) &= G \boldsymbol{\epsilon}_d : \boldsymbol{\epsilon}_d \\ W_2(\epsilon_v) &= \frac{1}{2}K\epsilon_v^2 \end{aligned} \quad (4.50)$$

This result will be generalized for hyperelastic materials.

4.1.6.2 Hyperelastic material model

Hyperelastic material is another sub-category of elastic materials for which the relation between the loading (stress) and the material strain response is non-linear (Figure 4.6 - curve (b)). It is the generalisation of linear elastic materials to large

⁴Isotropic materials are materials whose properties are the same in all directions

strains. Rubberlike materials and many human soft tissues are generally considered as hyperelastic materials [125]. The requirement for the strain energy function W is that it must satisfy the principle of frame indifference or objectivity⁵. Therefore, it is always possible to write the strain energy as a function of the right-Cauchy strain tensor \mathbf{C} that is derived from \mathbf{F} . The relation 4.48 under large strains becomes

$$\mathbf{S} = 2 \frac{\partial W(\mathbf{C})}{\partial \mathbf{C}} \quad (4.51)$$

where \mathbf{S} is the second Piola-Kirchhoff stress tensor.

For *isotropic materials*, one can express the strain energy density as a function of the strain invariants,

$$W(I_1, I_2, I_3) = \sum_{m+n+k=1}^{\infty} A_{mnk} (I_1 - 3)^m (I_2 - 3)^n (I_3 - 3)^k \quad (4.52)$$

where A_{mnk} are coefficients of polynomials, I_1 , I_2 and I_3 are invariants of the right Cauchy-Green deformation tensor respectively. It is a general formulation of compressible materials. It is common that a totally decoupled formulation of Equation 4.52 is assumed such that the deformation of a hyperelastic material can be decomposed into volumetric and distortional parts. The introduction of compressive materials is given later.

For *incompressible materials*, the strain energy density is purely a *distortional strain energy density* $W_1(I_1, I_2)$ and depends only of the first and the second invariants (Equation 4.53).

$$I_3 = 1$$

$$W_1(I_1, I_2) = \sum_{m+n=1}^{\infty} A_{mn} (I_1 - 3)^m (I_2 - 3)^n \quad (4.53)$$

Various incompressible material models have been proposed among which

- **Neo-Hookean model:** It can be derived from Equation 4.53 with $m = 1$ and $n = 0$

$$W_1(I_1) = A_{10}(I_1 - 3) \quad (4.54)$$

- **Mooney-Rivlin model:** It can be derived from Equation 4.53 where $m = 1$ and $n = 1$

$$W_1(I_1, I_2) = A_{10}(I_1 - 3) + A_{20}(I_2 - 3) \quad (4.55)$$

⁵Material properties are invariant under changes of observers.

- **Yeoh model:** It can be derived from Equation 4.53 where $n = 0$ and $m = 1, 2, 3$.

$$W_1(I_1) = A_{10}(I_1 - 3) + A_{20}(I_1 - 3)^2 + A_{30}(I_1 - 3)^3 \quad (4.56)$$

The incompressibility condition leads to volumetric locking problem in FE simulations. In fact, if the material is assumed to be incompressible, the volume remains constant for different values of pressure. A first step in solving the problem is to relax the incompressibility condition to a certain extent (Poisson coefficient $\nu \rightarrow 0.5$ instead of $\nu = 0.5$). The material is then considered as nearly incompressible material .

- **Nearly incompressible material:** For this materials, the strain energy density is written in a way that it can be separated into two distinct contributions (the distortional strain energy density and in dilatational one) by using the so-called reduced invariants J_1, J_2, J_3 .

$$W(J_1, J_2, J_3) = W_1(J_1, J_2) + W_2(J_3) \quad (4.57)$$

where $J_1 = I_1 I_3^{-1/3}$, $J_2 = I_2 I_3^{-1/3}$ and $J_3 = I_3^{-1/3}$.

$W_1(J_1, J_2)$ is the distortional strain energy density and $W_2(J_3)$ the dilatational strain energy density related to the equation of state. $W_1(J_1, J_2)$ can be defined by using Equation 4.53 where the invariants are substituted by reduced invariants. To model the rubber(like) materials and biological soft tissues as unconstrained materials, Equation 4.53 can be recasted in the form of Equation (Equation 4.57). The general formulation becomes

$$W(J_1, J_2, J_3) = \sum_{m+n=1}^{\infty} C_{mn}(J_1 - 3)^m (J_2 - 3)^n + W_2(J_3) \quad (4.58)$$

where C_{mn} are coefficients of polynomials.

There are various form of $W_2(J_3)$. One of the most referred formulation is given by Rivlin where

$$W(J_3) = \sum_{i=1}^N \frac{1}{D_i} (J_3 - 1)^{2i} \quad (4.59)$$

where D_i define the material compressibility and N , the polynomial degree.

If $N=1$, the Mooney-Rivlin model defined by Equation 4.60 becomes

$$W(J_1, J_2, J_3) = A_{10}(J_1 - 3) + A_{01}(J_2 - 3) + \frac{K}{2}(J_3 - 1)^2 \quad (4.60)$$

where A_{10} and A_{01} are material constants and $K = \frac{2}{D_2}$ is the bulk modulus.

- **Ogden model:** Instead of using a strain energy density, function of strain invariants of the right Cauchy-Green deformation tensor, Ogden proposed a model of the distortional strain energy density which is a function of the principal stretches and is given by Equation 4.63

$$W_1(\lambda_1, \lambda_2, \lambda_3) = \sum_{i=1}^N \frac{\mu_i}{\alpha_i} (\lambda_1^{\alpha_i} + \lambda_2^{\alpha_i} + \lambda_3^{\alpha_i} - 3) \quad (4.61)$$

where μ_i and α_i are material parameters and $N(\geq 1)$ is the polynomial degree. It is worth pointing out that for an incompressible material, the three principal stretches are dependent since one has $\lambda_1\lambda_2\lambda_3 = 1$.

If $N = 1$ and $\alpha_1 = 1$, one recovers the Neo-Hookean model and for $N = 2$, $\alpha_1 = 2$ and $\alpha_2 = -2$, the Mooney-Rivlin model [125]. In LS-DYNA, various hyperelastic models are implemented, from the simple models to the complex ones.

As mentioned previously, real materials have a complex behaviour and for many soft materials like human soft tissues, they exhibit not only hyperelastic, but also viscoelastic behaviour where time and rate of change play an important role. This means that rate effects should be taken into account for such models. In the following section, the viscoelastic material models are presented.

- **Compressible hyperelastic materials**

A general formulation of highly compressible materials have been developed by Ogden [140] is given by

$$W(\lambda_1, \lambda_2, \lambda_3) = \sum_{i=1}^N \frac{\mu_i}{\alpha_i} (\lambda_1^{\alpha_i} + \lambda_2^{\alpha_i} + \lambda_3^{\alpha_i} - 3) + F(J) \quad (4.62)$$

where C_j and α_j are material constants and $J = \lambda_1\lambda_2\lambda_3$ represents the ratio of deformed to undeformed volume and $F(J)$ is the volumetric function.

In [141], the Hill-Ogden formulation has been adopted

$$W(\lambda_1, \lambda_2, \lambda_3) = \sum_{j=1}^N \frac{\mu_j}{\alpha_j} \left[\lambda_1^{\alpha_j} + \lambda_2^{\alpha_j} + \lambda_3^{\alpha_j} - 3 + \frac{1}{n} (J^{-n\alpha_j} - 1) \right] \quad (4.63)$$

where n is a compressibility material constant. When n is large, the material is assumed to be incompressible like rubber. When n is small, the material is highly compressible like foam.

It has been shown in section of nearly incompressible materials that the strain energy density can be split into two decoupled contributions, the distortional strain energy density and the dilatational one (Equation 4.57) by using specific transformation as no condition was imposed on the material compressibility. Compressible or nearly incompressible materials can therefore be written in this formulation. An advantage of this decoupling is that the two terms can be treated independently in the framework of the FE development e.g. using different integration schemes to avoid locking problems. All the incompressible elastic models described previously have therefore their compressible counterpart models [141, 142]. Here an example of the compressible Mooney-Rivlin polynomial model which has already been described in the description of nearly incompressible models (Equations 4.58-4.59).

$$W(J_1, J_2, J_3) = \sum_{m+n=1}^{\infty} C_{mn}(J_1 - 3)^m(J_2 - 3)^n + \sum_{i=1}^N \frac{1}{D_i}(J_3 - 1)^{2i} \quad (4.64)$$

In [143], many expressions of the volumetric strain energy has been proposed

4.1.6.3 Viscoelastic material model

Human soft tissues generally are characterised by viscoelastic behaviour. Viscoelastic materials are materials that exhibit both fluid (viscosity) and solid (elasticity) characteristics. Viscoelastic materials are strain rate dependent materials (Figure 4.8(a)). Important properties of viscoelastic materials are:

- Stress relaxation under constant strain: a constant strain results in decreasing stress.
- Creep under constant loading: a constant stress results in increasing strain.
- Hysteresis: there is a stress-strain phase lag between the loading and the response (a stress-strain phase lag) [135]. As it has been mentioned in Chapter III, under loading, a part of energy involved in deformation is stored elastically and another part is dissipated through viscous mechanism. In Figure 4.8(b), the area unclosed by the loading and unloading paths corresponds to the energy dissipated during one cycle.

If linear materials are considered, the constitutive equation 4.41 of a model linear viscoelastic materials can be expressed in integral form (Boltzmann superposition

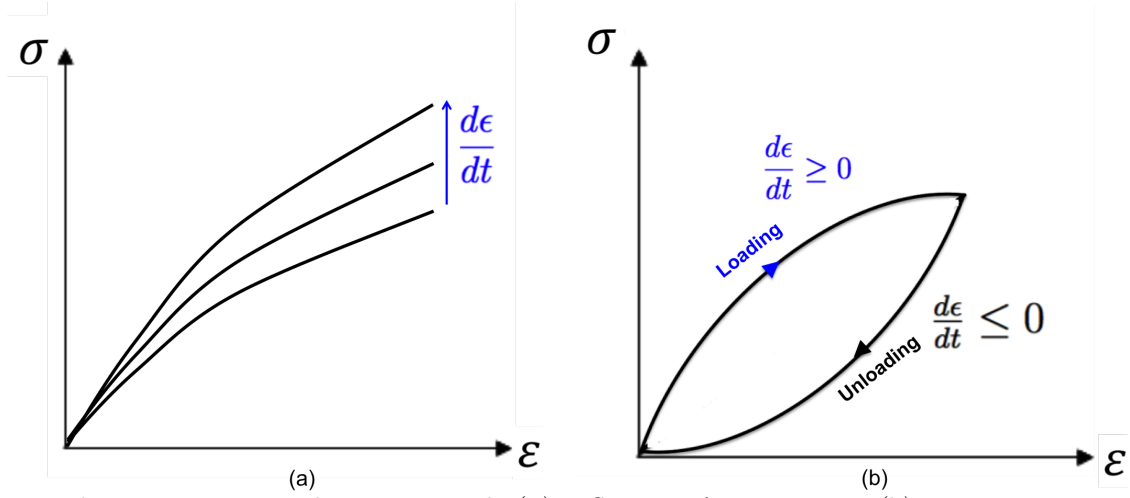


Figure 4.8. Viscoelastic materials (a) Influence of strain rate - (b) Dissipation during cyclic loading-unloading (Hysteresis).

model) and can be given by Equations 4.65 and 4.66 [137]

$$\epsilon(t) = \int_{-\infty}^t \mathbf{J}(t-s) \frac{d\sigma}{ds} ds \quad (4.65)$$

$$\sigma(t) = \int_{-\infty}^t \mathbf{G}(t-s) \frac{d\epsilon}{ds} ds \quad (4.66)$$

where $\mathbf{J}(t)$, the creep function, represents the material response function under constant stress and $\mathbf{G}(t)$ the stress relaxation function⁶ is the material response function under constant strain. Both functions are continuous with respect to time. Generally, they can be represented as Prony series of the forms

$$\mathbf{J}(t) = \mathbf{J}_0 + \sum_{k=1}^N \mathbf{J}_k (1 - e^{-(t/\eta_k)}) \quad (4.67)$$

with \mathbf{J}_0 is the elastic (time-independent) material characteristic constant, \mathbf{J}_k , $k=1,2,\dots,N$ are viscous material parameters (constants), η_k are characteristic times.

$$\mathbf{G}(t) = \mathbf{G}_\infty + \sum_{j=1}^M \mathbf{G}_j e^{-(t/\tau_j)} \quad (4.68)$$

with \mathbf{G}_∞ is the long-term (time-independent) material characteristic constant, \mathbf{G}_k , $k=1,2,\dots,M$ are viscous material parameters (constants) and τ_k are the corresponding

⁶In a general sense, the response can be divided in a volumetric contribution and a deviatoric contribution. But most often the viscous effects in the volumetric contribution are neglected. In this case, $\mathbf{G}(t)$ is the shear relaxation function as commonly used. The same reasoning can be made for $\mathbf{J}(t)$.

characteristic times. It results from Equations 4.67-4.68 that the response of a viscoelastic material can be divided into two components: an elastic component and a viscous component.

To get more understanding of linear viscoelastic materials, it is common to use an analogy with mechanical systems made of a combination of springs and dashpots [109, 135, 144].

4.1.6.4 Visco-hyperelastic material model

This kind of materials shows a hyperelastic as well as viscoelastic effects [145]. Both hyperelastic models and viscoelastic models have previously described. Therefore the visco-hyperelastic is obtained by combining the the elastic component with the viscoelastic component. It is described by

$$\boldsymbol{\sigma} = \boldsymbol{\sigma}_{hyperelastic} + \boldsymbol{\sigma}_{viscoelastic} \quad (4.69)$$

In LS-DYNA, viscoelastic behaviour is taken into account in hyperelastic models by using strain rate dependent curve characteristics.

4.1.7 Material model parameter identification

All the material models contain a number of material parameters which are to be determined from specific experiments with well tailored material specimens. There are two ways of determining these parameters.

- Material models can be determined by carrying out conventional standardized experiments and by using test specimens with a well-defined standardized geometry and under specific loading, to achieve particular conditions of stress and strain within the specimen. There are many well known standardized tests like uniaxial tensile and compression tests, bending tests. By measuring variables such as forces, displacements, material parameters like Young's modulus, bulk modulus can be determined through simple analytical relations.
- When the characteristics of a given material is not known or can not be determined through conventional methods, inverse methods can be used. These methods are based on determining the material model parameters from the responses of the system to given stimuli and through numerical simulations. The results of FE simulations are then compared to the measured responses and an iteration process is carried out until convergence.

Under (dynamic) loadings, the main characteristics which is used to provide basic information on the strength of materials is the stress-strain curve from which many other parameters (Young's modulus for example) can be derived. This curve is obtained via experiments. There are two ways of implementing this curve into the FE code, either by fitting an analytical curve to measured data, one determines material parameters of the chosen model to be used in the code (parameter material model law) or by using directly the experimental data into the code (tabulated law) (Figure 4.9). The former can be time-consuming when the number of the parameters in the model is large. In many FE codes, both methods are implemented.

The tabulated law method developed in [146] is based on a simplified formulation derived from the Ogden hyperelastic model where the stress-strain curves from uniaxial experiments are directly used in a tabulated form [144, 145, 147, 148]. No Ogden model parameter identification is necessary in this case. It is possible to use many load curves is used. In this case, they should cover the complete range of the expected loading [149]. The method is used for rubber-like or foam materials ⁷.

Viscoelastic effect can be incorporated by using experimental curves at different strain rates. Linear interpolation between two curves at different strain rates is performed to calculate the stress at a given strain if the current strain rate falls between the strain rates of the two considered curves. An advantage of this method is the direct use of the experimental data and no fitting is required to accommodate the shape of the experimental data curve is as long as it is increasingly monotonic.

The unloading is modelled by a direct input of the unloading curve or by using LS-DYNA user-defined parameters ⁸.

The tabulated law formulation has been developed for low rate phenomena (uniaxial quasi-static tests). Based on this approach, a method to characterise the projectile nose material of the 40 mm sponge grenades at high strain rate (up to 3000 s^{-1}) has been developed (Chapter VI).

The general procedure for solving problems in FE codes is summarized in Figure 4.10.

⁷This method is implemented in LS-DYNA [149] using the models MAT_SIMPLIFIED_RUBBER (MAT_181) for rubber-like models and rubber-like compressible materials, and MAT_FU_CHANG_FOAM (MAT_083) is used for material with a Poisson's ratio close to zero. An incompressible rubber-like behaviour is assumed for the Poisson's ratio is close to 0.5 (default value=0.495)

⁸Two LS-DYNA user-defined parameters HU, the hysteresis unloading factor ($0 \leq HU \leq 1$) and SHAPE, the shape factor for unloading can be set in order to simulate the unloading

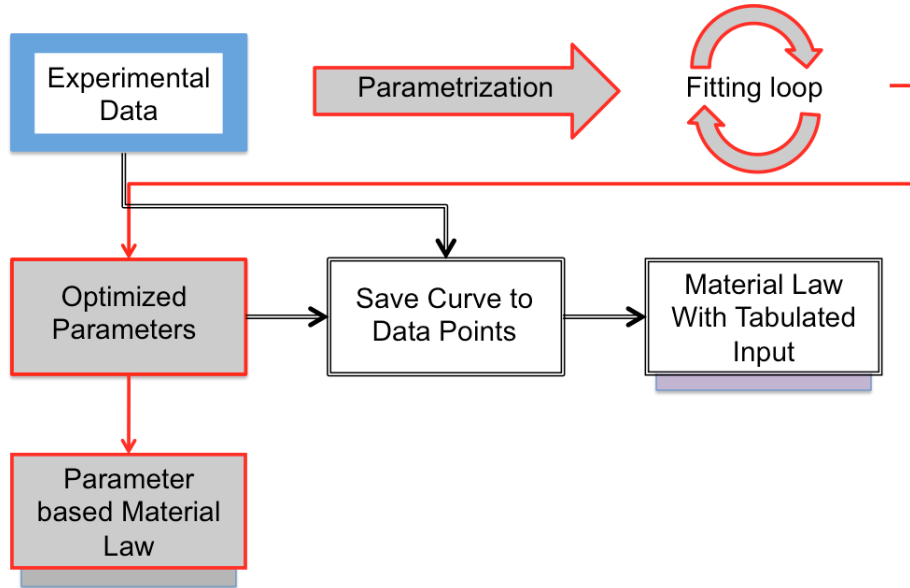


Figure 4.9. Procedures of material card generation: Parameter-based input versus Tabulated input [145].

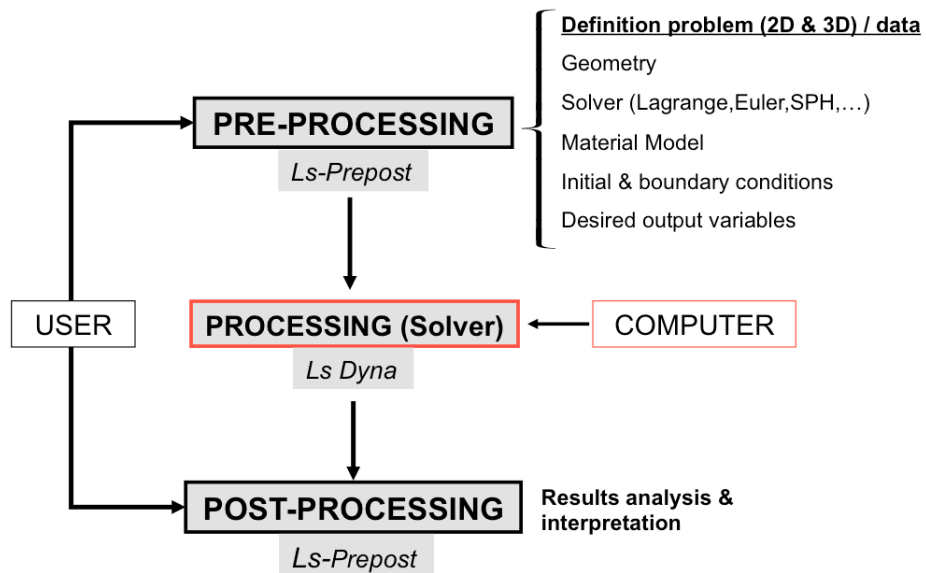


Figure 4.10. Steps for solving (dynamic) problems using FE codes/LS-DYNA code.

4.2 Methodology for non-lethal thoracic impacts

Modelling impact problems is not easy as it requires the understanding of the complexity of real impact events. This complexity is due to the time scale of the event, the different non-linearities (geometrical, material, contact) involved and the difficulty of obtaining effectively and efficiently continuous measurements of the impact event. In the case of thorax which is a deformable structure, one needs displacement measurements to derive the parameter for injury risk assessment of thoracic impacts. It is already difficult when the projectile is a "rigid" one and the problem becomes more complex when it comes to deformable projectiles (both bodies are then deformable bodies). How then to solve the problem? This is a question to which FE element can provide a solution.

To simulate the impact of KENL projectile on thorax for risk assessment, one needs (Figure 4.11):

- To numerically build the thorax model as well as the projectile model. The building of FE model requires to obtain the geometry, generate the mesh and to get the material characteristics (properties) via specific tests to feed the material models (see section 4.1.6).
- Each model should be validated i.e. the numerical results are compared to experimental measures of well designed tests.
- The assessment implies that one should know the interested measurable physical parameters relevant for the risk assessment.

As the thorax is a deformable structure, it is difficult to experimentally measure for example the thorax wall displacement during the impact of the thorax and the projectile without using indirect methods or invasive methods. The problem is even more complicated if the projectile deforms or breaks at impact (*soft-soft* impact). That is where the FE method with its powerful capabilities can help circumvent the experimental difficulty as it offers the possibility of directly extracting for example the displacement.

Before numerically impacting the projectile on the thorax, one needs validated models. The idea is therefore to split this step into two steps which are more experimentally manageable as measurements can be more or less easily performed (Figure 4.12). So the models could be validated. The first step is to consider the impact of a rigid projectile on thorax (*rigid-soft* impact). Experiments performed by C. Bir are used [40] in this case. The second one is to consider the impact of the projectile against a rigid wall (RW) structure (*soft-rigid* impact)[2]. Tests were

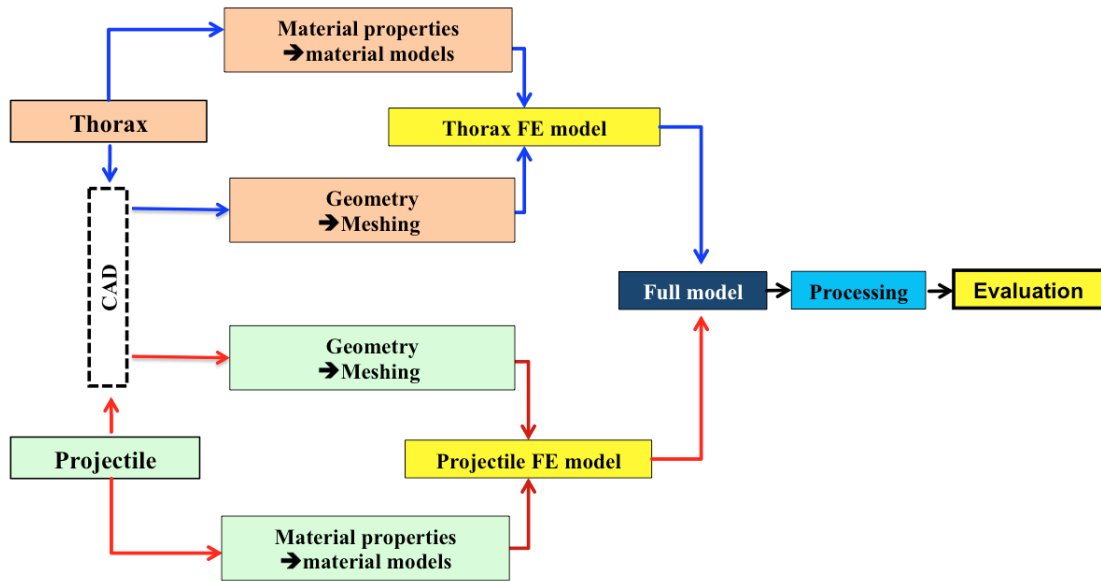


Figure 4.11. Model building scheme.

performed within the ABAL department by C. Robbe and A. Oukara. Moreover, based on the results of RW impacts, a new method (section 6.1.2) has been developed to characterise the deformable projectiles with sabot.

These two steps will feed the numerical models by providing baseline data for the validation of corresponding numerical models. Validation in the range of velocities encountered in real situations is necessary if one expects to get reliable results. Once the models are validated, the impacts can be simulated numerically and the desired physical quantities for example the viscous criterion in our case can be determined. To do this splitting operation, it is assumed that the thoracic model as well as the projectile model once validated by this procedure will yield correct results during the impact simulation.

Figure 4.12 depicts the general methodology that is used for the evaluation (assessment) of the impacts of KENL projectiles on thorax [2]. This evaluation is carried out (*soft-soft* impact) using appropriate criteria (see chapter VII).

This methodology is general and presents few advantages:

- It is independent of the injury criterion used in the sense that if a new thoracic criterion is defined, the methodology can be applied provided that the thorax model is validated accordingly if necessary.
- Parameter sensitivity can be carried to see the influence of a given parameter on the injury criterion i.e. on the injury outcome.

Building a FE model can be time-consuming and requires three main steps:

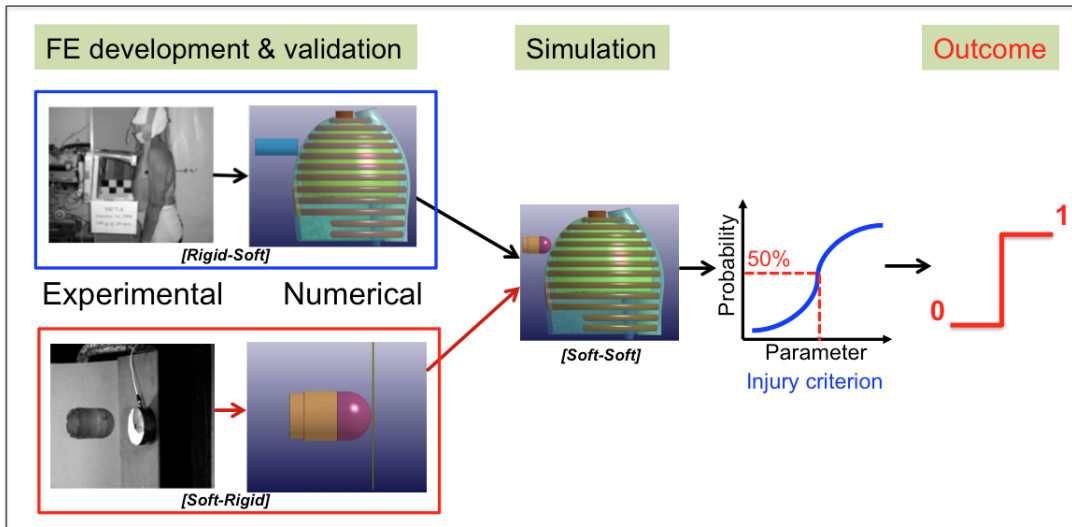


Figure 4.12. Methodology for KENLW assessment.

- The geometry and mesh generation: This was done using *Ansys*⁹ for the thorax and *Solidworks*¹⁰ and *Hypermesh*¹¹ for the projectiles. *Ls-Prepost* was used for the pre-processing (LS-DYNA model card generation) as well as for the post-processing.
- The material characterisation consists through experiments to derive material models that describe the material behaviour under specific loadings. Except for most of the 40 mm sponge grenades where the material models were derived from results of in-house experiments, all other material models were taken from the literature.
- The validation of the model: the numerical results should match the experimental results.

The validation process of the thorax and the projectile models are given in Chapter V and Chapter VI respectively.

4.2.1 Conclusions

Modelling impact problems is not easy as it requires not only the understanding of the complexity of real impact events but also the mathematical tools to describe the phenomena. In that purpose, an overview of FE method, the widely used mathematical method has been given. To carry out the numerical simulations, a methodology

⁹More details at www.ansys.com
¹⁰More details at www.solidworks.fr
¹¹More details at www.altair.fr

has been defined for the evaluation of the impact of the projectile on thorax. It consists of three main steps: the building of the thorax model as well as the projectile models, the validation of these models and finally the evaluation of the impact of the projectile on the thorax. In the next chapter, the thorax model will be developed and validated.

Chapter 5

Thorax Finite Element model

5.1 Development of the thorax FE model

The development of the thorax model is divided in three main steps. Firstly the thorax geometry using a CAD software, then it meshed. Secondly, material properties of different organs were obtained from the literature. Finally, the model is validated by using biomechanical corridors defined in Bir's experiments. In this chapter, firstly, a thorax FE model, the SHTIM (Surrogate Human Thorax for Impact Model) is built, secondly L5 projectile FE model is built, finally the validation is performed.

5.1.1 The SHTIM model

Because of the complexity of the geometry, two axes of the development were investigated (Figure 5.1). The first axis was the development of a very simple model (the simplified model) made of cylindrical and annular geometries. This model is a very simple representation of the thorax far from the real thorax geometry. Details of the model can be found in [150]. But there was a need to go for an improved model to be as close as possible to the real thorax. The second one was the development, in collaboration with the University of Liège, of an anthropometric model whose geometry was obtained from ct-scan images [151]. The geometry of the different thorax organs was correctly represented. But this model has a stiffer response than expected. Therefore, an intermediate model namely the SHTIM, was developed as a compromise between the simplified model and the anthropomorphic model because it was necessary to have as quick as possible a model available for the risk assessment.

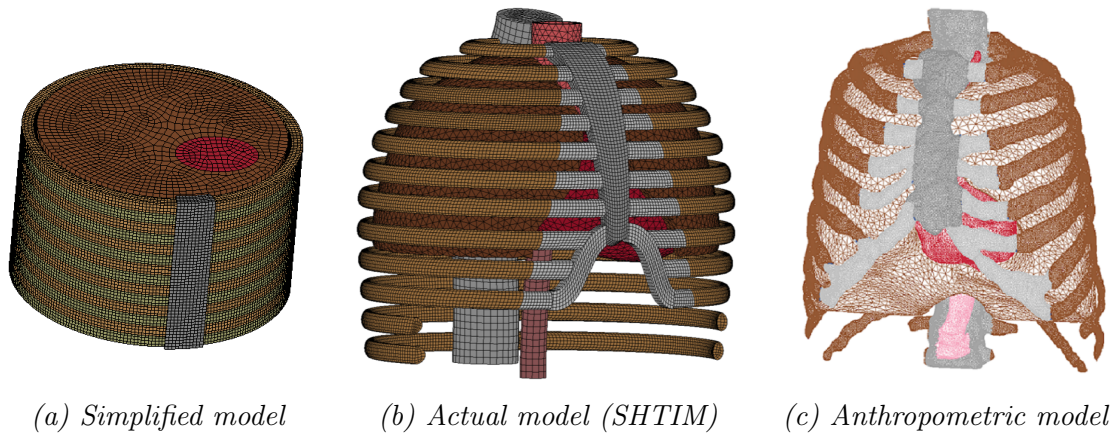


Figure 5.1. *Different thorax models.*

5.1.2 The SHTIM model description

Each person being unique, there exists great variations in size and shape of the thorax geometry, and in material properties among the population due to many factors: sex, age, health, ... An average man (50th percentile) has been defined as a standard especially in the crash test field [152–155] and is also used in non-lethal field. Here the developed thorax model is not a 50th percentile. Instead it is a roughly representation of the thorax principal organs (Figure 5.2). It consists of the skeletal structure (12 pairs of ribs, sternum, spine vertebrae), the heart, the lungs, the costal cartilages, intercostal muscles, the fatty tissues and the skin.

The thorax organs can be classified into two main categories as represented on Figure 5.3, the thorax wall and the internal organs (Chapter III). For modelisation purpose, all the soft tissues wrapping up the thoracic skeleton (intercostal muscles, the fatty tissues and the skin) have been grouped into one part called "flesh" (Figure 5.3) with the same properties. The crossed-out parts have not been modelled nor the space between different organs. There is only void.

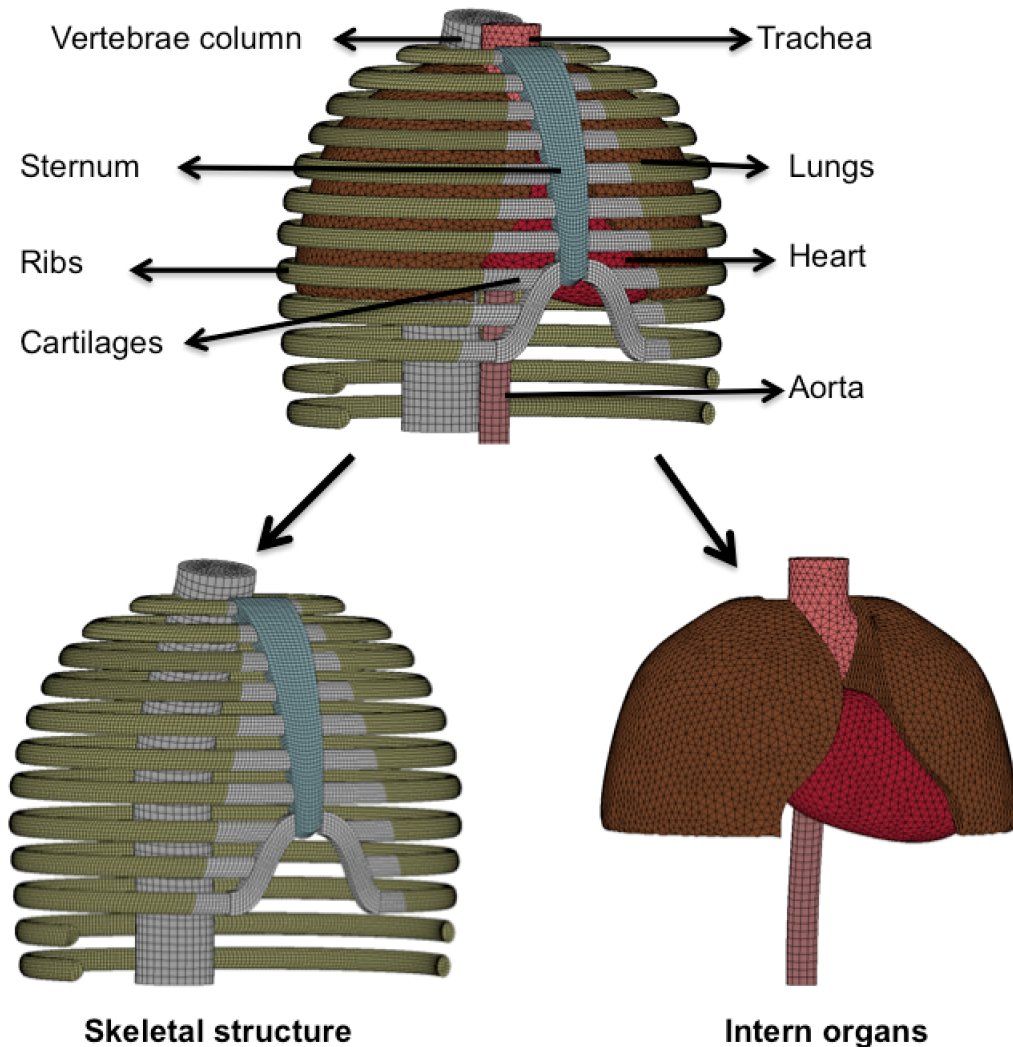


Figure 5.2. *Thorax model (flesh not represented).*

5.1.2.1 Geometry and mesh characteristics

Some assumptions on the geometry are made in order to reduce the time of the model development and the complexity of the problem:

- Ribs are modelled as continuum solid parts in horizontal planes with elliptic constant cross-sections although in reality each rib has a limited varying curvature along its path and lies in an oblique plane with respect to coronal plane and generally its cross-section is not constant (Figure 5.1(b)-(c)). This obliquity slightly varies from a rib plane to another.
- The sternum is modelled as a continuum.

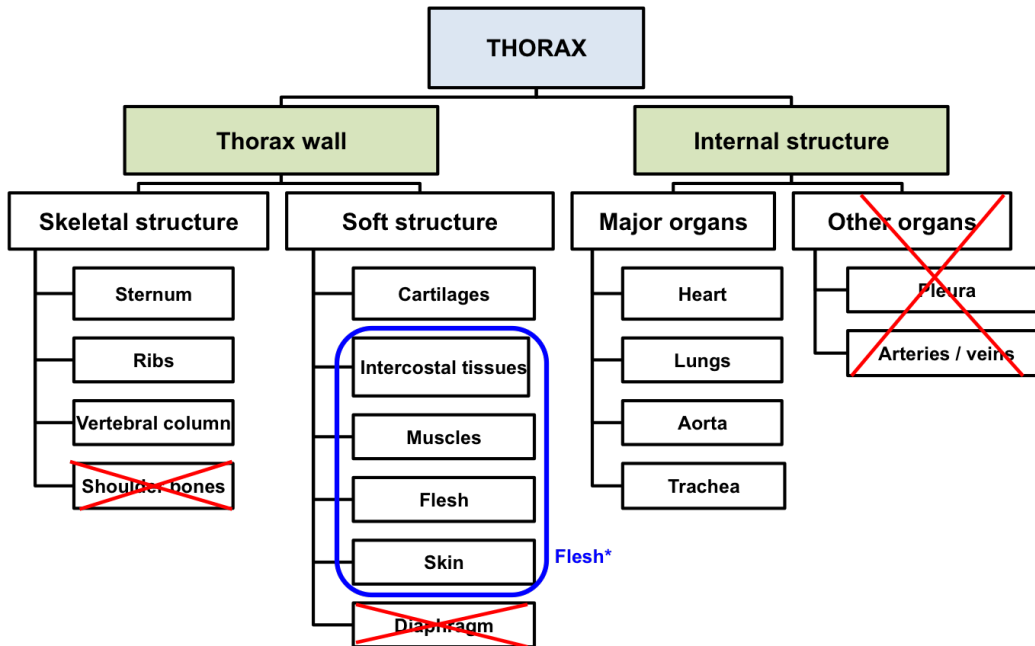


Figure 5.3. Different organs of the thorax that have been modelled.

- Vertebrae column is modelled as a single continuum as one solid part). Moreover, there is no need of modelling this part in details as it is almost motionless due to the localised nature of the impacts. All the impacts are performed on the anterior part of the thorax.
- The "flesh" consisting in this present work of intercostal muscles, the fatty tissue of the thoracic cage and the skin are modelled as a single continuum part wrapping up the thoracic cage;
- The lungs, filled partially with air and the heart, filled with blood, are modelled also as continuum respectively.
- There are voids between organs in the thoracic cavity as fluid, blood vessels or other internal tissues are not taken into account.
- The diaphragm which is a membrane that separates the thorax from the abdomen is not modelled as well as the abdominal organs which constitute boundary in the lower part of the thorax.

The thoracic cage is modelled with hexahedral elements except for the "flesh" (not represented in Figure 5.3 which is modelled with tetrahedral elements. All the internal organs are modelled with tetrahedral element except for the aorta and the trachea. The number of elements of the organs is given in Figure 5.2.

5.1.2.2 Material characteristics

Most human tissues are composite materials¹ with non-homogeneous and anisotropic properties. Their properties vary from point to point and their respective response depends of the loading directions. Because of this complexity and the complex loadings that the thorax can sustain, they are not easy to model. Therefore some assumptions are made: all the thorax material tissues are considered as homogeneous and isotropic. The material properties of different thorax organs were taken from literature and are given in Table 5.1.

- The ribs, the sternum and vertebrae column and the costal cartilages were modelled as linear elastic materials² [95].
- The heart, the flesh, the aorta and the trachea were modelled as hyperelastic materials³. There is a loading curve for this material. It is based on Treloar experimental data and is given on Figure 5.4 [6, 156, 157]. The lung is modelled with a hyperelastic model⁴ [158, 159]. Its formulation is given on Figure 5.4.

No rupture model is implemented as the criterion linked to the occurrence of the fracture that was determined is only based on the thorax deflection.

During the impact, the different thorax organs come each other in contact. Normally, sliding can occurs between organ. It is not taken into account. Therefore all the internal organ are tied. The ribs and the sternum are also tied to the cartilage and the "flesh" and a penalty contact type is defined between the thorax wall and the internal organs⁵.

¹composite material consists of different materials with different properties

²This model is implemented in LS-DYNA as *MAT_ELASTIC (5)

³This model is implemented in LS-DYNA as *MAT_SIMPLIFIED_RUBBER/FOAM (181)

⁴This model is implemented in LS-DYNA as *MAT_LUNG_TISSUE (129)

⁵Interface contacts have been defined between different organs such as: TIED_NODES_TO_SURFACE or TIED_SURFACE_TO_SURFACE between the different organs of the same structure (external or internal) and AUTOMATIC_SURFACE_TO_SURFACE between the internal and the external structures

Parts	Material parameters				Element type/ Number of elements	
	Density [kg/mm^3]	Young modulus [Pa]	Poisson's ratio		Hexa	
Ribs	1581	$7.9 \cdot 10^9$	0.379		Hexa/ 56320	
Sternum	1354	$3.5 \cdot 10^9$	0.387		Hexa/ 2750	
Vertebrae column	1644	$9.6 \cdot 10^9$	0.376		Hexa/ 6696	
Costal cartilage	1281	$4.9 \cdot 10^6$	0.400		Hexa/ 5513	
Heart	1050	$2.2 \cdot 10^9$	0.495		Tetra/ 31071	
			Loading curve		Tetra/ 31071	
LC			Tetra/ 100894			
			Hexa/ 968			
			Tetra/ 3122			
Lungs	118	$1.18 \cdot 10^5$	C	Δ [m]	α	Tetra/ 143074
			0.50350	0.00007	0.08227	
			β	C1	C2	
			-2.46000	0.00654	2.87600	

Table 5.1. *Material characteristics of the SHTIM parts.*

where $C1$, $C2$, Δ , α and β are material constants, LC is the loading curve.

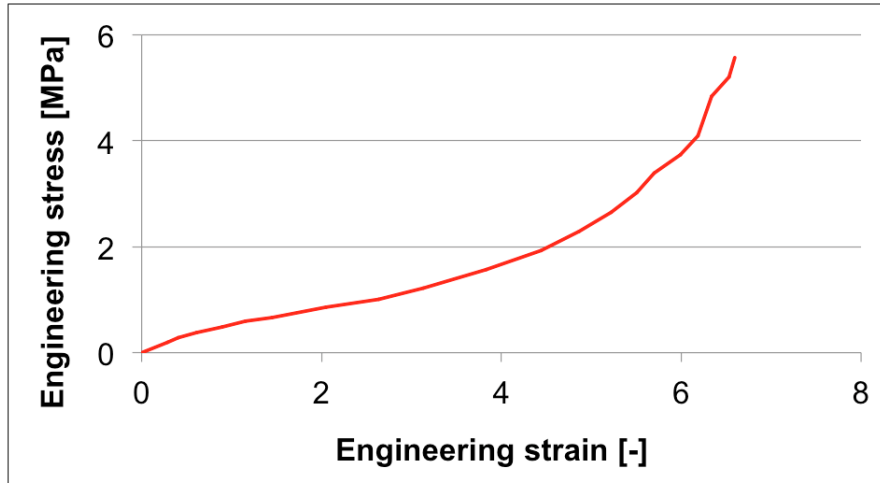


Figure 5.4. Load curve (LC) for the "flesh", aorta and trachea material models [6].

As previously mentioned, the thorax FE model will be validated thanks to Bir's experiments where L5 projectiles were used for the determination of the biomechanical corridors. In the following sections, first L5 projectile FE models are built, then contacts are defined between the projectile and the thorax and finally the validation is performed.

5.1.3 L5 projectile FE model

The L5 projectiles is described in section 2.4.2.6. The two projectiles that was used have the same material properties and the same diameter but different lengths (Figure 5.5).

5.1.3.1 Geometry and mesh

The projectile geometric characteristics are given in Figure 5.5.

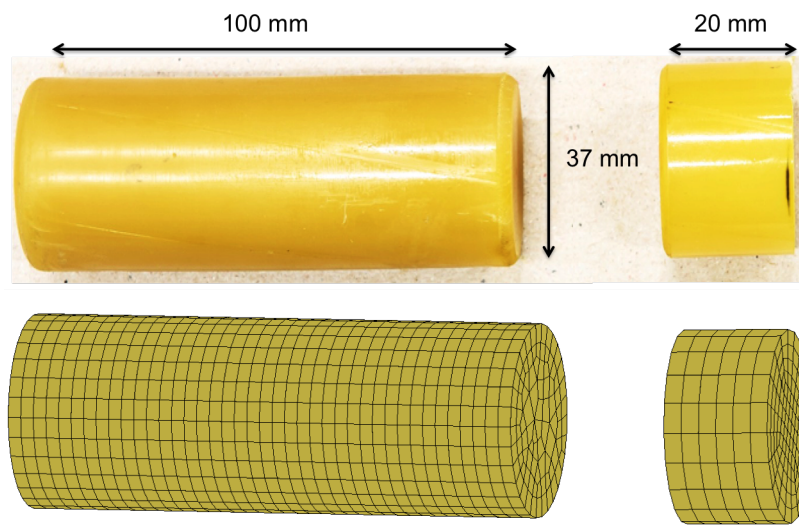


Figure 5.5. *PVC projectile characteristics.*

5.1.3.2 Material characteristics

A linear model is used for the PVC projectile with the parameters given in Table 5.2. where the conditions *A/B* correspond to the impact of the L5 projectile with the mass of 140 g at 20 m/s and 40 m/s respectively, the condition *C* corresponds to the impact of another L5 projectile with a mass of 30 g at 60 m/s.

Parts	Material parameters			Element type/ Number of elements
	Density [kg/mm^3]	Young modulus [Pa]	Poisson's ratio	
Condition A / B	1380	$2.3 \cdot 10^9$	0.33	Hexa/ 3600
Condition C	1380	$2.3 \cdot 10^9$	0.33	Hexa/ 630

Table 5.2. *Different properties of the PVC projectile.*

5.1.4 Validation

5.1.4.1 Setup

The setup to numerically simulate Bir's experiments is shown on Figure 5.6 with the impact direction. This impact direction is defined because of the thorax model curvature as to achieve normal impacts like in Bir's experiments. Moreover, normal impacts are the worst cases in term of viscous injury criterion so as it was demonstrated in [160, 161]. But all measurements are performed in X-direction as it is in this direction that are located the organs under consideration which might be injured.

A penalty contact type⁶ is defined between the projectile and the thorax model.

5.1.4.2 Filtering problematic

There is generally noise in measured experimental signals. This noise is mitigated by the use of a filter. But it is not clear which kind of filter was used as no precision is given in [40]. Therefore a choice was made not to filter the numerical data unless stated otherwise. Filtering generally lowers the amplitude, making this choice conservative.

⁶AUTOMATIC_SURFACE_TO_SURFACE

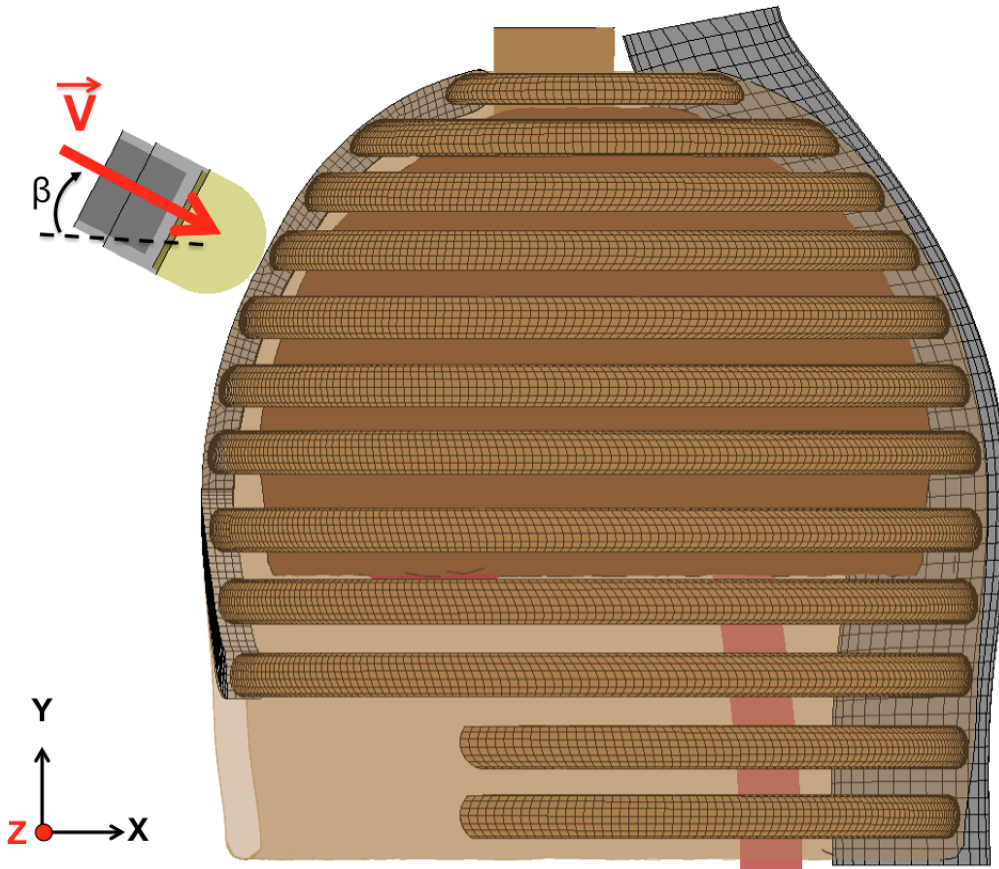


Figure 5.6. Setup for normal impacts.

5.1.4.3 Results of SHTIM validation

To validate the model, Bir's results are used where for each projectile and each velocity, biomechanical corridors were determined giving the upper and the lower limits of the biomechanical responses of the impact on PHMS. Because of the difficulty of tracking the thorax displacement, an indirect method was used. Using a camera, it consisted of tracking the motion of a marker attached to the projectile relative to a reference attached to the PMHS. But this method is no more efficient when it comes to a deformable projectile or a projectile that breaks at impact. Numerical simulations offer then the capabilities to directly track the thorax displacement via the thorax impact zone nodes (markers). But it is important to check first that the thorax displacement determined via the projectile marker bears the same results as the one obtained via the thorax marker to see if both measures are consistent. Figure 5.7(a) shows a good correspondence between the two methods except for the unloading. Therefore to deal with deformable projectile and frangible projectile, the thorax displacement is determined by the tracking of a thorax node in the impact zone, the one with a VC_{max} maximal. Results are similar for the other Bir's conditions.

5.1 Development of the thorax FE model

Figure 5.7(b-c) shows the velocity and the viscous derived from the thorax node displacement (Figure 5.7(a)). The viscous criterion can be then determined. Figure 5.7(d) shows the results for all the 3 conditions of $(VC)_{max}$. The three values fall within the experimental $(VC)_{max}$ boundaries.

By comparing the three curves (Figure 5.7(a-c)), it is noted that their respective maxima do not occur at the same time. The thorax maximum velocity is first reached at the early stage of the impact at $t_{(VC)_{max}}=0.08$ ms, followed by the maximum of the viscous response at $t_{(VC)_{max}}=0.78$ ms and finally the thorax maximum displacement at $t_{(VC)_{max}}=1.54$ ms.

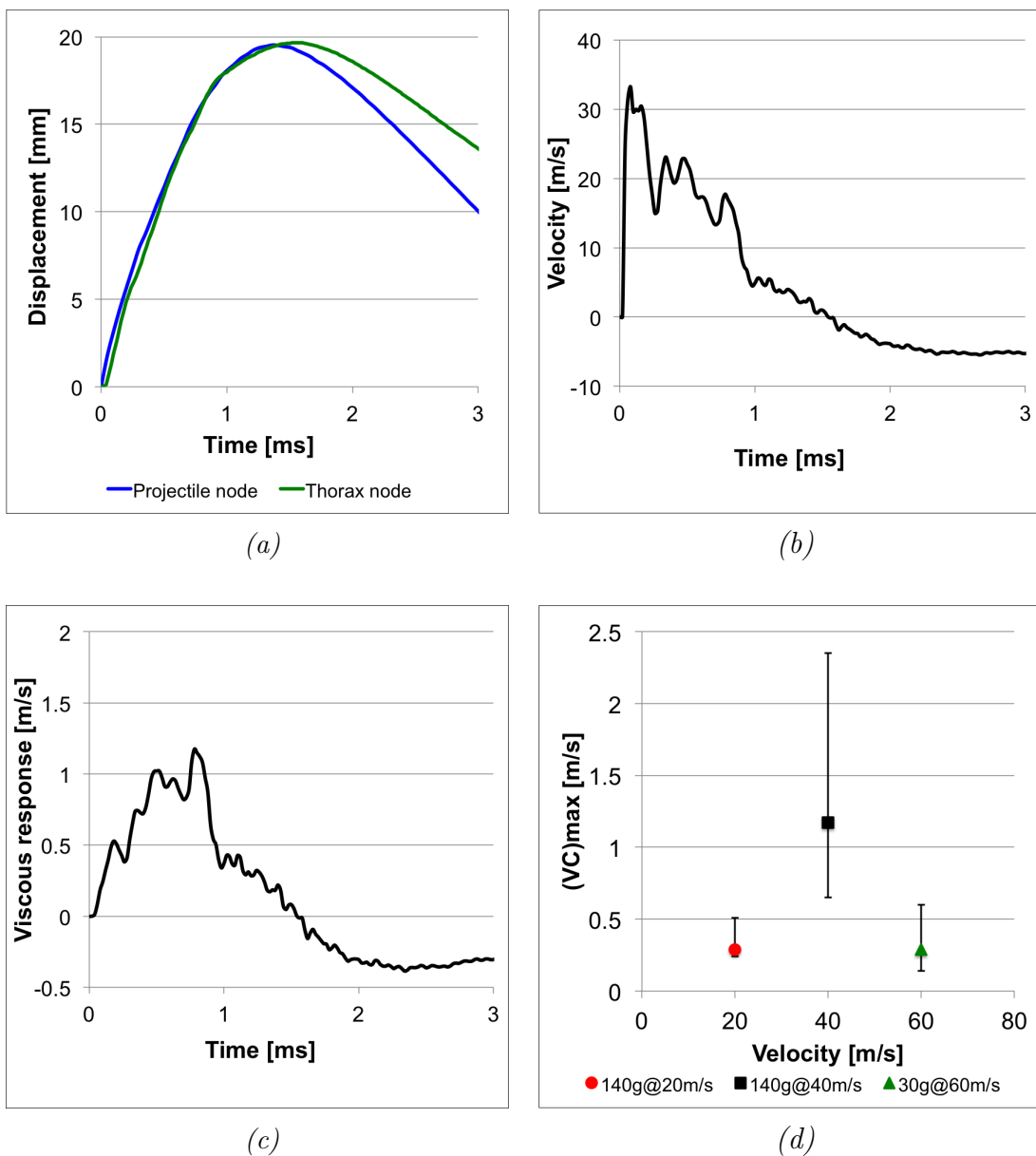


Figure 5.7. Thorax responses for an impact velocity of 40 m/s

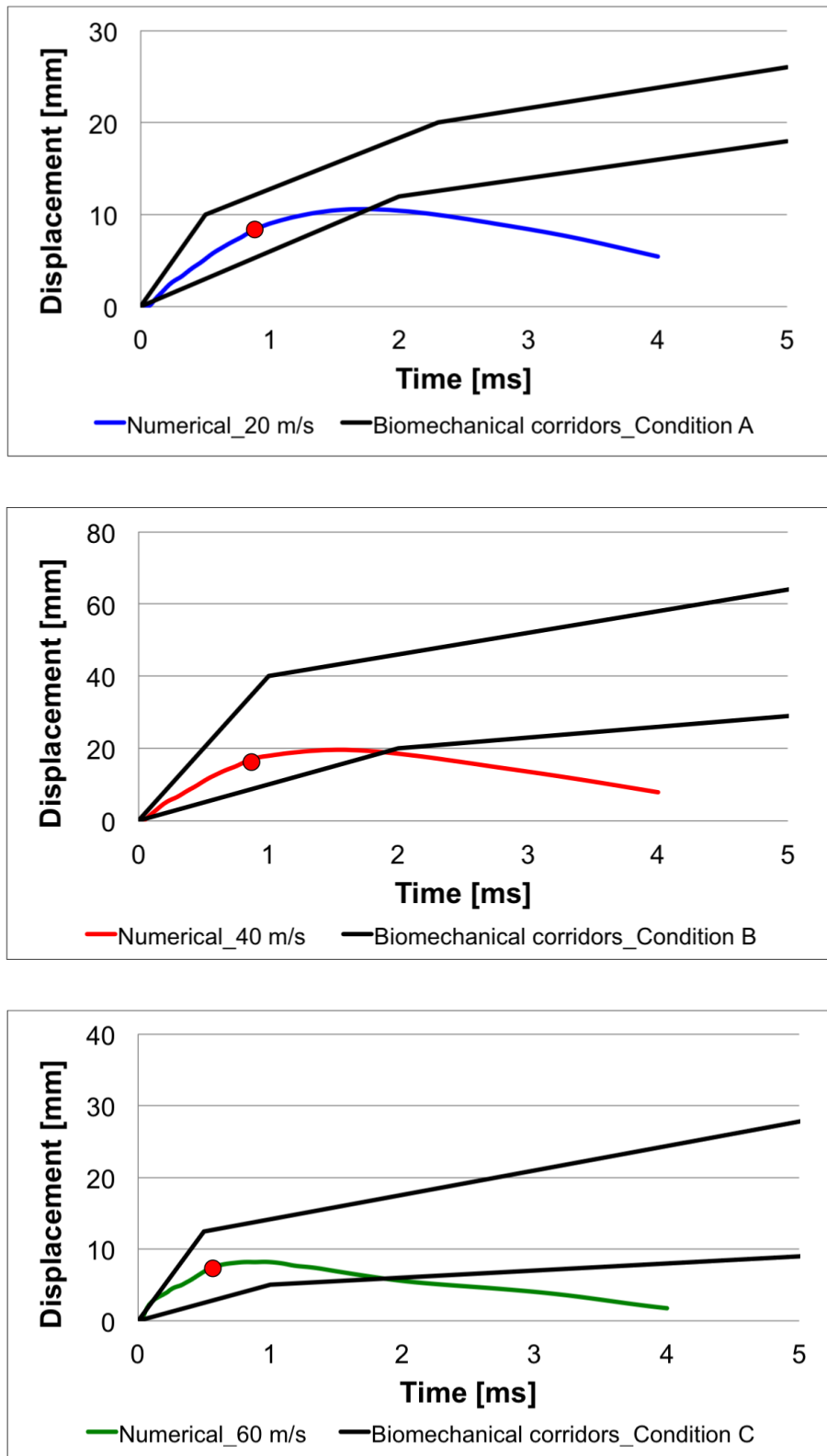


Figure 5.8. Comparison of numerical results with biomechanical data for different impact velocities. The red spot corresponds to $(VC)_{max}$

5.1 Development of the thorax FE model

Impact condition	Projectile mass [g]	Velocity [m/s]	$(VC)_{max}$ [m/s]		$(\text{Time})_{(VC)_{max}}$ [ms]
			Numerical	Biomechanical limits	
A	140	20	0.29	[0.24-0.51]	0.80
B	140	40	1.17	[0.65-2.35]	0.78
C	30	60	0.29	[0.14-0.60]	0.44

Table 5.3. Comparison of numerical results (Injury criterion $(VC)_{max}$).

5.1.4.4 Discussions

The fact that the curves do not lie entirely within the biomechanical corridors after about 2 ms shows that the model has somewhat a stiffer response (Figure 5.8). This shows that the whole behaviour of the thorax dynamics is not correctly captured as the simulated phenomenon is too fast. Therefore work has to be done to improve the compliance of the model. Nevertheless the observation window is sufficient for the determination of the injury criterion. In fact, it can be shown that the $(VC)_{max}$ is reached early at the beginning of the impact, in the zone where the response is entirely within the corridors. This can be seen in Figure 5.3 where the red spots correspond to the point of $(VC)_{max}$. Therefore regarding the $(VC)_{max}$, the model has been validated. It is worth to point out that $(VC)_{max}$ is achieved before the maximum deformation is reached. What about the difference between a PMHS and a human living? On the one side, the PMHS used for the determination of biomechanical corridors are old people and it is a well known fact that the human body properties change with age and material property changes in the biological structures decreases the thoracic injury tolerance [162–164]. On the other side, for the PMHS, as all the physiological functions are irremediably off, the body undergoes the rigor mortis process. This means that using the $(VC)_{max}$ value of 0.8 m/s determined from PMHS is conservative.

The only injuries that were investigated are the rib and sternal fractures in Bir's experiments. In general, rib fractures are a good indicator of the severity of an impact to the thorax as the protection to the internal organs such as the lungs and the heart is greatly reduced with the increasing number of fractured ribs [165]. Once the model validated, other criteria can be investigated.

Only one source of data for validation may not be enough giving the limited number of PMHS from which data for validation come from and the great variability among people, but for now they are the only data available in open literature. As soon as new PMHS data are available, the model can be checked and eventually tuned with new biomechanical corridors.

5.1.5 Conclusions

The SHTIM model has been described and modelled. The L5 projectiles which served as the benchmark projectiles in Bir's experiments in Bir's experiments were modelled. The impact of L5 projectiles on the SHTIM have been performed. Displacement curves were used for validation. Comparison between the experimental data and the numerical ones has been done. Although many assumptions were made concerning the thorax geometry and the material models, good results have been achieved and the thorax model has been validated. All the numerical responses fall within the biomechanical corridors. The SHTIM is therefore validated. In the next chapter, KENLW projectile FE model will be developed and validated.

Chapter 6

KENL projectile models

6.1 KENL projectile FE modelisation

In the previous chapter, the thorax model was validated. In this chapter the FE models of different KENL projectiles are validated. To validate the models, numerical results are compared to experimental ones. The general procedure of validating a projectile is described in Figure 6.1. To build the projectile FE model, projectile

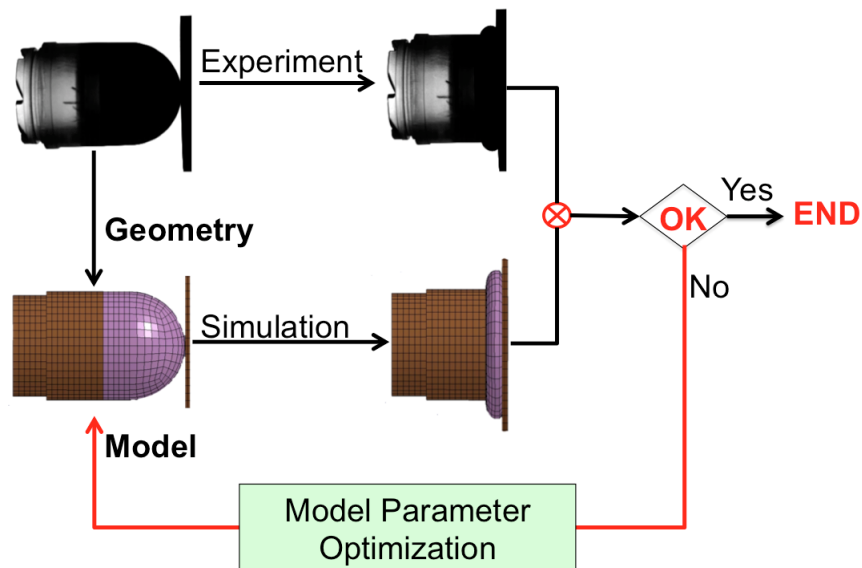


Figure 6.1. Validation of non-lethal projectile model.

geometry and material models should be obtained. The geometry of the projectile is relatively easy to obtain compared to the thorax geometry. Therefore the challenging problem is the material modelling.

As there are different types of materials from which non-lethal projectiles are made, they also behave differently under loadings, hence the need to characterise each material. Moreover, an impact event being a dynamic phenomenon, it is then necessary to dynamically characterise the projectile materials in order to obtain valid results. But there are some issues that have to be considered:

- Most of the times, only static material characteristics are available and sometimes, they are not sufficient to obtain valid results. Impact conditions imply loading rates which are outside of the range of quasi-static tests, resulting in behaviour that can then be very different [166–169]. Thus constitutive models, which take into account the dynamic behaviour of the projectile should be used. They should be able to predict the material response under operational loading conditions.
- The dynamic characterisation of such material¹ requires specific testing facilities as the time scale of such phenomenon is very short and highly nonlinear phenomena are involved. There are a few standard tests like the Hopkinson Pressure Bars, but they require specimen with well-defined geometries and loading rate conditions similar to the ones found in the real applications.
- The projectile manufacturer never, to best knowledge of the author, delivers (dynamic) characteristics of the projectile materials in the considered dynamic range, nor the corresponding material blocks from which classic specimens could be cut for material characterisation purpose.

The method that was applied is to find the material characteristics of the projectile in the literature and by iteration process within a certain range to obtain the best suited material characteristics (Figure 6.1) for the validation of the FE projectile model. That is the procedure that has been used for the KENL projectiles like the FN303 projectile, the 37 mm L5 projectile and the RB1FS in the present thesis. But for specific projectiles like the 40 mm sponge grenades, made of a stiff or "rigid" body and a deformable nose, a new method has been investigated. The principle of this method is:

- To use the results of real direct projectile firings against a Rigid Wall (RW) structure which is a supposedly infinitely rigid target equipped with a force sensor.
- Then to numerically simulate the impact and by following the same procedure described on Figure 6.1.

¹It consists in characterizing the high strain rate response of materials (up to $4.10^3 s^{-1}$ In our applications, the strain rate)

- one can finally determine the projectile material parameters by matching the experimental and the numerical results until convergence (dynamic characterisation). The specificity of the method is that one obtains the characterisation of the projectile nose material characteristics and at the same time the validation of the projectile. This is cost-effective as no characterisation tests is needed and the results if the real firing tests are directly used for both purposes, the projectile material characterisation and the projectile validation. The method is not appropriate for the stiff projectiles like the L5 projectile because at high velocity they can break and for heavy mass projectiles, RW structure force sensor can be damaged. Likewise the method is not appropriate for the frangible projectile (FN303) as it breaks at impact into debris without significant deformation. Moreover, modelling the rupture mechanism is complicated.

In the present chapter, KENLW projectiles are characterised. Firstly, the RW structure which is the setup used for the projectile characterization is described. Secondly, a new method of characterising the 40 mm sponge grenades is exposed. Thirdly, the new method is applied to two projectiles: SIR-X and CONDOR projectiles. Finally, characterization of other types of projectiles is performed by using parameters found in the literature.

6.1.1 Rigid Wall setup

The RW setup is used in order to obtain projectile firing data for validation and characterisation purposes. The RW experimental setup is shown in Figure 6.2. The main components are:

1. A pneumatic launcher for launching the projectile at desired velocity.
2. A light screen barrier for the impact velocity measurement.
3. A set of led lights for the high-speed camera.
4. A high-speed camera for impact events recordings. A great amount of information can be obtained through the processing of the impact videos as the projectile velocity measurement, projectile displacement tracking and projectile attitude before, during and after the impact, the rebound velocity...
5. The impacting projectile.
6. A RW structure equipped with a force sensor for the force measurement.

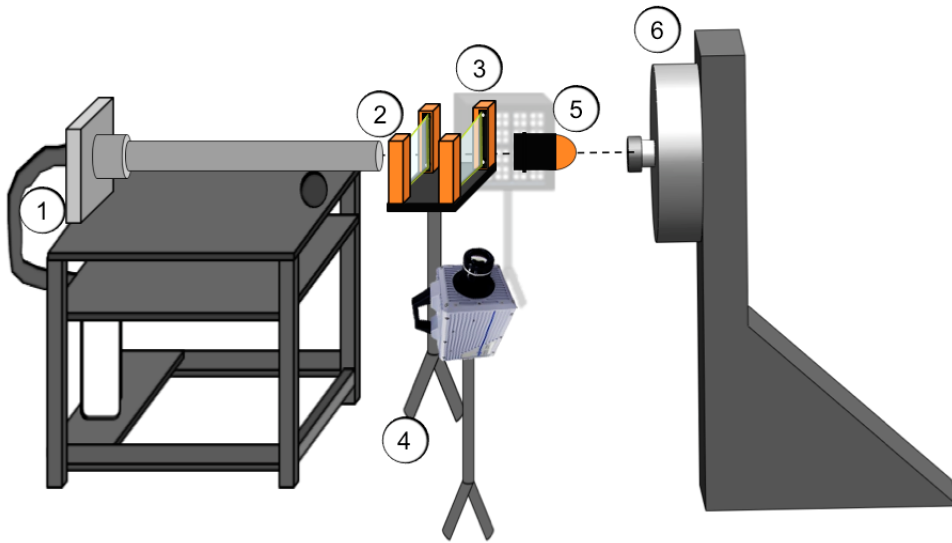


Figure 6.2. *RW setup [2, 3].*

The main physical quantities that can be measured or determined are:

- The force $F(t)$ applied on the wall as a function of time,
- The impact velocity and the rebound velocity (from high speed camera images),
- The time-evolution of the projectile length $L(t)$ (projectile displacement) during the impact corresponding to the crushing process and release of the projectile (from high speed camera images),
- The time-evolution of the impact surface contact diameter $D(t)$ between the projectile and the RW projectile length during the impact (from high speed camera images).

These quantities allow to capture the dynamics of the impact and are the most important dynamic variables that will be used for the projectile characterization. In order to process the high speed camera images, an in-house tracking software has been used, so dynamic measurements of non-lethal projectile impacts can be performed [2].

In theory, the RW is supposed infinitely rigid but in practice, it is not the case, therefore the structure will vibrate during impact. As exposed in [3, 170], measurements can be affected by mechanical resonance of the RW. This noise will affect the entire measured signal even if it is particularly visible after the impact as shown in Figure 6.3. Therefore a RW wall dedicated filter (FRF-Frequency Response Function) was developed to mitigate the resonance frequencies. Alternatively, CFC

(Channel-Frequency-Class) filter defined in [3] with a cut-off 9000 Hz can be used. Normally, the resonance frequencies are not present in the numerical simulations of the projectile impacts on RW, but to have the same comparison reference, both experimental and numerical signals are filtered with the CFC filter.

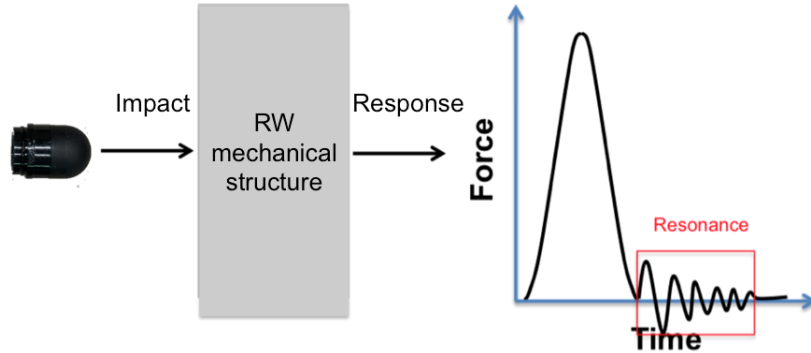


Figure 6.3. *Resonance of excited RW structure; Adapted from [3].*

In the following section, the method for dynamically characterising the 40 mm sponge grenade projectiles is presented.

6.1.2 Dynamic characterisation method for sponge grenades

This method is based on a tabulated law where the stress-strain curves derived from the projectile real firings on a RW structure are directly used as input in the material model. As it will be explained in this section, the difference with conventional testings is due to the fact that the material characteristics of the projectile deformable nose is directly obtained from the real firing tests instead of characterising this material from a small well tailored specimen using conventional testings. To the best knowledge of the author, there is no report in the literature of such a method for characterising non-lethal projectiles.

There is a similitude between the two testings. Indeed, the 40 mm sponge grenades are made of a stiff plastic body (sabot) and a deformable nose in foam or rubber-like material. The sabot (the body part), the heaviest part of the projectile is important as it allows the full straining of the deformable nose such as the nose energy absorbing capacity is used and the projectile still have enough energy to transmit to the target. In that sense, it can be compared in a certain way to the moving crosshead in conventional compression tests. Nevertheless, the conditions required for conventional testings are not met with this method.

The rubber or foam materials characteristics under loadings are generally described by the typical curve given on Figure 6.4 [171]. Both material types (foam

and rubber) are used in many applications because of their high energy absorbing capabilities. They are designed in a way that a substantial part of the initial energy is absorbed or dissipated by the projectile nose itself reducing the energy transferred to the target and the risk of causing severe injury during impact. Thus the projectile can be fired at higher velocity and longer distances of engagement can be achieved. To have valid measurements, few assumptions are made.

6.1.2.1 Assumptions

- Necessity for each curve to have a densification zone as in the velocity range, the projectile nose is generally fully strained.
- Normal impact (yaw angle $\leq 5^\circ$). The normal impact is the worst case as it was shown in [160, 161]
- The two parts remained fastened during impact or at least during the loading phase as the mechanism of separation between the two parts is difficult to master;
- No plastic deformation or breaking of the sabot , no rupture or tearing of the deformable part during impact: the breaking of the sabot and the tearing of the nose are not expected during the impact on the thorax. Moreover, they are difficult to master.

6.1.2.2 Methodology

In order to determine the (dynamic) compressive $\sigma - \epsilon$ response curves used as direct inputs in a tabulated law, compressive or tensile tests of well tailored specimen with specific geometric characteristics are performed by following standard procedures [166, 169]. The purpose is to reduce errors due to many factors such as the shape effects, the inhomogeneity of deformation... Therefore certain requirements are to be met like a uniform straining of the specimen or achieving constant strain rate [166–168]. The approach we use in this study is far from meeting the requirements of conventional testing procedures.

The main difference between conventional tests and this new approach comes from the fact that we are not characterising a cylindrical specimen out of which the material response is obtained. Instead, we are characterising the non-lethal projectile as a whole structural part by finding a model suitable for the deformable part as the sabot is considered as "rigid".

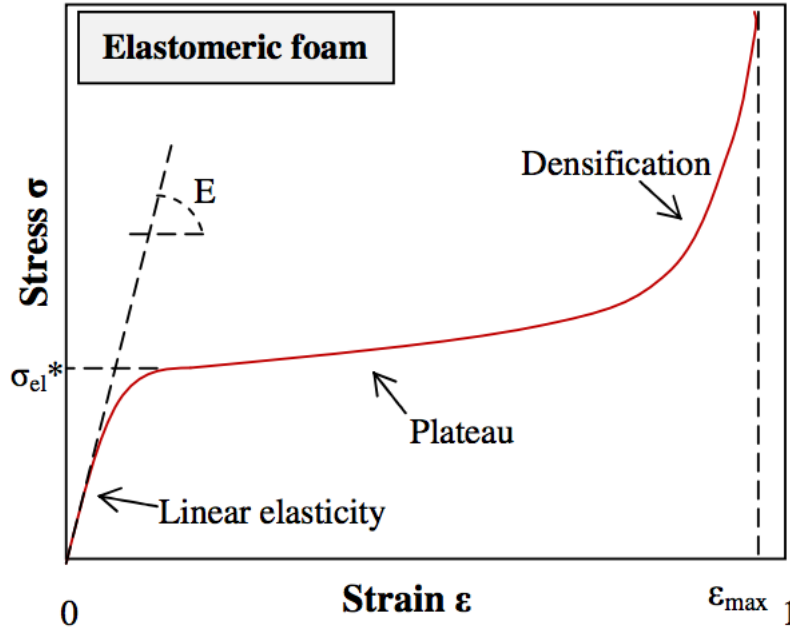


Figure 6.4. Schematic compressive stress-strain response for elastomeric foams [4].

In fact, during the impact against the RW, the projectile nose undergoes large deformation and is squeezed between the RW and the sabot which act as a constraint. The impact can then be considered as a classical compression test although all the conditions of a classical compression test are not met. The nose drives the shape of the force-time profiles by acting as an energy absorber that limits the impact force. This means that only the nose part is considered for the characterisation process as for the sabot, a simple elastic model is used. After choosing the appropriate nose material model, the effort is focused on adapting the parameters until acceptable correspondence between the numerical and the experimental results is achieved. The mode of loading being predominantly compressive, only *the loading parts* of the curves will be used as input in the material model. The unloading part of the experimental curves is not used due to the post impact oscillations. Therefore the unloading is managed in LS-DYNA through the user-defined unloading parameters in the material model [149].

The variables that are used for matching the numerical and experimental results in order to characterise the impact phenomenon are the same as the measured variables in experiments and are described in Figure 6.5.

- $\vec{F}(t)$, the impact force as a function of time
- $L(t)$, the axial displacement corresponding to the variation of projectile length (compression and relaxation) in the impact direction, as a function of time,

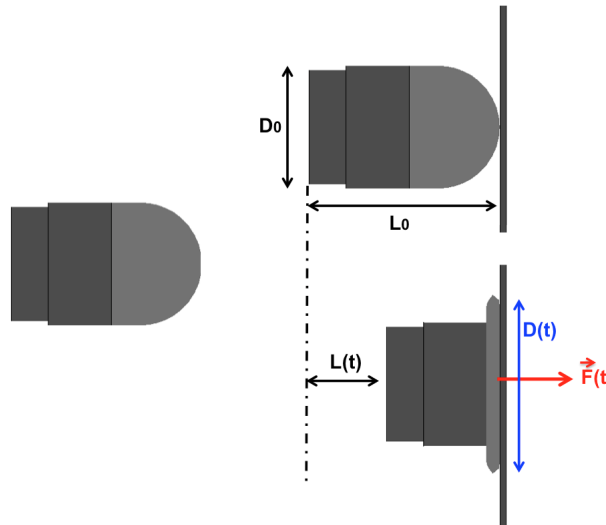


Figure 6.5. *Projectile impact dynamics characteristics.*

L_0 is the initial length of the projectile. The sabot being considered as 'rigid', $L(t)$ is obtained by tracking the back of the sabot.

- $D(t)$, the evolution of the impact surface diameter as a function of time. It is a secondary variable that can also be used for comparison. D_0 is the nominal diameter of the projectile. The effort of characterization is most directed towards what is going on in the impact direction.

In order to derive the stress-strain curves of the nose material, programs developed in LabVIEW environment are used. The main steps are given schematically in Figure 6.6:

1. From impact videos, projectile displacement curves as a function of time are generated by using an in-house tracking software [2, 172].
2. From the force sensor signals, curves of the impact force as a function of time are generated.
3. The force signals are afterwards filtered to remove the undesired frequency contents due to the resonance of the rigid wall structure [3, 170].
4. As the force and the displacement curves are obtained from two different measurement systems, they should be synchronised.
5. The engineering stress-strain curves at different strain rates are the loading curves in the (hyperelastic) material model. They are generated from the force-displacement curves and the projectile characteristics.

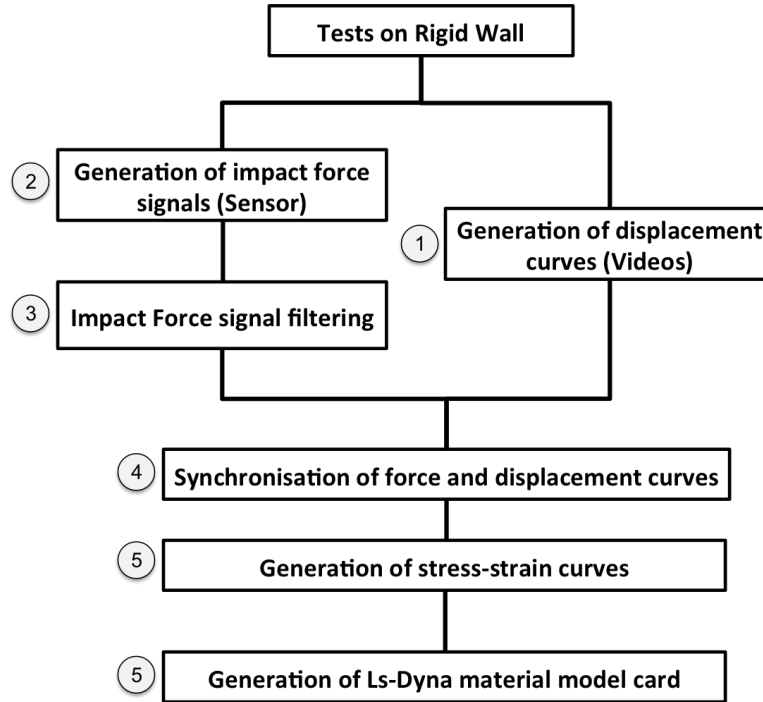


Figure 6.6. Main steps for non-lethal characterisation method.

It has to be noted that

- As the engineering stress-strain curves are used, the initial length of the projectile nose is defined as the reference length for the strain calculation. Due to the hemispherical shape of the nose, the projectile nominal diameter is chosen as the reference diameter for the stress calculation.
- The definition of the tabulated law in Ls-Dyna models requires *smooth, monotonic and non-overlapping*² stress-strain data [147]. Strategies like smoothing, fitting methods,... can be used to remedy to the problem [147, 173].
- To validate the projectile numerical model, one can use for each strain rate, an experimental reference curve³ or experimental corridors built from experimental response data [147, 173]. All the calculation are done in one dimension. The nominal strain rate is approximated by

$$\dot{\epsilon} = \frac{V_{impact}}{L_{nose}} \quad (6.1)$$

where V_{impact} is the projectile impact velocity. L_{nose} is the projectile initial nose length

²Stress increases when strain rate increases.

³The reference curve is obtained by averaging the experimental curves at a given strain rate or by choosing one curve if only few results are available.

In one dimension, the nominal engineering stress and the nominal engineering strain are given by

$$\sigma_{eng} = \frac{F}{S_0} \quad (6.2)$$

$$\varepsilon_{eng} = \frac{\Delta L}{L_{nose}} \quad (6.3)$$

where $S_0 = \frac{\pi D_0^2}{4}$, D_0 is the nominal diameter of the projectile nose, F_{impact} the impact force and ΔL the change in length of the nose. As the projectile is assumed rigid, ΔL corresponds to $L(t)$ (Figure 6.5).

6.1.2.3 Practical aspects of the non-lethal projectile characterisation method

In practice,

- One should perform shots on the RW at different velocities. A minimum of three experimental impact velocities will be enough in order to derive the corresponding stress-strain curves with in mind, the idea to cover the entire operational range. This is a compromise between the resources to be devoted and getting statistically relevant data. As a rule of thumb, the projectile has to be launched at nominal velocity, at two-third and finally at one-third of the nominal velocity. For each velocity, the reproducibility of each curve was checked by performing three shots under the same conditions.
- Filter all impact force signals using the CFC filter with a cut-off frequency of 9000 Hz.
- Most of the projectile noses are made of rubber(like) or foam material and for such type of materials, hyperelastic or viscohyperelastic models are best suited [144, 148, 174]. Depending of the value of the Poisson's ratio, a different (visco)hyperelastic is used ⁴ [145].

In the two following sections, the method is applied to the SIR-X projectile as well as to the CONDOR projectile.

⁴If the Poisson effect is negligible, MAT_FUNG_CHANG model is used otherwise SIMPLIFIED_RUBBER_MAT mat is used.

6.1.3 SIR-X projectile FE model

The description of the SIR-X projectile is given in 2.4.2.3. The RW setup used for the projectile characterisation is given at Figure 6.2. The methodology that is followed through the validation procedure is described in section 6.1.2.2 summarised in Figure 6.1 and Figure 6.6. There are one reason for which the SIR-X projectile is chosen for applying the new method: The SIR-X projectile is the projectile that has been chosen in the NATO standardisation framework by NLKE ToE group as one of the projectiles for the validation of the thorax surrogates [5]. More details are given in section ???. Moreover, it is a sponge grande which corresponds to the category of projectiles to which the method can be applied.

It is then used to explain in details the application of the new characterisation method of deformable projectiles. For the other deformable projectiles, only results of validation will be given as the procedure is the same and the same conclusions can be drawn. To cover the entire domain of application as previously stated (section 6.1.2.3), the projectile is shot against RW at three different velocities. The three impact velocities are: 30 m/s, 58 m/s and 81 m/s. The two last velocities are the velocities where $(VC)_{max}=0.4$ m/s and $(VC)_{max}=0.8$ m/s are expected respectively. Validation is made by matching experimental and numerical results. All the experiments were performed by my NLW teammates Dr. Cyril Robbe and Dr. Amar Oukara [2, 3]. The force-time results are filtered using a CFC filter with a cut-off frequency of 9000 Hz [3]. The impact dynamics (Figure 6.5) is characterized by

- $F(t)$, the impact force as a function of time.
- $L(t)$, the axial displacement as a function of time.
- $D(t)$, the impact diameter as a function of time.

In the following sections, experimental results are exposed. Geometrical and material characteristics are described. Experimental data are processed to generate the compressive engineering stress-strain curves which are inputs of loading curves used in the material model of the nose. The model is validated followed by discussions of the results. Finally, conclusions are drawn.

6.1.3.1 Experimental results

The projectile force-time signals and the projectile displacement-time curves are generated from the sensor and the impact videos respectively. Experimental results are presented in Figure 6.20 for the three impact velocities. The focus will be mainly on the loading phase. A first general observation shows that:

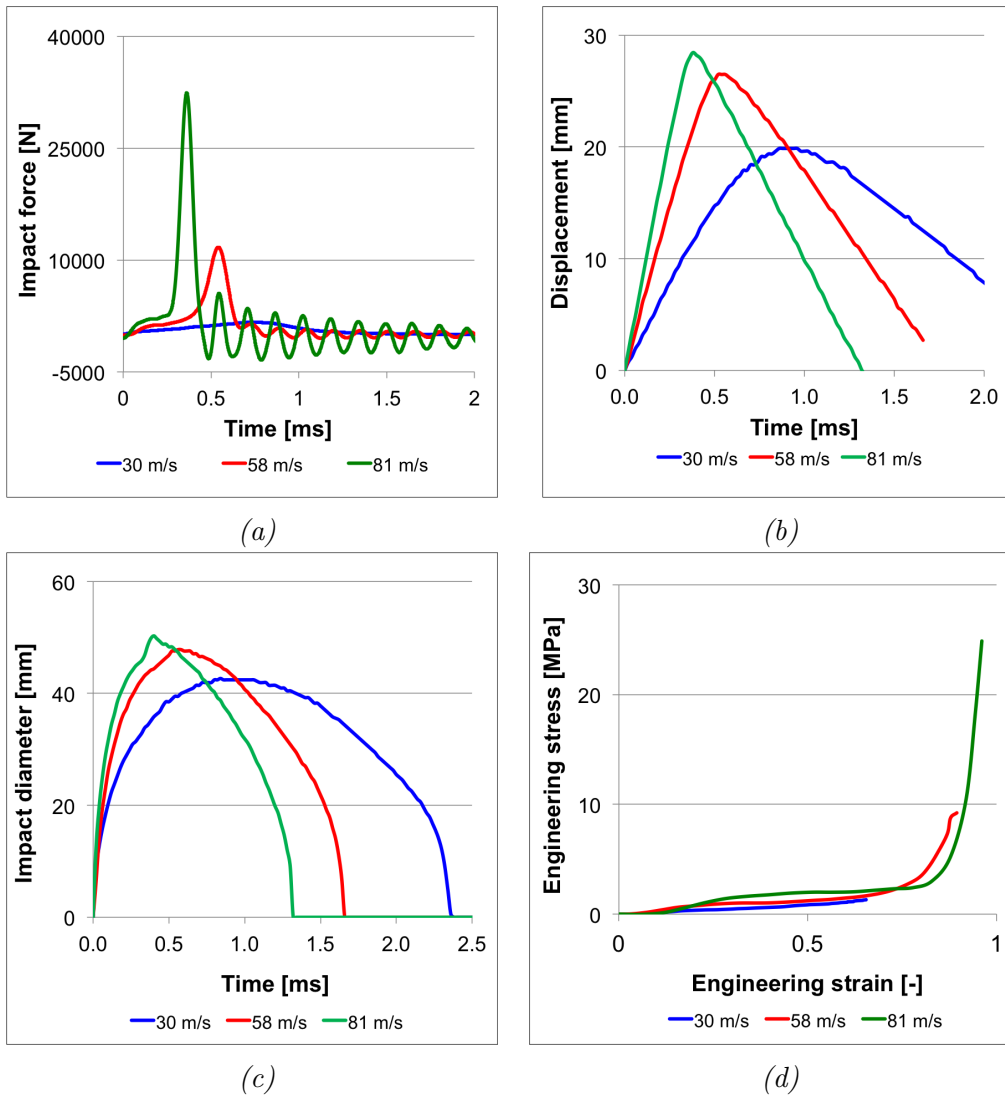


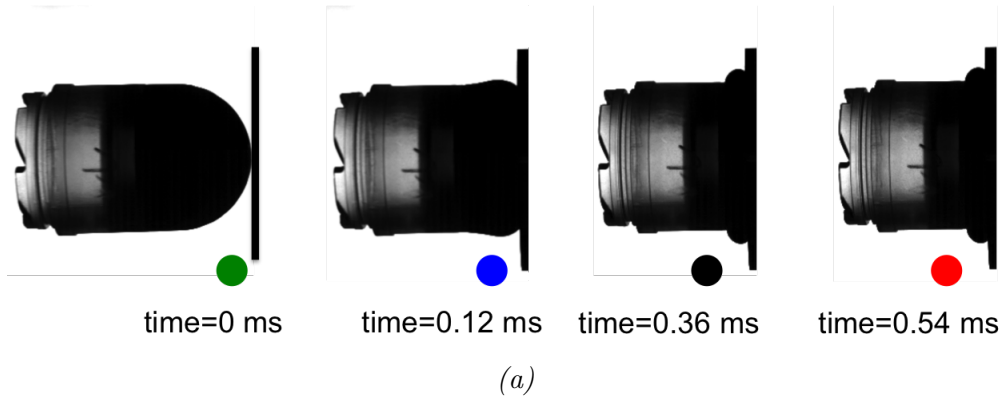
Figure 6.7. *Experimental results of the the impact of the SIR-X projectile on RW at different impact velocities.*

- There are still residual post-oscillations due to the resonance of the RW even though the CFC filter has been applied on the force signals (Figure 6.7(a)).
- When the velocity increases, the maximum of force, displacement and diameter increase and shift to the left (velocity effect) as can be seen in Figure 6.7(a)-(c).
- The displacement curve can be divided into three parts: a linear part during the loading, a linear part during unloading and a transition phase between the two (Figure 6.7(b)).
- The phenomenon seems to show a strain rate dependence (Figure 6.7(d)). But other reasons can also explain this behaviour like the dispersion on mea-

surements. Only the loading phase is considered (phase up to the maximum amplitude).

- The maximum surface impact diameters are larger than the nominal diameter which correspond also to the projectile nominal diameter. As the impact diameter increases during the impact, this means that force could be spread on a larger surface. It has an effect on the impact duration and the maximum force. On the other side, because of diameter variation, the Poisson's effect of the nose is not negligible.

But there are more interesting features that can be highlighted. For that purpose, instead of overloading the graphs in Figure 6.7, results at 58 m/s are considered knowing that the same features are also observed for other velocities. Results are shown in Figure 6.8. In Figure 6.8(a), are represented snapshots of the impact



loading sequences at specific times. These times are chosen by comparing Figure 6.4 to the loading curve of Figure 6.8(e). The corresponding times (coloured dots) are reported in the different graphs. At time 0.12 ms, the nose is no longer hemispherical due to its straining but becomes more or less cylindrical (linear regime). Time 0.36 ms is chosen as the time of the onset of the densification zone (end of the plateau regime). The time 0.54 ms is the end of densification regime as well as the end of the loading phase. Describing those three regimes, each graph will highlight some features.

- A first zone at the beginning of the impact event, with a relatively slight increase of the force. Only the nose tip is deformed, corresponding to a deformation of about 20% (Impact sequence in Figure 6.8(a) corresponding to the blue dot in Figure 6.8(e)).
- A second zone where the force continues to increase in a gradual way. Referring to Figure 6.8(e), the deformation and the gradient of deformation continue to

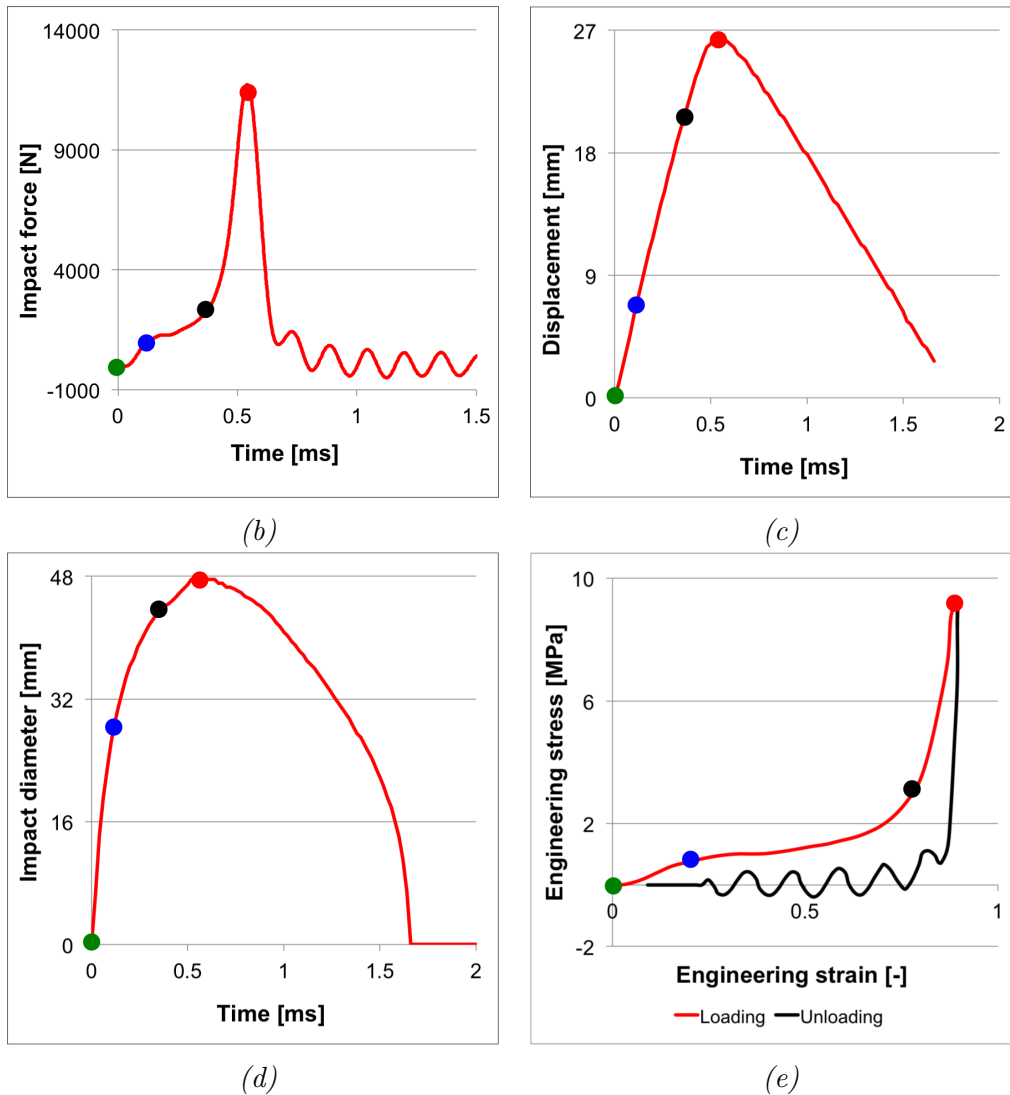


Figure 6.8. Impact sequences - main features.

increase but in a moderate way. This corresponds to the compaction of the nose. The nose plays here a major role by its energy absorbing capacity (area under the curve between the blue and the black dots).

- A third zone corresponding to a drastic rise of the amplitude to its maximum and a reduced absorbing capacity of nose. It corresponds to the full crushing process of the nose. (area between black and red dots in Figure 6.8(e)). The projectile behaves almost like a rigid projectile.
- Finally the zone after the maximum amplitude.
- The three first zones are related to the loading phase and the last one to the unloading.

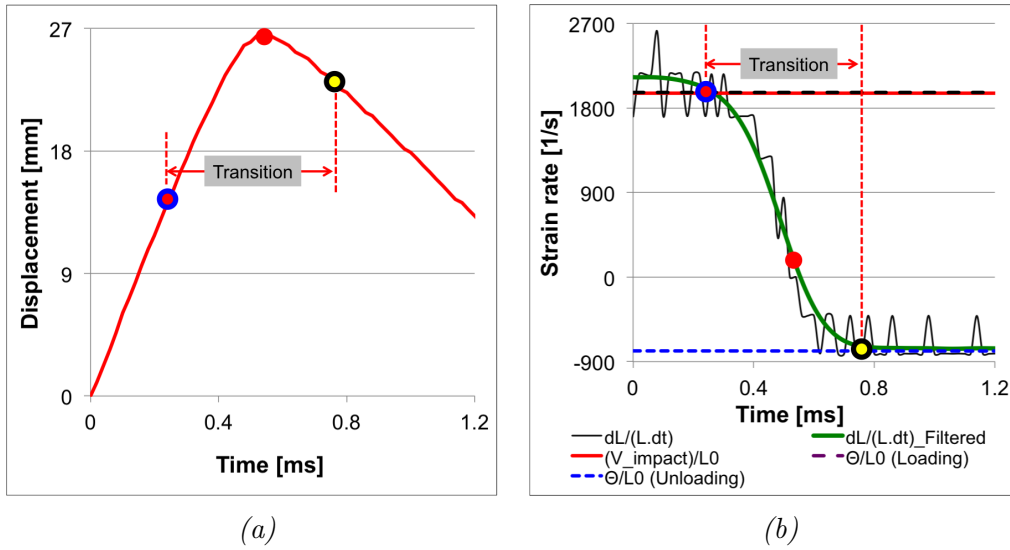
The graph of displacement as function of time (corresponding to the tracking of a rear side of the sabot) shows that

- The displacement curve can be divided in three parts: two parts where the displacement curve is linear during one part of the loading or unloading phase, and a third part corresponding to a transition zone where the displacement is no more linear (Figure 6.9 (a)). For each linear part, the slope Θ_i corresponds to a velocity V_i , either the impact velocity or the rebound velocity depending of the part considered (Equation 6.4). This gives a way to determine those velocities from the displacement curve. By dividing by the initial length L_0 of the nose, one can determine the global engineering strain rate by using the slope or the initial impact velocity. (Table 6.1).

$$V_i = \Theta_i = \left(\frac{\Delta L}{\Delta t} \right)_i \quad (6.4)$$

where i represents the linear part of the displacement curve considered.

By this equation, one recovers the experimental impact velocity as well as the experimental rebound velocity (Table 6.1).



Knowing L_0 , the initial length of the nose, the global engineering strain rate is determined by Equation 6.5 or by Equation 6.6 for each linear part (Figure 6.9 and Table 6.1).

$$\dot{\epsilon}_i = \frac{\Theta_i}{L_0} \quad (6.5)$$

$$\dot{\epsilon}_i = \frac{V_i}{L_0} \quad (6.6)$$

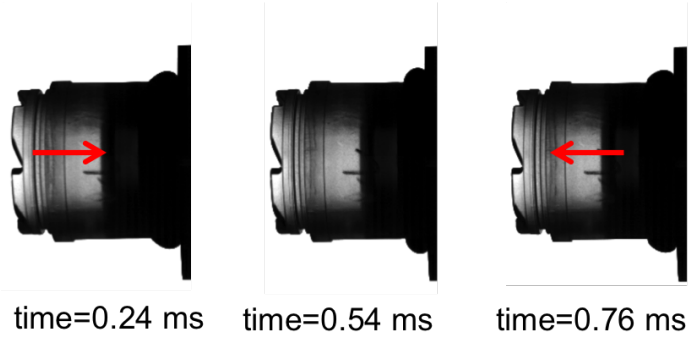


Figure 6.9. Impact sequences - Variation^(c) of strain rate during the impact event at 58 m/s.

where V_i is V_{impact} , the impact velocity or $V_{rebound}$ for the unloading phase. There is a good agreement between the experimental and the computed loading strain rate values (Table 6.1). Figure 6.9(c) shows three snapshots at specific times during the loading, the transition and the unloading phases respectively.

Impact velocity [m/s]	Rebound velocity [m/s]	Strain rate [1/s] computed via			
		$\frac{V_{impact}}{L_0}$	$\frac{\Theta}{L_0}$ (Loading)	$\frac{V_{rebound}}{L_0}$	$\frac{\Theta}{L_0}$ (Unloading)
30	-13	1014	1047	427	439
58	-23	1959	1967	719	787
81	-32	2736	2736	1052	1077

Table 6.1. Rebound velocity and strain rate calculation.

If $L(t)$ is the current nose length at time t , the local true strain rate is expressed by

$$\dot{\epsilon} = \frac{1}{L} \frac{dL}{dt} \quad (6.7)$$

where $\frac{dL}{dt}$ is the local slope of the displacement

The strain rates computed with different equations 6.1-6.4 and Equation 6.7 are represented in Figure 6.9(b). Global strain rates during each phase is constant except for the transition zone and varies as expected with the velocity. The local strain rate curve and the corresponding filtered one are also represented in Figure 6.9(b). There is a good agreement between the experimental and the computed loading strain rate values (Figure 6.9(b)).

Three zones can be considered as for the displacement. The coloured dots on Figure 6.9(b) are the specific marks which delimit the three zones and the

corresponding screenshots of the impact sequences. The first zone corresponds to the time slot where the projectile sabot continues with the same velocity while the nose is already undergoing deformation. At the end of this time (blue centre dots), the projectile begins to decelerate when the wave of nose deformation reaches to the sabot. Then begins the second zone (transition zone) where the projectile is drastically decelerated till its velocity drops to zero (red dot) (full compaction of the nose material). Due to the elastic energy stored in the nose, the relaxation or unloading phase begins when the projectile begins to rebound. The average slope of this transition zone gives an idea on how fast the projectile is decelerating. The end of the zone corresponds to the time when the projectile sabot has a constant velocity.

- The phenomenon is dissipative as the loading path is different from the unloading one (Figure 6.8(e)). This can be seen also with Table 6.1 as the impact velocities are different from the rebound velocities.

6.1.3.2 Geometry and mesh

The geometrical and mesh characteristics are given in Figure 6.10. The projectile is modelled with hexahedral solid elements (Figure 6.10). A continuous mesh is used at the interface by merging the nodes of the two parts.

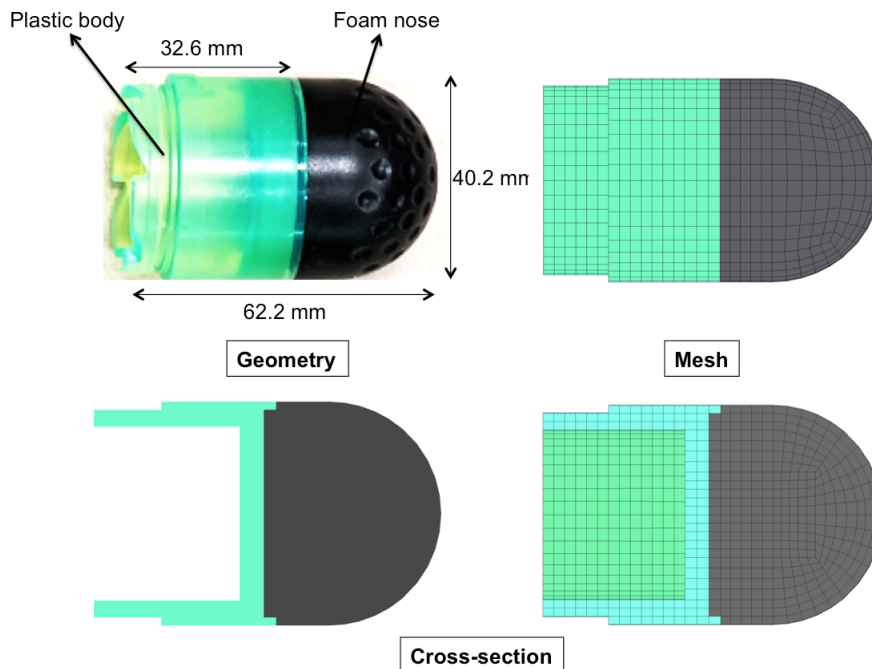


Figure 6.10. SIR-X projectile characteristics.

Before describing the material properties, data for the material model generation are processed.

6.1.3.3 Data preparation for material characterisation

The stress-strain data are derived from the force signal and displacement as function of time after synchronisation. The initial length and the initial diameter of the nose are used to define the engineering strains and the nominal cross section, the engineering stresses. Using the reverse engineering method, the projectile nose is characterised. The stress-strain data which describe the behaviour of the nose material, are used as input for the material model (Figure 6.8(e)). The parts of stress-strain curve of interest for the characterisation is the loading part.

Many features of the impact dynamics have been highlighted in the previous section. Referring back to (Figure 6.8(e)), during the loading phase, three main zones have been distinguished: a linear regime at the very beginning of the impact followed by a plateau which corresponds to the compression of the deformable part and finally a drastic increase of the stress corresponding to the densification zone where the projectile behaves almost like a rigid body. This type of behaviour is characteristics of foam materials (Figure 6.4). There might be a slight difference of this linear regime due to the hemispherical projectile nose compared to the classical testings where cylindrical samples are used.

There is a wide variety of foams with different behaviours depending on the application. Two main parameters drive the foam behaviour: the matrix material and the morphology of the gaseous phase. There are two generic morphologies: the open cell and the closed cell. The initial zone corresponds to the deformation of the matrix, the plateau to the phase where the gas exits from the open cell foams or is compressed in the closed cell ones and finally the densification zone where the cells are completely crushed (no more deformation) corresponding a steep stress increase [3, 175].

The stress-strain characteristics derived from experimental tests shown should be processed to be amenable for the simulation of the phenomenon. Figure 6.11 shows the stress-strain curves for different impact velocities of the SIR-X projectile. They seem to show moderate strain rate dependence. One can notice that there are curve overlapping at the beginning of the impact and at the beginning of the densification zone. These are critical zones and this kind of features is not desired as higher stresses are expected for results at higher strain strain rates. How to solve the problem? There is no efficient scientific approach now to solve this problem. Empirical method has been used by moving in an arbitrary way some points or

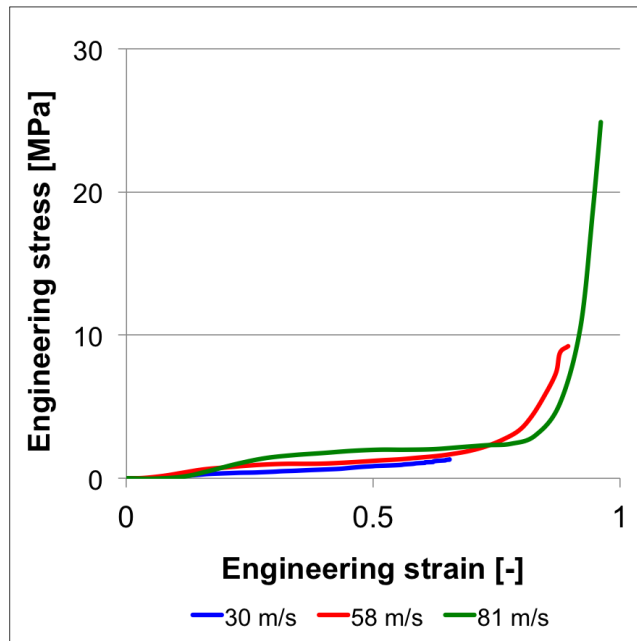


Figure 6.11. *Engineering strain-stress curves for impact velocities 30 m/s, 58 m/s and 81 m/s.*

extrapolating (if necessary) in the interested region in order to satisfy the criterion "increasing stress curves for increasing strain rates". One approach for simplicity that might be used is to approximate the curves by polylines [173] which make the process more tractable.

Causes of this curve overlapping can be multiple. One of them is the dispersion. Indeed, at the beginning of the impact, the forces are relatively low (small impact surface) and the sensibility to the impact angle can be high even though one could expect a normal impact. Therefore the dispersion can be high. This has an influence on the global result. If the sensibility to strain rate is not high, the risk of curve overlapping can also be great. In the densification zone, for high velocities, the probability of the occurrence of uncontrollable phenomena (partial separation of the sabot and the nose) is great and the related time occurrence is not known. Therefore the risk of overlapping curves in this zone can be high.

But in this case, some observations can be made.

- The curve at 30 m/s does not present a densification zone (section 6.1.2.1). The curve is also discarded.
- The strain corresponding to the maximum displacement at 81 m/s is close to 100% (Figure 6.11). This seems unrealistic unless other non mastered phenomena have occurred like the plastic deformation of the sabot. One can also notice that the impact diameter curve at 81 m/s is not smooth at its maxi-

imum. These features are not expected. For all these reasons, the curve at 81 m/s is discarded.

Therefore, only the curve at 58 m/s is used for the calibration of the model (Figure 6.12). After making the curve monotonic, it can directly be used in the material model as the load curve. This loading curve is used as the loading curve for an hyperelastic material, a model that is suited for modelling rubber and foam loading characteristics. As the phenomenon is dissipative, the impact velocity and the rebound velocity are not different, unloading should also be modelled ⁵. For the sabot, a linear elastic model is used.

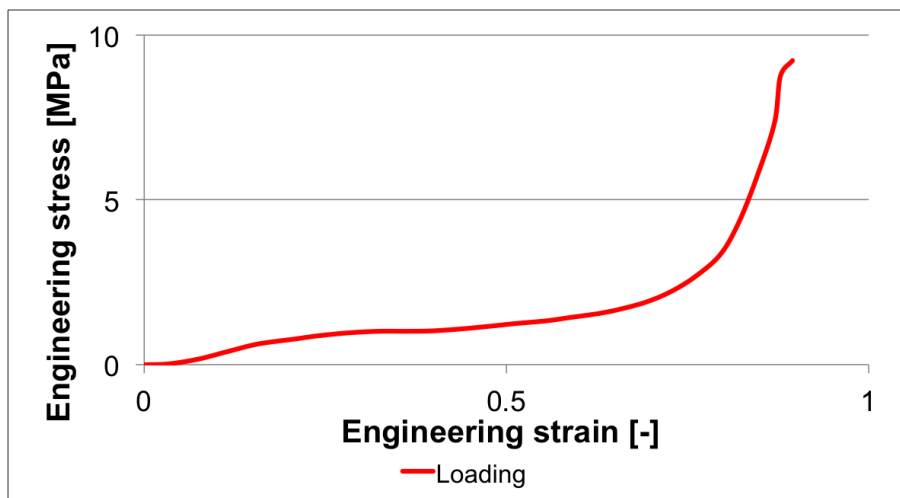


Figure 6.12. Compressive loading curve at 58 m/s.

6.1.3.4 Material characteristics

The SIR-X material characteristics are given in Table 6.2. A linear elastic model is assumed for the sabot and a visco-hyperelastic model for the nose. where the unloading material parameters HU and $SHAPE$ ⁶ are the hysteresis factor and the shape factor, LC is the loading curve. The loading curve ((Figure 6.12), derived from the impact results on RW at 58 m/s is not directly used as input loading curve in the material model for the reason explained below. Instead the curve in Figure 6.13 is used.

Indeed, during the calibration of the model, it has been found that using the original stress-strain data (baseline data) in Figure 6.12 leads to results that was

⁵In LS-DYNA, the choice is made to use the material model for rubber and foam `MAT_181: Simplified Rubber/Foam` which offer to the possibility of modelling the unloading via the parameters HU and $SHAPE$

⁶The parameters HU and $SHAPE$ are used to introduce dissipation in the model. If $HU=1$, there is no dissipation in the material model, and the model is elastic

Parts	Material parameters				Element type/ Number of elements
	Density [kg/mm^3]	Young modulus [Pa]	Poisson's ratio		
Sabot	1354	$2.3 \cdot 10^{10}$	0.387		Hexa/ 2032
Nose	231	Bulk modulus [Pa]	0.200		Hexa/ 4336
	HU 0.10	SHAPE 15	SFA 0.9	Loading curve LC	

Table 6.2. *Different properties of the SIR-X projectile.*

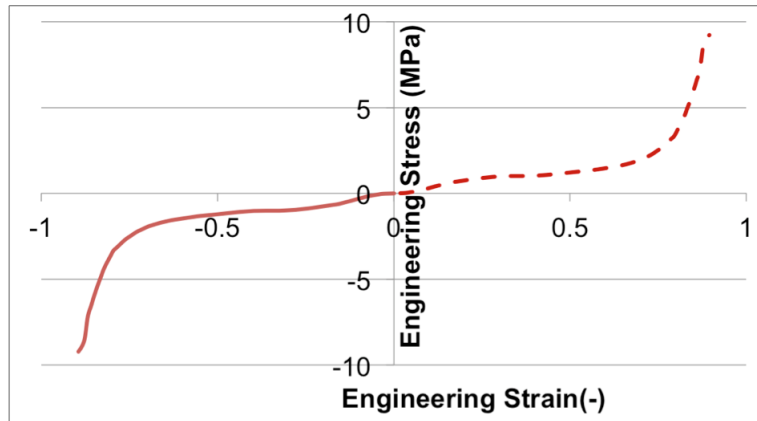


Figure 6.13. *SIR-X engineering stress-strain characteristics.*

not quite satisfying (Figure 6.14). A good correspondence was only achieved for the displacement. To improve the results, the idea was to extend the compressive data to the tensile range. As no tensile curve was available for this material, the baseline data was extended by mirroring effect with respect to the origin (Figure 6.13). The modified curve (modified baseline data) is thus used as input in material model card. Results of the comparison are given in Figure 6.14.

6.1.3.5 Validation

A parametric study of the nose model has been carried out to find the optimal model parameters (Table 6.2). Comparison between the experimental and the numerical results are given in Figures 6.15-6.16. Good correspondence is achieved for the force and displacement. Satisfying results are achieved for the impact diameter. Table 6.3 shows the comparison of rebound velocities with a good agreement between

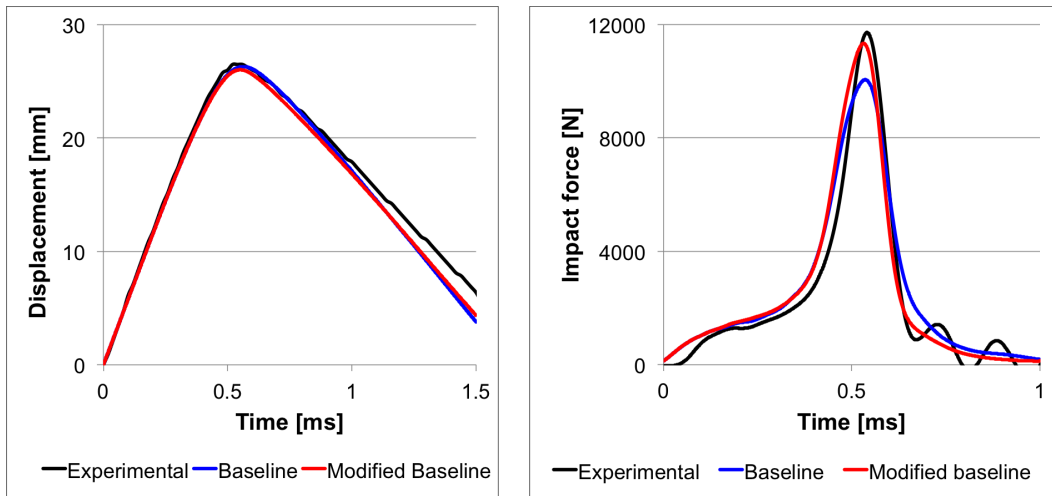


Figure 6.14. Comparison of numerical results for the baseline data and the modified baseline data taking into account tensile curve as loading curves at 58 m/s.

experimental and numerical results. One can conclude that the physics of the impact is correctly captured.

Impact velocity [m/s]	Rebound velocity [m/s]	
	Experimental	Numerical
30	-13	-13
58	-23	-24
81	-32	-35

Table 6.3. Comparison between experimental and numerical rebound velocities.

6.1.3.6 Discussions

As the sabot is considered as "rigid", it is the nose that mainly drives and shapes the macroscopic impact dynamic profile. Figure 6.17 shows the energy evolution. The nose kinetic energy curve shows three zones with different slopes during the loading corresponding to different energy absorption/dissipation rates of foam material nose (Figure 6.17(a)). By relating it to Figure 6.17(b), it is only after 0.20 ms that the front wave from the impact site due to the deformation of the nose will reach the sabot. Then the sabot will begin to decelerate. At this time, the nose has already absorbed/dissipated more than half of its energy (first zone). The rate of the energy loss is higher. After this time, the nose continues to deform with a lower rate of energy (second zone (plateau)). The sabot undergoes a high deceleration and the whole projectile progressively behaves like a non-deformable structure. The end of the second zone (black dot - time 0.36 ms) corresponds to an increase of energy rate of the nose which begins the third zone (densification) Almost all of the

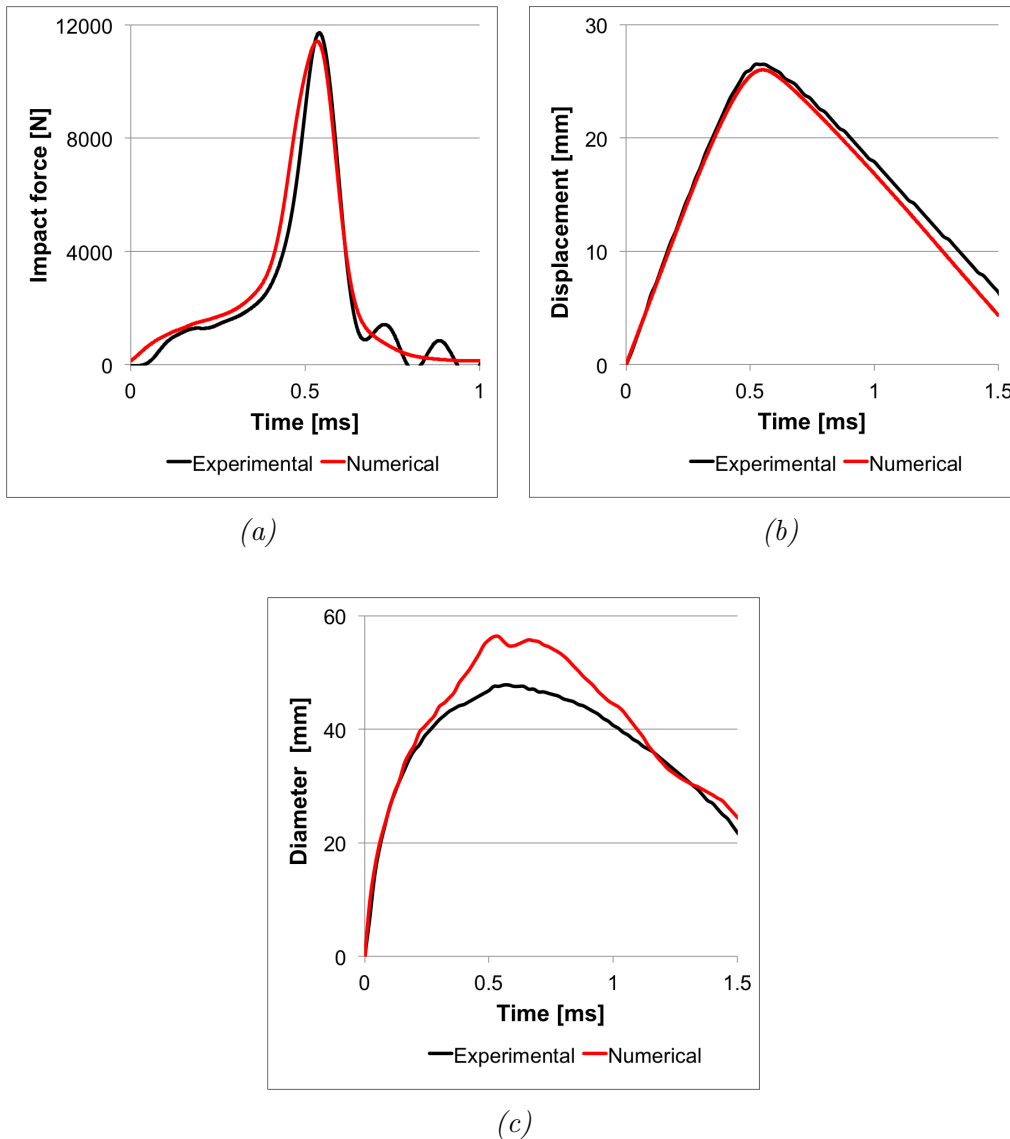


Figure 6.15. Comparison between experimental and numerical results at 58 m/s.

initial energy of the projectile is dissipated or absorbed by the foam nose at 0.54ms (end of the loading phase - red dot). Therefore when it comes to the impact of a deformable projectile with a hard sabot on RW, its behaviour can be compared to a rigid-like behaviour when the nose is completely crushed. Therefore it is like the rigid behaviour is delayed in time. The "*delayed effects*" are initiated because of the presence of the deformable material.

Only a small part of the energy is stored as elastic energy and is available for the rebound phase, the other being dissipated through irreversible processes. The ratio between the energy for the rebound and the initial energy gives an idea of the dissipative capabilities of the foam material (Figure 6.18). The lower is this ratio,

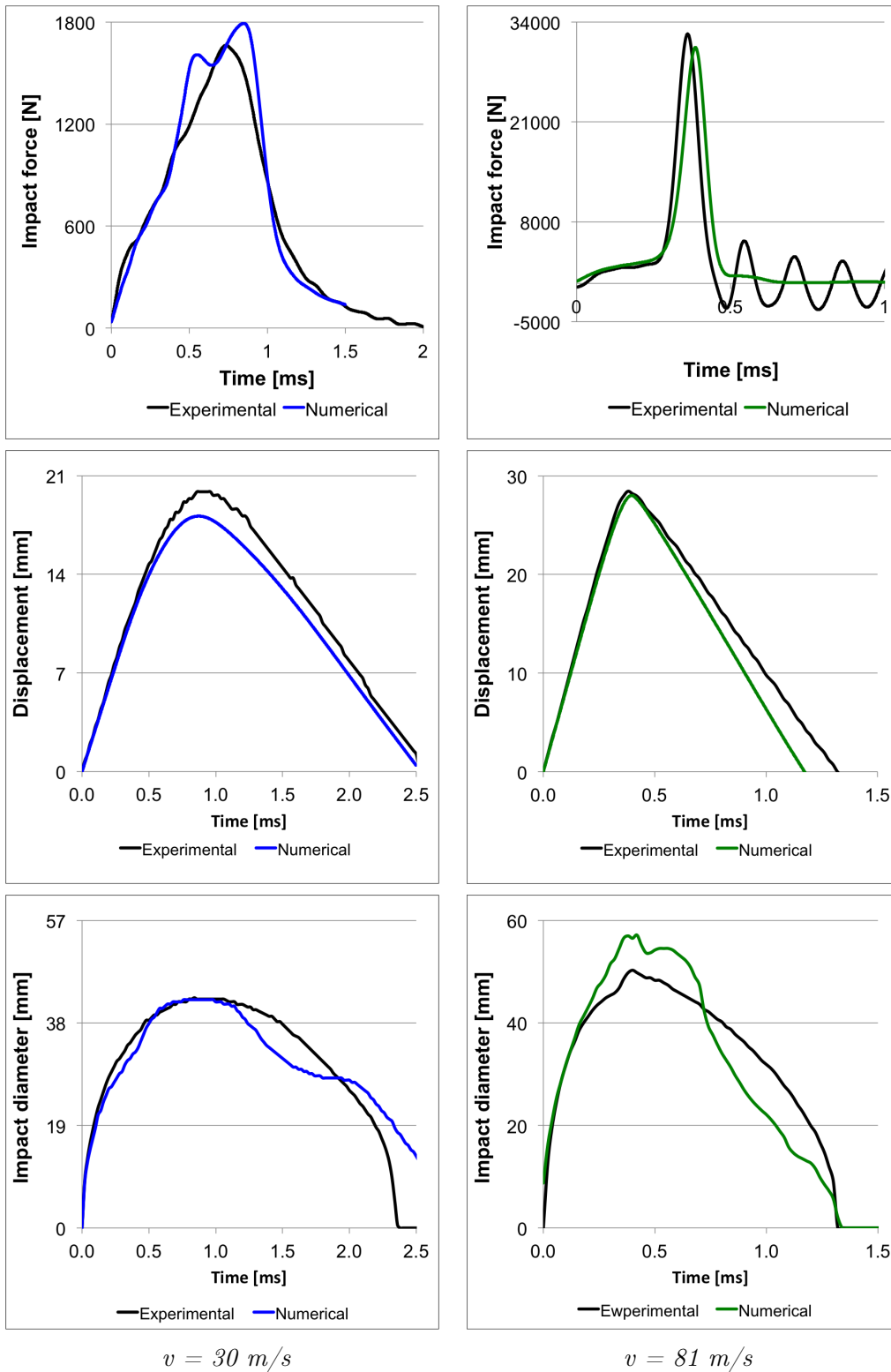


Figure 6.16. Comparison between experimental and numerical results at 30 m/s and at 81 m/s.

the higher is the dissipative capacity of the foam. For a perfect elastic material, this ratio before and after the impact is 1. Here, the ratio is 0.17 which means that only 17% of the initial energy is recovered for the rebound (assuming that all the elastic energy is converted into kinetic energy).

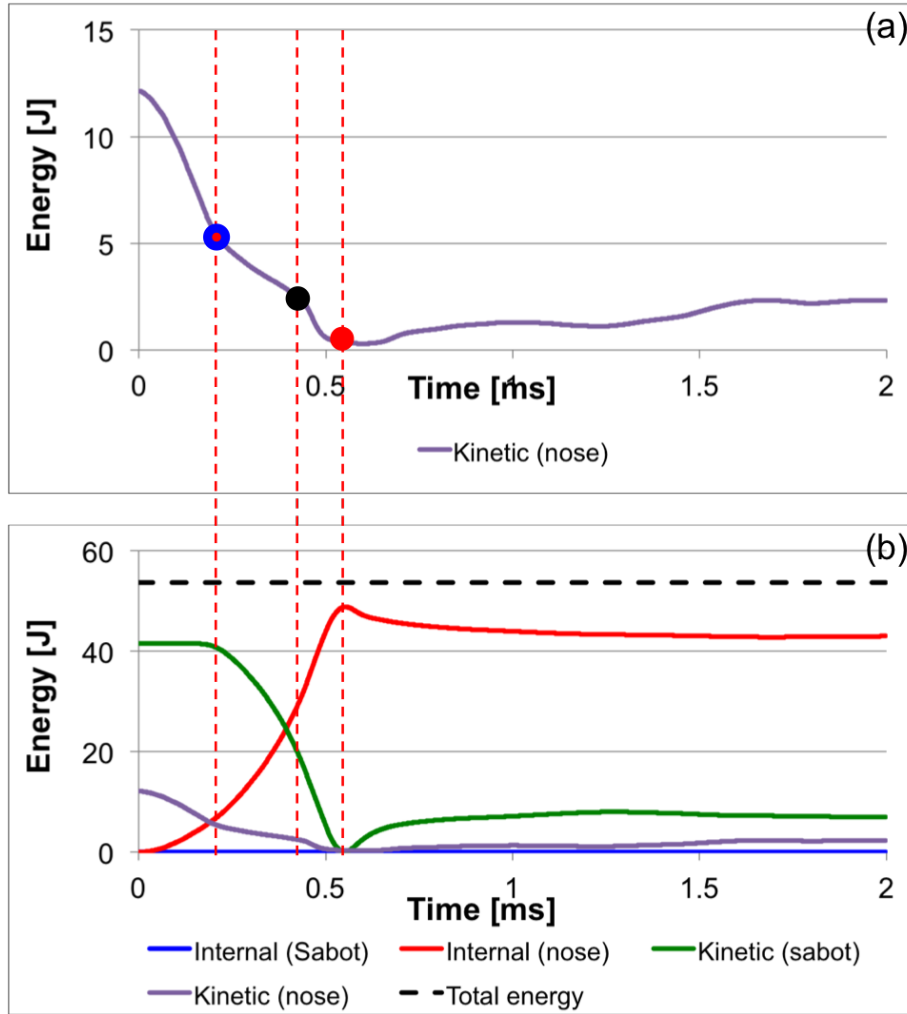


Figure 6.17. Energies of the SIR-X projectile parts at 58 m/s.

Three curves at different impact velocities were considered to cover the domain of application. Two were discarded as they did not satisfy to the requirement. With one single loading curve used as loading curve in the material model, the physics of the impact was correctly captured. This means that in the domain of our application, there is only a weak dependence of the SIR-X foam material upon the strain rate. This is a particular case. In general case, for a highly strain rate dependent material, the same approach should be used.

There are two critical zones where the uncertainty can be high in the stress-strain curves. the first critical zone is the very beginning of the impact where the stress is too small due to the hemispherical nose (contact on one point) and the resolution

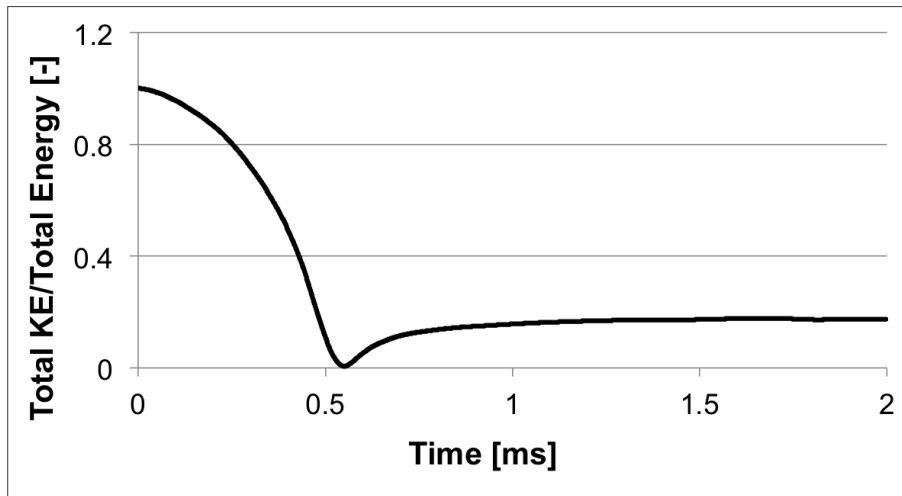


Figure 6.18. *Ratio of total kinetic energy to initial energy at 58 m/s.*

of the sensor might be too low to measure such low amplitude forces. The second critical zone is the beginning of the densification zone due to some non-mastered phenomena that can occur for example the nose slipping out of the sabot or the glue at the sabot-nose interface not resisting higher impact forces...

The original stress-strain curve is not used as loading curve in the material model. Instead the modified one where the data have been extended to the tensile range is used. Better results are obtained. The reason of this improvement is due to the fact that the nose is under multi-axial stress state during the deformation especially in traction at the nose periphery in the transversal direction. The material model should incorporate other modes of deformation in order to capture the whole behaviour of the nose material. But this should be more investigated.

Satisfying results is achieved at 30 m/s. the force error is 8% and the displacement error is 9%. It is worth pointing out that the considered velocity is the lowest velocity for which there is a densification zone. Good correspondence is found at 81 m/s between the numerical and experimental data except for the diameter where the error is 18%. The results of impact diameter show the maximum impact diameter are overestimated. However this has a little importance in the global response as from our experiences in simulating deformable materials, the pressure on RW is very small outside the region of one initial projectile diameter (similitude with a material flowing in radial direction). Nevertheless the impact diameter during most part of the loading phase is correctly captured (Figure 6.15-6.16). The unloading is not correctly captured in the radial direction. There is two combined effect for the radial behavior: the Poisson's effect and the unloading parameters used to simulate the dissipation. An optimum of these parameters was not found to correctly capture the phenomenon in the radial direction. One possible solution to investigate is the use of the unloading curve obtained during the firings. But the difficulty with this

curve comes from the fact that the actual filter can not mitigate completely the resonance frequencies content.

The scaling factor abscissa value SFA was adjusted and set to 0.9. The reason for that can be explained by uncertainties at the beginning of the stress-strain curve where the stress is very low. As a consequence, the stress keeps a very lower values up to a certain value of strain. It was observed during the model calibration that the time corresponding to maxima of numerical curves of the force and displacement as function of time were reached slightly at a latter time compared to the experimental ones. a choice was made to adjust this parameter.

Using hexa-elements with one point of Gauss in large displacement problems may lead to problems of hourglass. Figure 6.19 shows that the problem of hourglass is mastered only by using the default values in LS-DYNA. The thumb rule is that the ratio between the hourglass energy and the internal energy has to be less than 10% [149] and that is the case.

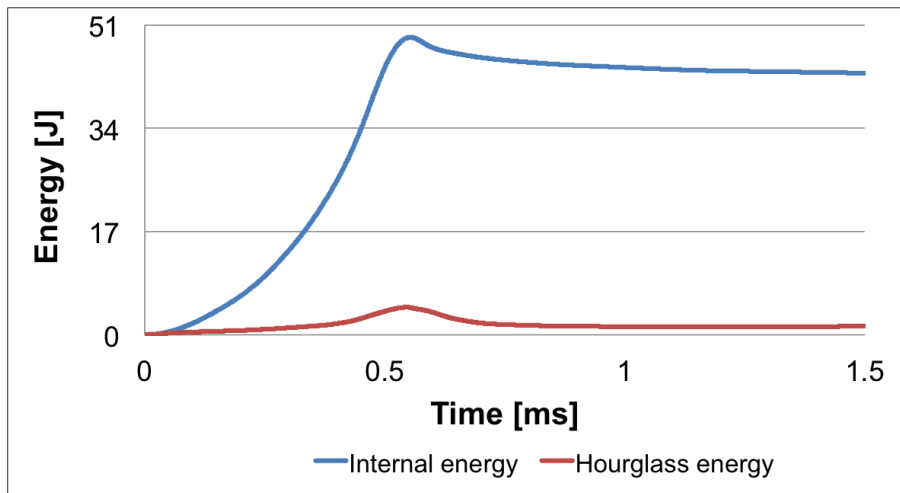


Figure 6.19. Comparison of internal and hourglass global energies at 58 m/s.

6.1.3.7 Validation in NATO standardisation framework

As mentioned previously, the projectile SIR-X has been also chosen as one of the reference projectiles in NATO standardisation framework by the NLKE ToE group⁷ and a validation process has been defined. However does the SIR-X projectile FE model satisfies the NATO validation requirement?

⁷A group of experts at NATO level (NLKE ToE) chaired by Belgium is working on the elaboration of standardized test procedures on KENLW to which every KENL system or projectile should comply to be valid within NATO.

NLKE ToE group has defined a method for the SIR-X projectile FE to be considered as validated against a RW. For that purpose, SIR-X force corridors and displacement corridors have been defined. They were generated from real firings of the SIR-X projectiles on RW at two different impact velocities 29 m/s and 61 m/s. In order to be considered as validated, the numerical responses of the SIR-X impacting the RW should fall within the corridors defined in [5].

The SIR-X projectile has been chosen for thorax surrogates validation purpose. For numerical thorax surrogates, one needs a projectile validated model. Results given in Figures 6.20 shows that the SIR-X FE model satisfy the requirement as the curves fall within the corridors.

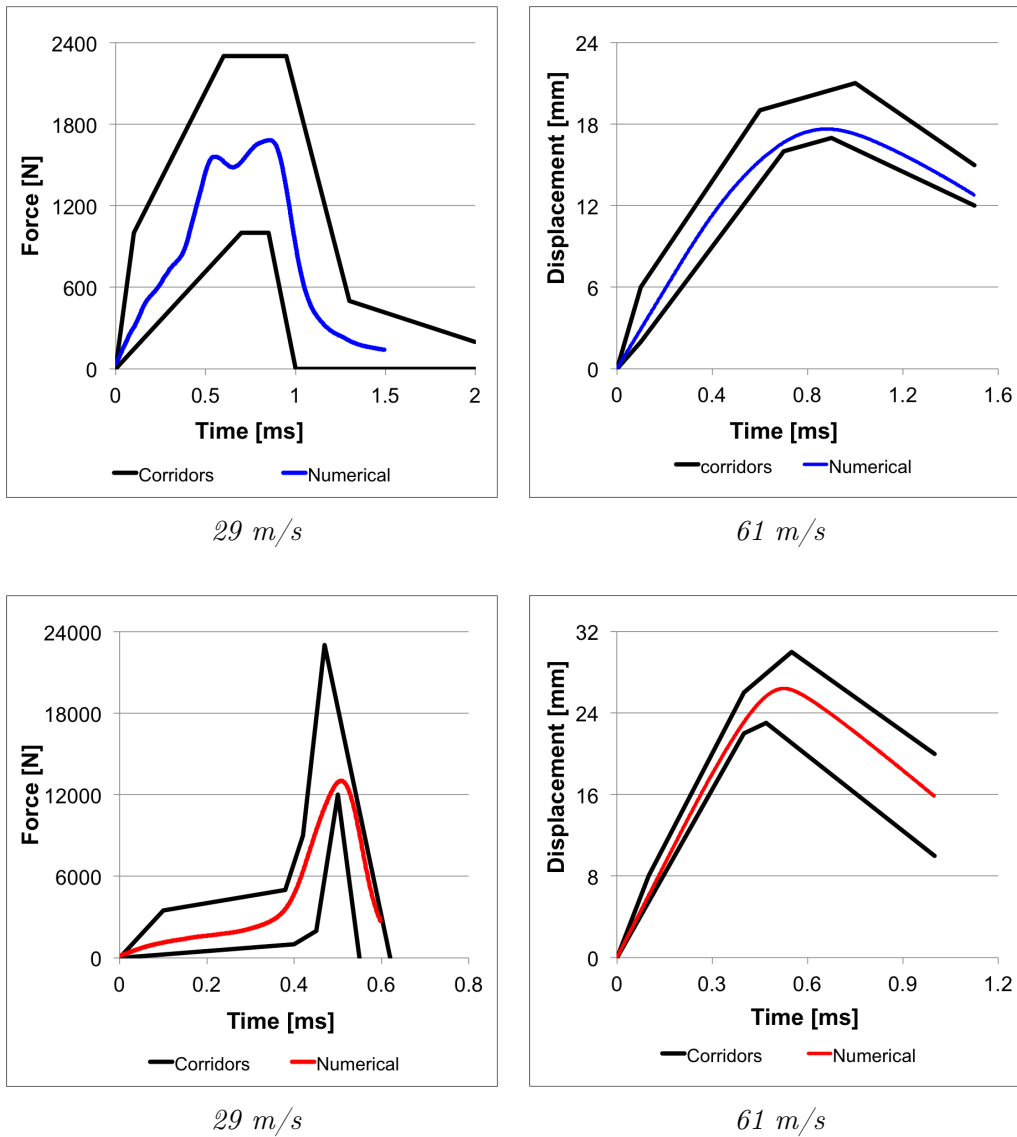


Figure 6.20. Validation of SIR-X projectile using corridors defined in [5].

6.1.3.8 Conclusions

The projectile SIR-X has been characterised by applying the new characterisation method. It has been validated for a certain range of velocities. Good correspondence has been achieved between the numerical and the experimental results. It has been shown that with one loading curve used as input for nose material characterisation, the dynamics of the impact was correctly captured. The nose material shows no or little strain rate dependence. Many features have been described by considering the dynamics of the impact according to different perspectives: the impact force, the displacement or the different energies involved. The projectile SIR-X has also been

validated in the NATO standardisation method framework. It can be then used in the standardisation process within NATO.

To show the consistency of the new method of characterisation, it will now be applied to another projectile.

6.1.4 CONDOR NT901 projectile FE model

The description of the CONDOR NT901 projectile is given in Figure 2.4.2.4. Three impact velocities were chosen: 38 m/s, 63 m/s and 88 m/s for the projectile characterisation. There is a great similarity between the SIR-X and the CONDOR projectiles. Therefore the same procedure for the validation of the SIR-X projectile is applied for the CONDOR projectile as well. Only differences if any would be highlighted. Nevertheless, there is a difference in projectile mass and in nose density.

6.1.4.1 Experimental results

Experimental results are given in Figure 6.21. As expected, the results are similar to the results obtained with the SIR-X projectile. The same observations are made: Poisson's effect is not negligible. The same analysis concerning the different features highlighted for the SIR-X projectile can be made also for the CONDOR projectile.

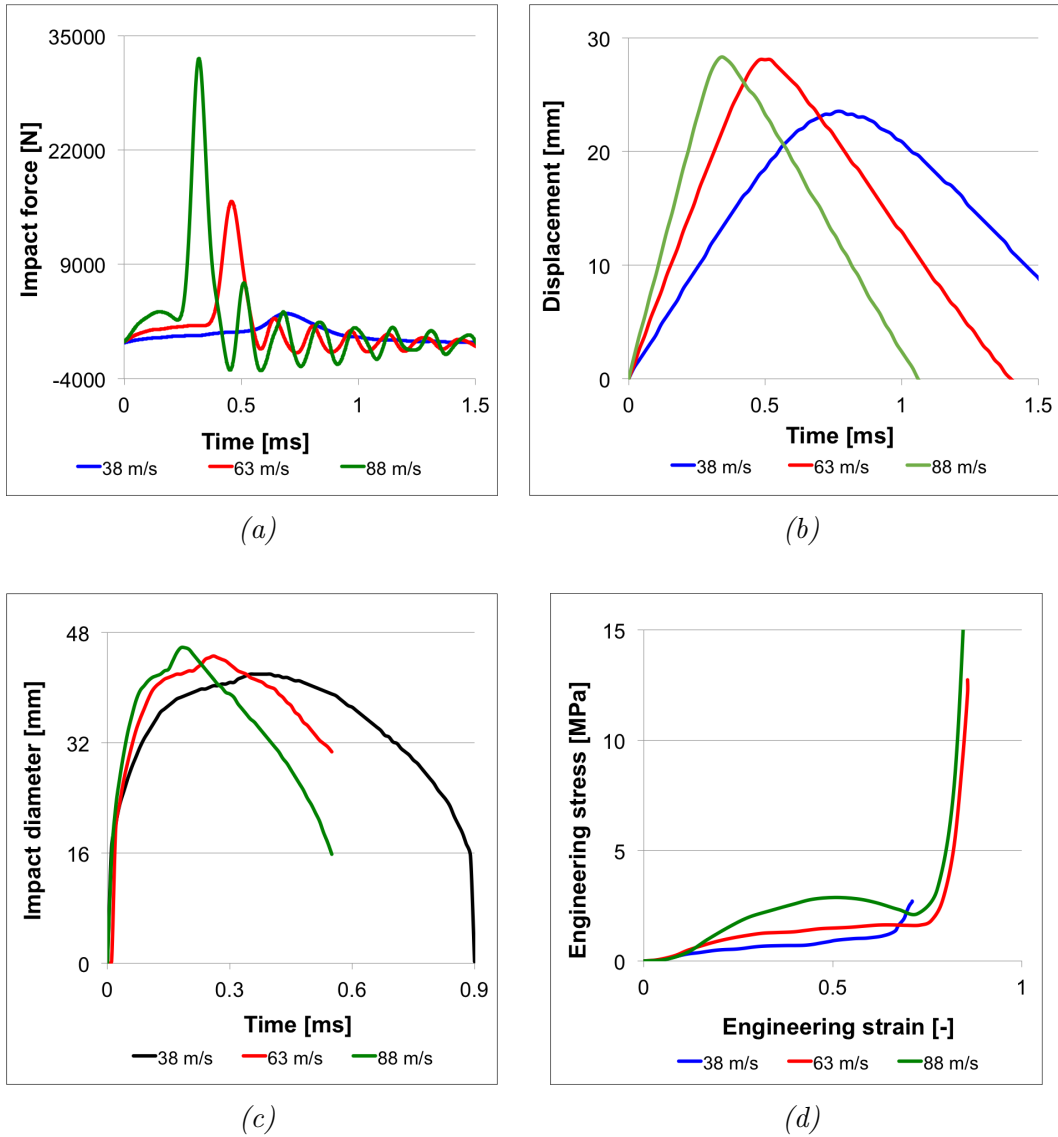


Figure 6.21. Experimental results of the the impact of the CONDOR projectile on RW at different impact velocities.

6.1.4.2 Geometry and mesh

The geometrical and mesh characteristics are given in Figure 6.22. The projectile is modelled with hexahedral solid elements. The numbers of elements of the sabot and the nose are given in Table 6.4. A continuous mesh is used at the interface by merging the nodes of the two parts. The cylindrical holes have been replaced by prismatic holes by deleting few hexa-elements but with the same pattern.

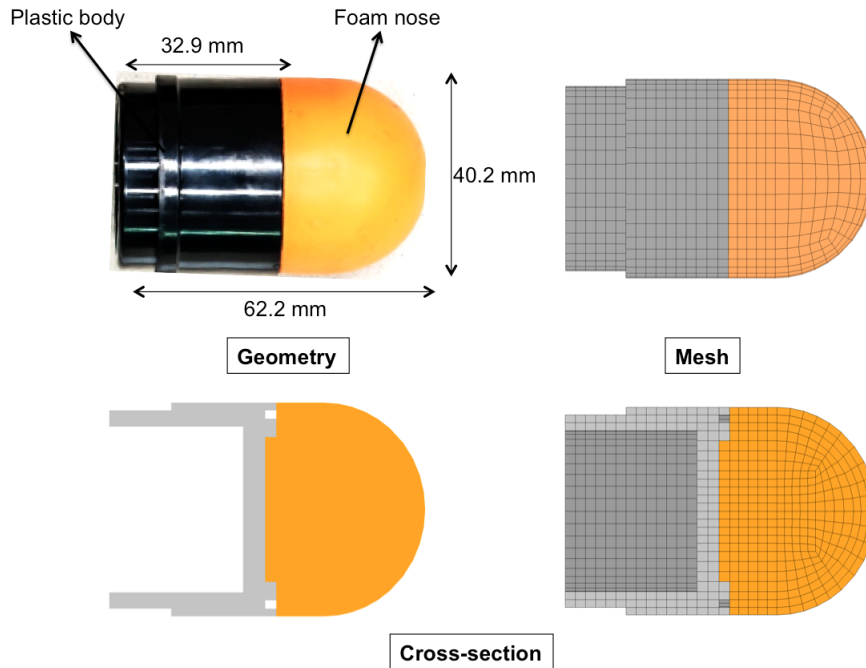


Figure 6.22. *CONDOR* projectile characteristics.

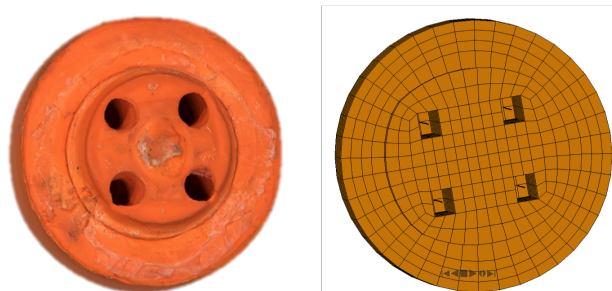


Figure 6.23. *CONDOR* projectile nose with four holes.

6.1.4.3 Material characteristics

A linear elastic model is used for the sabot and a visco-hyperelastic model for the nose. The nose material model parameters was identified using the method described in section 6.1.2.2. The loading curve used as input for the material model is given in Figure 6.25. All the material characteristics are given in Table 6.4.

where LC is the loading curve, the unloading parameters HU and $SHAPE$ are the hysteresis factor and the shape factor, and MU , the damping coefficient.

The validation process of the *CONDOR* projectile is described in next section.

Parts	Material parameters					Element type/ Number of elements
	Density [kg/mm^3]	Young modulus [Pa]	Poisson's ratio			
Sabot	1030	$2.3 \cdot 10^{10}$	0.33			Hexa/ 2112
Nose	328	Bulk modulus [Pa] $5.0 \cdot 10^9$	0.100			Hexa/ 4072
	HU 0.50	SHAPE 15	SFA 1.0	MU 0.05	Loading curve LC	

Table 6.4. Material characteristics of the CONDOR projectile.

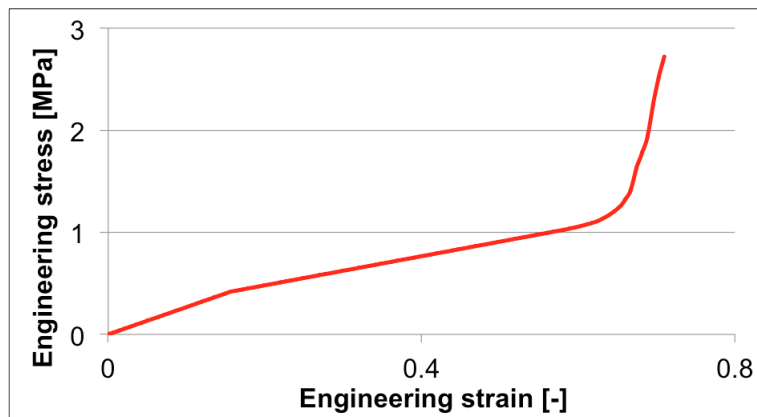


Figure 6.24. CONDOR engineering compressive smoothed stress-strain curve.

6.1.4.4 Validation

A parametric study of the nose model has been carried out to find the optimal model parameters (Table 6.4). Results of the calibration of the model are given in Figure 6.25 obtained by smoothing the original curve. Comparison between the experimental and the numerical results are given in Figures (Figures 6.26-6.27). Good correspondence is achieved for the force and displacement as function of time. Satisfying results are achieved for the impact diameter. The physics of the impact is correctly captured.

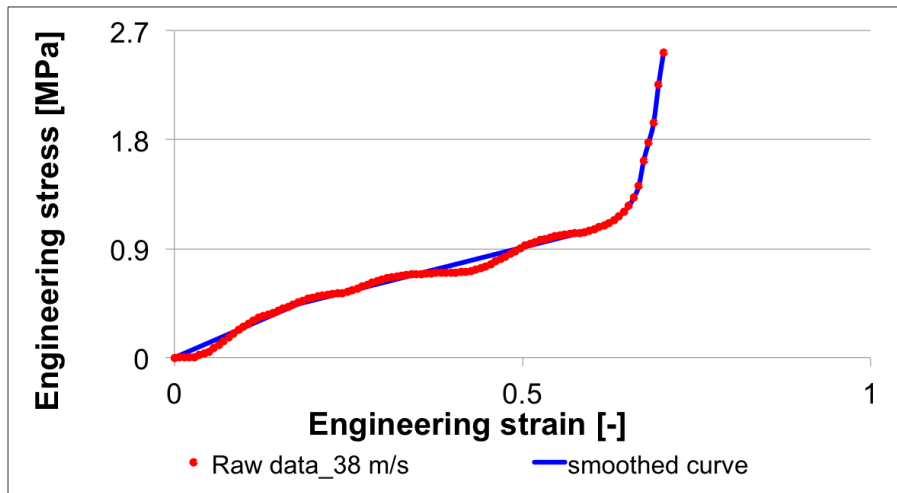


Figure 6.25. *CONDOR* compressive loading curve derived from characteristics at 38 m/s.

6.1.4.5 Discussions

Although they have different masses and different nose densities, they shows similar behaviour at impact. The same discussions and conclusions drawn with the SIR-X projectile are also done for the CONDOR projectile.

The three stress-strain curves derived from the force and displacement overlap (Figure 6.21 (d)). It is assumed that there is a weak dependence to the strain rate. By using the same approach as for the SIR-X projectile, the curve corresponding to the lowest velocity (38 m/s) with a densification zone is considered (Figure 6.25). The final curve is obtained after modifying the original stress-strain curve by smoothing it and by approximating portions of curves by lines except for the densification region. Good results were achieved as one can see on Figures 6.26-6.27.

Only with one loading curve, the curve with the lowest velocity (38 m/s) with a densification zone, the physics of the impact phenomenon is correctly captured. Good correspondence is found for the force and displacement as a function of time. But the same remark as the one made for the SIR-X projectile can be made about the impact diameter . There is some discrepancies in the value of the maximal impact diameter at certain velocities. The maximum error 23% was obtained with the highest velocity. The unloading phase for the transverse direction was not correctly captured. The reasons of these discrepancies can be explained by a high dissipation of the nose material model.

As for SIR-X projectile, the loading curve was symmetrized about the origin to add a tensile curve to see if results could be improved. Results are given in Figure 6.28. They show that extending the stress-strain curve to the tensile range did not

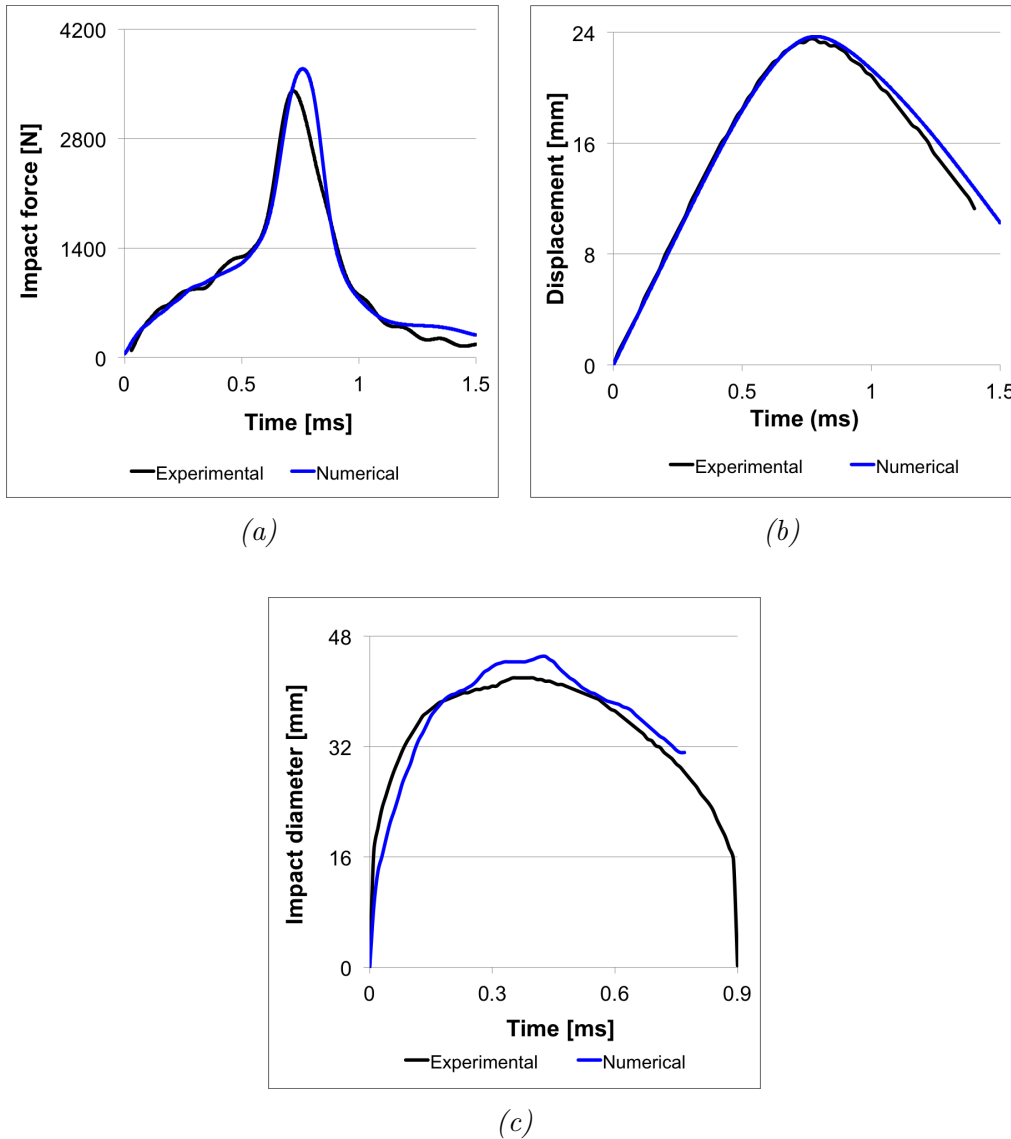


Figure 6.26. Comparison between *CONDOR* experimental and numerical results at 38 m/s.

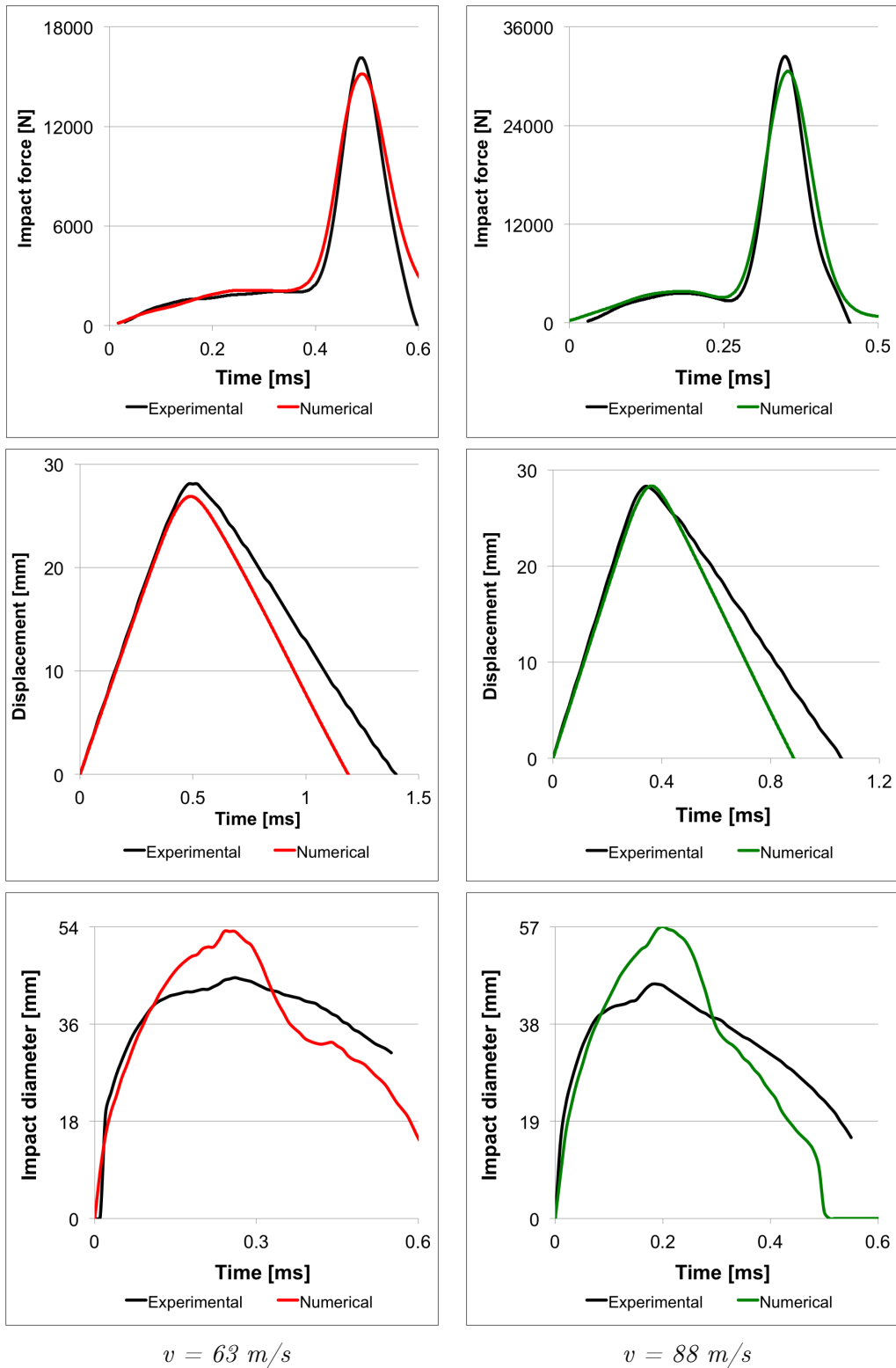


Figure 6.27. Comparison between CONDOR experimental and numerical results at 63 m/s and at 88 m/s.

improve the result. There is no difference for the displacement but a slight difference in force (the maximum error is $<10\%$).

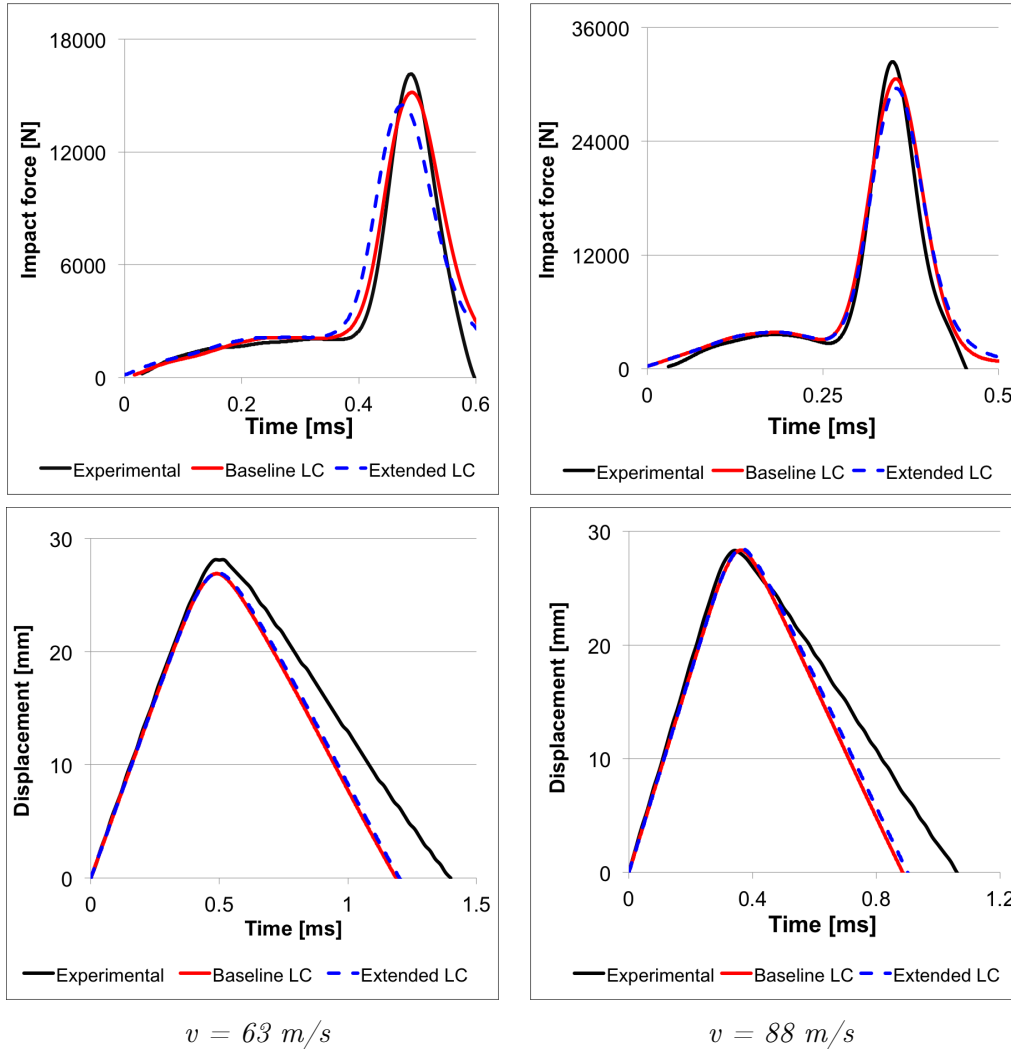


Figure 6.28. Comparison of CONDOR results using the baseline loading curve (LC) and the extended loading curve where the baseline LC has been symmetrized in order to have a tensile loading curve for impact velocities 63 m/s and 88 m/s .

There is a slight difference in the structure of the nose between the CONDOR and the SIR-X projectile. There are holes in the CONDOR nose. To show the influence of these holes in the global response, they are filled with the same material by keeping the projectile mass constant. Two alternative cases are considered. In the first case (Case B), the nose density is adapted and the sabot mass is kept constant. In the second case (Case C), the same density as the actual projectile nose density (Case A) is used and the sabot mass is adapted accordingly. Simulations have been

performed at 63 m/s. One can see that the same results are achieved for the three cases (Figure 6.29) i.e. the holes have no influence in the impact dynamics.

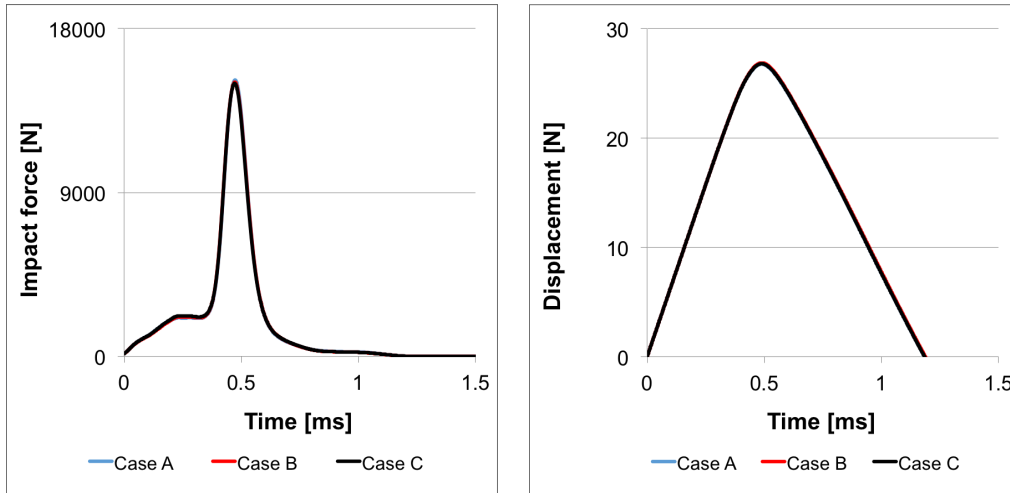


Figure 6.29. *CONDOR hole influence: Case A-same nose density, Case B-same sabot density, Case C-actual projectile.*

6.1.4.6 Conclusions

The condor projectile has been validated. As explained, there is a similarity of the impact phenomena between the SIR-X and the CONDOR projectiles. Therefore the main conclusions apply to both projectiles even though there is a difference in the nose structure and masses between the two projectiles.

The CONDOR nose contains four cylindrical holes or cavities but they have no influence on the global dynamics.

6.1.5 Nobel Sport (NS) Spartan LE 40 Schock projectile FE model

The description of the NS projectile is given in section 2.4.2.5. The NS projectile has a structure that is different from the SIR-X and CONDOR projectiles. It has a hollow nose structure and higher mass, 40 g from the NS projectile and 32 g for the SIR-X projectile.

6.1.5.1 Experimental results

Two impact shots were chosen as representative of the available firing series at 36 m/s, 60 m/s for the projectile characterization. A third series of shots at 92 m/s

were discarded as all the projectiles at this velocity broke during the impact on RW. Validation is made only using the impact results at 2 impact velocities. The experimental curves (Figure 6.30) show the same behaviour as the ones obtained for the SIR-X and the CONDOR projectiles. It is observed a linear phase, a plateau and a drastic increase in force followed by the unloading phase. One could expect to have then the same phenomenon but there is a difference in the structure of the NS nose and the deformation mechanism is not the same.

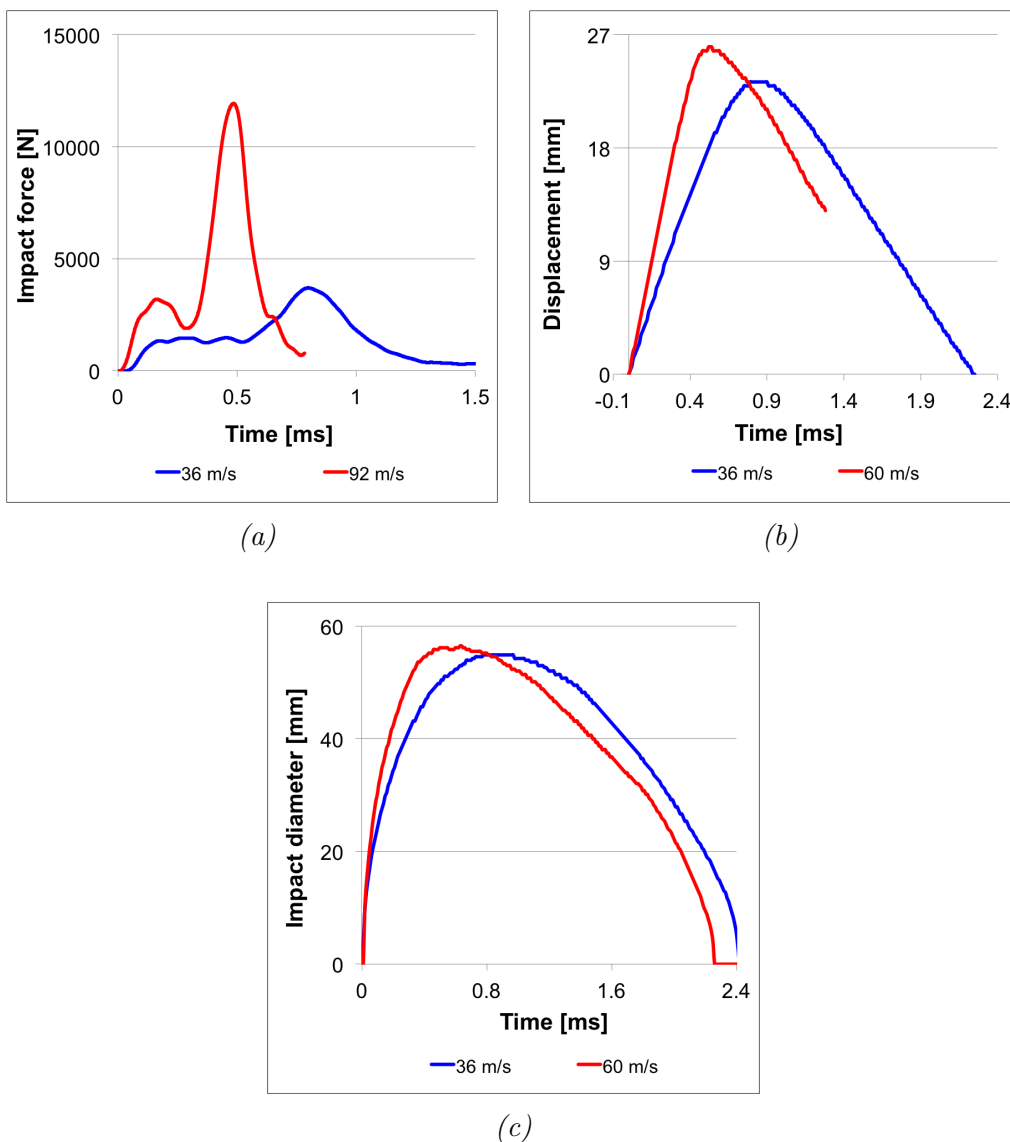


Figure 6.30. NS experimental results on RW.

6.1.5.2 Geometry and mesh

The geometrical and mesh characteristics are given in Figure 6.31. The projectile is modelled with hexahedral solid elements. The numbers of elements of the sabot and the nose are given in Table 6.5. A continuous mesh is used at the interface by merging the nodes of the two parts.

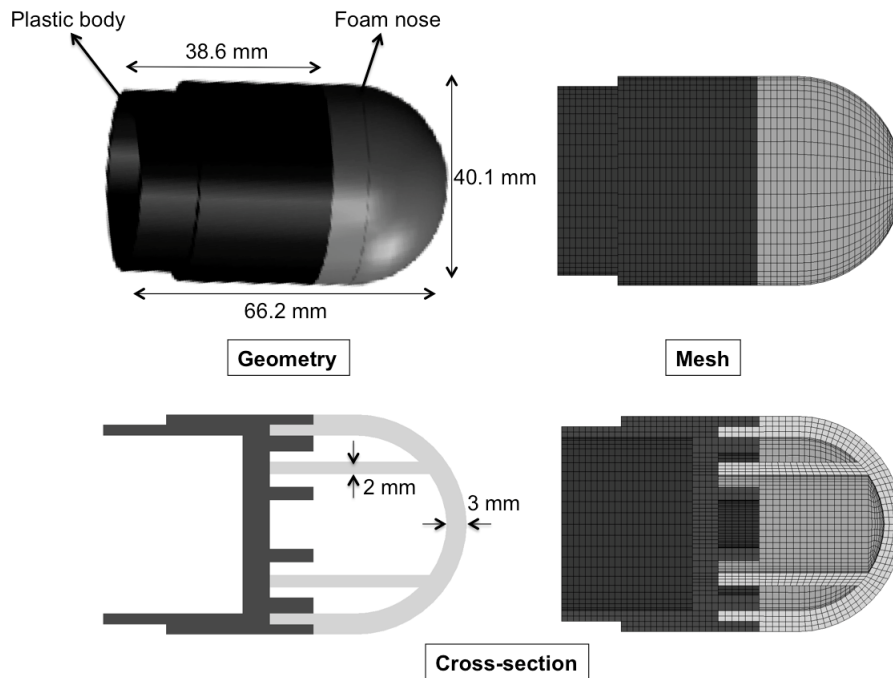


Figure 6.31. NS projectile characteristics.

6.1.5.3 Material characteristics

The new method of characterization for sponge grenades could not be applied as the NS nose is not a solid full homogeneous solid (see section 6.1.2.1). A hyperelastic material is assumed for the nose rubber material and the loading curve is taken from the literature [6]. A linear elastic model is used for the sabot. The material characteristics for the projectile is given in Table 6.5 and Figure 6.32. The validation process of the NS projectile is described in the next section.

6.1.5.4 Validation

A parametric study of the nose material model has been carried out to find the optimal model parameters (Table 6.5). Comparison between the experimental and the numerical results are given in Figures 6.33. The results show differences between

Parts	Material parameters			Element type/ Number of elements
	Density [kg/mm^3]	Young modulus [Pa]	Poisson's ratio	
Sabot	1206	$2.3 \cdot 10^{10}$	0.387	Hexa/ 2032
Nose	1000	Bulk modulus [Pa] $5.0 \cdot 10^9$	0.495	Hexa/ 4336
	HU 1	SHAPE 0	Loading curve LC	

Table 6.5. Material characteristics of the NS projectile.

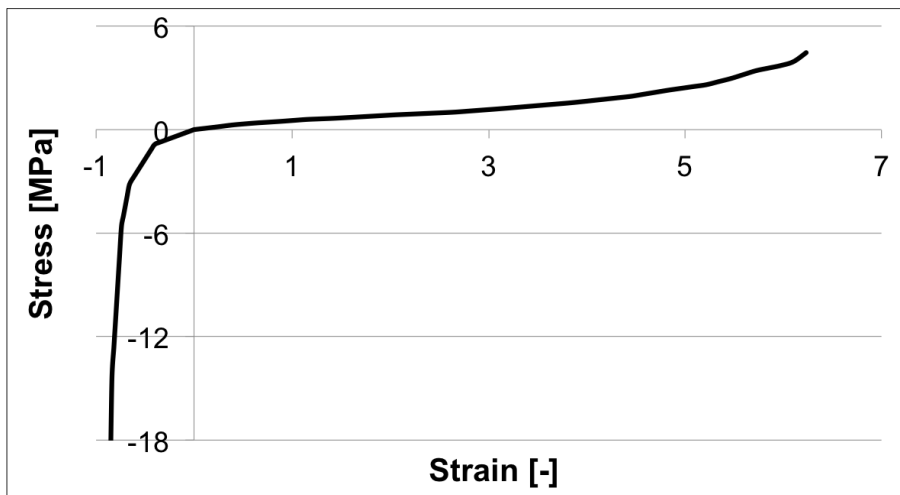


Figure 6.32. Loading curve for the NS projectile nose [6].

the two types of results especially for the impact forces. Nevertheless, satisfying results are achieved for the displacement.

6.1.5.5 Discussions

Results at 60 m/s show a maximum error of 15 % in term of maximum impact force. Most of the loading part is correctly captured. Two directions of investigation can be considered:

- How the air enclosed in the nose could affect the results if it is modelled. It may offer an additional resistance to the nose deformation acting then as a damper.

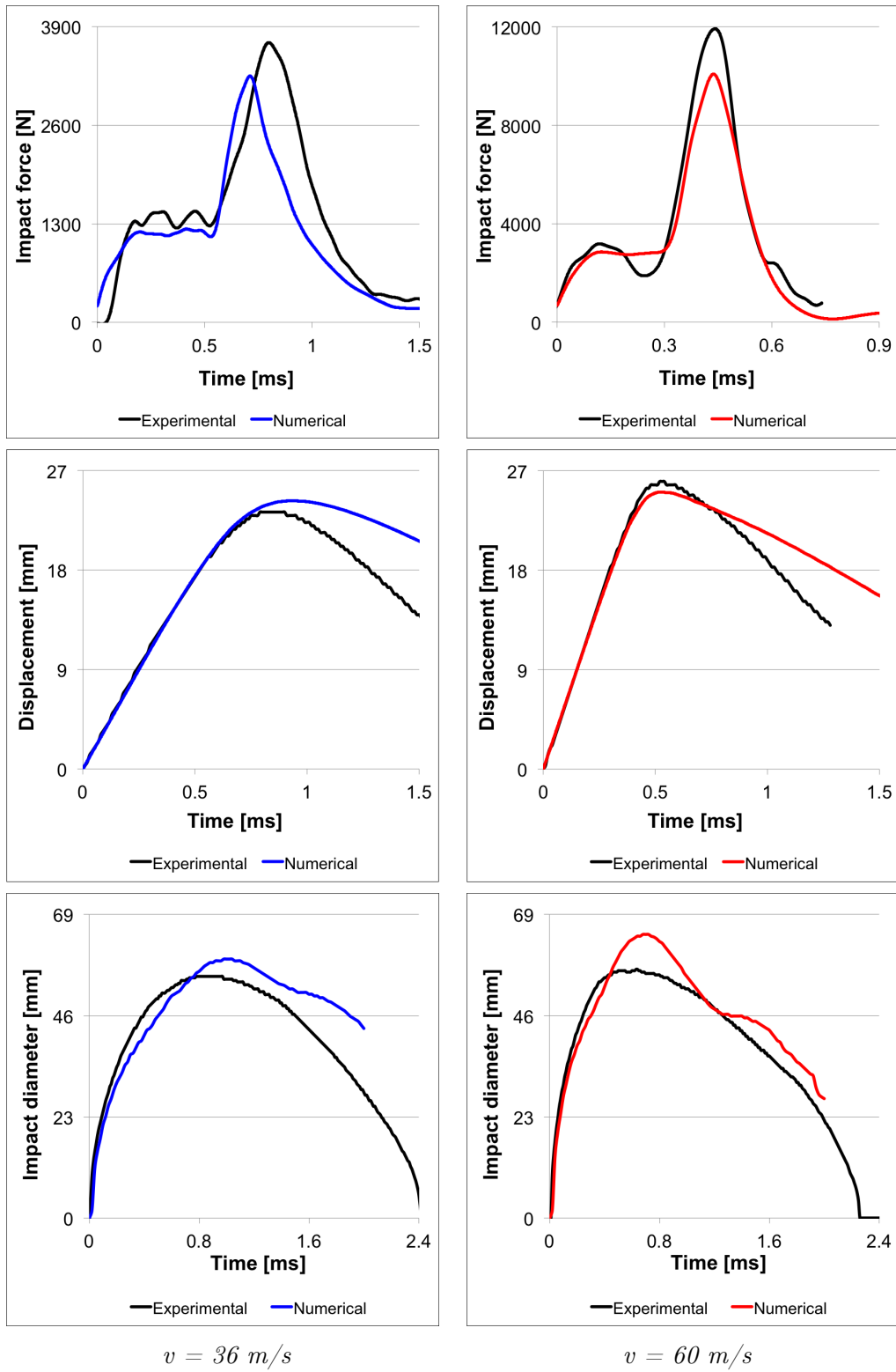


Figure 6.33. Comparison between NS experimental and numerical results at 36 m/s and at 60 m/s.

6.1 KENL projectile FE modelisation

- The maximal error on the maximum force is 15 %. As the model did not capture correctly the physics of the impact, one way to improve the validation is by investigating elastic models.

When comparing the NS results to SIR-X results, there is to a certain extent a similitude. The force curves can be divided into three zones: a more accentuated linear zone, then a plateau with higher amplitude and a zone where there is a drastic increase of force. But the underlying deformation mechanisms are very different especially due to the presence of cavities within the nose. In fact, the snapshots of the cross-sections of the NS projectile during impact (Figure 6.34) show that firstly, the column resist the deformation corresponding to the linear phase, followed by the plateau phase until total buckling of the column occurs at time=0.34 ms. Then the force increases drastically. This phase is similar to the densification of the material in the case of the SIR-X projectile. The unloading phase begins at time=0.51 ms.

Although the NS projectile is heavier than the SIR-X and CONDOR projectiles, at same velocities, the NS projectile performs well in term of induced force on RW as for example at 60 m/s forces are of the same order. One can note that the deformation mechanism induced in NS projectile through buckling seems more efficient in this case.

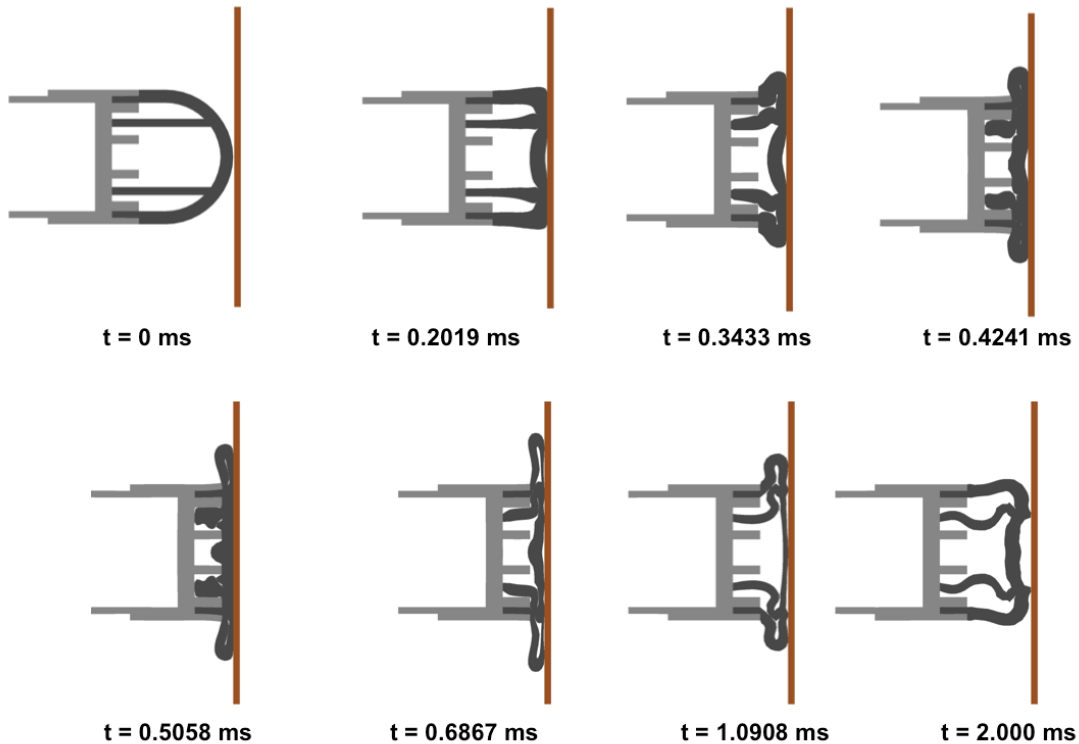


Figure 6.34. *Cross-section NS impact sequences at 60 m/s.*

Energy histories show the same trend as for the SIR-X (Figure 6.17), but for the NS projectile, the second (similar to plateau) is not clear (Figure 6.35). The ratio of kinetic energy before and after the impact gives an idea of the energy dissipated through irreversible process, i.e. the dissipative capabilities of the nose material. This ratio is equal to 0.02. The numerical ratios are lower than the experimental ones. This can be seen when one refers to the slope of the unloading phase for the NS projectile impact on RW. Table 6.6 gives comparison of rebound velocities between experiments and numerical simulations. The discrepancy partially comes from the fact that unloading was not correctly captured using the built-in unloading parameters in LS-DYNA. The numerical model seems more dissipative than the real case.

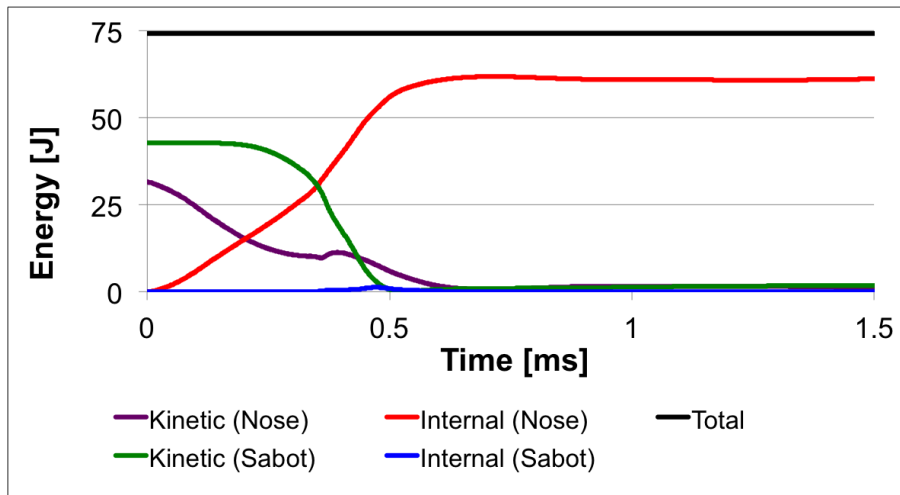


Figure 6.35. *Energy histories for the NS projectile at 60 m/s.*

Impact velocity [m/s]	Rebound velocity [m/s]	
	Experimental	Numerical
36	-20	-12
60	-17	-7

Table 6.6. *Comparison between experimental and numerical rebound velocities.*

The maximum impact diameter is overestimated, and the unloading is not correctly captured. To better capture the whole dynamics, the material characteristics should include other modes of deformation.

During the loading, a dynamic cavity is created (Figure 6.34). Indeed due to the presence of cavities, nodes of the projectile nose, particularly the ones close to the projectile axis are accelerated in one and the other direction along the projectile axis, the highest acceleration being achieved for the nodes on the axis. Therefore a dynamic small cavity is created at the interface projectile-RW as this can be seen in

Figure 6.34 at time 0.20 ms. Figure 6.36 shows the velocity of node A corresponding to the projectile nose tip. By examining what is going along the projectile axis, at the beginning of the impact, the velocity of this node drops to zero before moving in the opposite direction. After the node moves again forward. There are three specific times: At time T1, the total collapse of the column takes place inducing a high velocity peak and the projectile continues to move forward. At time T2, the central part of the sabot squeezes the nose against the RW. At time T3, the small cavity closes definitely during the unloading phase. By considering a few nodes located along the radial direction on the front external surface of the nose, the same behaviour with more or less much emphasis depending of the node's distance from the projectile axis can be observed (Figure 6.37).

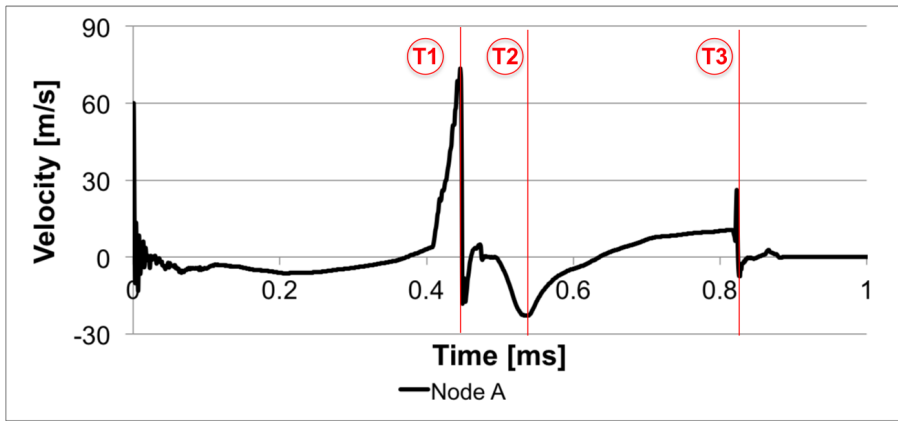


Figure 6.36. Velocity along the projectile longitudinal axis of node A corresponding to the projectile nose tip for an impact velocity of 60 m/s

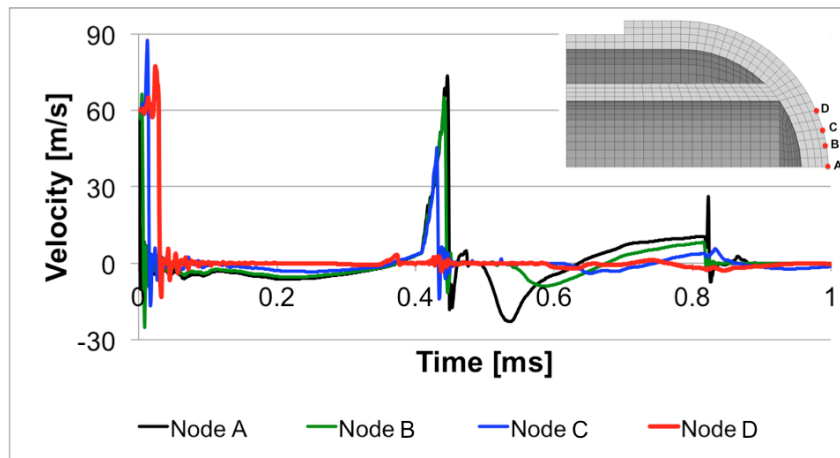


Figure 6.37. Velocity of nose nodes located along the radial direction for an impact velocity of 60 m/s.

6.1.5.6 Conclusions

Satisfying results have been achieved for the validation of the NS projectile. The mode of deformation of the NS projectile is very different from the SIR-X and CONDOR projectiles due to its hollow structure. During impact, the column resists the deformation until complete buckling of the nose followed by a rigid-like behaviour of the projectile. This mode of deformation seems to bear better results in terms of impact force compared to the SIR-X and CONDOR projectiles although it is heavier than the latter.

6.1.6 FN303 projectile FE model

The description of the FN303 projectile is given in section 2.4.2.8.

6.1.6.1 Experimental results

All experimental results have been given in [2]. Three impact velocities are considered, 35 m/s, 60 m/s and 93 m/s. For each series of firings, only one curve representative of each series is used. Figure 6.38 shows the corresponding results. As the projectile breaks at impact, tracking the displacement and the impact diameter is therefore meaningless and only curves of force as function of time are considered. The description of the geometrical and material models are given in the sections 6.1.7.2 and 6.1.6.3, respectively.

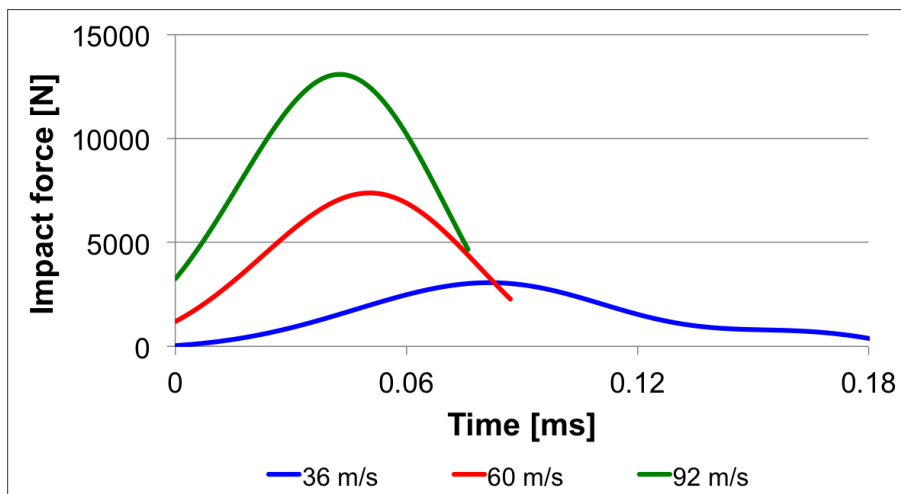


Figure 6.38. Experimental results of FN303 impacts on RW at different velocities.

6.1.6.2 Geometry and mesh

The main issue here is to define an appropriate formulation due to the different characteristics of the materials of the FN303. SPH formulation is used to model the bismuth grains and the glycol (which is modelled as water). For the polystyren parts, lagrangian formulation is used (Figure 6.39). The body and the disk are modelled with hexahedral elements.

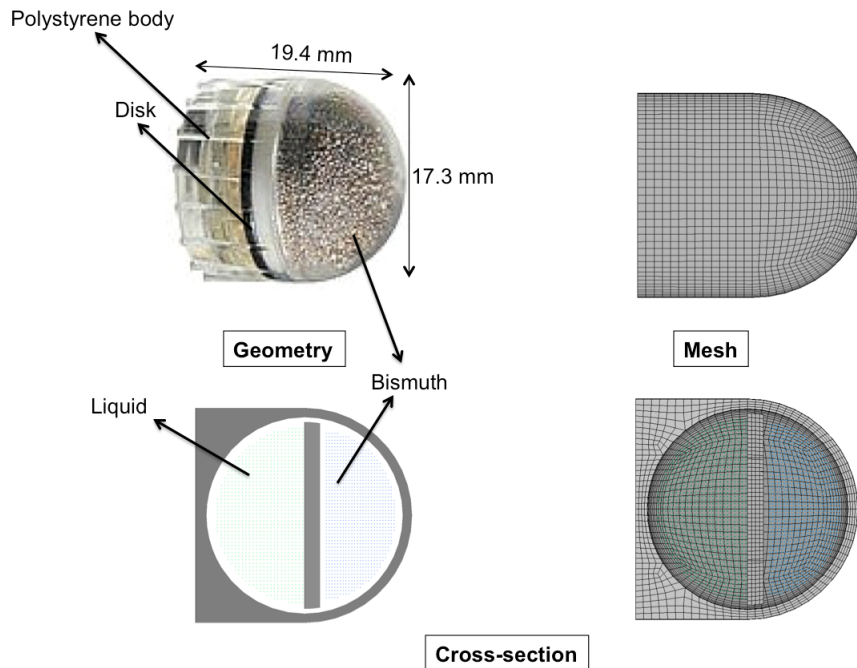


Figure 6.39. *FN303 projectile geometrical and mesh characteristics.*

6.1.6.3 Material characteristics

The material characteristics are given in Table 6.7. Linear elastic behavior is assumed for the polystyrene material. The glycol is modelled as water. Water is modelled with a linear EOS and bismuth material are modelled using a linear elastic EOS and a viscous (deviatoric term)⁸. A fluid-like material model with a linear EOS is used for water and a linear model EOS with a viscous term for the bismuth.

Even though the FN303 is a composite projectile with many parts coming into contacts one another, only one contact type is defined. The contact type used for all these parts is AUTOMATIQUE_NODE_TO_SURFACE contact defined between the polystyrene parts and the bismuth and water, respectively. As it breaks at impact, a principal stress failure criterion for the polystyrene parts is defined and set to 200 MPa.

6.1.6.4 Validation

Results of FN303 validation given in Figure 6.40 show a good correspondence between the experimental and the numerical results.

⁸This material model implemented in LS_DYNA as *MAT_NULL is used to model fluid-like material and with an optional viscous (deviatoric) term can also be added [149]

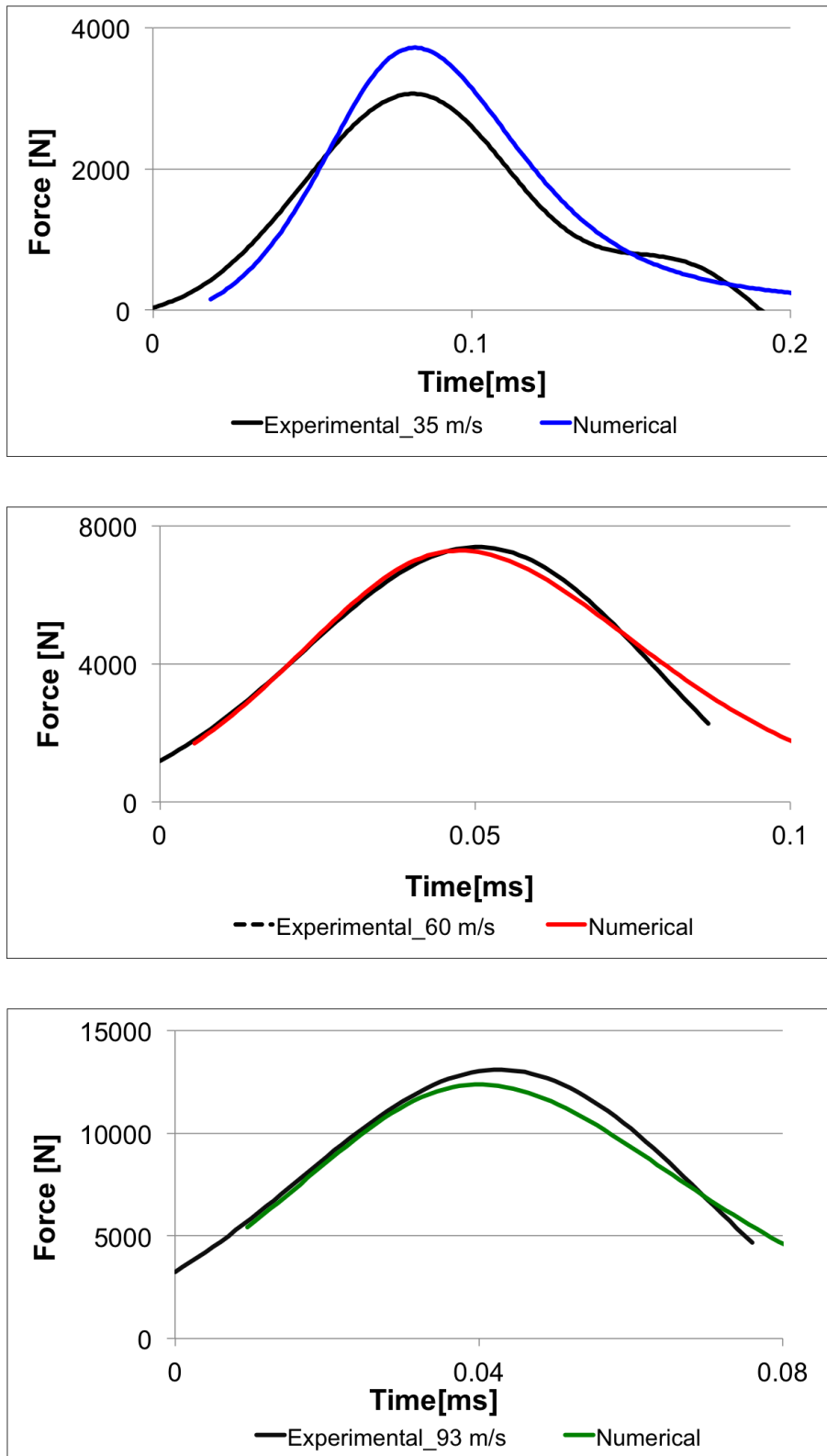


Figure 6.40. Comparison between FN303 experimental and numerical results for different impact velocities.

Parts	Material parameters			Element type/ Number of elements
	Density [kg/mm^3]	Young modulus [Pa]	Poisson's ratio	
Body	810	$5.5 \cdot 10^9$	0.300	Hexa/ 15808
Disk	810	$5.5 \cdot 10^9$	0.300	Hexa/ 7624 /
centering	*MAT_NULL			
	Linear elastic EOS		Viscous term	
		Bulk modulus [Pa]	Viscosity μ [$Pa.s$]	
Bismuth	9790	$3.1 \cdot 10^{10}$	500	SPH/ 32876
Water	1000	$2.2 \cdot 10^9$	-	SPH/ 32876

Table 6.7. *Material characteristics of the FN303 projectile.*

6.1.6.5 Discussions

The FN303 projectile is lighter than the 40 mm sponge grenades and its mass is three to five times smaller. Its impact duration is also much shorter than the 40 mm sponge grenades impact duration.

The impact dynamics of the FN303 projectile is different from all the previous projectiles that have already been modelled. This projectile breaks at impact. It is characterised by a rapid increase of the force up to the maximum followed by a rapid decrease of the force. It is worth pointing out that a part of the initial energy of the projectile, difficult to quantify is used to break the projectile into many pieces. The breaking of the projectile is important as it will 'artificially' increase the impact diameter by letting the bismuth flowing and spreading on the impact surface (Figure 6.41). Therefore the force is not concentrated on a small region but on a larger impact surface which has an effect on the impact time duration i.e. on the maximum force.

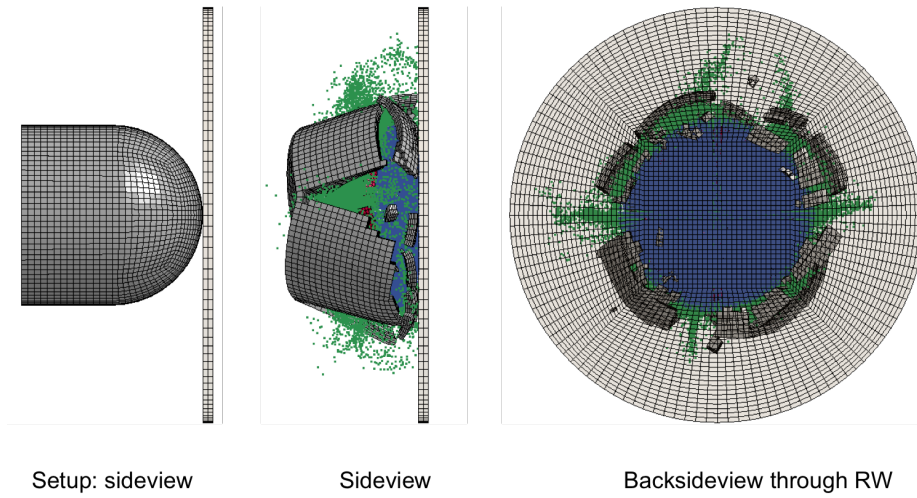


Figure 6.41. *FN303 projectile breaking: Dynamic Increase of impact surface .*

6.1.6.6 Conclusions

Although the complexity of the projectile due to multiple interactions between the FN303 projectile parts, the dynamics of the impact has been correctly captured. The main characteristics of the FN303 projectile is that it breaks at impact. The breaking of the projectile is important in order to increase in an 'artificial way' the impact diameter. This has an effect on the duration of the impact i.e. the whole impact dynamics.

6.1.7 RB1FS projectile FE model

The description of the RB1FS projectile is given in section 2.4.2.7. It is made of one single material: the rubber material.

6.1.7.1 Experimental results

All experimental results have been given in [2]. Three impact velocities are considered, 35 m/s, 60 m/s and 90 m/s. For each series of firings, only one curve representative of each series is used. Figure 6.42 shows the experimental results.

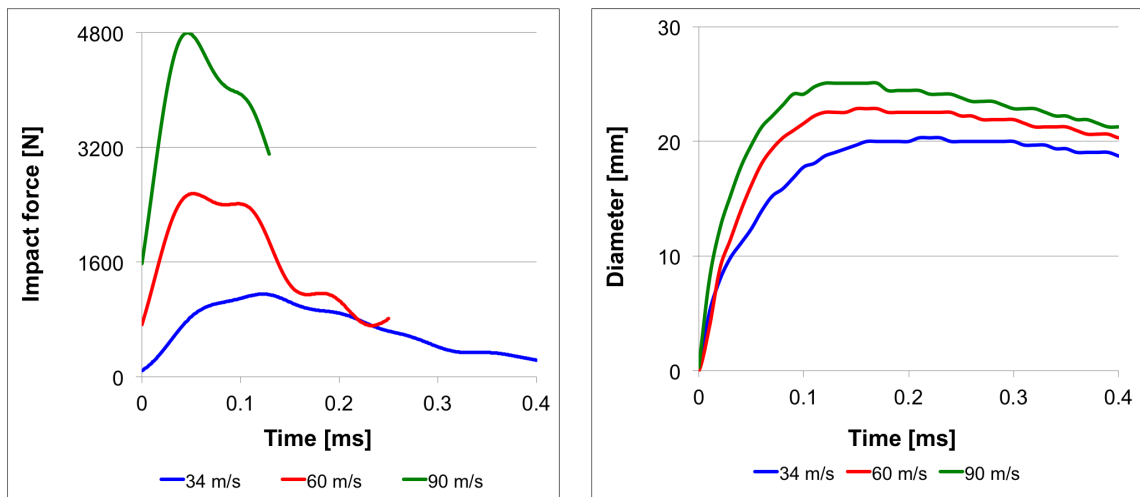


Figure 6.42. *Experimental results of RB1FS impacts on RW at different velocities.*

It is not possible to use the displacement for validation purpose as it was pointed by C. Robbe ([2]), the tracking of the rear of the projectile could not be done correctly as the projectile tail tends to move vertically and rotate during the flight. This makes things difficult at impact in order to track the rear side of the projectile. Therefore only the impact force and the impact diameter will be used.

The description of the geometrical and material models are given in the sections 6.43 and 6.8, respectively.

6.1.7.2 Geometry and mesh

The geometrical and mesh characteristics are given in Figure 6.43.

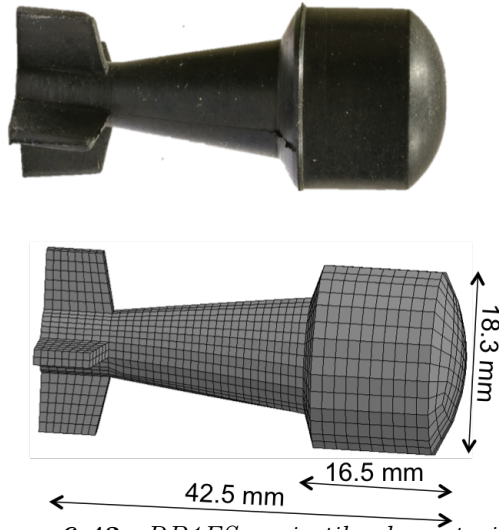


Figure 6.43. RB1FS projectile characteristics.

6.1.7.3 Material characteristics

Upon the impacts, the projectile undergoes large deformations. An hyperelastic (YEOH) model is used for the rubber material. This model provides a good fit over large strain ranges [176]. The material properties are determined thanks to the reverse engineering method. They are given in Table 6.8. where $C10$, $C20$ and $C30$

Parts	Material parameters			Element type/ Number of elements
	Density [kg/mm^3]	Poisson's ratio		
Rubber	1000	0.498	-	Hexa/ 7487
	C10	C20	C30	
	$5 \cdot 10^9$	$-2 \cdot 10^5$	$2 \cdot 10^5$	

Table 6.8. Material characteristics of the RB1FS projectile.

are material model constants.

6.1.7.4 Validation

Results of RB1FS validation given in Figure 6.44 show a good correspondence between the experimental and the numerical results, especially during the loading phase.

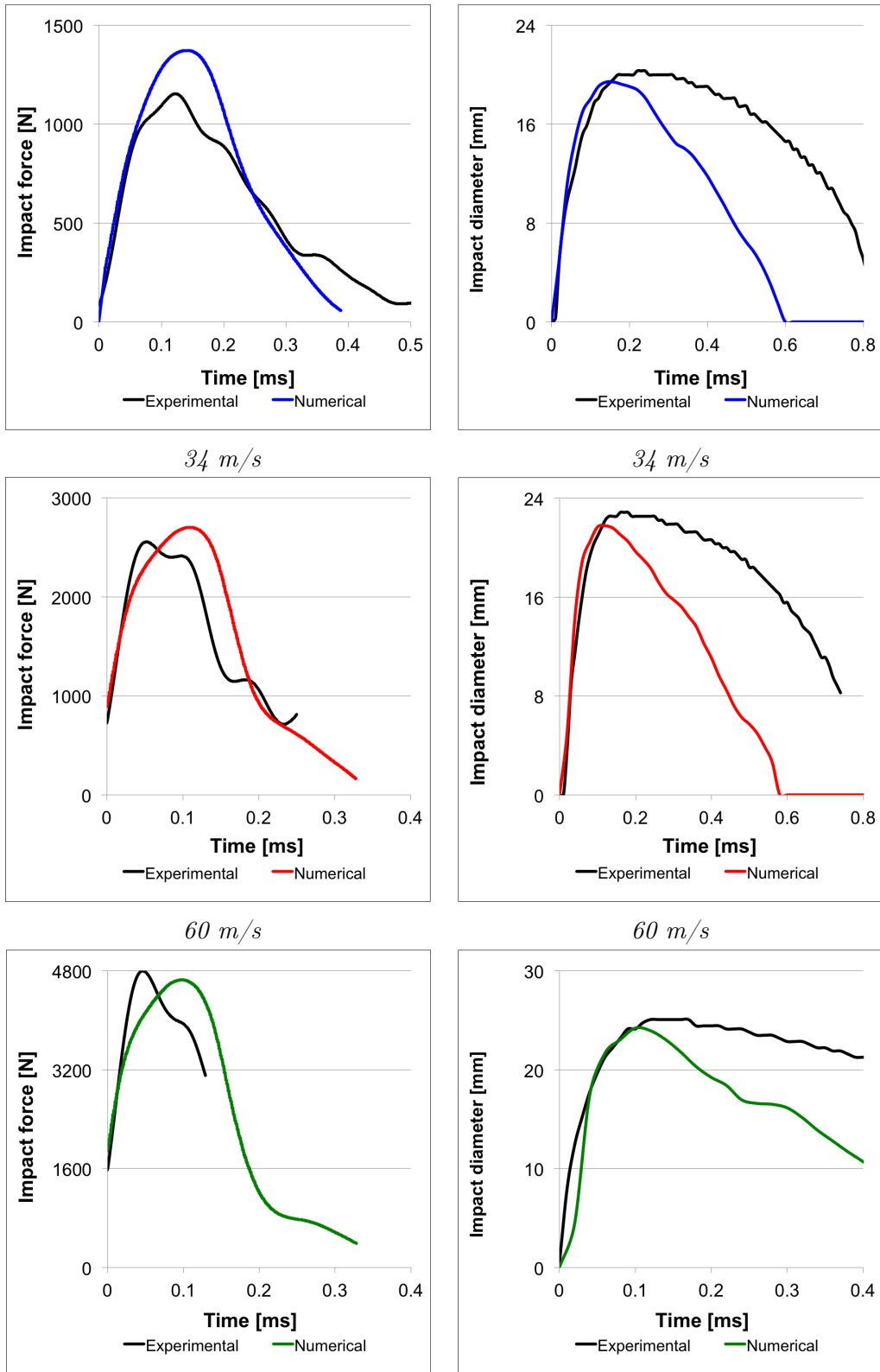


Figure 6.44. Comparison between RB1FS experimental and numerical results for different impact velocities.

6.1.7.5 Discussions

The RB1FS projectile is lighter than the 40 mm sponge grenades. Its impact duration is also much shorter than the 40 mm sponge grenades impact duration.

Unlike the FN303 which breaks at impact, the RB1FS deforms at impact. They are both smaller projectiles compared to the 40 mm sponge grenades. Referring to the impact of 40 mm sponge grenades against RW where an analogy was made to conventional compression tests (the sample is placed between two rigid surfaces), the RB1FS upon impact against RW remains free on the other side. This type of impact departs even more from the conventional testings compared to the method of characterisation of sponge grenades. This makes things more complicated for the projectile characterisation. Therefore the method for sponge grenades could not be applied. An hyperelastic model (Yeoh model) is chosen and parameters of the model are found by indirect engineering method.

Loading is generally correctly captured even though the numerical impact force is overestimated for impact of 34 m/s. The corresponding maximum error is 19%. Unloading is not correctly captured as this can be clearly seen in Figure 6.44. Although unloading is not the main issue, the results can be probably improved by including viscoelasticity in the model.

6.1.7.6 Conclusions

The RB1FS has been characterised. The deformation mechanism is slightly different from the 40 mm sponge as the non-presence of the sabot causes the unloading to take place earlier.

6.1.8 Main conclusions

In this chapter, different projectile FE models have been validated. Due their different characteristics, many methods of characterisation have been used.

A new method of characterising deformable projectile has been applied to SIR-X and CONDOR projectiles. In this method, engineering stress-strain curves are generated and used as input in the material model card. Although the method departs from the requirements of classical testings methods, interesting results have been achieved. Good correspondence has been found between the experimental and numerical results. It has been shown that the deformable nose plays a key role in the global impact response profiles. Most of the projectile initial energy is dissipated through irreversible processes. The great potential of foam/rubber material to absorb or dissipate the energy has been highlighted. This method is applied for full solid deformable projectile nose. The SIR-X projectile model has been validated in the framework of NATO standardisation methods for evaluating the KENLW projectiles and can be used in the standardisation process within the NATO.

For other projectiles, the material model parameters have taken from the literature. The projectiles was validated by adjusting within a certain range the parameters. Satisfying results have been obtained.

Different deformation mechanisms have been identified between the projectiles by taking into account their behaviour upon impact, their structure. The SIR-X and condor projectile noses during impact absorb/dissipate the initial energy by crushing mechanism while the NS projectile by resisting the deformation mainly through its column before the collapse of the nose (or buckling process). The FN303 projectile breaks at impact. Those mechanisms help reduce the energy transmitted to the body.

Unlike deformable projectiles, the FN303 projectile, which is lighter and has a smaller diameter has different characteristics as it breaks at impact. Its dynamics is very different from the deformable projectile. During the impact, the breaking of the projectile helps spread the bismuth grains on the impact surface, increasing 'artificially' the impact area, so the force is applied over a large surface and the energy transmitted to the body is reduced. Nevertheless, a small quantity of energy is used for the breaking of the projectile.

The FN303 and RB1FS projectiles are smaller projectiles compared to the other projectiles. Their masses and diameters are lower. Unlike the FN303 projectile which breaks at impact, the RB1FS deforms at impact like the 40 mm sponge

6.1 KENL projectile FE modelisation

projectiles but has a free surface during the impact on the other side. As there is no sabot.

Chapter 7

Thorax Injury Risk Assessment

In previous chapters, both the SHTIM and the different projectile FE models have been validated. So far, all models (thorax, projectiles) that were developed were prerequisites in order to assess KENLW projectile impacts on the thorax. The goal of this chapter is:

- To assess the thorax injury risk when impacted by a non-lethal projectile.
- To determine the corresponding minimum engagement distance in order to avoid serious injury to the target.
- As a corollary, comparison of the different projectiles in terms of their dangerousness can be made.

In this chapter, the projectiles are evaluated in term of skeletal injury risk. Firstly, some considerations about the evaluation process are first described. Secondly, for each projectile, simulations are then performed at different impact velocities and for each velocity the viscous criterion is computed. Assessment is carried out by comparing the computed viscous criterion to the threshold value. Then the comparison between the 3RBID and the SHTIM model is made. Finally, conclusions are presented.

7.1 Some considerations of the evaluation process

The evaluation process consists here in numerically impacting a KENLW projectile on the thorax and post-processing the results. Based on the viscous criterion, the projectile lethality and the associated injury risk can be determined.

The conditions of impact (especially the impact velocity and the angle of impact) and the impacted body zone are paramount in the evaluation process, mainly for the risk injury assessment. They depend upon the projectile initial velocity, the external environmental conditions, the ballistic characteristics of the projectile and the distance from which the projectile is launched. Although all these parameters are to be taken into account for a full evaluation of the projectile, focus is put on a number of considerations for the risk assessment:

1. There is a relation between the velocity of the projectile and the distance of engagement given by the retardation function (Equation 7.1). This relation is determined experimentally through fitting.

$$V = V_0 e^{-\lambda x} \quad \text{with} \quad \lambda = \frac{\pi d^2 \rho_{air} C D_0}{8m} \quad (7.1)$$

where V_0 , V , d , m , ρ_{air} and $C D_0$ represent the initial velocity, the projectile velocity corresponding to the firing distance x , the projectile diameter, the projectile mass, the air density and the drag coefficient, respectively.

The closer the distance of engagement, higher the corresponding velocity and higher is the risk of serious injury. To assess this risk, for each impact velocity, $(VC)_{max}$, which is the criterion related to the occurrence of the injury, is calculated and compared to the injury tolerance $(VC)_{max}=0.8$ m/s (Section 3.2.3.3). $(VC)_{max}$ value of 0.8 m/s corresponds to 50 % chance of having a thoracic injury of AIS ≥ 1 . The velocity for which $(VC)_{max}=0.8$ m/s is the critical velocity $(V)_{crit}$. To the critical velocity corresponds a critical distance of engagement i.e. the safe distance or the minimum firing distance below which there is higher probability of sustaining an injury with a level of seriousness characterised by a certain AIS (≥ 1 in this case). This sets up a lower limit for the distance of engagement in order to ensure that the projectile is not too dangerous. In the present thesis, this minimum distance of engagement is determined. This is important for the end-users (military, police).

2. The only injuries investigated in the model are rib or sternal fracture as this is the type of injury considered for the definition of the viscous criterion.
3. The thorax deflection is determined by tracking the displacement of the node in the impact zone giving the maximum value of viscous response [160]. It is the key physical parameters from which the injury metrics $(VC)_{max}$ is computed. But there is a condition on the thorax velocity for the validity of the $(VC)_{max}$. It should be between 3 m/s and 30 m/s.
4. The viscous criterion was determined by C. Bir [40] in her experiments by using the impact of rigid projectiles. But most of the actual KENLW projectiles

7.1 Some considerations of the evaluation process

are deformable projectiles. Therefore it is assumed that *"the viscous injury criterion is still valid for other types of KENLW projectiles"* (Section 3.2.1).

5. The normal impact is the worst case in term of injury risk [160, 161]. Therefore, all the impacts considered in the present work are normal to the sternum impact surface (Figure 7.1). Nevertheless *all the physical quantities and the injury metrics are calculated in the horizontal direction X*.
6. The viscous criterion depends on the impacted zone. On the one hand, it is only calculated at the impacted zone due to the localised nature of KENLW impacts. On the other hand, due to high sensitivity of the viscous response on the impact location, all the impacts are performed at the same location corresponding to the configuration used for the thorax model validation [160].

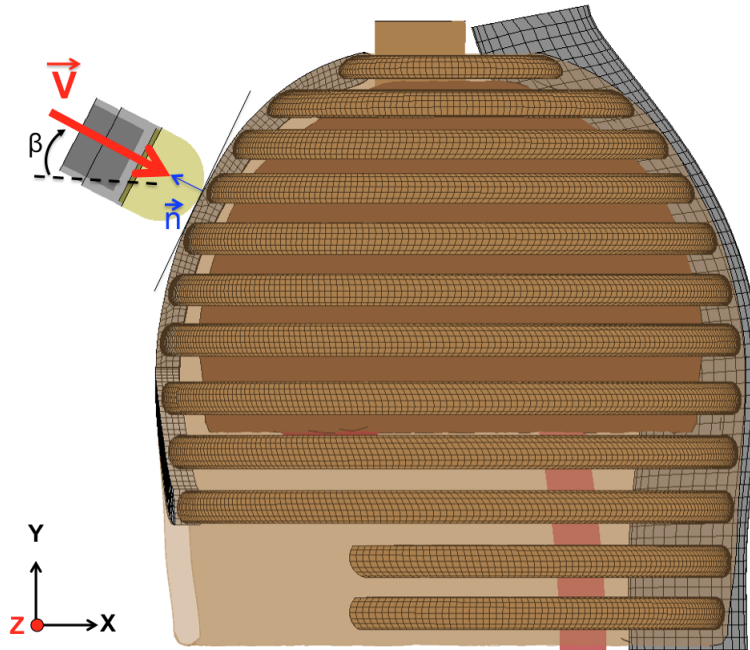


Figure 7.1. Normal impact.

7.2 Thorax impact assessment

Different impact velocities are considered. The evaluation of the SIR-X impact on thorax is carried out in details. For the other projectiles, only important results are given putting emphasis on their specific features.

7.2.1 SIR-X projectile evaluation

The thorax dynamics is the result of the interaction between the projectile and the thorax. Therefore it is important to understand how this interaction affects the dynamics of both the projectile and the thorax. Firstly, the dynamics of the thorax is described, secondly the dynamics of the projectile by comparing the impact on thorax and the impact on RW, the risk assessment is carried out, then the comparison between the actual SIR-X projectile and the SIR-X assumed rigid projectile is made, finally conclusions are presented.

7.2.1.1 Thorax dynamics

The thorax dynamics is described through its deflection and corresponding velocity by tracking the displacement of a node in the impact zone. The impact velocity of 80 m/s is considered to study the dynamics of the thorax. A similar analysis can be made for other velocities. Figure 7.2 shows the thorax deflection, its corresponding velocity and the corresponding impact sequences where one can highlight some specific features. Many interesting phases can be identified.

The first phase (up to time 0.32 ms) can be described by the setting in motion of the thorax where displacement is very low. The second phase is identified by thorax linear velocity behaviour up to the maximum velocity reached at time 0.46 ms. In these two zones, the thorax displacement and velocity are both increasing. In the third phase up to time 0.70 ms corresponding also to the full compression of the projectile, the velocity is decreasing while the projectile displacement is still increasing but with a decreasing rate. Then after that time, the projectile unloading phase begins. During this phase, the velocity globally decreases even though there is a small velocity increase which ends at time 0.82 ms between the red and green dots in Figure 7.2(c). The reason is still not clear But the thorax displacement continues to increase up to the maximum reached at time 1.18 ms. This time corresponds also to the beginning of the thorax unloading phase.

Figure 7.2(c) shows that at this impact velocity, the viscous criterion is satisfied as the thorax maximum velocity is almost equal to 30 m/s (the limit for the condition

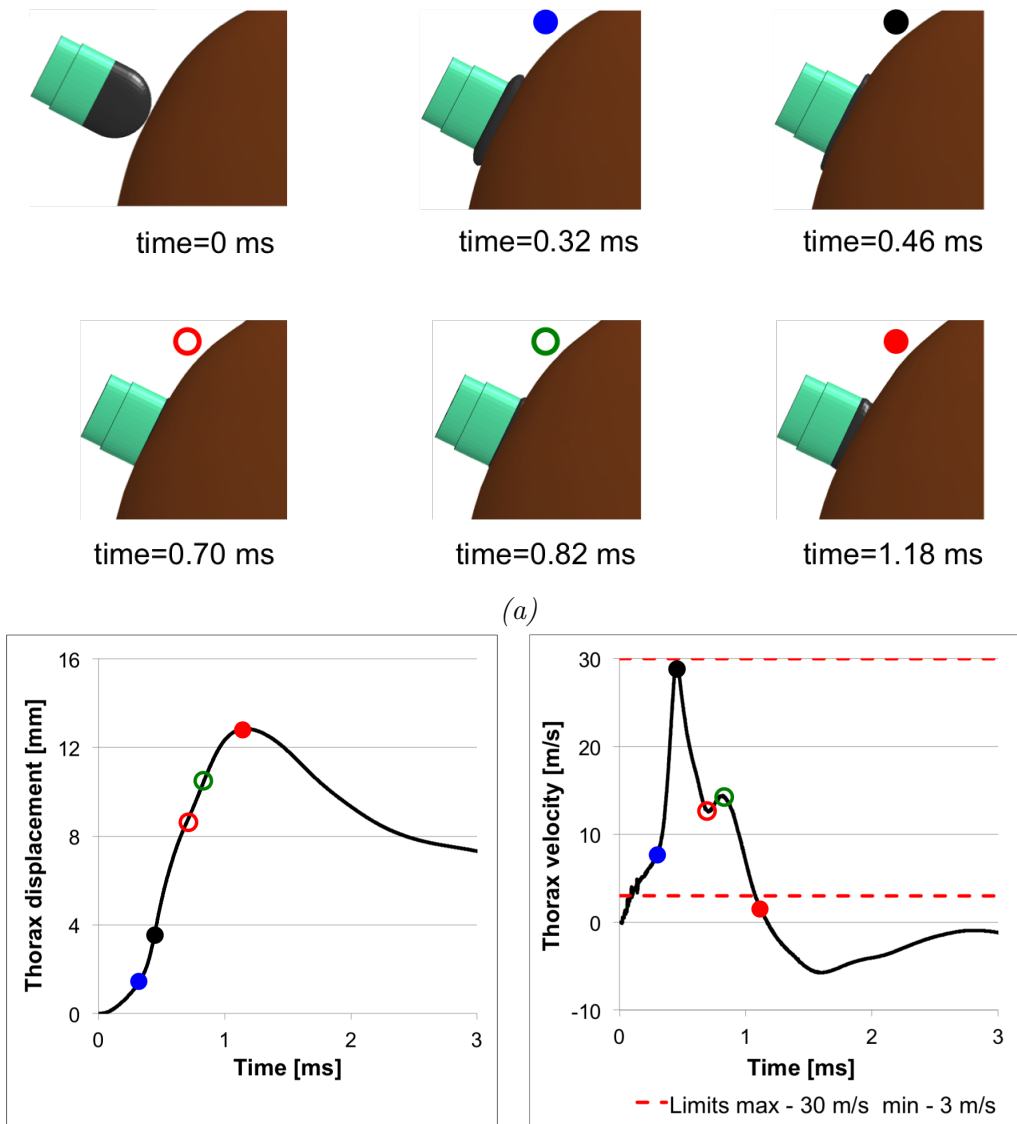


Figure 7.2. ^(b) Thorax dynamics for an impact velocity of ^(c) 80 m/s.

of the validity for viscous mechanism (Section 3.2.1)). Above of 80 m/s, it is then assumed that the criterion is no longer satisfied.

It is pointed out that the maximum displacement is reached later than the maximum velocity.

For lower velocity as for example 40 m/s, the thorax dynamics is quite different as it will be shown later.

7.2.1.2 Comparison of SIR-X dynamics on rigid wall and on thorax

The SIR-X dynamics gives a clue for a better understanding of the difference in target impact dynamics of a deformable structure (thorax) compared to a rigid one (RW) by only examining the projectile. For this purpose, the impact results of the SIR-X projectile on thorax (Figure 7.3) at 80 m/s can be compared to the ones on RW (Figures 6.8 (b)-(c), 6.9(b) and 6.18) at 58 m/s. There is a similarity up to a certain extent (especially during loading) between these curves. Therefore, The whole process can be described in the same manner as for the SIR-X impact on RW (section 6.1.3).

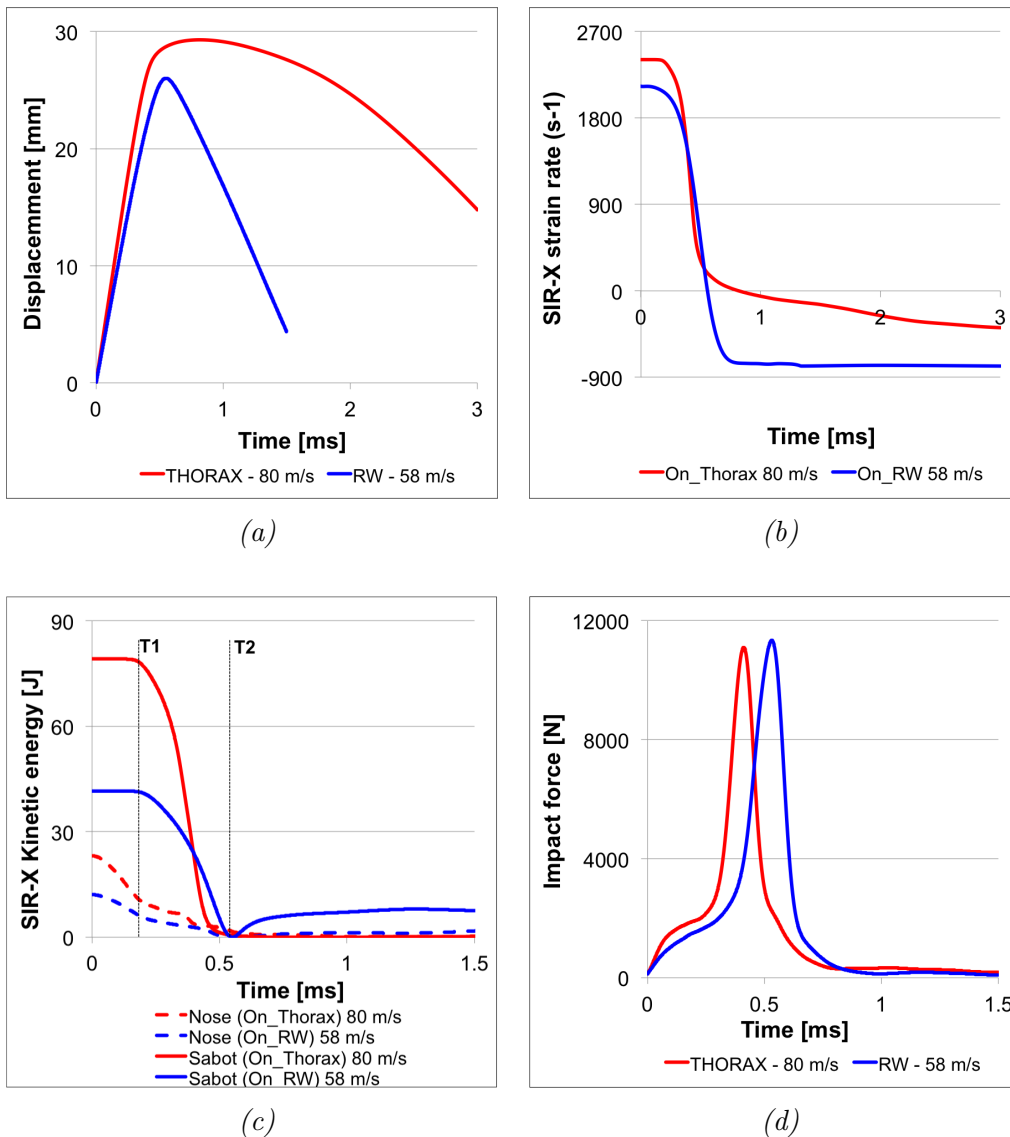


Figure 7.3. Comparison of SIR-X impact dynamics on RW at 58 m/s and on thorax at 80 m/s.

The displacement curve shows that the loading takes place at a constant rate. The evolution of the strain rate determined via Equations 6.5-6.7 is given in Figure ??(b) and measured at the projectile rear side. Unlike the RW impact during the unloading, here the strain rate is no more constant after the transition phase. In Figure 7.3(c), the sabot begins to decelerate at $T1=0.2$ ms. Then, the kinetic energy of the sabot as well as the kinetic energy of the nose drops drastically and is almost equal to zero at $T2=0.7$ ms corresponding to the end of the projectile loading phase as shown in Figure 7.3(d). The projectile behaves then like a rigid projectile as the nose is completely compressed between the projectile and the thorax. Only then begins the projectile unloading. The time interval between $T1$ and $T2$ corresponds to the period where most of the projectile energy is absorbed and the highest absorption energy rate is achieved. This same observation is made with the impact on RW but the absorption rates are different.

The unloading paths are very different, linear in the case of RW and non-linear in the case of the impact on thorax. The reason of this behaviour is the thorax compliance. Recall the rebound velocity is related to the slope of the unloading path. The non-linear behaviour of the thorax unloading shows that the time of contact between the projectile and the thorax is larger compared to the RW case. The consequence is that the energy stored in the nose is released with a lower rate than for the RW. As the energy is only absorbed during the loading phase, it is possible to determine the part of initial energy available for thorax deformation. One can write the energy balance by the equation 7.2 [177].

$$E_{tot} = (E_{kin}^0)_{proj} = \underbrace{(E_{kin} + E_{int} + E^*)_{proj}}_{(E)_{proj}} + \underbrace{(E_{kin} + E_{int} + E^*)_{thx}}_{(E)_{thx}} \quad (7.2)$$

where E_{tot} , E_{kin}^0 , E_{kin} , E_{int} and E^* are the total energy, the initial kinetic energy, the kinetic energy, the internal and other types of energy (hourglass energy as example), respectively. The subscripts *proj* and *thx* refer to the projectile and the thorax respectively. All these quantities are retrieved from LS-DYNA, $E_{kin}^0=102.2$ J and $(E)_{proj}=55.8$ J. One can determine the available energy for the thorax $(E)_{thx}=46.4$ J. It corresponds to 45.4 % of the initial energy. In the case of the RW, all the initial energy is absorbed by the projectile either by deformation or by dissipation processes as the impact is on RW. For the thorax, only a reduced energy is transferred, so is the the risk of injury.

67.4% of the energy transferred to the thorax is dissipated through irreversible processes. One possible axis of investigation is to try to correlate this energy to the occurrence of injury.

The contact force evolution is given in Figure 7.3(d). The whole dynamics in term of force profile and maximum force on the thorax can be compared to the one on RW except that the strain rates are different, higher for the impact on thorax.

As the strain rates are different even though there is a similarity in the projectile dynamics between the two targets, the target material has also an influence on the strain rate (Figure 7.3(a)-(b)). Therefore, impact velocity can not be the only parameter that is used to discriminate the impact force or displacement, one has to take into account other characteristics like the target material. This raises an issue about the projectile characterisation: What is the range of velocities to be considered for the validation of the projectile? One could expect to validate the projectile model at lower impact velocities on RW and impact the projectile on deformable target at high velocity. This might be not the case at the light of the observation. Moreover, the major difficulty would be to find the correspondence at which the validation on RW should be made. More investigation is then necessary.

All these considerations lead to the fact that the impact of SIR-X projectile on the thorax as a deformable structure can be considered as an impact on RW but at a reduced impact velocity, the behaviour being similar during the loading. This seems to confirm the assumption previously made on the validity of the viscous criterion for deformable projectiles.

7.2.1.3 SIR-X risk assessment

Figure 7.4 gives $(VC)_{max}$ for impact velocities of 40 m/s and 80 m/s. A number of features can be highlighted.

- The behaviour at lower velocities is different from the one at higher velocities. Indeed, at 80 m/s, the viscous response as well as the velocity, function of time shows two peaks where there is only one at 40 m/s.
- For 80 m/s, there are two peaks in the curve and the maximum value of $(VC)_{max}$ is achieved on the second peak while there is only one peak for lower velocity. The values of $(VC)_{max}$ for 40 m/s and 80 m/s are 0.15 m/s and 0.64 m/s respectively.

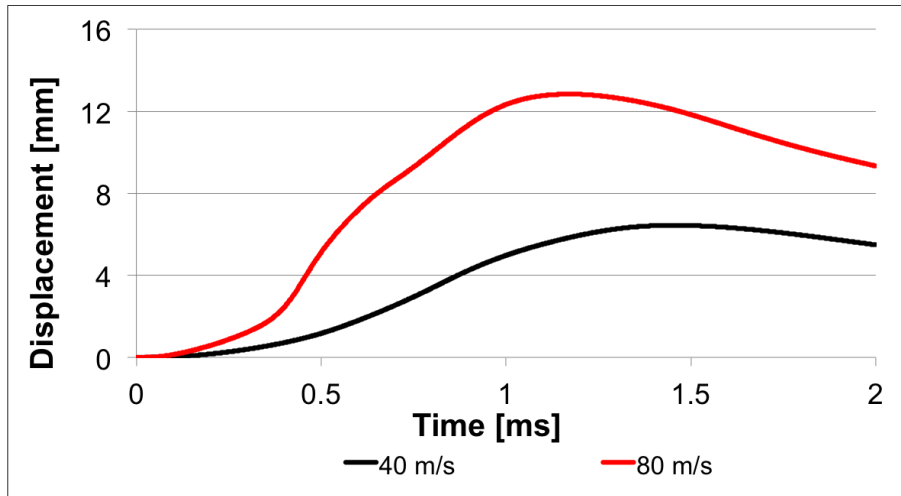
Figure 7.5 gives the results of $(VC)_{max}$ for all considered impact velocities. The critical velocity corresponding to a $(VC)_{max}$ value of 0.8 m/s is equal to 91 m/s (Figure 7.5). But for velocities higher than 80 m/s (Figure 7.4(b)), the criterion is no longer satisfied. So the results are given in this case as an indication. Recall the condition on the validity for viscous criterion is that the thorax velocity is between 3 m/s and 30 m/s (Section 3.2.1).

The nominal velocity in our case is 105 m/s. Using the retardation relation (Equation 7.1) which gives the relation between the firing distance and the corresponding velocity, the safe distance can be determined. With a value of $CD_0=0.2$, the distance can be calculated (Equation 7.1). Therefore the safe distance can be determined and is equal to 28 m. The results of the full risk assessment of the SIR-X is given in Table 7.1. It gives the firing distance and the corresponding velocity. For each velocity, the ad hoc criterion is checked. The red cells means that the viscous criterion has failed, the impact is considered as dangerous in term of injury. The yellow cells means that criterion is satisfied but the condition of maximum velocity 30 m/s (limit for the viscous mechanism) is not satisfied, therefore certain reservations can be expressed regarding their relevance. The viscous criterion is satisfied for all the velocities less than the critical velocity. But one has to check also for other criteria as the R90 criterion linked to the dispersion [2].

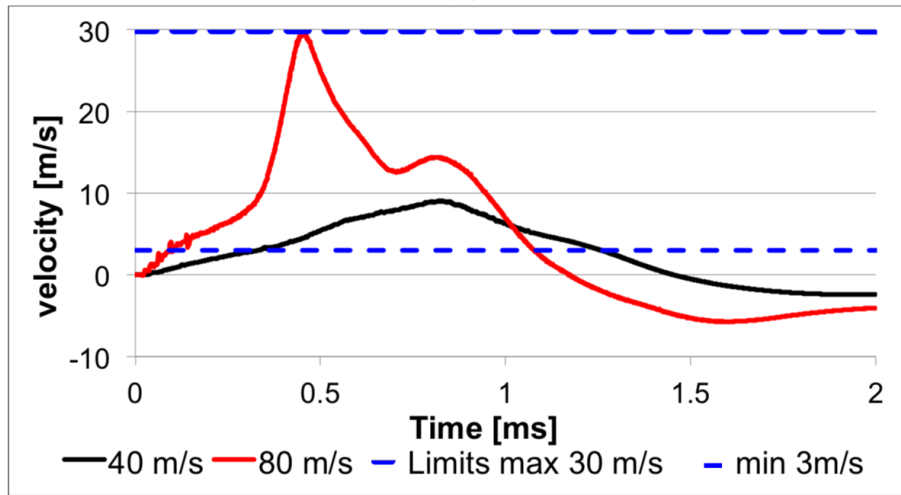
firing distance [m]	Projectile velocity [m/s]	$(VC)_{max}$ [m/s]	Result/failed criterion
0	105	1.09	$(VC)_{max}$
10	100	0.98	$(VC)_{max}$
20	95	0.88	$(VC)_{max}$
30	90	0.79	OK
40	86	0.71	OK
<i>Red=dangerous - Yellow= $(VC)_{max}$ satisfied but the condition 30 m/s is violated</i>			

Table 7.1. Final result of the lethality analysis of the SIR-X projectile.

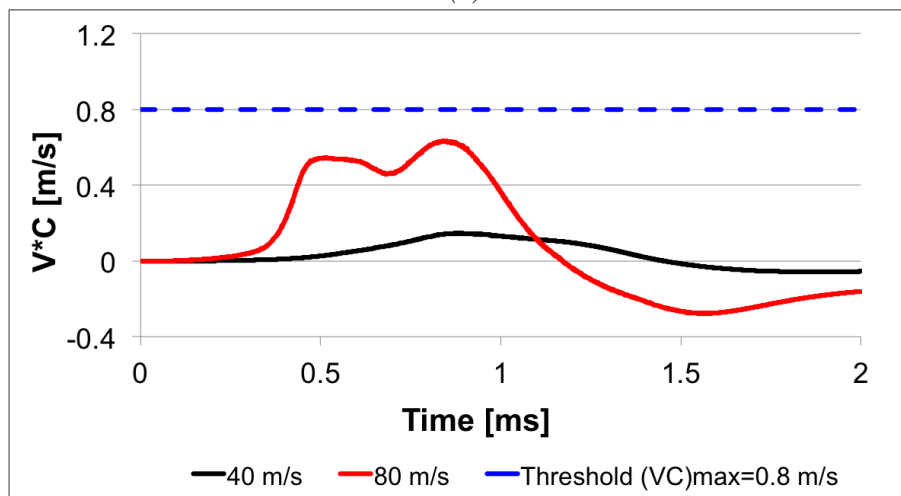
The first generation of KENLW projectiles was made of stiff or rigid projectiles. Then, the question that comes to the mind is 'how the thorax would behave if the SIR-X projectile was a rigid projectile', all other characteristics being equal? The analysis will be made in following section.



(a)



(b)



(c)

Figure 7.4. Thorax $(VC)_{max}$ calculation for SIR-X impact velocities of 40 m/s and 80 m/s.

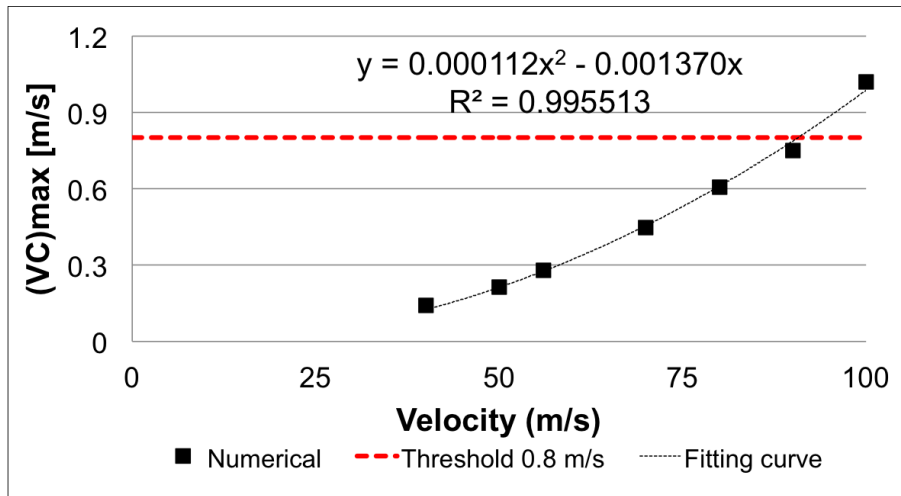


Figure 7.5. $(VC)_{max}$ for different velocities for SIR-X projectile.

7.2.1.4 SIR-X versus assumed SIR-X rigid projectile

By assuming a SIR-X rigid projectile with the same mass as the actual SIR-X projectile, the comparison can be made between the two cases. For that purpose, an average density is calculated and assigned to the rigid projectile. Figure 7.6 shows the comparison of the thorax dynamics induced by the impact of NS projectile and its corresponding rigid projectile.

Focussing on the velocity graph (Figure 7.6(b)), the behaviour of the rigid projectile corresponds to the curve with steepest slope. Although the condition on the thorax velocity being less than 30 m/s is not satisfied for the rigid case, it is used as illustration to compare the two dynamics. For the actual NS projectile case, the part of the curve between A and B corresponds to the compression of the nose and the part of curve between B and C to the rigid like behaviour. Indeed, the BC slope gives the extent at which the NS projectile behaviour is close to the rigid behaviour during the loading. The higher is the impact velocity, the steeper is this slope, and more the behaviour is similar to the rigid projectile behaviour. The effect of the nose is highlighted by a drastic reduction of the pic of the rigid projectile case and the delayed effect of the rigid-like behaviour.

Therefore the thorax response due to the SIR-X projectile impact is like time-shifted with respect to the rigid one. This shift interval δ is the laps of time corresponding to the deformation of the nose. After this interval, the projectile behaves like a rigid projectile. The thorax velocity and the viscous response graphs show that the slope become steeper after δ ms.

The amplitudes of the thorax velocity and contact force are different, higher for the rigid projectile. Because this combined effect of delayed effect and the rigid-like

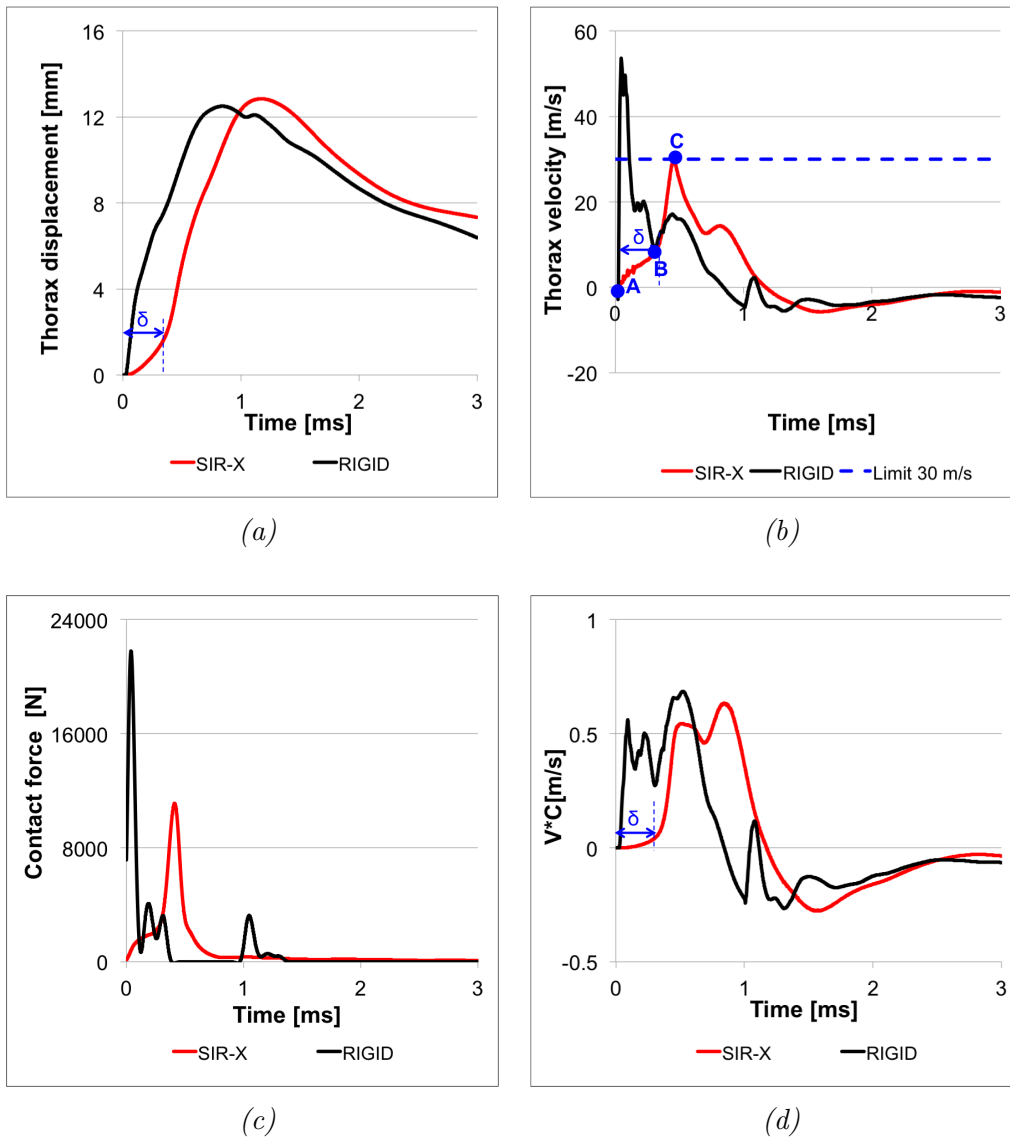


Figure 7.6. Comparison of SIR-X impact and the corresponding rigid one impact on the thorax at 80 m/s.

behaviour, the SIR-X projectile behaviour during impact can be compared to the behaviour of a rigid projectile with a time-delayed effect but at a reduced energy as part of the energy is absorbed/dissipated by the nose.

Comparison of $(VC)_{max}$ is given in Figure 7.7. The values of $(VC)_{max}$ are of the same order. This is a surprising result but in reality there are two different mechanisms taking place. Indeed, the condition on the maximum velocity (30 m/s) is more rapidly reached for the rigid projectile than in the case of the corresponding deformable projectile. It is generally admitted that above this velocity, the injury mechanism that is activated is similar to blast effect (section 3.2.1). It should be pointed out that only rib and sternal fractures are considered when it comes to the

viscous criterion. Nothing can be said about other types of injury. Therefore it can be said that for the rigid projectile, the dynamics is more driven by the velocity while for the deformable projectile in the considered range of velocities, the phenomenon is driven by the viscous response from which $(VC)_{max}$ is derived. Moreover, maximum forces are higher for the rigid projectile.

For now, the results have been taken with precaution.

There is almost no difference between the $(VC)_{max}$ values with the SIR-X projectile and with the assumed rigid one. This is a surprising result as one could expect to have higher values for the rigid projectile. But not necessary the same mechanisms are activated as the condition on the thorax velocity is not satisfied for the rigid projectile almost in the entire velocity range.

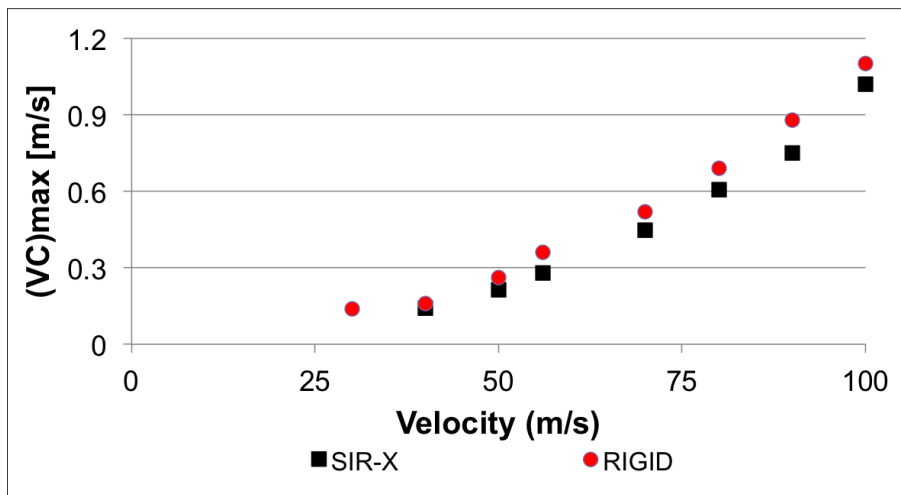


Figure 7.7. Comparison of $(VC)_{max}$: SIR-X projectile vs SIR-X assumed rigid projectile.

7.2.1.5 Conclusions

The impact dynamics of the SIR-X projectile on thorax was investigated. Based on the viscous criterion, minimum firing distances, the safe distances were determined. It is pointed out that in certain cases, the condition on thorax velocity was violated. The results should then be taken with precaution.

By comparing the dynamics of the projectile during the impact on thorax and on RW, it was shown that the dynamics of the SIR-X projectile on thorax at a given velocity especially during the loading is similar to the SIR-X dynamics on RW but with lower impact velocity even though the strain rates are different. This can be explained by the fact on RW, all the energy is absorbed by the projectile and that is no more the case when it is a deformable target. Only a part of initial energy

is transmitted to the thorax. Therefore the risk of injury is reduced. The energy transfer rate to the thorax is the highest during the loading after the deformable nose has been fully crushed.

Comparison was made between the real projectile and an assumed SIR-X rigid projectile. It has been found that there was almost no difference by comparing $(VC)_{max}$ values with the actual SIR-X projectile. This is a surprising result as one could expect a higher values for the rigid projectile. Is the problem related to the nature of the deformable nose material used? More investigation is needed to confirm or infirm this conclusion by using other deformable projectiles. The SIR-X projectile under impact on thorax behaves like a corresponding rigid one with a delayed effect. The delayed effect corresponds to the deformation of the nose is related to the energy absorbing capacity of the nose material. Higher is the impact velocity, more the SIR-X projectile will behave like a rigid projectile during the impact as the deformation rate of nose is increased. This tends to confirm the assumption that has been made about the viscous criterion, it is still valid for deformable projectiles.

7.2.2 CONDOR projectile evaluation

The CONDOR impact dynamics on thorax is quite similar to the SIR-X one. Only the final results on the lethality are given. Figure 7.8 represents $(VC)_{max}$ as function of the velocity.

Using the criterion and the nominal velocity of 105 m/s, the determined critical velocity is 88 m/s corresponding to a firing distance of 31 m calculated via the retardation relation. Table 7.2 gives the final result of the risk assessment. It is worth pointing out that above the safe distance (or below the critical velocity), the viscous criterion is satisfied. In this case, the limiting factor is the R90 criterion (dispersion) that has to be checked [2].

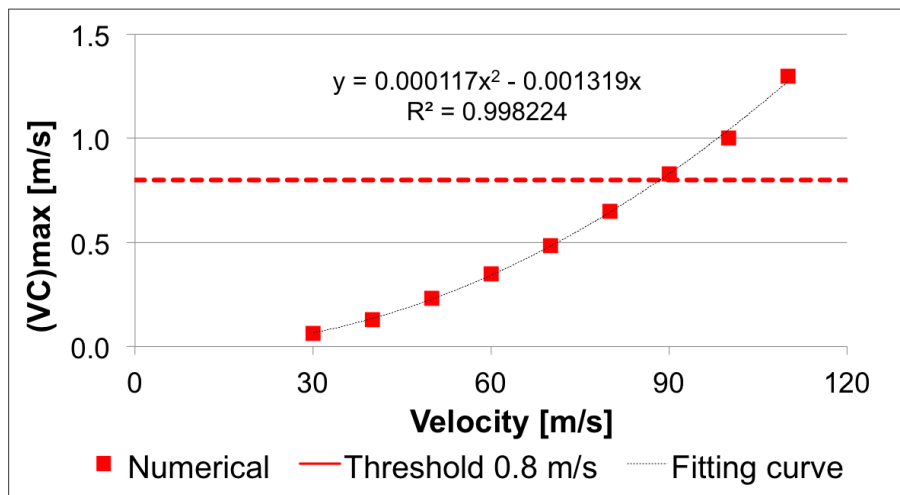


Figure 7.8. $(VC)_{max}$ for different impact velocities of the CONDOR projectile on thorax.

firing distance [m]	Projectile velocity [m/s]	$(VC)_{max}$ [m/s]	Result/failed criterion
0	105	1.15	$(VC)_{max}$
10	99	1.02	$(VC)_{max}$
20	94	0.91	$(VC)_{max}$
30	89	0.81	$(VC)_{max}$
40	84	0.71	OK

Red=dangerous - *Green*=acceptable - *N/A*=not available

Table 7.2. Final result of the lethality analysis of the CONDOR projectile .

7.2.3 NS projectile evaluation

NS projectile has been described in section 2.4.2.5 and 6.1.5. No detailed analysis is carried out as the one performed of the SIR-X projectile, but only final results will be given and differences highlighted.

7.2.3.1 NS risk assessment

As previously stated, even if the NS projectile has a different deformation mechanism than the SIR-X projectile, the same methodology is used as for the SIR-X projectile. The thorax dynamics for 40 m/s and 80 m/s is given in Figure 7.9 and is quite similar to the thorax dynamics for the impact of SIR-X projectile (Figure 7.4). For each velocity, $(VC)_{max}$ can be determined and results are given in Figure 7.10.

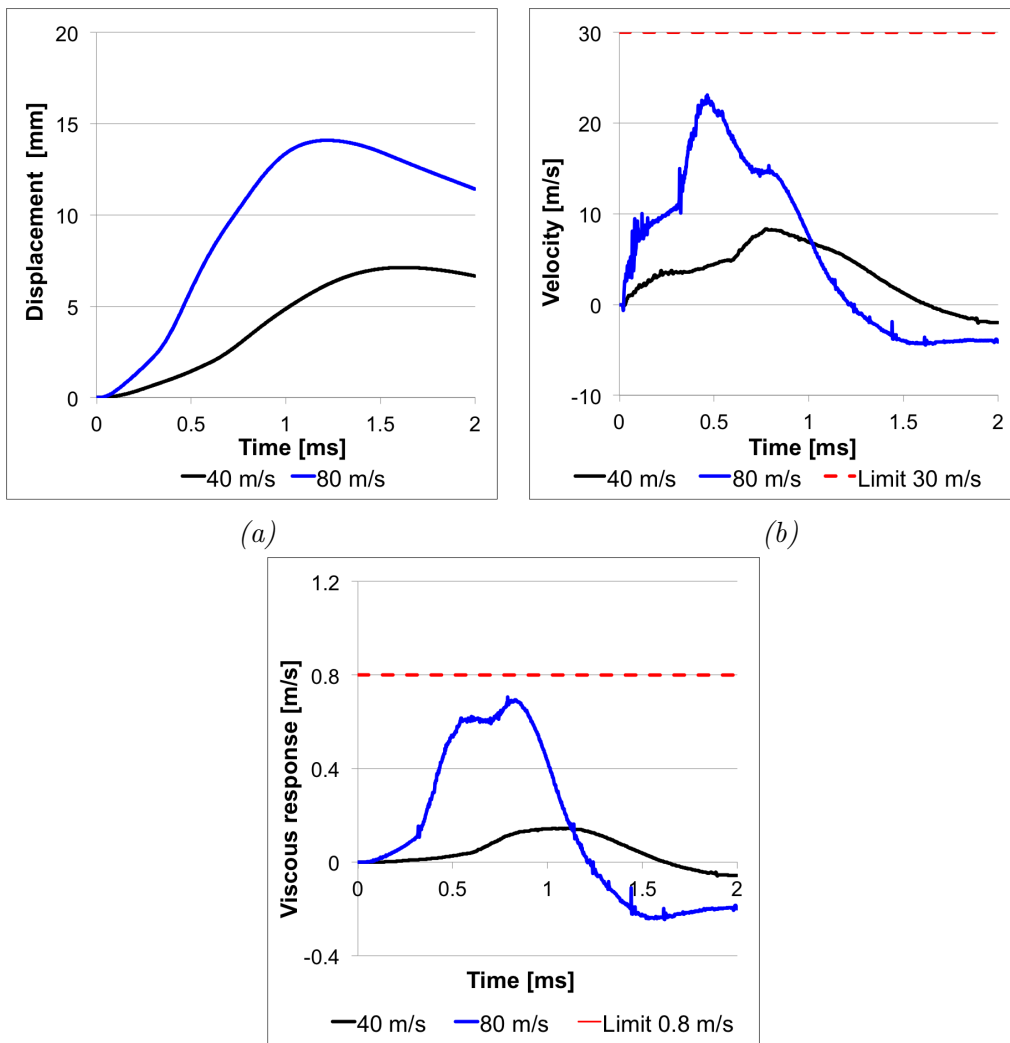


Figure 7.9. Comparison of NS impact^(c) on thorax for 40 m/s and 80 m/s.

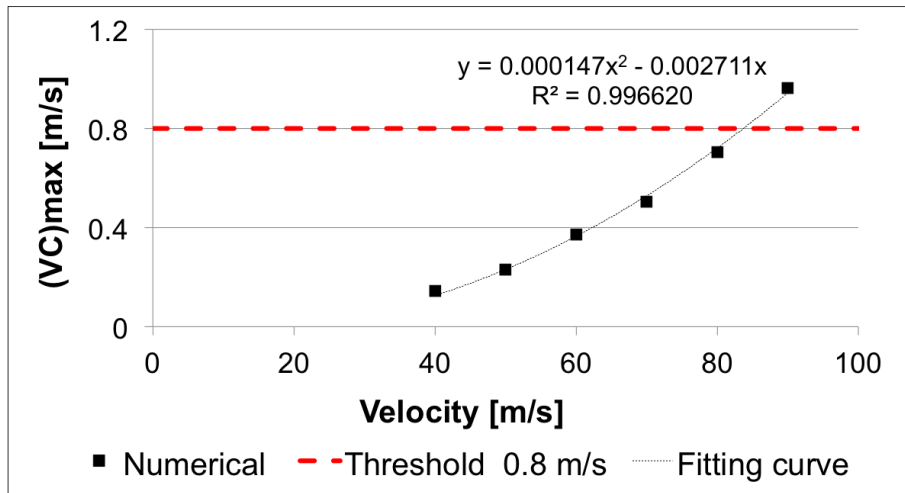


Figure 7.10. $(VC)_{max}$ for different impact velocities of the NS projectile on thorax.

Using the criterion, the determined critical velocity is 84 m/s corresponding to a firing distance of 16 m calculated via the retardation relation. Table 7.3 gives the final result of the risk assessment. It is worth pointing out that above the safe distance (or below the critical velocity), the viscous criterion is satisfied. In this case, the limiting factor is the R90 criterion (dispersion) that has to be checked [2].

firing distance [m]	Projectile velocity [m/s]	$(VC)_{max}$ [m/s]	Result/failed criterion
0	92	0.99	$(VC)_{max}$
10	87	0.87	$(VC)_{max}$
20	82	0.76	OK
30	77	0.66	OK
40	72	0.56	OK
<i>Red</i> =dangerous - <i>Green</i> =acceptable			

Table 7.3. Final result of the lethality analysis of the NS projectile .

7.2.3.2 Comparison of NS dynamics on rigid wall and on thorax

It is interesting to apply the same approach with the one followed for the SIR-X projectile to see if the same conclusion can be drawn.

One can see that there is no difference between the two cases during a great part of the loading phase showing that the behaviour of the NS projectile on thorax is similar to the behaviour of the same projectile on RW at lower velocity. This tends to confirm the assumption on the validity of $(VC)_{max}$ for deformable projectiles. It is the similar conclusion that has been drawn for the SIR-X projectile.

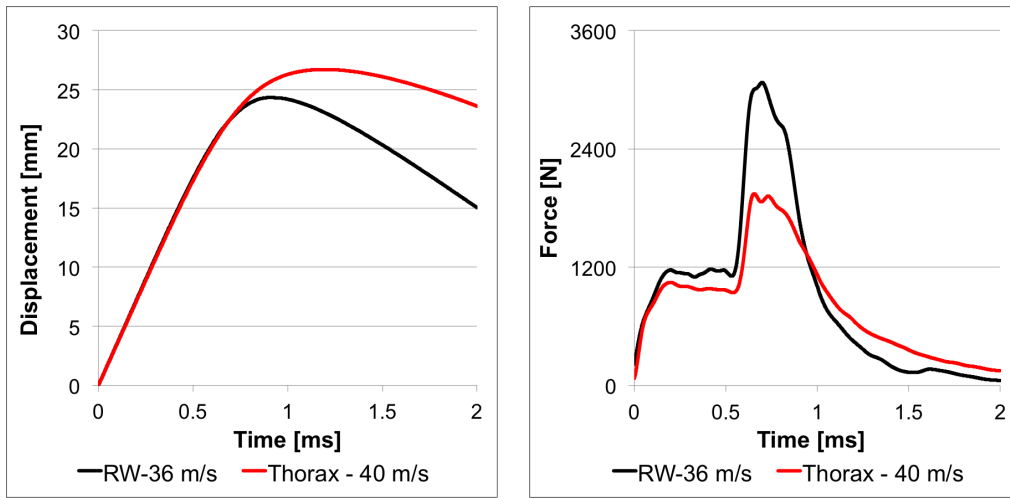


Figure 7.11. Comparison of NS impact dynamics on RW at 36 m/s and on thorax at 40 m/s.

7.2.3.3 NS projectile versus assumed NS rigid projectile

The same approach of an assumed rigid projectile used for the SIR-X projectile is also applied to the NS projectile.

In Figure 7.12 is shown the comparison between the thorax displacement and the corresponding velocity for the NS projectile and its corresponding rigid projectile. Focussing on the velocity graph, the behaviour of the rigid projectile corresponds to the curve with steepest slope. Although the condition on the thorax velocity being less than 30 m/s is not satisfied for the rigid case, it is used as an illustration to compare the two dynamics. For the actual NS projectile case, the part of the curve between A and B corresponds to the compression of the nose and the part of curve between B and C, to the rigid like behaviour. Indeed, the BC slope gives the extent at which the NS projectile behaviour is close to the rigid behaviour during the loading. Higher is the impact velocity, steeper is this slope, more the behaviour is similar to the rigid projectile behaviour. The effect of the nose is highlighted by a drastic reduction of the peak of the rigid projectile case and the delayed effect of the rigid like behaviour.

The viscous criterion can be determined for both cases and the results are given in Figure 7.13. The results of the assumed rigid projectile is higher than the ones with the actual projectile. By comparing the results to the results obtained with SIR-X and CONDOR projectiles, the difference between the actual projectile and the assumed rigid one is higher.

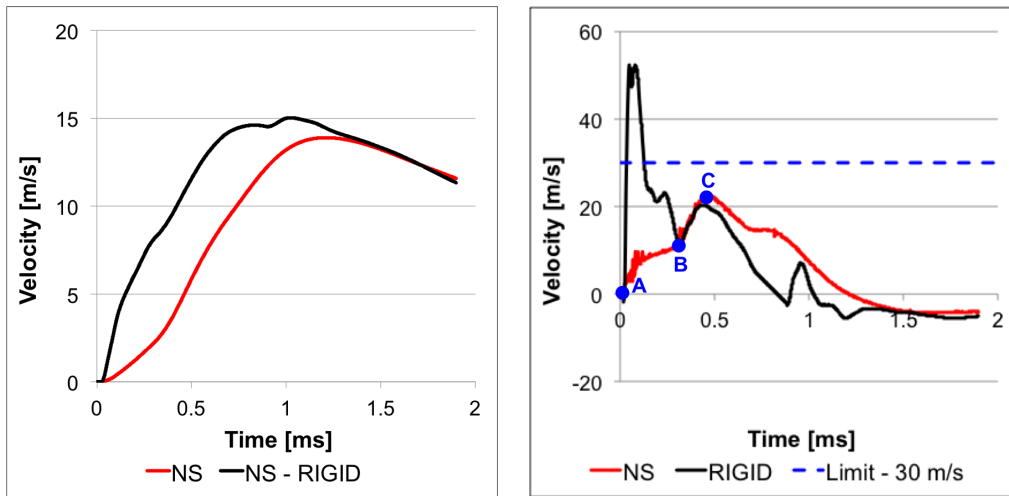


Figure 7.12. Comparison of thorax displacement and velocity at 80 m/s: NS vs assumed NS Rigid projectiles.

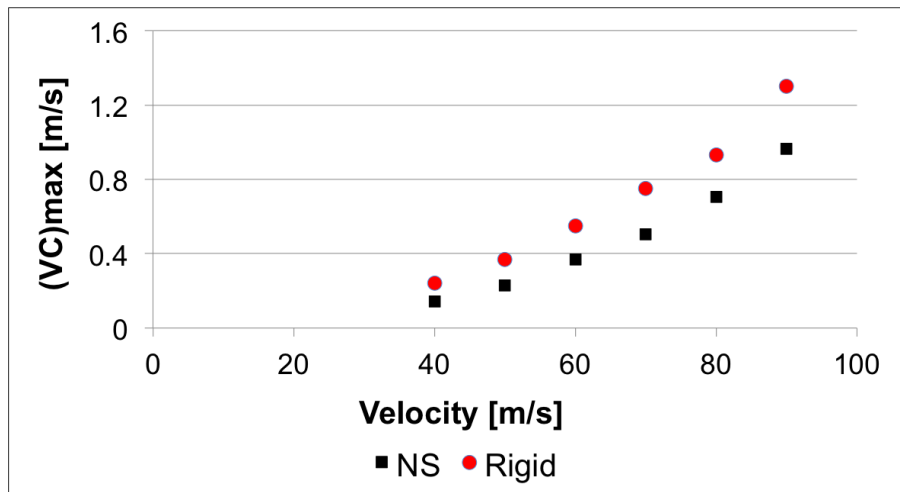


Figure 7.13. Comparison of $(VC)_{max}$: NS vs assumed NS Rigid projectiles.

7.2.3.4 Conclusions

The evaluation of the NS projectile has been made. The range within which the NS projectile is effective without causing higher risk of injury has been determined. The NS dynamics on thorax has been compared to the one on RW. It is shown that to a certain extent, the NS dynamics on thorax is similar to the one on RW but at lower velocity. This shows that the assumption made on the validity of the viscous criterion for deformable seems consistent. Thorax dynamics due to the impact of the actual NS projectile has been compared to the impact of an assumed NS rigid projectile. The values of the criterion are different and are higher for the rigid projectile impact.

7.2.4 FN303 projectile evaluation

The FN303 projectile has been described in section 2.4.2.8. Unlike the 40 mm diameter projectiles evaluated up to now, the FN303 projectile is a light small projectile. In the following sections, the assessment of FN303 will be carried out.

7.2.4.1 FN303 risk assessment

Figure 7.14 shows the thorax deflection (displacement) at 90 m/s and the corresponding velocity from which the viscous response and the $(VC)_{max}$ are derived. Results of $(VC)_{max}$ for all impact velocities are given in Figure 7.15 and in Table 7.4. Most of these results were taken from [2].

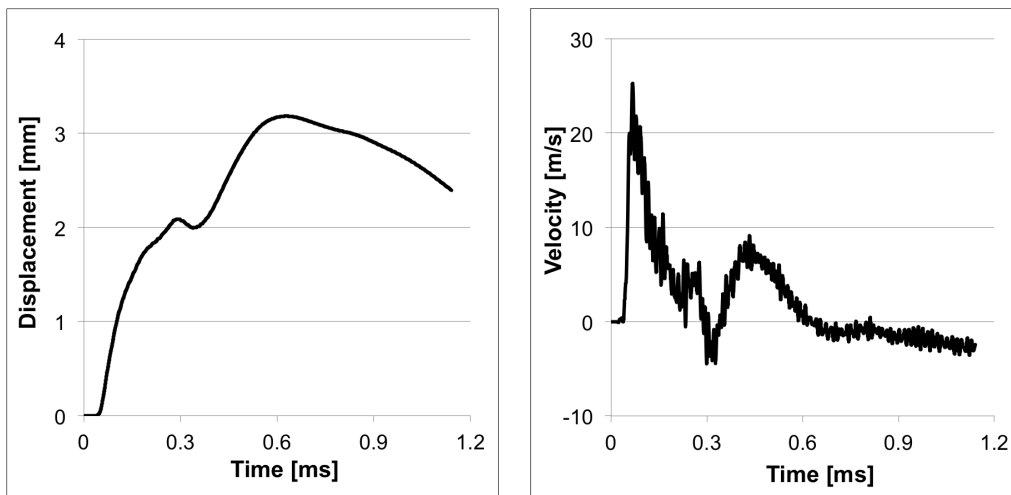


Figure 7.14. Thorax dynamics due to the impact of FN303 projectile at 90 m/s.

It is observed that the displacements obtained with the FN303 projectile is very low compared to the ones obtained with the 40 mm sponge grenades. Likewise, the $(VC)_{max}$ values are very low compared to the threshold 0.8 m/s. Indeed, the FN303 projectile is very small and light. It has a lower kinetic energy, lower momentum and a smaller impact surface compared to the 40 mm sponge grenades. As a result, it is more difficult for this projectile to deform the thoracic cage as much as the 40 mm projectiles do. The condition of thorax velocity being less than 30 m/s is not always satisfied for all the nodes of the impact zone at higher velocities. But this problem has already been addressed previously. Beyond this limit, other injury mechanism type is activated. The $(VC)_{max}$ values being extremely low, there is no minimum safe distance with this projectile. One can shoot at very close distance with a relative low risk of injury (rib/sternal fracture). This is very interesting for indoor engagements where the distances of engagement are often very short.

Although the viscous criterion is satisfied for all velocities, one still have to check for the skin penetration and the dispersion criterion[2].

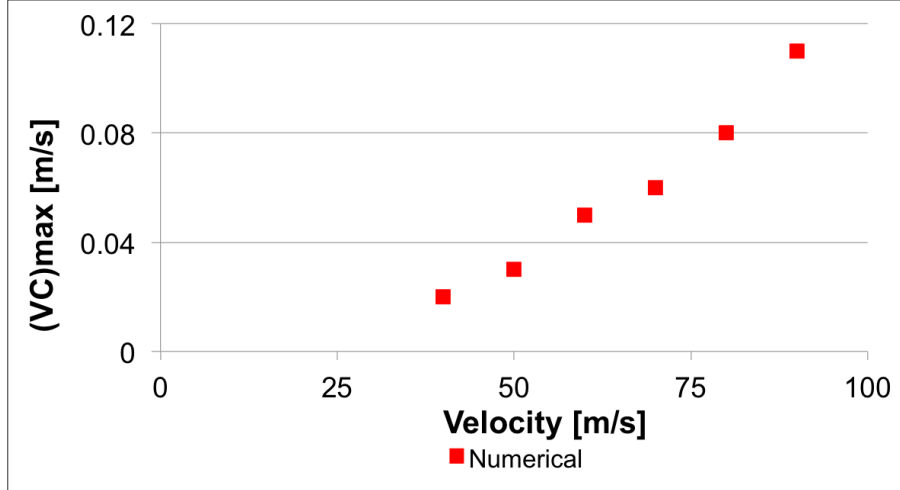


Figure 7.15. $(VC)_{max}$ for different impact velocities of the FN303 projectile on thorax.

firing distance [m]	Projectile velocity [m/s]	$(VC)_{max}$ [m/s]	Result/failed criterion
0	90	0.11	OK
10	84	<0.11	OK
20	78	<0.11	OK
30	73	<0.11	OK
<i>Red=dangerous - Green=acceptable</i>			

Table 7.4. Final result of the lethality analysis of the FN303 projectile fired from the FN303 launcher.

7.2.4.2 Conclusions

The FN303 projectile has been evaluated. It has been shown that the displacements at all impact velocities are very low, so are the $(VC)_{max}$. The reason is its low mass and its small diameter. There is no minimal safe distance. Therefore the FN303 projectile can be used at close distance without higher risk of injury.

7.2.5 RB1FS projectile evaluation

The RB1FS projectile has been described in section 2.4.2.7. It can be compared in terms of mass and nominal diameter to the FN303 projectile. In the following sections, the assessment of FN303 will be carried out.

7.2.5.1 RB1FS risk assessment

Figure 7.16 shows the thorax deflection (displacement) at 90 m/s and the corresponding velocity from which the viscous response and the $(VC)_{max}$ are derived. Results of $(VC)_{max}$ for all impact velocities are given in Figure 7.17 and in Table 7.4.

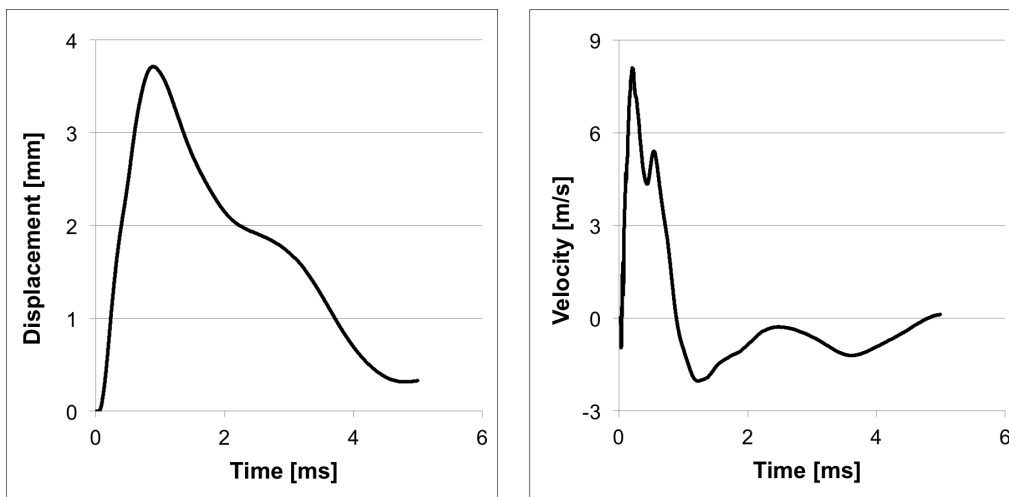


Figure 7.16. *Thorax dynamics due to the impact of RB1FS projectile at 90 m/s.*

It is observed that the displacements obtained with the RB1FS projectile are of the same order than the ones obtained with the FN303 projectile. Likewise, the $(VC)_{max}$ values are very low compared to the threshold 0.8 m/s. Indeed, like the FN303 projectile, the RB1FS projectile is very small and light with a lower kinetic energy, lower momentum and a smaller impact surface compared to the 40 mm sponge grenades. As a result, it is more difficult for this projectile to deform the thoracic cage as much as the 40 mm projectiles do. Nevertheless the corresponding induced velocities are very different, lower for the RB1FS projectile (Figures 7.15 and 7.17.) The reason might be the different projectile material characteristics. The RB1FS projectile is a homogenous projectile made of rubber material which at impact deforms while for the FN303 projectile, it breaks at impact.

The condition of thorax velocity (30 m/s) is always satisfied for all the considered velocities.

The $(VC)_{max}$ values being extremely low, there is no minimum safe distance with this projectile. One can shoot at very close distance with a relative low risk of injury (rib/sternal fracture). As there is no data available for the dispersion, the criterion R90 has been checked on data. Therefore only the viscous criterion is taken into account in Table 7.5. This projectile is no more available on the market.

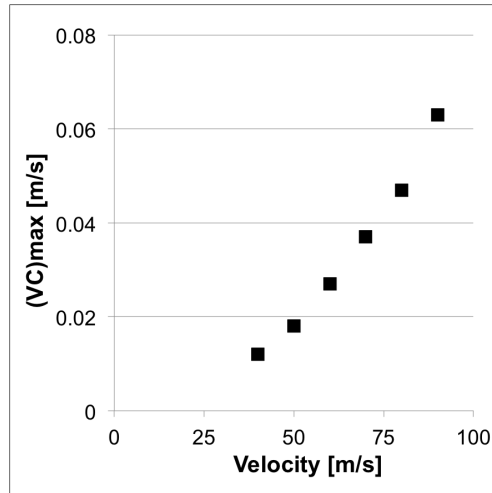


Figure 7.17. $(VC)_{max}$ for different impact velocities of the RB1FS projectile on thorax.

Projectile velocity [m/s]	$(VC)_{max}$ [m/s]	Result/failed criterion
90	0.07	OK
80	<0.07	OK
70	<0.07	OK
60	<0.07	OK
<i>Green=acceptable</i>		

Table 7.5. Final result of the lethality analysis of the RB1FS projectile.

7.2.5.2 Conclusions

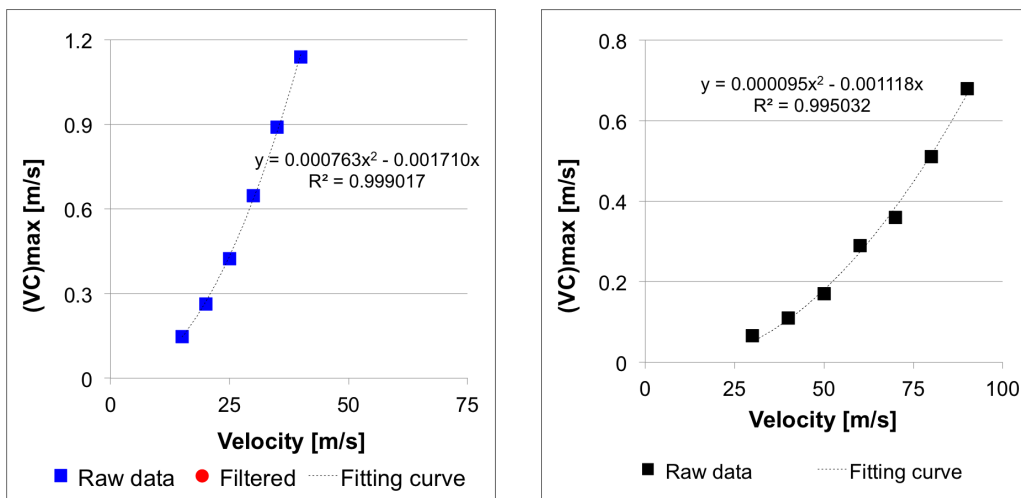
The RB1FS projectile has been evaluated. It has been shown that the displacements at all impact velocities are very low, so are the $(VC)_{max}$. The reason is its low mass and its small diameter. There is no minimal safe distance. Therefore the RB1FS projectile can be used at close distance without higher risk of injury. Nothing could be said about the R90 criterion as data are not available. But this projectile is no longer available on the market.

7.2.6 L5 projectile evaluation

The L5 projectiles are the two projectile types used in Bir's experiments for the validation of the SHTIM in Chapter 5.1. These types of projectiles are from the old generation and are no longer used. The first projectile L5 used in condition A and B, has a mass of 140 g and a length of 100 mm and the second one L5 used in condition C have a mass of 30 g and a length of 20 mm. Both projectiles have been already described in Chapter 5.1.

The results of their evaluation given in Figure 7.18 will be used in the next section as a comparison between the old KENLW generation and the new KENLW generation projectiles in term of risk of injury. Using the viscous criterion, the critical velocities are determined: 34 m/s for the projectile L5@140g (Figure 7.18(a)) and 98 m/s for the projectile L5@30g (Figure 7.18(b)). No dispersion data is available.

Because of its higher mass, the risk of injury due to the impact of L5@140g projectile is higher than the one by an impact of L5@30g projectile. The $(VC)_{max}$ values for the L5@30g projectile are in the same range as the ones for the 40 mm sponge grenades assessed previously.



(a) projectile L5@140g - Condition A-B (b) projectile L5@30g - Condition C
Figure 7.18. $(VC)_{max}$ for different impact velocities of the L5 projectiles on thorax.

7.2.7 Summary of all projectiles

Figure 7.19 gives a summary on the lethality of the different projectiles. It should be pointed out that

- There are three groups of projectiles that can be considered: the projectiles with low mass and small diameter like the FN303, the large diameter projectiles among which the 40 mm sponge grenade projectile and the large diameter projectiles which are heavy like the L5@140g projectile.
- There is no risk of skeletal fracture of thorax for light projectiles as the $(VC)_{max}$ values are extremely low at the considered velocities. But
- Heavier projectiles tend to induce higher risk of injury if shot at higher velocity. Increasing the mass of the projectile must be coupled with a reduction of the velocity at which it is shot to avoid increased risk of skeletal injury. This seems to show that the momentum has something to do with the risk of injury. More investigation is needed to see if an injury criterion based on momentum could be appropriate. Nevertheless, in a previously published paper [178], different injury criterion candidates were investigated and evaluated. The impulse (implicitly the momentum) was one of the candidates that have shown a high correlation in term of injury. But they have to be experimentally validated.
- The graph shows that there is not great difference in terms of $(VC)_{max}$ between the different 40 mm sponge grenades although the difference in mass can be great for example for the NS projectile, the heaviest one which performs well. But in terms of minimum firing distances, a difference of 1m or 2m can make a huge difference in terms of injury.
- The L5@30g, an old generation projectile with its mass in the same range as the 40 mm sponge grenades has similar performance in term of risk injury based on the viscous criterion. The mass is therefore one of driving parameter in term of injury.
- There are two ways of reading the graph. Firstly, at a given velocity, the heavier projectile has the higher lesional potential as long as $(VC)_{max}$ is concerned. Secondly, to have the same level of injury risk, the lighter projectile should be shot at higher velocity.

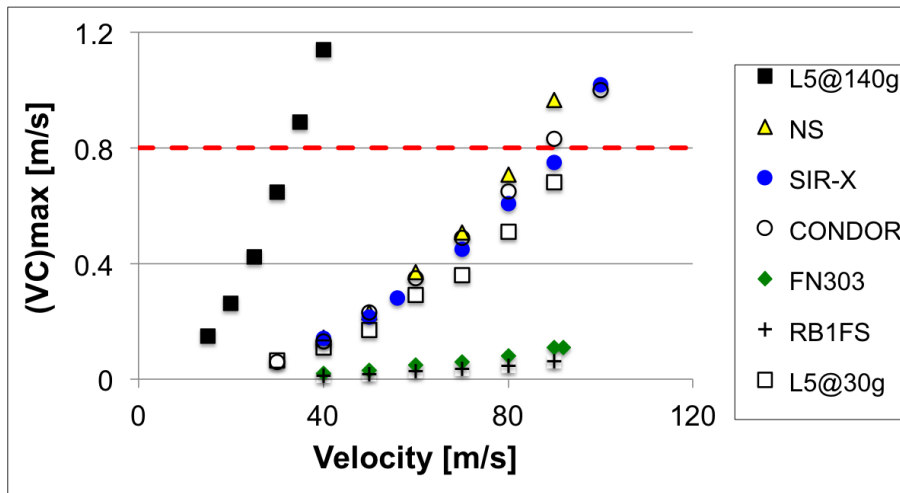


Figure 7.19. $(VC)_{max}$ summary for impact of different projectiles on thorax.

7.3 Comparison of SHTIM model and the 3RBID surrogate

In order to see the consistency of numerical results, comparison is made with the 3RBID. The 3RBID responses are defined through corridors to take into account the dispersion. To have the same basis of comparison, all the displacement results from which the $(VC)_{max}$ is calculated are filtered with a CFC-1666 filter. First, the 3RBID setup is briefly described, then comparison for the 3RBID and the SHTIM is made for the SIR-X projectile, then a comparison is made between all the projectiles followed finally by a discussion of the results.

7.3.1 3RBID setup

The 3RBID is another means available in ABAL for KENLW thoracic impact evaluation, validated on the same data as the SHTIM. It is then natural to compare both means to see their consistency regarding this evaluation. The 3RBID experimental setup is shown in Figure 7.20. The main components are:

1. A pneumatic launcher for launching the projectile at desired velocity.
2. A light screen barrier for the impact velocity measurement.
3. A set of led lights for the high-speed camera.
4. A high-speed camera for impact event record used especially for projectile velocity measurement, projectile displacement tracking and projectile attitude...

5. The 3RBID system
6. A 3RBID is equipped with an accelerometer for the displacement determination.
7. The impacting projectile.

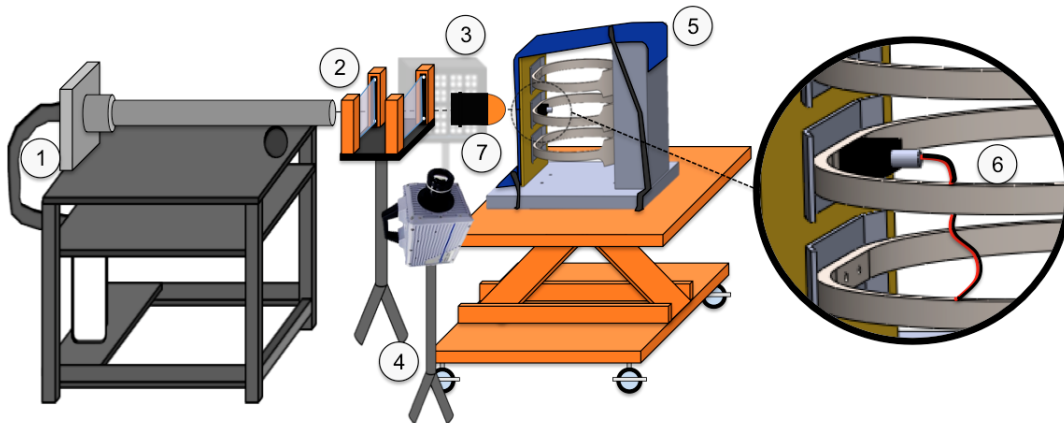


Figure 7.20. 3RBID setup.

7.3.2 Comparison of SHTIM and 3RBID for SIR-X projectile

The SIR-X projectile has been chosen as one of the projectiles for validation of the thorax surrogates (numerical or experimental) in the standardisation framework within NATO (section ??) [5]. Corridors were defined based on the impact of SIR-X on 3RBID for validation purpose of the thorax surrogate. The surrogate is considered as validated if the surrogate responses fall within these corridors and the $(VC)_{max}$ values within the 3RBID boundaries. Two impact velocities were defined 56 m/s and 86.5 m/s.

As one can see in Figure 7.21, satisfying results are achieved. The numerical curve has been shifted in time because of the difficulty to set the effective initial time of the impact in the experiments.

For the displacement, as previously mentioned during its validation, the SHTIM gives a response that is stiffer than the experimental results. This can be seen as the correspondence is good in the early stage of the impact. After, the SHTIM displacement fails to fall within the corridors. Therefore, it is one of the perspective to improve the compliance of the SHTIM.

Table 7.6 shows that for a velocity of 56 m/s, the SHTIM $(VC)_{max}$ value falls within the 3RBID boundaries and the value at 86.5 m/s fails to satisfy the require-

ment with an error of 6%. Concerning $(VC)_{max}$, good correspondence is found even though all the values fall in the lower limit of the corridors.

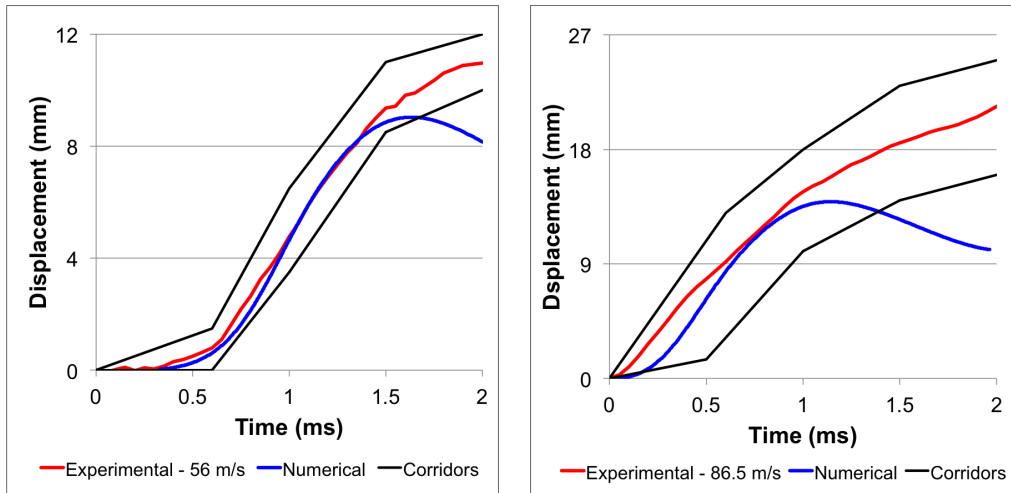


Figure 7.21. Comparison between 3RBID and SHTIM surrogates at 56 m/s and 86.5 m/s.

Velocity [m/s]	$(VC)_{max}$ [m/s]	
	Numerical	3RBID limits
56.0	0.30	[0.28-0.32]
86.5	0.73	[0.78-0.85]

Table 7.6. Comparison of numerical results with the 3RID $(VC)_{max}$ results.

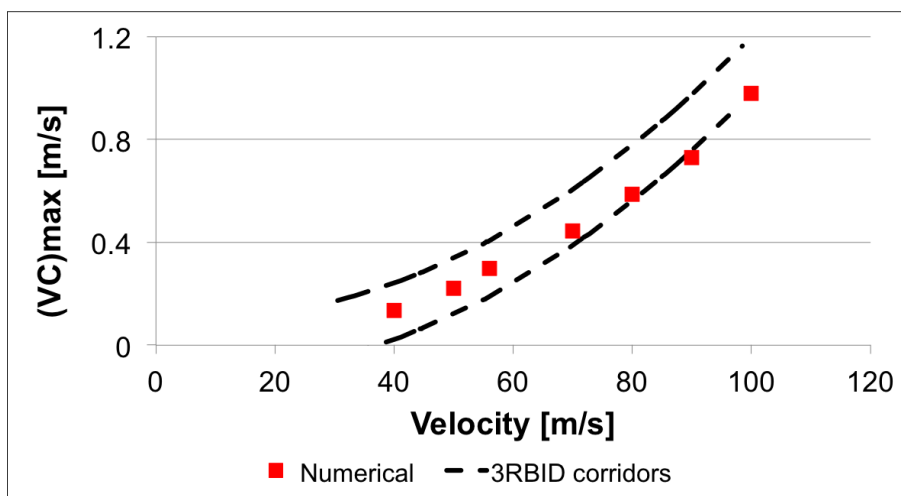


Figure 7.22. Comparison between 3RBID and numerical results for SIR-X projectile.

7.3.3 Comparison of SHTIM and 3RBID for all projectiles

7.3.3.1 Results

Results of the comparison between the SHTIM and 3RBID for the different projectiles are given in Figure 7.23.

7.3.3.2 Discussions

For each projectile, a brief analysis is performed.

SIR-X projectile

The SIR-X (Figure 7.23(a)) has already been analysed in section 7.3.2.

CONDOR projectile

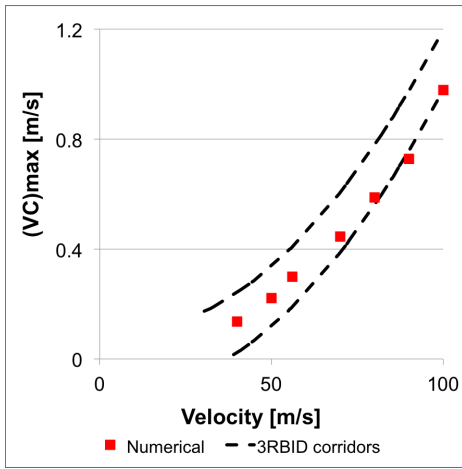
Figure 7.23 shows that in the considered domain, all the numerical data fall within the corridors. Because of missing data at lower velocities, there is a gap and no extrapolation of the corridors has been made in the lower velocity range. Nevertheless, it can thus be concluded that a good correspondence is achieved between the 3RBID and the SHTIM.

NS projectile

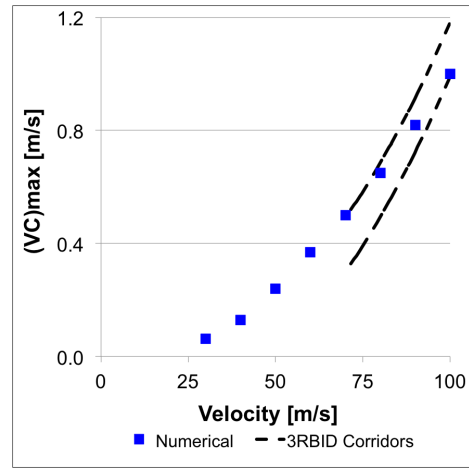
Good agreement is found with the NS projectile. The SHTIM predicts values that are in the lower limit of the 3RBID corridors.

FN303 projectile evaluation and the L5@30g projectile

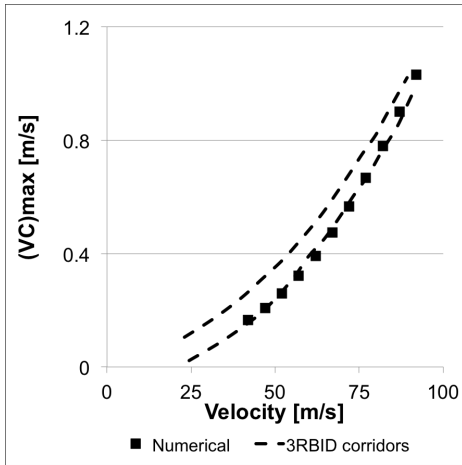
The SHTIM underestimates the values of $(VC)_{max}$ i.e. the risk of injury compared to the 3RBID.



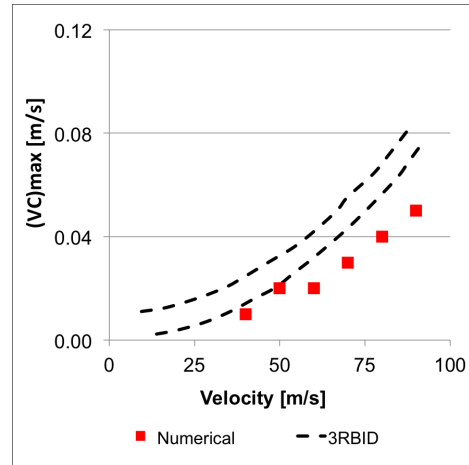
(a) SIR-X



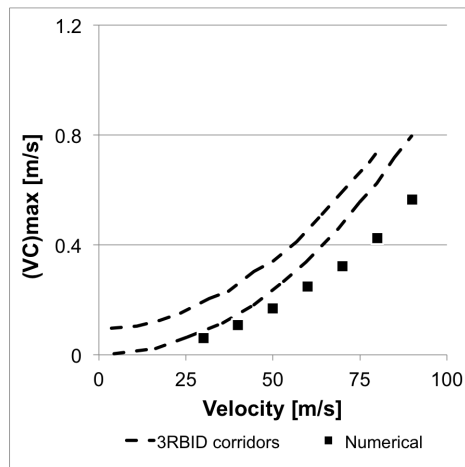
(b) CONDOR



(c) NS



(d) FN303



(e) L5@30g

Figure 7.23. Comparison of SHTIM and 3RBID results.

7.4 Conclusions

Evaluation of KENLW projectiles has been carried out. This evaluation consisted in determining the minimal firing distance to avoid serious injury. Critical velocity for each projectile was determined from which the safe distance was derived using the retardation relation.

Assessing the KENLW projectile lethality is very complicated because of the wide variety of projectiles currently in use, their characteristics as well as the complexity that characterises the interaction between the projectile and the human body.

For deformable projectiles, an in-depth analysis was performed. It has been shown that the dynamics of the deformable projectiles on the thorax surrogate can be compared to its dynamics on RW but at a lower velocity. A comparison of the projectile with its assumed rigid projectile was performed in order to understand the difference in dynamics. The deformable projectile introduces a delayed effect in response compared to the rigid projectile. After this delayed effect, the projectile behaviour is similar to the rigid projectile to a certain extent.

Comparison was made between the SHTIM and the 3RBID. For heavier projectiles like the 40 mm sponge grenades, good correspondence has been achieved although the SHTIM $(VC)_{max}$ values were found in the lower limit of the 3RBID corridors except for the L5@30g projectile where the values are underestimated. For light projectiles like the FN303 projectile, the SHTIM underestimates the $(VC)_{max}$ results.

Chapter 8

Conclusions and avenues for future investigation

The purpose of this chapter is to highlight the aim and achievements of the present dissertation in order to summarize the key findings, and propose different axes where future investigations are possible.

8.1 Aim

The aim of this work was to develop a numerical tool for the injury risk assessment of non-penetrating thoracic impacts due to KENL projectiles. To do so, a thorax model (SHTIM) as well as FE models of six KENL projectiles were developed. For the risk assessment, the only injury that were investigated was the rib and sternal fracture.

8.2 Achievements and results

Three steps was considered for the assessment of the effects of KENL projectiles on thorax:

- The development of a thorax FE model. The geometry was generated with a CAD program and material models were taken from the literature. The model was validated using the biomechanical corridors generated from the impacts of stiff cylindrical projectiles on PMHS. This means that the numerical responses

of the thorax model, in terms of displacement and $(VC)_{max}$ should stay within the experimental corridors and boundaries.

- The development of projectile FE models. The geometry was generated with a CAD program. There are a variety of KENL projectiles. Some of them are no more in use like the L5 projectiles. Nowadays most of KENL projectiles are deformable projectiles like the 40 mm sponge grenades. There is one, the FN303 projectile which has a specific characteristics, it breaks at impact. Therefore each projectile has its own characteristics. This makes things not easy for the material modelisation. Two different approaches were investigated in order to characterize them.

In the first approach, the material models and material parameters of most projectiles were based on published data. The validation of the projectile was carried out. Using an iterative process within a limited range of model parameters, optimum model parameters were obtained by comparing the numerical results to the experimental ones, the results of the real firings of the same projectile on a rigid wall (RW) structure at different velocities.

For the 40 mm sponge grenades, a specific method was developed in order to characterize the projectile deformable nose. This method is based using the experimental results of the firing of the 40 mm sponge grenade on a rigid wall structure. The experimental signals (force, displacement as a function of time) were processed and engineering strain-stress curves were derived. These curves were used as loading curves in the material model for the nose. Using the reverse engineering method by comparing the numerical data to experimental ones, the deformable projectile material was determined. It is worth pointing out that for the sabot of the 40 mm sponge grenades, material characteristics was taken from literature. This method is cost-effective as with the results of the firings tests on RW, the characteristics of the nose material is obtained and at the same time the projectile FE model is validated. Moreover, the conditions of the tests are close to the operational conditions of the use of these projectiles.

- The risk assessment. With the validated thorax model and validated projectile models, one can proceed to the risk assessment. The viscous criterion used for injury risk assessment was defined by using stiff projectiles. But today, most of projectiles are deformable. Therefore, an assumption was made: this criterion is still valid for deformable projectiles. The risk assessment was then carried out by first numerically impacting the projectile and the thorax at different velocities. Secondly by processing the results, the viscous criterion is determined for each velocity. A critical velocity can then be determined for each projectile, corresponding to the velocity for which one obtains the

tolerance value of 0.8 m/s. It is the value of the criterion corresponding to the probability of 50 % of sustaining the skeletal thoracic injury of AIS>1. Using the retardation, a minimum firing distance was calculated. Below this distance, there is a higher risk of injury.

It has been shown that the bigger projectiles like the 40 mm sponge grenades shows a higher risk of sustaining skeletal fracture compared to the smaller projectiles like the FN303 projectile. There is no risk of skeletal injury with the smaller projectiles. One has to pay attention that only the risk of skeletal fracture has been considered. But smaller projectiles can present a risk of skin penetration, problematic that was not covered here.

A few years ago, ABAL acquired a thorax mechanical surrogate, the 3RBID for thoracic risk assessment. For different projectiles, biomechanical corridors were built. The performance of the SHTIM was then compared to the 3RBID based on these corridors. The numerical responses of the thorax model, in terms of displacement of the point of impact as a function of time, should stay within the 3RBID corridors and boundaries. Results show good correspondence especially for the bigger projectiles.

8.3 Avenues for future investigation

To improve some aspects, recommendations and future possible enhancements are proposed.

The only one criterion that was used is the viscous criterion. The SHTIM can be used for the investigation of new criteria. The results obtained in Chapter 6 show that the momentum can be a possible candidate. In Chapter 5, the energy dissipated into the thorax has been calculated. Further investigations can be made to see if this dissipated energy can be linked to the occurrence of injury.

The SHTIM can also be extended to other applications like the BAPT. The filling-up of the internal space of the SHTIM can help the study of blast effects or the propagation of waves into the body.

Finally, the major improvement that can be achieved is the development of a new anthropometric thorax FE model. The SHTIM is a model whose geometry has been simplified. Therefore the new model can take into account the real geometry of the thorax.

It has been found that adding a tensile curve to the SIR-X model improved the results. It is necessary to investigate this aspect in order to get more understanding of this aspect

Although the results of validation of many KENL projectiles were satisfying, investigating the possibility of using other material models could further improve the FE models.

Bibliography

- [1] M. Franke, C. Hesch, and P. Betsch. An augmentation technique for large deformation frictional contact problems. *International Journal for Numerical Methods in Engineering*, 94(5):513–534, May 2013. ISSN 1097-0207. doi: 10.1002/nme.4466. URL <http://onlinelibrary.wiley.com/doi/10.1002/nme.4466/abstract>.
- [2] C. Robbe. *Experimental Evaluation of the Thoracic Impact of Non-Lethal Projectiles*. PhD thesis, Royal Military Academy & University of Liège, 2013.
- [3] A Oukara. *Assessment of Non-Lethal Projectile Head Impacts*. PhD thesis, Royal Military Academy & University of Liège, 2015.
- [4] L. J. Gibson and M. A. Ashby. Cellular solids - structure and properties, isbn 0-521-49911-9. 2001.
- [5] NATO/PFP unclassified. STANREC 4744 ed. 3 (draft) - AEP-99 ed.A, vol.1 (draft) on thorax injury risk assessment of non-lethal projectiles.
- [6] L. R. G. Treloar. *The Physics of Rubber Elasticity*. Oxford University Press, USA, December 1975. ISBN 978-0-19-152330-4.
- [7] C. Bir. *The evaluation of blunt ballistic impacts of thorax*. PhD thesis, Wayne State University, 2000.
- [8] Sun Tzu. *The Art of War by Sun Tzu - Classic Collector's Edition: Includes The Classic Giles and Full Length Translations*. Special Edition Books, El Paso, Tex., reprint edition edition, June 2009. ISBN 978-1-934255-15-5.
- [9] N Davison. *'Non-Lethal' Weapons*. Palgrave Macmillan, Basingstoke ; New York, NY, 1st edition edition, July 2009. ISBN 9780230221062.
- [10] N Davison. The early history of non-lethal weapons, December 2006. URL http://www.bradford.ac.uk/acad/nlw/research_reports/docs/BNLWRP_OP1_Dec06.pdf.

- [11] Charlie Mesloh, Ross Wolf, Mark Henych, and Frank L. Thompson. Less Lethal Weapons for Law Enforcement: A Performance-Based Analysis. *Law Enforcement Executive Forum*, 8(1):17, 2008. URL <https://www.ncjrs.gov/App/publications/Abstract.aspx?id=243041>.
- [12] John B. Alexander. *Future War: Non-Lethal Weapons in Modern Warfare*. Thomas Dunne Books, 1st edition edition, April 1999. ISBN 9780312194161.
- [13] N Davison. *Non Lethal Weapons*. Global Issues, 2009.
- [14] R Scott. *Conflict without casualties: Non-lethal weapons in irregular warfare*. PhD thesis, Naval postgraduate School, Monterey, California, 2007.
- [15] G Allison and P Kelly. Non lethal weapons and capabilities. Concil on Foreign Relations, USA, <http://www.cfr.org/issue/nonlethal-weapons/ri61>, 2004. Accessed on 25 August 2015.
- [16] Erik L. Nutley. *Non-Lethal Weapons: Setting Our Phasers on Stun? Potential Strategic Blessings and Curses of Non-Lethal Weapons on the Battlefield - Schol.* Scholar's Choice, 2015. ISBN 978-1-297-04445-8.
- [17] Angela Hegarty. Observing the Rules of Law: Experiences from Northern Ireland. *Fordham Law Review*, 66(2), 1997. URL <http://ir.lawnet.fordham.edu/cgi/viewcontent.cgi?article=3402&context=flr>.
- [18] Brian Rappert. *Non-lethal Weapons as Legitimizing Forces?: Technology, Politics, and the Management of Conflict*. Psychology Press, 2003. ISBN 9780714654409.
- [19] The Focus. The principle of proportionality and the concept of margin of appreciation in human rights law. December 2013. URL http://www.doj.gov.hk/eng/public/basiclaw/basic15_2.pdf.
- [20] Georges-Henri Bricet des Vallons. L'arme non létale dans la stratégie militaire des Etats-Unis : imaginaire stratégique et genèse de l'armement. *Cultures & Conflits*, (67):63–82, November 2007. ISSN 1157-996X. doi: 10.4000/conflits.3116. URL <http://conflits.revues.org/3116>.
- [21] RTO. The Human Effects of Non-Lethal Technologies (Impacts humain des technologies non létales). Technical Report AC/323(HFM)TP/65, NATO.
- [22] C. Robbe, A. Papy, and N. Nsiampa. Impact measurements of different 40mm non-lethal sponge grenades. In Ernest Baker and Douglas Templeton, editors, *Ballistics 2011: 26th International Symposium*, volume 2. Ballistics Division

-
- of National Defense Industrial Association (NDIA) with the cooperation of the International Ballistics Society (ISB), September 12-16 2011.
- [23] DoD Executive Agent for Non-Lethal Weapons (NLW) and NLW Policy. USD (A&T) 3000.03E, US Department of Defense, April 2013.
- [24] Nick Lewer and N Davison. Non-lethal technologies - an overview. URL http://www.peacepalacelibrary.nl/ebooks/files/UNIDIR_pdf-art2217.pdf.
- [25] P. Thys, Th. Jacobs, L. Hougardy, and E. Lemaire. Les armes de neutralisation momentanée utilisant l'énergie cinétique. Technical report, GESLR - Groupe d'Etude des Systèmes à Létalité Réduite, November 2009. URL <http://www.violence.ulg.ac.be/armescinetiques.pdf>.
- [26] University of Nebraska Lincoln. Toxicology and exposure guidelines, Accessed, Augustus 2015. URL http://ehs.unl.edu/documents/tox_exposure_guidelines.pdf.
- [27] L Koene, F Id-Boufker, and A Papy. Kinetic non-lethal weapons. In *Netherlands Annual Review of Military Studies: Sensors, Weapons, C4I and Operations Research*, pages 9–24. Hupkens, T and Monsuur, H (EDS.), 2008.
- [28] Ken Hubbs and Klinger David. Impact Munitions Data Base of Use and Effects. Technical Report 204433, U.S. Department of Justice (NIJ), February 2004. URL <https://www.ncjrs.gov/pdffiles1/nij/grants/204433.pdf>.
- [29] Tibor Bartha. Non-lethal weapons in peace support operations. *AARMS - Informatics Robotics*, Vol. 2, No. 2:293–305, 2003.
- [30] Ahmad Mahajna, Nabil Aboud, Ibrahim Harbaji, Afo Agbaria, Zvi Lankovsky, Moshe Michaelson, Doron Fisher, and Michael M. Krausz. Blunt and penetrating injuries caused by rubber bullets during the Israeli-Arab conflict in October, 2000: a retrospective study. *Lancet (London, England)*, 359(9320): 1795–1800, May 2002. ISSN 0140-6736. doi: 10.1016/S0140-6736(02)08708-1.
- [31] W Bozeman and J Winslow. Medical aspects of less lethal weapons. *The Internet Journal of Rescue and Disaster Medicine*, 5(1):6. URL <http://print.ispub.com/api/0/ispub-article/7142>.
- [32] Miles G Tawell. *Kinetic Energy Less Lethal Weapons And Their Associated Blunt Trauma Injuries*. PhD thesis, Defense College of Management And Technology, 2005. URL <https://dspace.lib.cranfield.ac.uk/bitstream/1826/4655/1/Tawell%20PhD.pdf>.
-

- [33] Accessed 27 August 2015. URL https://en.wikipedia.org/wiki/Plastic_bullet.
- [34] Kevin Maguire, Declan M Hughes, M Sinead Fitzpatrick, Fergal Dunn, Laurence G R Roche, and Catherine J Baird. Injuries caused by the attenuated energy projectile: the latest less lethal option. *Emergency Medicine Journal : EMJ*, 24(2):103–105, February 2007. ISSN 1472-0205. doi: 10.1136/emj.2006.039503. URL <http://www.ncbi.nlm.nih.gov/pmc/articles/PMC2658181/>.
- [35] De Ganck Bruno. Evaluatie van minder letale kinetische wapens (in Dutch). Master's thesis, Royal Military Academy, Bruxelles, 2008.
- [36] Naval study board. *An Assessment of Non-Lethal Weapons Science and Technology*. National Academy of Sciences Naval Studies Board, 2003.
- [37] C. Robbe, E. Lemaire, A. Papy, and V Esters. *Traité de médecine légale, Chapitre "Armes non-létales"*. Deboek, 2011.
- [38] EWG-NLW (European Working Group Non-Lethal Weapons). Catalogue of weapons and ammunitions, Accessed on 21th April 2016. URL <http://www.non-lethal-weapons.org/>.
- [39] Romain Gouard. Definition of non-lethal simulating projectiles (in French). Master's thesis, Royal Military Academy, Bruxelles, 2015.
- [40] C. Bir, D. Viano, and A. King. Development of biomechanical response corridors of the thorax to blunt ballistic impacts. *Journal of Biomechanics*, 37: 73–79, 2004.
- [41] C. Bir, S. J. Stewart, and M. Wilhelm. Skin penetration assessment of less lethal kinetic energy munitions. *Journal of Forensic Sciences*, Vol 50(6):4, November 2005.
- [42] C. Bir, Steward S., and M. Wilhelm. Skin penetration assessment of kinetic energy munitions. Jane's Less-Lethal Weapons Conference, Leeds, unpublished, available at the author, 2005.
- [43] Belgium FN Herstal. Less lethal launcher fn303, 2006.
- [44] A. J. Ritchie. Plastic bullets: significant risk of serious injury above the diaphragm. *Injury*, 23(4):265–266, January 1992. ISSN 0020-1383. doi: 10.1016/S0020-1383(05)80013-0. URL <http://www.injuryjournal.com/article/S0020138305800130/abstract>.

-
- [45] M. Mackay. The increasing importance of the biomechanics of impact trauma. *Sadhana*, 32(4):397–408, December 2007. ISSN 0256-2499, 0973-7677. doi: 10.1007/s12046-007-0031-9. URL <http://link.springer.com/article/10.1007/s12046-007-0031-9>.
- [46] K. Schmitt, P. Niederer, and M. Muser. *Trauma biomechanics: accidental injury in traffic and sports*, volume 2nd edition. Springer, 2007.
- [47] Don Whitson. *A Guidebook for Less-Lethal devices*. The Pennsylvania State University, first edition edition, March 2010. URL [https://www.justnet.org/pdf/WPSTC-GUIDE-FINAL-\(2010.05.07\)-COMPLETE.pdf](https://www.justnet.org/pdf/WPSTC-GUIDE-FINAL-(2010.05.07)-COMPLETE.pdf).
- [48] R. Drake. *Thorax: Chapter 3 of Gray’s Basic Anatomy*. Churchill Livingstone, April 2012.
- [49] C. Dean and J. Pegington. *Core Anatomy for Students: Vol. 2: The Thorax, Abdomen, Pelvis and Perineum: Thorax, Abdomen, Pelvis and Perineum v. 2*. Bailliere Tindall, London, October 1995. ISBN 978-0-7020-2041-4.
- [50] K. P. Roberts and A. J. Weinhaus. Anatomy of the Thoracic Wall, Pulmonary Cavities, and Mediastinum. In Paul A. Iaizzo, editor, *Handbook of Cardiac Anatomy, Physiology, and Devices*, pages 25–50. Humana Press, 2005. ISBN 978-1-58829-443-2 978-1-59259-835-9. URL http://link.springer.com/chapter/10.1007/978-1-59259-835-9_3. DOI: 10.1007/978-1-59259-835-9_3.
- [51] Accessed 24 January 2016. URL <http://www.daviddarling.info/encyclopedia/R/rib-cage.html>.
- [52] Accessed 26 November 2015. URL <http://www.dreamstime.com/stock-image-man-anatomy-thorax-cutaway-heart-main-blood-veins-arterias-lungs-image31372971>.
- [53] Accessed 5th May 2016. URL http://fr.123rf.com/photo_19893709_man-anatomie-du-thorax-coupe-avec-le-coeur-avec-les-principaux-veines-du-sang-et-les-poumons-arteria.html.
- [54] K. Yuen. The Development of a Numerical Human Body Model for the Analysis of Automotive Side Impact Lung Trauma. January 2010. URL <https://uwspace.uwaterloo.ca/handle/10012/5005>.
- [55] C. Robbe, A. Papy, N. Nsiampa, and A. Oukara. A new thoracic surrogate for assessing the impact of kinetic energy non-lethal projectiles. In *PASS (Pass Armour Personal Symposium) conference proceedings, Nuremberg*, 2014.
-

- [56] D. Viano and A. King. *The Biomedical Engineering Handbook: Second Edition, chapitre "Biomechanics of Chest and Abdomen Impact"*, page 13. CRC, Springer, 2000.
- [57] E. Lemaire. Summary on impact impact projectiles (note de synthèse concernant les projectiles d'impact). In French, Not published, Available at request to the author, 2008.
- [58] J-P. Beauthier. *Traité de médecine légale*. De Boeck Supérieur, August 2011. ISBN 9782804163327.
- [59] N. Thoongsuwan, J. P. Kanne, and E. J. Stern. Spectrum of blunt chest injuries. *J Thorac Imaging*, 20(2), 2005. Accessed 02 October 2015. URL http://seicat.org/repo/static/public/documentos/top10-toracica/Spectrum_of_Blunt_Chest_Injuries.pdf.
- [60] "Non-lethal" Police Weapons, Accessed, 10 September 2015. URL <https://voodoodr06.wordpress.com/2011/11/14/non-lethal-police-weapons/>.
- [61] <http://www.cainstructor.com/Articles/Kinetics.html>. May the proper force be with you, Accessed, 17 September 2015.
- [62] C. A. Bir and D. C. Viano. Biomechanical predictor of commotio cordis in high-speed chest impact. *The Journal of Trauma*, 47(3):468–473, September 1999. ISSN 0022-5282.
- [63] J. Horsch, I. Lau, D. Viano, and D. Andrzejak. Mechanism of abdominal injury by steering wheel loading. In *29th Stapp Crash Car Conference*, 1985.
- [64] D. Viano and I. Lau. Thoracic impact: A viscous tolerance criterion. In *Tenth International Conference on Experimental Safety Vehicles*, 1985.
- [65] Accessed 30th April 2016. URL http://web.iitd.ac.in/~achawla/public_html/736/13-biomech-II-thorax-low-extremity-v2.pdf.
- [66] G. Lu and T. X. Yu. *Energy Absorption of Structures and Materials*. Elsevier, October 2003. ISBN 9781855738584.
- [67] J. Widder. Assessing the blunt trauma potential of free flying projectiles for development and safety certification of non lethal kinetic impactors. Battelle Columbus operations, <http://www.dtic.mil/cgi-bin/GetTRDoc?AD=ADA351147>, 1998; Accessed, March 2013.
- [68] L. W. Schneider, A. I. King, and M. S. Beebe. Design requirements and specifications: Thorax abdomen development task - interim report: Trauma

-
- assessment device development program. November 1989. URL <http://trid.trb.org/view.aspx?id=344025>.
- [69] NATO. Test methodology for protection of vehicle occupants against anti-vehicular landmine effects, chapter 3 - injury criteria and tolerance levels". RTO-TR-HFM-090, not published, <https://www.cso.nato.int/pubs/rdp.asp?RDP=RTO-TR-HFM-090>, 2007.
- [70] VPAM. General basis for ballistic material, construction and product testing. Technical Report VPAM-APR 2006, VPAM (Association of Test Laboratories for bullet resistance materials and constructions, 2009-05-14.
- [71] M. Maldague. Evaluation of some methods in order to determine v50. In *PASS (Pass Armour Personal Symposium) conference proceedings, Brussels - Belgium*, 2008.
- [72] M. Maldague. Evaluation of the gauss probability function in case of low (high) values of perforation probability. In *PASS (Pass Armour Personal Symposium) conference proceedings, Quebec - Canada*, 2010.
- [73] J. Widder, C. Perhala, and J. Rascoe. Caseless, variable velocity systems for precision non-lethal fires to beyond 100 meters - part ii: Terminal effects study, selection of projectile parameters. *The AMMTIAC WSTIAC Journal, Volume 1, Number 2*, 1(2).
- [74] Scott R. Lucas, Joseph C. McGowan, Tack C. Lam, Gary T. Yamaguchi, Matthew Carver, and Andrew Hinz. Assessment of the TASER XREP blunt impact and penetration injury potential using cadaveric testing. *Journal of Forensic Sciences*, 58 Suppl 1:S60–68, January 2013. ISSN 1556-4029. doi: 10.1111/j.1556-4029.2012.02298.x.
- [75] NATO. Dat 11 blunt trauma experts workshop final report. Unpublished, Shared within the OTAN DAT and LCG groups, 2010.
- [76] NATO. The unsuitability of kinetic energy and the blunt criterion bc as criteria for assessing blunt trauma by a low lethality projectile. Unpublished, communication during the meeting NATO-LCG-DSS-NLC-SG-NLKE-TOE, 2012.
- [77] J. Pavier, A. Langlet, N. Eches, J. Jacquet, and R. Cayzac. Analysis of existing injury criteria in order to evaluate the severity of thoracic impact injury. In *Ballistics 2011: 26th International Symposium*, 2011.
-

- [78] C. Bir and D. Viano. Design and injury assessment criteria for blunt ballistic impacts. *The journal of Trauma, injury, infection, and critical care*, page 7, 2004.
- [79] D. Viano. Biomechanical responses and injuries in blunt lateral impact. In *33rd Stapp Car Crash Conference*, pages 113–142, 1989.
- [80] J. Cavanaugh, Y. Zhu, and Y. Huang. Injury and response of the thorax in side impact cadaveric tests. In *Proceedings of the 37th Stapp Car Crash Conference*, pages 199–222, 1993.
- [81] M. Courtney and A. Courtney. Apparent measurement errors in "Development of biomechanical response corridors of the thorax to blunt ballistic impacts". *arXiv:0812.4755 [physics]*, December 2008. URL <http://arxiv.org/abs/0812.4755>. arXiv: 0812.4755.
- [82] NATO. Comments from france on the document: The evaluation of blunt ballistic impact of the thorax by bir - wsu (unpublished). communication lors de la réunion NATO-LCG-DSS-NLC-SG-NLKE-TOE, mars 2012, non publiée.
- [83] J. N. Kianianthra and D. T. Willke. Comparative performance of SID, BIOSID, and EUROSID in lateral, pendulum, sled, and car impacts. *13th International conference on Experimental Safety Vehicles*, November 1991. Accessed, 28th September 2015. URL <http://www.sbes.vt.edu/gabler/publications/ESV-1991-S5-0-16.pdf>.
- [84] B.N. Fides, J.C. Lan, J. Lenard, , and A.P. Vulcan. Passenger car and occupant injury : Side impact crashes,. Number ISBN 642 510995. Monash University Accident Research Center, April 1994.
- [85] *Computational Models for the Human Body: Special Volume*. Elsevier Science Ltd, Amsterdam, 1 edition edition, July 2004. ISBN 9780444515667.
- [86] K. Meersman. Comparison between the force wall method and the surrogate method for the characterization of non-lethal impacts. Master's thesis, Royal Military Academy, 2014.
- [87] C. Maurah and S. Guha. Updates to LSTC's Ls-Dyna anthropomorphic models, 2012. Accessed, 27th September 2015. URL <http://www.dynalook.com/international-conf-2012/occupantsafety08-c.pdf>.
- [88] Humanetics. <http://www.humaneticsatd.com/crash-test-dummies>, Accessed, 01 October 2015.

-
- [89] LSTC (Livermore Software Technology Corporation). <http://www.lstc.com/products/models/dummies>, Accessed, 01 October 2015.
- [90] P. Forbes. *Development of a Human Body Model for the Analysis of Side Impact Automotive Thoracic Trauma*. PhD thesis, Waterloo, Ontario, Canada, 2005.
- [91] K. H. Yang, J. Hu, N. A. White, Albert I. King, Clifford C. Chou, and Priya Prasad. Development of numerical models for injury biomechanics research: a review of 50 years of publications in the Stapp Car Crash Conference. *Stapp Car Crash Journal*, 50:429–490, November 2006. ISSN 1532-8546.
- [92] W. Shen, Y. Niu, R. F. Mattrey, A. Fournier, J. Corbeil, Y. Kono, and J. H. Stuhmiller. Development and validation of subject-specific finite element models for blunt trauma study. *Journal of Biomechanical Engineering*, 130(2): 021022, April 2008. ISSN 0148-0731. doi: 10.1115/1.2898723.
- [93] C. Brett M. *A Numerical Side Impact Model to Investigate Thoracic Injury in Lateral Impact Scenarios*. PhD thesis, University of Waterloo - Ontario - Canada, 2009.
- [94] M. Jansová, L. Hynčič, H. Čechová, J. Toczyski, D. Gierczycka-Zbrozek, and P. Baudrit. Evaluation of human thorax FE model in various impact scenarios. *Applied and Computational Mechanics*, 9(1), June 2015. ISSN 2336-1182. URL <http://www.kme.zcu.cz/acm/acm/article/view/285>.
- [95] A. Bouamoul and H. Levesque. Development and validation of a finite element human torso model under blunt ballistic impact drdc-valcartier-tm-2006-560, 2007. URL <http://pubs.rddc.gc.ca>.
- [96] A. D. Greer. *Deng Y., Kong W., Ho H., Development of a Finite Element Human Thorax Model for Impact Injury Studies*. PhD thesis, Waterloo - Ontario - Canada, 2006.
- [97] D. Cronin, C. Salisbury, and A. Greer. Numerical modeling of blast injuries - phase I report. Technical report, DRDC Valcartier, Canada, March 2004.
- [98] D. Cronin, C. Salisbury, and A. Greer. Numerical modeling of blast injuries - phase II report. Technical report, DRDC Valcartier, Canada, October 2004.
- [99] D. Cronin, C. Salisbury, and A. Greer. Numerical modeling of blast injuries - phase III report. Technical report, DRDC Valcartier, Canada, March 2005.
-

- [100] N. M. Thota, J. A. Eepaarachchi, and K. T. Lau. Develop and validate a biomechanical surrogate of the human thorax using corrugated sheets: a feasibility study. In *Proceedings of the 7th Australasian Congress on Applied Mechanics (ACAM 2012)*, pages 220–229, Canberra, Australia, December 2012. Engineers Australia. ISBN 9781922107619. URL <http://www.engineersaustralia.org.au/acam-2012/>.
- [101] N. Thota, J. Epaarachchi, and K. T. Lau. Viscous criterion and its relation with the projectile-thorax energy interactions. Melbourne, Australia, November 2014. Institution of Engineers, Australia. URL <http://eprints.usq.edu.au/26503/>.
- [102] AFRL (The Air Force Research Laboratory). Non-lethal weapons human effects. <http://www.dtic.mil/ndia/2008Intl/HumanEffectsandEffectiveness.pdf>, May 2008. Accessed September 29th, 2015.
- [103] J. Simonds. Non-lethal weapons human effects. AFRL (Air Force Research Laboratory), May 2014 - Accessed September 29th, 2015.
- [104] S. Roth, F. Torres, P. Feuerstein, and K. Thorat-Pierre. Anthropometric dependence of the response of a thorax FE model under high speed loading: validation and real world accident replication. *Computer Methods and Programs in Biomedicine*, 110(2):160–170, May 2013. ISSN 1872-7565. doi: 10.1016/j.cmpb.2012.11.004.
- [105] A. A. Goumtcha. *Modélisation centrée sur l’homme par la méthode des éléments finis: Application à la biomécanique des chocs dans un contexte civil et militaire*. PhD thesis, Université de Technologie Belfort-Montbéliard, 2015.
- [106] LSTC (Livermore Software Technology Corporation), Accessed, 01 October 2015. URL <http://www.lstc.com>.
- [107] T. Belytschko, W. K. Liu, B. Moran, and K. Elkhodary. *Nonlinear Finite Element for Continua and Structures*. John Wiley & Sons, November 2013. ISBN 9781118700082.
- [108] S. R. Wu and L. Gu. *Introduction to the Explicit Finite Element Method for Nonlinear Transient Dynamics*. Wiley, Hoboken, NJ, 1st edition, September 2012. ISBN 978-0-470-57237-5.
- [109] C. Oomens, M. Brekelmans, and F. Baaijens. *Biomechanics: Concepts and Computation*. Cambridge University Press, Cambridge; New York, 1st edition, August 2010. ISBN 9780521172967.

-
- [110] J.-F. Imbert. *Analyse des structures par éléments finis*. Editions Cépaduès, Toulouse, September 1979. ISBN 2854280512.
- [111] A.J.M. Spencer. *Continuum Mechanics*. Dover Publications, Mineola, N.Y, dover edition, April 2004. ISBN 9780486435947.
- [112] O. C. Zienkiewicz and R. L. Taylor. *The Finite Element Method: The Basis*. Butterworth-Heinemann Ltd, Oxford ; Boston, 5th revised edition, 2000. ISBN 978-0-7506-5049-6.
- [113] O. C. Zienkiewicz and R. L. Taylor. *The Finite Element Method: Solid Mechanics*. Butterworth-Heinemann Ltd, Oxford ; Boston, 5th revised edition, 2000. ISBN 978-0-7506-5055-7.
- [114] R. D. Cook, D. S. Malkus, M. E. Plesha, and R. J. Witt. *Concepts and Applications of Finite Element Analysis*. Wiley, New York, NY, 4th edition, October 2001. ISBN 978-0-471-35605-9.
- [115] L. Noels. *Contributions aux algorithmes d'intégration temporelle conservant l'énergie en dynamique non-linéaire des structures*. PhD thesis, Université de Liège, 2004.
- [116] LS-DYNA theory manual, 2013. Accessed 14th November 2015. URL http://ftp.lstc.com/anonymous/outgoing/trent001/manuals/ls-dyna_theory_manual_2006.pdf.
- [117] T.R Chandrupatla and A.D Belegundu. *Introduction to Finite Elements In Engineering*. Prentice Hall, 3th edition, 2002.
- [118] D.L. Logan. *A first Course in the Finite Element Method*. Chris Carson, 4th edition, 2007. ISBN 0-534-55298-6.
- [119] X. Bourdin, X. Trosseille, P.Petit, and P. Beillas. Comparison of tetrahedral and hexahedral meshes for organ finite element modeling: An application to kidney impact, 2007. Accessed, 7th October 2015. URL <http://www-nrd.nhtsa.dot.gov/pdf/esv/esv20/07-0424-W.pdf>.
- [120] M. A. Puso and J. Solberg. A stabilized nodally integrated tetrahedral. *International Journal for Numerical Methods in Engineering*, 67(6):841–867, August 2006. ISSN 1097-0207. doi: 10.1002/nme.1651. URL <http://onlinelibrary.wiley.com/doi/10.1002/nme.1651/abstract>.
- [121] R. Boman. *Développement d'un formalisme Arbitraire Lagrangien Eulérien tridimensionnel en dynamique implicite. Application aux opérations de mise à forme*. PhD thesis, Université de Liège, 2010.
-

- [122] J. Donea, A. Huerta, J. P. Ponthot, and A. Rodríguez-Ferran. Arbitrary lagrangian–eulerian methods. In *Encyclopedia of Computational Mechanics*. John Wiley & Sons, Ltd, 2004. ISBN 9780470091357. URL <http://onlinelibrary.wiley.com/doi/10.1002/0470091355.ecm009/abstract>.
- [123] G. R. Liu and M. B. Liu. *Smoothed Particle Hydrodynamics: A Meshfree Particle Method*. World Scientific, October 2003. ISBN 981-238-456-1. URL <http://www.worldscientific.com/worldscibooks/10.1142/5340>.
- [124] J. J. Monaghan. SPH without a Tensile Instability. *Journal of Computational Physics*, 159(2):290–311, April 2000. ISSN 0021-9991. doi: 10.1006/jcph.2000.6439. URL <http://www.sciencedirect.com/science/article/pii/S0021999100964398>.
- [125] N-H. Kim. *Introduction to Nonlinear Finite Element Analysis*. Springer US, Boston, MA, 2015. ISBN 978-1-4419-1745-4, 978-1-4419-1746-1. URL <http://link.springer.com/10.1007/978-1-4419-1746-1>.
- [126] T. A. Laursen. *Formulation and treatment of frictional contact problems using finite elements*. PhD thesis, Standford University, 1992.
- [127] M. Legrand. *Modèles de prédiction de l’interaction rotor/stator dans un moteur d’avion*. PhD thesis, Ecole Centrale de Nantes; Université de Nantes., 2005.
- [128] Peter Wriggers. *Computational Contact Mechanics*. Springer Berlin Heidelberg, Berlin, Heidelberg, 2006. ISBN 978-3-540-32608-3 978-3-540-32609-0. URL <http://link.springer.com/10.1007/978-3-540-32609-0>.
- [129] M. Gitterle. *A dual mortar formulation for finite deformation frictional contact problems including wear and thermal coupling*. PhD thesis, Technical University of Munich, 2012.
- [130] Z-H. Zhong. *Finite Element Procedures for Contact-Impact Problems*. Oxford University Press, Oxford ; New York, 1st edition, July 1993. ISBN 978-0-19-856383-9.
- [131] N. Grujovic S. Vulovic, M. Zivkovic and R. Slavkovic. Ballistic skin simulant. *Journal of the Serbian Society for Computational Mechanics JSSCM*, 1(1), 2007.
- [132] R. Weyler, J. Oliver, T. Sain, and J.C. Cante. On the contact domain method: A comparison of penalty and Lagrange multiplier implementations. *Computer Methods in Applied Mechanics and Engineering*, 205-208:

-
- 68–82, January 2012. ISSN 00457825. doi: 10.1016/j.cma.2011.01.011. URL <http://linkinghub.elsevier.com/retrieve/pii/S0045782511000120>.
- [133] Oasys Limited. Oasys LS-DYNA environment 8.1 volume 3 User guide, May 2001. Accessed 14th November 2015.
- [134] Accessed on 26 January 2016. URL <http://www.d3view.com/contact-interior-for-foams-honeycombs-and-rubbers/>.
- [135] H. T. Banks, Shuhua Hu, and Zackary R. Kenz. A brief review of elasticity and viscoelasticity. *Advances in Applied Mathematics and Mechanics*, 3 (1):1–51, May 2010. URL https://www.researchgate.net/publication/265279377_A_Brief_Review_of_Elasticity_and_Viscoelasticity#full-text.
- [136] A. F. Bower. *Applied Mechanics of Solids*. CRC Press, Boca Raton, 1st edition, October 2009. ISBN 9781439802472.
- [137] Kyriacos A. *Introduction to Continuum Biomechanics*. Morgan and Claypool Publishers, San Rafael, Calif., 1st edition, July 2008. ISBN 978-1-59829-617-4.
- [138] J. H. Argyris, K. Straub, and Sp. Symeonidis. Nonlinear finite element analysis of elastic systems under nonconservative loading—natural formulation part II. Dynamic problems. *Computer Methods in Applied Mechanics and Engineering*, 28(2):241–258, September 1981. ISSN 0045-7825. doi: 10.1016/0045-7825(81)90107-9. URL <http://www.sciencedirect.com/science/article/pii/0045782581901079>.
- [139] Century Dynamics. Autodyn introductory training course, 2004.
- [140] R. W. Ogden. Large Deformation Isotropic Elasticity - On the Correlation of Theory and Experiment for Incompressible Rubberlike Solids. *Proceedings of the Royal Society of London. Series A, Mathematical and Physical Sciences*, 326(1567):565–584, 1972. ISSN 0080-4630. URL <http://www.jstor.org/stable/77930>.
- [141] W. W. Feng and J.O. Hallquist. On constitutive equations for elastomers and elastomeric foams, 2003. URL <https://www.dynamore.de/en/downloads/papers/03-conference/material/on-constitutive-equations-for-elastomers-and>.
- [142] R. Dupuis M.L. Ju, H. Jmal and E. Aubry. Visco-hyperelastic model for polyurethane foam: comparison among polynomial, reduced polynomial, and ogden models. In *21ème Congrès Français de Mécanique, Bordeaux - France*,
-

2013. URL http://documents.irevues.inist.fr/bitstream/handle/2042/52238/a_5218UI7P.pdf?sequence=1.
- [143] S. Doll and K. Schweizerhof. *On the development of volumetric strain energy functions*. PhD thesis, University of Karlsruhe, Accessed on 24th April 2016. URL https://www.ifm.kit.edu/download/1999_SD_KS_1.pdf.
- [144] V. Effinger and P. Du Bois. Modelling of viscoelastic material with ls-dyna, Ulm, 2012 - Accessed 28th November 2015. URL <https://www.dynamore.de/de/download/papers/ls-dyna-forum-2012/documents/materials-4-1>.
- [145] S. Kolling and A. Haufe. Material models of polymers for crash simulation. an overview with focus on the dynamic test setup impetus by 4a engineering, 2009. Accessed 10th November 2015. URL <https://www.dynamore.de/de/download/presentation/dokumente/2009-4a-impetus/ls-dyna-materialmodelle-fuer-polymere-werkstoffe.pdf>.
- [146] P. Du Bois. A simplified approach to the simulation of rubber-like material under dynamic material, Ulm, 2003 - Accessed 28th November 2015. URL <https://www.dynamore.de/en/downloads/papers/03-conference/material/a-simplified-approach-to-the-simulation-of-rubber/view?searchterm=paul+du+bois>.
- [147] E. Serifi, A. Hirth, S. Matthaei, and H. Müllerschön. Modelling of foams using MAT 83 – preparation and evaluation of experimental data. *4th European LS-DYNA Users Conference*, 2008. URL <http://www.dynalook.com/european-conf-2003/modelling-of-foams-using-mat83-2013-preparation.pdf>.
- [148] S. Kolling, P. A. Du Bois, and D. J. Benson. A simplified rubber model with damage, Bamberg 2005 - Accessed 28th November 2015. URL <https://www.dynamore.de/de/download/papers/forum05/a-simplified-rubber-model-with-damage>.
- [149] LS-DYNA keyword user's manual volume II material models, 2013. Accessed 10th November 2015. URL http://ftp.lstc.com/anonymous/outgoing/trent001/manuals/LS-DYNA_manual_Vol_II_R7.0.pdf.
- [150] N. Nsiampa, C. Robbe, A. Oukara, and A. Papy. Development of a thorax finite element model for thoracic injury assessment. In *8th European LS-DYNA Users Conference, Strasbourg - France*, 2011.
- [151] V. D'Otreppe. *From medical imaging to finite element simulation, a contribution to mesh generation-free formulations of tetrahedra*. PhD thesis, University of Liège, 2012.

-
- [152] L. Hynčík M. Jansová. Evaluation of human thorax FE model in various impact scenarios. *Applied and Computational Mechanics*, 9(1):5–20, 2015.
- [153] R. Kant R. Verhoeve and L. Margerie. Advances in numerical modelling of crash dummies, Accessed 28th of April 2016. URL <http://www-nrd.nhtsa.dot.gov/pdf/esv/esv17/Proceed/00007.pdf>.
- [154] P. Vezin and J.P. Verriest. Developement of a set of numerical human models for safety, Accessed 28th fo April 2016. URL <http://www-nrd.nhtsa.dot.gov/pdf/esv/esv19/05-0163-o.pdf>.
- [155] APROSYS. Integrated project on advanced protection systems (ap-90-0005), 2014. Accessed 28th of April 2016. URL http://www.transport-research.info/sites/default/files/project/documents/20120313_144837_42330_Final%20SP5%20report%20AP-90-0005.pdf.
- [156] F. T. Stumpf and R. J. Marczak. Optimization of constitutive parameters for hyperelastic model satisfying the baker-ericksen inequalities. In Eduardo Dvorkin, Marcela Goldschmit, and Mario Storti, editors, *Mecanica Computacional*, volume XXIX, pages 2901–2916. Asociacion Argentina de Mecanica Computacional, 18-15 Noviembre 2010.
- [157] H. Zheng. *On the predictive capability and stability of rubber material models*. Thesis, Massachusetts Institute of Technology, 2008. URL <http://dspace.mit.edu/handle/1721.1/45144>.
- [158] J Stitzel, F Gayzik, J Hoth, J Mercier, D Gage, K Morton, S Duma, and R Payne. Development of a finite element-based injury metric for pulmonary contusion part i: Model development and validation. *Stapp Car Crash Journal*, 49:271–289, 2005.
- [159] D. L. Vawter. A finite element model for macroscopic deformation of the lung. *Journal of Biomechanical Engineering*, 102(1):1–7, February 1980. ISSN 0148-0731. doi: 10.1115/1.3138193. URL <http://dx.doi.org/10.1115/1.3138193>.
- [160] N. Nsiampa, C. Robbe, A. Oukara, and A. Papy. Sensibility study of viscous criterion for kinetic energy non lethal projectile thoracic impacts. In *International Symposium of Ballistics 2013 proceedings*, 2013.
- [161] N. Nsiampa, C. Robbe, A. Oukara, and A. Papy. Comparison of less lethal 40 mm sponge projectile and the 37 mm projectile for injury assessment on human thorax. In *10th International Conference on the Mechanical and Physical Behaviour of Materials under Dynamic Loading-DYMAT 2012*, EDP Sciences, Freiburg, Germany, September 2-7, 2012.
-

- [162] A. Tamura, I. Watanabe, and K. Miki. Elderly human thoracic FE model development and validation. In *Proceedings of the 19th International Technical Conference on the Enhanced Safety of Vehicles (ESV)*, 2005. URL <http://wbl.db.lievers.net/10057055.html>.
- [163] I.S. Han, Y.E. Kim, and C. Soo-won. Effects of aging factors on thoracic injury risk under blunt impact loading. *International Journal of Precision Engineering and Manufacturing*, 16(4):813–821, April 2015. ISSN 2234-7593, 2005-4602. doi: 10.1007/s12541-015-0107-0. URL <http://link.springer.com/article/10.1007/s12541-015-0107-0>.
- [164] J.D. Stitzel, J. M. Cormier, E. A. Kennedy J. T. Barretta, E. P. Smith, A. L. Rath, S. M. Duma, and F. Matsuoka. Defining regional variation in the material properties of human rib cortical bone and its effect on fracture prediction. volume 47, pages 243–265, 2003.
- [165] D. Subit, E. de Dios del Pozo de Dios, J. Valazquez-Ameijide, C. Arregui-Dalmases, and J. Crandall. Tensile material properties of human rib cortical bone under quasi-static and dynamic failure loading and influence of the bone microstructure on failure characteristics. *arXiv:1108.0390 [physics]*, August 2011. URL <http://arxiv.org/abs/1108.0390>. arXiv: 1108.0390.
- [166] D. Luong, D. Pinisetty, and N. Gupta. Compressive properties of closed-cell polyvinyl chloride foams at low and high strain rates: Experimental investigation and critical review of state of the art. *Composites Part B: Engineering*, 44(1):403–416, January 2013. ISSN 1359-8368. doi: 10.1016/j.compositesb.2012.04.060. URL <http://www.sciencedirect.com/science/article/pii/S1359836812002995>.
- [167] J. E. Field, S. M. Walley, N. K. Bourne, and J. M. Huntley. Experimental methods at high rates of strain. *Journal de Physique IV - Proceedings*, 04(C8): 20, 1994. doi: 10.1051/jp4:1994801.
- [168] D.S. Cronin, C.P. Salisbury, and C.R. Horst. High rate characterization of low impedance materials using a polymeric split hopkinson pressure bar, 2006 - Accessed 21 October 2015. URL <http://sem-proceedings.com/06s/sem.org-2006-SEM-Ann-Conf-s15p05-High-Rate-Characterization-Low-Impedance-Materials-Using-Polymeric.pdf>.
- [169] B. Song and W. Chen. Split hopkinson pressure bar techniques for characterizing soft materials. *Latin American Journal of Solids and Structures, an ABCM Journal*, 2(2):113–152, June 2005. ISSN 1679-7825. URL <http://www.lajss.org/index.php/LAJSS/article/view/73>.

-
- [170] A. Oukara, C. Robbe, N. Nsiampa, and A. Papy. The influence of experimental environment on the piezoelectric force measurement. In *Fifth International Conference of Metrology - CAFMET Comité Africain de Métrologie, Pretoria, South Africa*, 2014.
- [171] D.M.W.M. de Vries. Characterization of polymeric foams, July 2009. URL http://www.mate.tue.nl/mate/pdfs/10702_sec.pdf.
- [172] C. Robbe, N. Nsiampa, A. Papy, and A. Oukara. Practical considerations for using high-speed camera to measure dynamic deformation occurring at the impact of a kinetic energy non-lethal weapon projectile on ballistic simulant. In *Pass conference proceedings, Nuremberg*, 2012.
- [173] N. Nsiampa, C. Robbe, A. Oukara, and A. Papy. Dynamic characterization of kinetic energy non-lethal deformable projectiles using experimental stress-strain curves. In R.G Ames and R.D. Boeka, editors, *International Symposium of Ballistics 2014 proceedings*, pages pages 1642–1651, September 22-26, 2014.
- [174] P.A. Du Bois, M. Koesters, T. Frank 2, and S. Kolling. Crashworthiness analysis of structures made from polymers, Bamberg 2004 - Accessed 28th November 2015. URL <http://citeseerx.ist.psu.edu/viewdoc/download?rep=rep1&type=pdf&doi=10.1.1.208.607>.
- [175] B. Croop and H. Lobo. Selecting material models for the simulation of foams in LS-DYNA. In *7th European LS-DYNA Conference*, DYNAmore GmbH, Salzburg, Austria, May 14-15, 2009.
- [176] Accessed 15 March 2016. URL http://ansys.net/ansys/papers/nonlinear/conflong_hyperel.pdf.
- [177] Accessed, 27th February 2016. URL <http://www.dynasupport.com/tutorial/ls-dyna-users-guide/energy-data>.
- [178] N. Nsiampa, C. Robbe, A. Papy, A. Oukara, and V. Chaidron. Comparison of thoracic injury criteria for non-lethal impacts using numerical simulations. *7th European Symposium on Non-Lethal Weapons 2013 proceedings*, June 3-5 2013.

Annexes

Annex A

A few key results of the WSU study by C. Bir

The results presented in this Annex consist of the displacement biomechanical corridors not included in the main document obtained via the firing of non-lethal projectiles at a PMHS thorax at WSU, conducted by C. Bir [7]. Measurements for the $(VC)_{max}$ criterion for all of the tests carried out are presented.

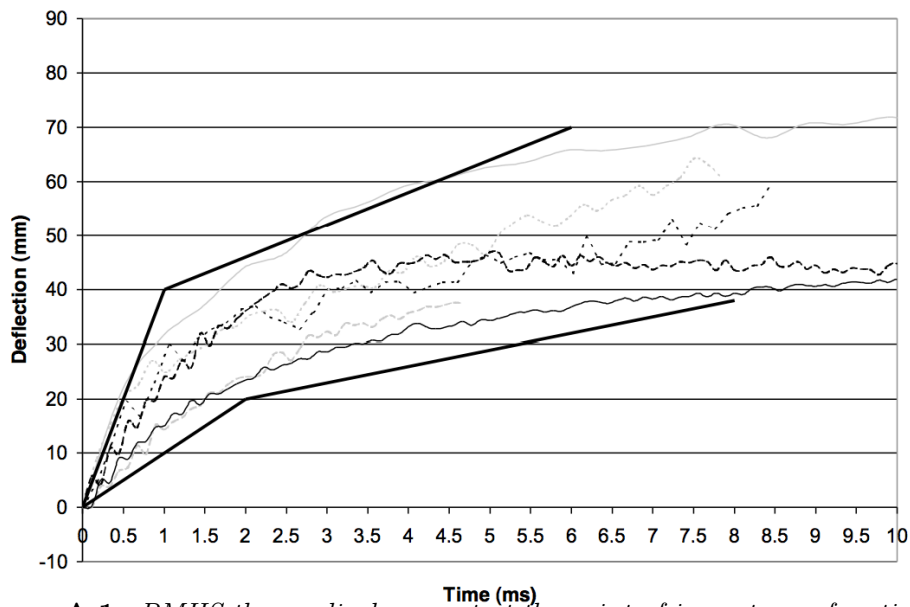


Figure A.1. *PMHS thorax displacement at the point of impact as a function of time for impact condition B [7].*

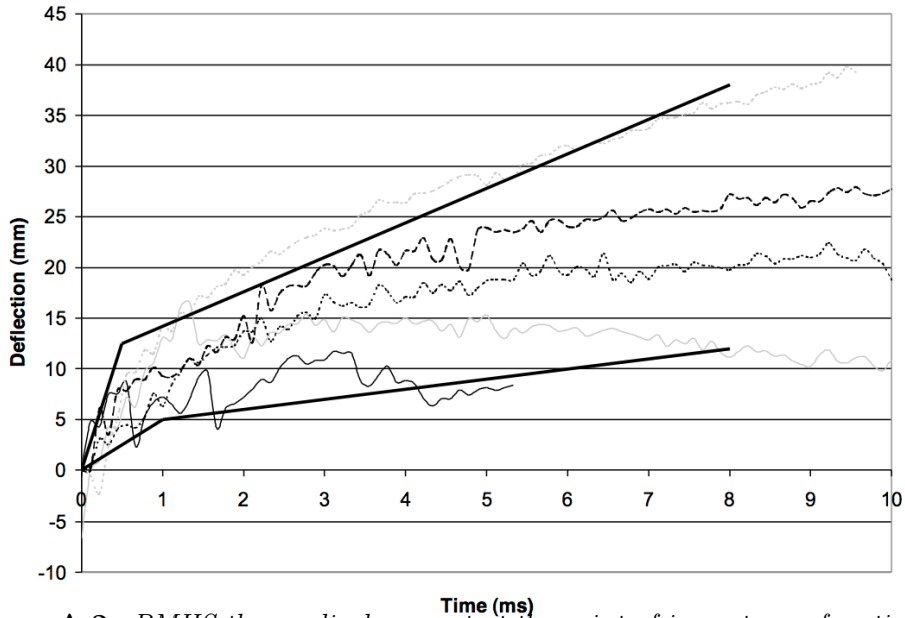


Figure A.2. PMHS thorax displacement at the point of impact as a function of time for impact condition C [7].

Specimen ID	Impact condition	VC _{max}	AIS
NIJ10	A	.51	0
NIJ11	A	.24	0
NIJ12	A	.46	0
NIJ13	A	.24	0
NIJ8	A	.26	0
NIJ7	B	1.97	2
NIJ8	B	2.35	2
NIJ10	B	2.18	2
NIJ11	B	1.01	3
NIJ13	B	.65	2
NIJ9	C	.14	0
NIJ10	C	.59	0
NIJ11	C	.24	0
NIJ12	C	.60	2
NIJ13	C	.30	0

Table A.1. Measured $(VC)_{max}$ values obtained while firing non-lethal projectiles on PMHS thorax, condition A, B and C [7].

Annex B

Influence of HU and SHAPE parameters

The results presented in this Annex show a sensitivity study of HU and SHAPE parameters of the hyperelastic model (*MAT_SIMPLIFIED RUBBER/FOAM) implemented in LS-DYNA.

Figure B.1 and Figure B.2 shows the effect of the HU parameter on the impact force and the displacement of the projectile respectively. Figure B.3 and Figure B.4 shows the effect of the SHAPE parameter on the impact force and the displacement respectively. Figure B.5 and Figure B.6 shows the effect of each parameter on the corresponding internal energy.

HU parameter and SHAPE parameter has an influence on the unloading. During the loading phase, there is no difference in the curves. When HU decreases, the dissipation increases. The effect is more highlighted with the HU parameter which is the hysteresis parameter. The effect of the SHAPE is very limited.

Normally without dissipation, all the energy stored on the projectile is recovered. But decreasing the HU parameter has a dissipative effect as represented in the figure B.5. The main parameter for dissipation is HU.

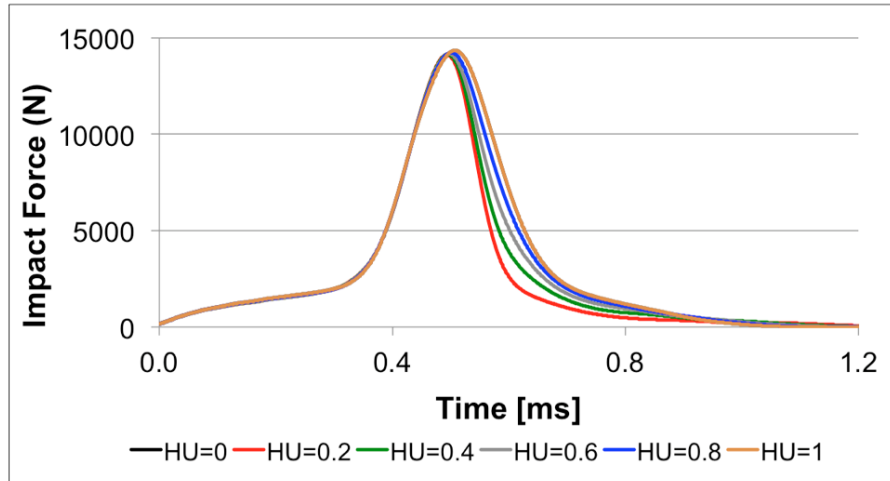


Figure B.1. *SIR-X* impact force on rigid wall as a function of time at $v=61$ m/s.

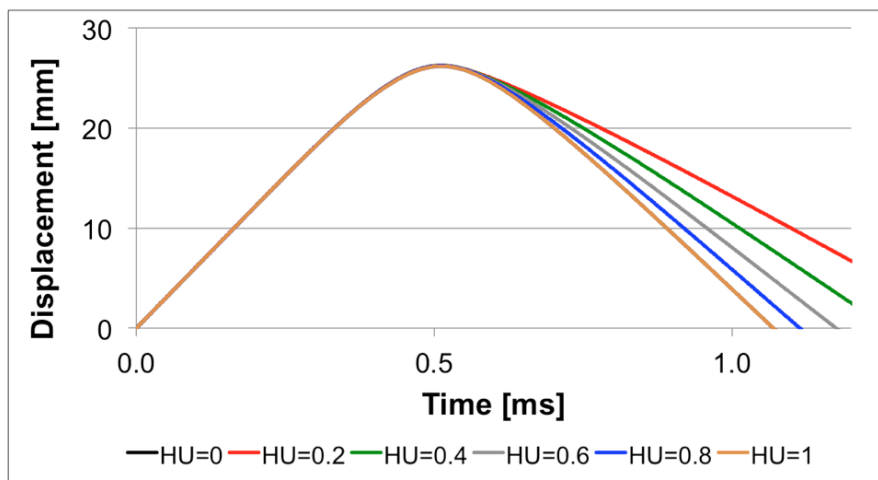


Figure B.2. Displacement of the rear face of the *SIR-X* projectile as a function of time at $v=61$ m/s.

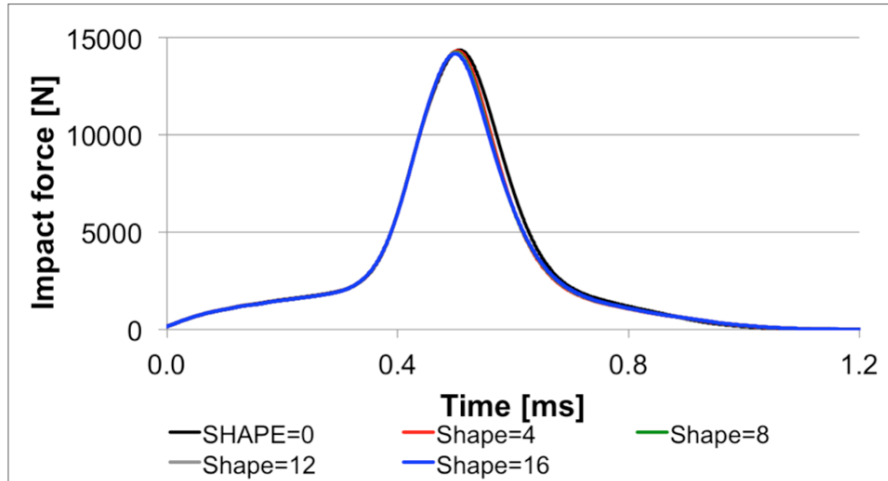


Figure B.3. *SIR-X* impact force on rigid wall as a function of time at $v=61$ m/s.

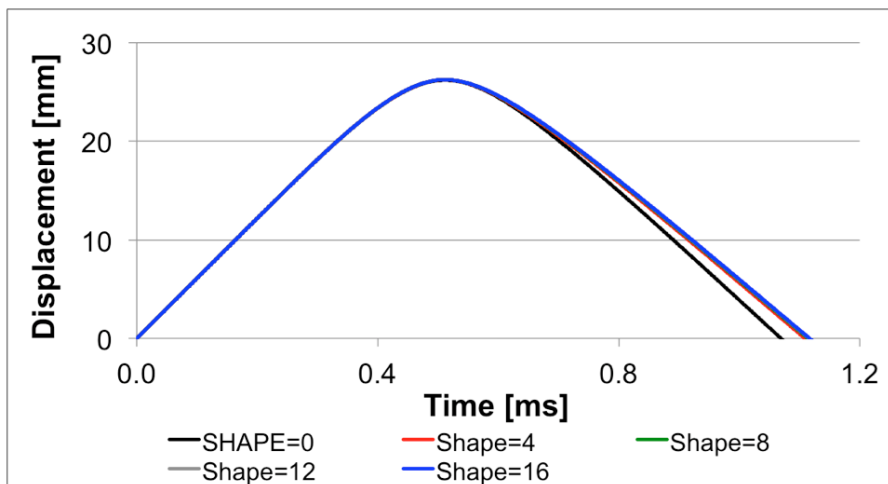


Figure B.4. *Displacement of the rear face of the SIR-X projectile as a function of time at $v=61$ m/s.*

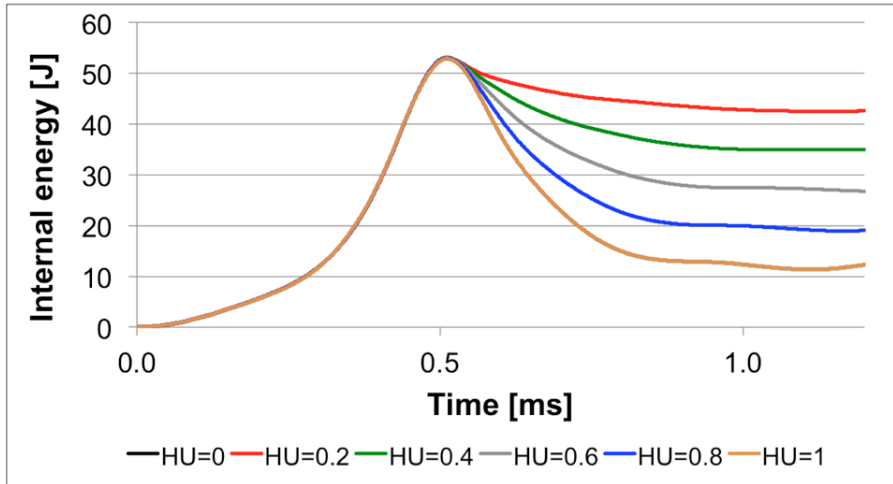


Figure B.5. Internal energy of the SIR-X projectile as a function of time at $v=61$ m/s.

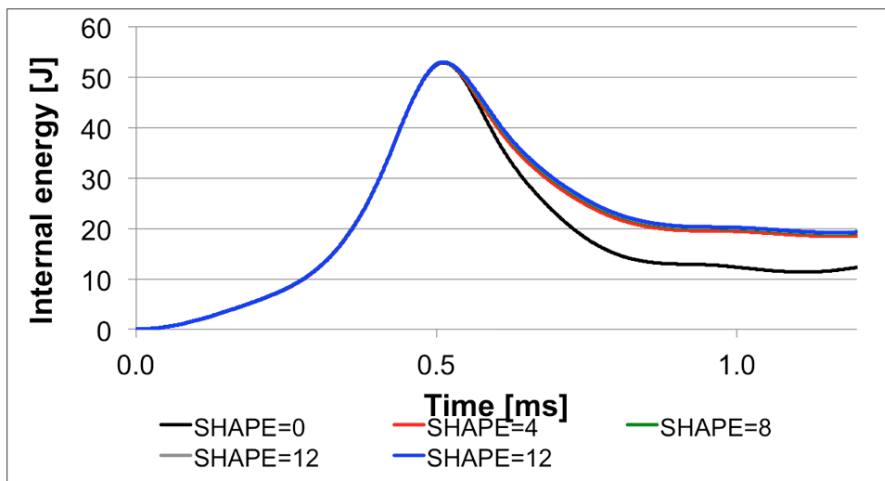


Figure B.6. Internal energy of the SIR-X projectile as a function of time at $v=61$ m/s.

Annex C

Publications in the framework of the present thesis

1 As first author

1.1 Articles in a peer-reviewed journal

1.2 Conference proceedings and presentations

- N. Nsiampa, C. Robbe, A. Oukara, and A. Papy. Development of a thorax finite element model for thoracic injury assessment. In *8th European LS-DYNA Users Conference*, Strasbourg , France, 2011.
- N. Nsiampa, C. Robbe, and A. Papy. Development of a thorax CT-scan based finite element model for thoracic injury assessment. In *Fifth International Conference on Advanced COmputational Methods in ENgineering (ACOMEN 2011)*, Liège, Belgium, 2011.
- N. Nsiampa, C. Robbe, A. Oukara, and A. Papy. Comparison of less lethal 40mm sponge projectile and the 37 mm projectile for injury assessment on human thorax. In *10th International Conference on the Mechanical and Physical Behavior of Materials under Dynamic Loadings-DYMAT2012*, EDP Sciences, Freiburg, Germany, 2012.
- N. Nsiampa, C. Robbe, A. Oukara, and A. Papy. Investigation of non-lethal projectile injury on thorax using laboratory test data. In *Aeroballistic Range Association (ARA) Meeting*, Brussels, Belgium, 2012.

- N. Nsiampa, C. Robbe, A. Oukara, and A. Papy. Sensibility study of viscous criterion for kinetic energy non-lethal projectile thoracic impacts. *27th International Symposium on Ballistics*, pages 547-557, Edited by Wickert M. and Salk M., Freiburg, Germany, 2013.
- N. Nsiampa, C. Robbe, A. Papy, and A. Oukara. Comparison of thoracic injury criteria for non-lethal impacts using numerical simulations. In *7th European Non-Lethal Weapon Symposium*, Fraunhofer ICT, Ettlingen, Germany, 2013.
- N. Nsiampa, C. Robbe, A. Papy, and A. Oukara. Dynamic characterization of kinetic energy non-lethal deformable projectiles using experimental stress-strain curves. In *28th International Symposium on Ballistics*, Edited by R.G Ames and R.D Boeka , pages 1642D1651, Atlanta, USA, 2104.

2 As co-author

2.1 Articles in a peer-reviewed journal

- A. Oukara, C. Robbe, N. Nsiampa, and A. Papy. Injury Risk Assessment of Non-lethal Head impact, *The Open Biomedical Engineering Journal*. 8: 75-83, Bentham Open, 2014.
- C. Robbe, N. Nsiampa, A. Oukara, and A. Papy. Quantification of the uncertainties of high-speed camera measurements. *International Journal of Metrology and Quality Engineering*, 5(2) 9-17, EDP Sciences, 2014.

2.2 Conference proceedings and presentations

- A. Papy, C. Robbe, N. Nsiampa, A. Oukara, and J Goffin. Definition of a standardized skin penetration surrogate for blunt impacts. In *IRCOBI Conference*, Dublin, Ireland, 2012.
- A. Oukara, C. Robbe, N. Nsiampa, and A. Papy. Experimental study of kinetic energy non-lethal projectiles impacts. In *Aeroballistic Range Association (ARA) Meeting*, Brussels, Belgium, 2012.
- C. Robbe, N. Nsiampa, A. Oukara, and A. Papy. Development of a tracking software for assessing the impacts of kinetic energy non-lethal weapon projectiles. In *Aeroballistic Range Association (ARA) Meeting*, Brussels, Belgium, 2012.

-
- C. Robbe, N. Nsiampa, A. Papy, and A. Oukara. Practical considerations for using high-speed camera to measure dynamic deformation occurring at the impact of a kinetic energy non-lethal weapon projectile on ballistic simulant. In *PASS conference proceedings*, WIWeB, Nuremberg, Germany, 2012.
 - A. Oukara, C. Robbe, N. Nsiampa, and A. Papy. Assessment of kinetic energy non-lethal projectile impacts using a validated finite element head model. In *7th European Non-Lethal Weapon Symposium*, Fraunhofer ICT, Ettlingen, Germany, 2013.
 - A. Papy, C. Robbe, N. Nsiampa, and A. Oukara. Enhancement of a skin penetration surrogate for non-lethal kinetic impacts. *27th International Symposium on Ballistics*, pages 558-563, Edited by Wickert M. and Salk M., Freiburg, Germany, 2013.
 - A. Oukara, C. Robbe, N. Nsiampa, and A. Papy. Comparison of the lethality of different kinetic energy non-lethal projectiles using a new French assessment approach for head impacts. In *27th International Symposium on Ballistics*, pages 564-575, Edited by Wickert M. and Salk M., Freiburg, Germany, 2013.
 - C. Robbe, N. Nsiampa, A. Oukara, and A. Papy. An hybrid experimental/numerical method to assess the lethality of a kinetic energy non-lethal weapon system. *27th International Symposium on Ballistics*, pages 482-493, Edited by Wickert M. and Salk M., Freiburg, Germany, 2013.
 - C. Robbe, N. Nsiampa, A. Oukara, and A. Papy. A complete injury assessment of FN303 and FN303p impacts. In *7th European Non-Lethal Weapon Symposium*, Fraunhofer ICT, Ettlingen, Germany, 2013.
 - C. Robbe, N. Nsiampa, A. Oukara and A. Papy. A new thoracic surrogate for assessing the impact of kinetic energy non-lethal projectiles. In *PASS conference proceedings*, Cambridge, United Kingdom, 2014.
 - A. Oukara, C. Robbe, N. Nsiampa, A. Papy, and J Martino. The influence of experimental environment on the piezoelectric force measurement. In *6th International Metrology Conference CAFMET2014*, Pretoria, South Africa, 2014.
 - A. Papy, C. Robbe, N. Nsiampa, A. Oukara, and T Dombard. Influence of Counter-Measures on Kinetic Energy Non-Lethal Weapons. In *8th European Non-Lethal Weapon Symposium*, Fraunhofer ICT, Ettlingen, Germany, 2015.
 - C. Robbe, N. Nsiampa, A. Papy, A. Oukara, and L Fizaine. Guidelines to develop kinetic energy non-lethal projectiles. In *8th European Non-Lethal Weapon Symposium*, Fraunhofer ICT, Ettlingen, Germany, 2015.

- A. Oukara, C. Robbe, N. Nsiampa, and A. Papy. Assessment methods for the non-lethal projectile head impact injury prediction. In *8th European Non-Lethal Weapon Symposium*, Fraunhofer ICT, Ettlingen, Germany, 2015.

3 Works conducted as supervisor by the present thesis author

- N. Maes, Etude paramétrique d'impacts thoraciques non létaux. Master thesis, Royal Military Academy, Brussels, Belgium, 2011.
- V. Chaidron, Contribution à la simulation numérique d'impacts thoraciques avec des armes cinétiques à létalité réduite. Master thesis, Royal Military Academy, Brussels, Belgium, 2012.
- S. Derwael. Bijdrage tot de evaluatie van niet letale projectielen aan de hand van numerieke simulaties. Master thesis, Royal Military Academy, Brussels, Belgium, 2015.